Stratigraphy, Chronology, Tectonics, and Subsurface Properties of Ganymede: Deciphering Light Terrain Formation Using Impact Craters

DISSERTATION

Thesis submitted in partial fulfilment of the requirements of the degree Doctor rer. nat. of the
Faculty of Environment and Natural Resources,
Albert-Ludwigs-Universität Freiburg im Breisgau, Germany
by

Namitha Rose Baby

Freiburg im Breisgau

2024

Dean: Dr. Frank Preusser

Supervisor and first reviewer: Prof. Dr. Thomas Kenkmann

Second reviewer: Prof. Dr. Harald Hiesinger

Second supervisor: Prof. Dr. Ralf Jaumann

Date of the defense:

STATEMENT OF AUTHORSHIP

I hereby certify that this thesis has been composed by myself and describes my own work unless otherwise acknowledged in the text. All references and verbatim extracts have been quoted and all sources of information have been specifically acknowledged. This thesis has not been accepted in any previous application for a degree.

Ich erkläre hiermit, dass ich die vorliegende Arbeit ohne unzulässige Hilfe Dritter und ohne Benutzung anderer als der angegebenen Hilfsmittel angefertigt habe. Die aus anderen Quellen direkt oder indirekt übernommenen Daten und Konzepte sind unter Angabe der Quelle gekennzeichnet. Insbesondere habe ich hierfür nicht die entgeltliche Hilfe von Vermittlungs- bzw. Beratungsdiensten (Promotionsberaterin/-berater oder anderer Helferinnen/Helfer) in Anspruch genommen. Die Arbeit wurde bisher weder im In- noch im Ausland in gleicher oder ähnlicher Form einer anderen Prüfungsbehörde vorgelegt.

Freiburg, den 16.01.2024 Unterschrift _____

1

From the Sidereus Nuncius (1610)[1]

„ . . . I therefore concluded and decided unhesitatingly, that there are three stars in the heavens moving about Jupiter, as Venus and Mercury round the Sun; which at length was established as clear as daylight by numerous subsequent observations. These observations also established that there are not only three, but four, erratic sidereal bodies performing their revolutions round Jupiter...the revolutions are so swift that an observer may generally get differences of position every hour . . . " Galileo Galilei

SIDEREVS
NVNCIVS
MAGNA, LONGEQVE ADMIRABILIA
Spectacula pandens, suspiciendaque proponens
vnicuique, præsertim verò
PHILOSOPHIS, atq; ASTRONOMIS, quæ à
GALILEO GALILEO
PATRITIO FLORENTINO
Patauini Gymnasij Publico Mathematico
PERSPICILLI
Nuperrimè à se reperta beneficio sunt obseruata in LVNÆ FACIE, FIXIS IN-
NVMERIS, LACTEO CIRCVLO, STELLIS NEBVLOSIS,
Apprime verò in
QVATVOR PLANETIS
Circa IOVIS Stellam disparibus intervallis, atque periodis, celeri-
tate mirabili circumvolutis; suos, neminem hanc vsque
diem cognitos, nouissimè Author depræ-
hendit primus; atque
MEDICEA SIDERA
NVNCVPANDOS DECREVIT.

VENETIIS, Apud Thomam Baglionum. M DC X.
Superiorum Permissu, & Privilegio.

[1] Galileo's report about his discovery of four objects that appeared to form a straight line of stars near Jupiter in the *Sidereus Nuncius*.

SUMMARY

Ganymede's geologic evolution has intrigued scientists since the first images were sent back from spacecraft visiting the Jovian system. In particular its unique surface features such as the complex network of light terrain that crisscross the ancient heavily cratered surface has been of major interest, since it has been formed during a period of geologic activity. Its formation is tightly related to Ganymede's internal evolution. In order to solve this relationship, it is needed to gain more insight into the stratigraphic position and the details of the formation process of the light terrain. Previous studies concentrated on the structural analysis of linear features in the dark and light terrain. In this work the focus lies on Ganymede's numerous impact craters and their potential to reveal the surface age and the stratigraphic position of the light terrain with respect to Ganymede's geologic evolution, how craters have been affected by the tectonic activity and which details can be derived about the light terrain formation processes due to the crater's potential to investigate the stratigraphy of Ganymede's subsurface.

The study was performed based on the data set collected by the Voyager, Galileo and Juno spacecrafts, which provide the only available data set with sufficient image resolution and coverage of Ganymede's surface so far. To address the research questions various methodologies were employed. Next to photogeological mapping techniques for defining and mapping geologic relevant surface units such as Ganymede's different terrain types as well as impact craters, measurements of the crater size-frequency distribution of dark and light terrain units were performed in order to derive their geologic ages and relative stratigraphy. Structural analysis as used in previous works for several dark and light terrains are applied to a special crater type, i.e. polygonal craters. The structural analysis of these craters in comparison to adjacent dark and light terrains were used for identifying which tectonic processes affected these craters and are responsible for their peculiar shape. The obtained results were then applied to evaluate the currently available crater counting models and their use to estimate the time and duration of the light terrain formation and thus to constrain the tectonic activity in Ganymede's geologic history. Furthermore, based on the recent knowledge about the impact process, the stratigraphy of the subsurface have been reconstructed for special crater types. The nature and distribution of their ejecta and depending on their position in either the dark or light terrain or at the border between them are used to investigate possible variations in the subsurface properties of Ganymede's dark and light terrain. This investigation explores any implications for the type of processes forming the light terrain in particular the mode of extension, whether it involves rifting or spreading.

The duration of this formation process of Ganymede's light terrain strongly depends on the cratering models used, specifically the Lunar-Derived chronology Model (LDM) and Jupiter-family Comet derived chronology Model (JCM) employed for deriving absolute crater ages. Using the LDM, the light terrains generally exhibit older ages and a shorter formation period compared to the JCM. However, both models support that Ganymede's light terrain began to form early in its history, with a short time gap of ~ 0.2 Ga between the end of dark terrain formation and the beginning of light terrain formation. The onset of tectonism in the formation of light terrains has been previously discussed to be attributed to various factors, including internal differentiation leading to global expansion, tidal heating due to Laplace resonance with Europa and Io, orbital recession, nonsynchronous rotation, and large impact events. Given the early start of the tectonic activity, internal differentiation and global expansion probably played a major role in the formation processes. It is possible that these factors or a combination of them contributed to the process and thus significantly affected the duration of the tectonic activity.

The presence of polygonal-shaped impact craters equally distributed across the surface, even in dark cratered terrains, furthermore support that Ganymede's tectonic activity not only concentrated on the light terrain, but that the dark cratered terrain also experienced normal faulting or spreading tectonism, leading to the gradual development of light terrain units. Polygonal craters suggest hidden fractures, which are indicators of the initiation of light terrain formation. During the modification stage of these craters, their rims aligned with tectonic linear structures through slumping or faulting along preexisting fracture and fault planes of weakness. These craters also support the idea that grooves and other fractures are indeed traces of faults.

Ganymede's unique dark ray and halo craters as well as bright ray craters emplaced onto the border between dark and light terrain support that the dark material of Ganymede’s ancient dark terrain forms a thin layer of less than 1 km on top of an icy crust with no significant differences in the subsurface properties of both terrains at greater depth. The in-depth analysis of dark halo craters located in Ganymede’s light terrain reveals significant heterogeneity in the uppermost portions of the icy crust at various locations. The presence of multiple layers of subsurface dark material is needed to explain the existence of small dark halo craters in the light terrain and their distribution of the dark ejecta deposits with maximum excavation depth of ~ 3 km. Such occurrences of near-surface dark terrain material imply a tectonic rifting mode as responsible for these portions of light terrain, indicating downfaulting of the dark terrain material in these locations.

ZUSAMMENFASSUNG

Die geologische Entwicklung Ganymeds fasziniert Wissenschaftler seit den ersten Bildern, die von Raumsonden, die das Jupitersystem besuchten, zurückgeschickt wurden. Vor allem dessen einzigartige geologischen Strukturen, wie das komplexe Netzwerk aus hellen Gebieten, welche die dunklen geologisch alten, dicht bekraterten dunklen Gebiete durchziehen, sind von großem Interesse, da sie während einer Periode globaler geologischer Aktivität entstanden sind. Deren Entstehung steht in engem Zusammenhang mit der inneren Entwicklung Ganymeds. Zur Klärung dieses Zusammenhangs ist es erforderlich, einen tieferen Einblick in die stratigraphische Position und die Einzelheiten des Entstehungsprozesses der hellen Gebiete zu gewinnen. Frühere Studien konzentrierten sich hierfür auf die strukturelle Analyse von linearen Strukturen in dunklen und hellen Gebieten. In der vorliegenden Arbeit liegt der Schwerpunkt auf den zahlreichen Einschlagskratern auf der Ganymedoberfläche und ihrem Potenzial, das Oberflächenalter und die stratigraphische Position der hellen Gebiete im Rahmen von Ganymeds geologischer Entwicklung zu erforschen und welche Details durch ihre detaillierte Analyse über die Bildungsprozesse der hellen Gebiete abgeleitet werden können. Besonderes Augenmerk liegt hier auf der Untersuchung spezieller Kraterformen und wie und diese von benachbarten tektonischen Strukturen beeinflusst wurden. Des Weiteren wird das Potential von Kratern und deren Auswurfsmaterialien genutzt, um die Beschaffenheit und die Stratigraphie des Untergrundes von Ganymed zu untersuchen.

Die Studie wurde im Wesentlichen auf der Grundlage der von den Raumsonden Voyager, Galileo und Juno gesammelten Daten durchgeführt, welche die einzigen bisher verfügbaren Datensätze mit ausreichender Bildauflösung und Abdeckung der Oberfläche von Ganymed darstellen. Zur Beantwortung der wissenschaftlichen Fragen wurden verschiedene Methoden eingesetzt. Neben photogeologischen Kartierungstechniken zur Definition, Erfassung und Charakterisierung geologisch relevanter Oberflächeneinheiten wie Ganymeds dunkle und helle Gebiete sowie Einschlagskrater wurden Messungen der Kratergrößen-Häufigkeitsverteilung der dunklen und hellen Gebiete durchgeführt, um deren geologisches Alter und relative Stratigraphie abzuleiten. Strukturelle Analysen, wie sie in früheren Arbeiten für verschiedene dunkle und helle Gebiete verwendet wurden, werden auf einen speziellen Kratertyp, genannt polygonale Krater, angewandt. Die Strukturanalyse dieser Krater im Vergleich zu den angrenzenden dunklen und hellen Gebieten wurde genutzt, um festzustellen, welche tektonischen Prozesse diese Krater beeinflusst haben und für ihre besondere Form verantwortlich sind. Die gewonnenen Ergebnisse wurden dann zur Bewertung der derzeit

verfügbaren Impaktchronologie-Modelle und ihrer Verwendung zur Abschätzung des Zeitpunkts und der Dauer der Bildung der hellen Gebiete und damit der tektonischen Aktivität in der geologischen Geschichte Ganymeds herangezogen. Darüber hinaus wurden basierend auf den bisherigen Kenntnissen zu Einschlagsprozessen die Krater Ganymeds und der Natur und Verbreitung ihrer Auswurfsmaterialien in Abhängigkeit ihrer Lage in dunklen oder hellen Gebieten bzw. an deren Grenze genutzt, die Stratigraphie des Untergrundes zu rekonstruieren und eventuelle Unterschiede in der Krustenbeschaffenheit und mögliche Implikationen für die Bildungsprozesse der hellen Gebiete zu untersuchen.

Die Dauer des Entstehungsprozesses des hellen Gebiets auf Ganymed hängt stark von den verwendeten Impaktchronologiemodellen ab, hier insbesondere vom mond-ähnlichen Model (LDM) und dem Kometenmodell (JCM), die zur Ableitung absoluter Krateralter verwendet werden. Bei Verwendung des LDMs weisen die hellen Gebiete im Allgemeinen ein höheres Alter und eine kürzere Entstehungszeit auf als beim JCM. Beide Modelle belegen jedoch, dass sich die hellen Gebiete von Ganymed schon früh in seiner Geschichte zu bilden begannen, mit einer kurzen Zeitspanne von ~ 0,2 Ga zwischen dem Ende der Bildung der dunklen Gebiete und dem Beginn der Bildung der hellen Gebiete. Die Diskussion von Faktoren, welche den Beginn der tektonischen Aktivität, die zur Bildung der hellen Gebiete geführt hat, verursacht haben könnten, umfasst vor allem die interne Differenzierung, die zu einer globalen Ausdehnung des Mondes führte, eine zeitweise verstärkte Gezeitenerwärmung aufgrund der sogenannten Laplace-Resonanz von Ganymed mit Europa und Io, orbitale Rezession oder nicht-synchrone Rotation der Kruste sowie große Einschlagsereignisse. Angesichts des frühen Beginns der tektonischen Aktivität spielten die interne Differenzierung und die globale Ausdehnung wahrscheinlich eine wichtige Rolle bei der Bildung der hellen Gebiete. Es ist möglich, dass die anderen Faktoren oder eine Kombination von ihnen zum Entstehungsprozess beigetragen haben und somit die Dauer der tektonischen Aktivität erheblich beeinflusst haben.

Das Vorhandensein von polygonalen Einschlagskratern, die gleichmäßig über die Ganymedoberfläche verteilt sind, selbst in den geologisch alten dunklen dicht bekraterten Gebieten, spricht außerdem dafür, dass sich die tektonische Aktivität auf Ganymed nicht nur auf das helle Gelände konzentrierte, sondern dass auch die dunklen Gebiete eine vergleichbare tektonische Aktivität erlebten, was zur allmählichen Entwicklung heller Gebiete führte. Polygonale Krater deuten auf verborgene Störungszonen hin, die auf den Beginn der Bildung der hellen Gebiete hinweisen. Während der Modifikationsphase dieser Krater haben sich ihre Ränder durch Absacken oder Verwerfungen entlang bereits vorhandener Bruch- und Verwerfungsebenen an lineare Strukturen tektonischen Ursprungs angepasst. Diese Krater

unterstützen auch die Idee, dass Rillen und andere Brüche in dunklen Gebieten tatsächlich Spuren von Verwerfungen sind.

Die einzigartigen dunklen Strahlen- und Halo-Krater auf Ganymed sowie die hellen Strahlenkrater, die an der Grenze zwischen dunklen und hellen Gebieten liegen, belegen, dass das dunkle Material der geologisch alten dunklen Gebiete Ganymeds eine dünne Schicht von weniger als 1 km auf einer eisreichen Kruste bildet, es aber in größerer Tiefe keine signifikanten Unterschiede in den Eigenschaften des Untergrunds beider Terrains gibt. Die eingehende Analyse der dunklen Halo-Krater in Ganymeds hellem Terrain offenbart eine erhebliche Heterogenität in den obersten Teilen der Eiskruste an verschiedenen Stellen in den hellen Gebieten. Das Vorhandensein mehrerer dünner Schichten dunklen Materials unter der Oberfläche ist notwendig, um die Existenz kleiner dunkler Halo-Krater in den hellen Gebieten und die Verteilung ihrer dunklen Ejekta mit einer maximalen Aushubtiefe von ~ 3 km zu erklären. Solche Vorkommen von oberflächennahem dunklem Material deuten auf einen tektonischen Verwerfungsmodus hin, der für die Bildung diese Bereiche im hellen Gebiet verantwortlich ist und auf einen Transport des dunklen Materials von der Oberfläche in tiefere Regionen an diesen Stellen hinweist.

STATEMENT OF THE CONTRIBUTION

This thesis has been arranged as a cumulative work, and it consists of two published, peer-reviewed articles as well as one submitted manuscript. The doctoral candidate is the first author of three papers. An introductory chapter has been meticulously crafted for this dissertation, with the aim of guiding any reader unfamiliar with the subject matter through the individual publications without requiring additional background information. These papers form chapters 2, 3 and 4, with references appropriately provided at the conclusion of each chapter. The papers included into this dissertation are enumerated below:

N.R. Baby, R.J. Wagner, K. Stephan and T. Kenkmann (2023) Stratigraphy, Crater Size–Frequency Distribution, and Chronology of Selected Areas of Ganymede's Light and Dark Terrains, The Planetary Science Journal, Vol. 4, No 9, 162, https://doi.org/10.3847/PSJ/acebed.

N.R. Baby, T. Kenkmann, K. Stephan, R. Wagner (2024) Polygonal impact craters on Ganymede, Meteoritics and Planetary Science, accepted.

N.R. Baby, T. Kenkmann, K. Stephan, R. Wagner, E. Hauber (2024) Ray and Halo craters on Ganymede – indicator for subsurface properties of light terrain formation, submitted.

This doctoral research was financially supported by a scholarship from the Deutscher Akademischer Austauschdienst (DAAD), under the grant number 57540125/91794973. This funding is a part of the DLR/DAAD Research Fellowships – Doctoral Studies in Germany, 2020.

ACKNOWLEDGMENTS

The past three years of my Ph.D. journey have been a truly remarkable and transformative experience. I am immensely grateful to the many individuals who made this journey possible.

I wish to express my sincere appreciation to the DAAD-DLR fellowship from DAAD (German Academic Exchange Service) for affording me the invaluable opportunity to pursue my Ph.D. at the German Aerospace Center (DLR). Their unwavering financial support has been instrumental throughout these years.

I am deeply indebted to Dr. Katrin Stephan for her mentorship and guidance since the beginning of my Ph.D. journey. Her expertise and supervision have been instrumental in my transition from geology to the world of Ganymedean geology and the broader realm of icy moons. I am profoundly grateful for her countless discussions, unwavering support, patience, research guidance, and overall excellence in mentoring.

I extend my sincere gratitude to Prof. Dr. Thomas Kenkmann of the University of Freiburg for accepting me as his Ph.D. student and providing excellent supervision. His extensive knowledge in cratering and structural geology, along with our numerous meetings and discussions, greatly contributed to my research. I express my gratitude to Prof. Dr. Ralf Jaumann from Freie University for agreeing to be my second supervisor.

I acknowledge the invaluable assistance of retired scientist Dr. Roland Wagner, who generously shared his expertise in Jupiter's moons and age determination techniques. His continuous support, discussions, and long-distance visits to Berlin have been immensely appreciated.

I also thank the entire department for their constructive feedback during my presentations, and I want to express my gratitude to Ernst Hauber for the discussions we had. Special thanks to Dr. Thomas Roatsch and Dr. Ganna Portyankina for their help with signatures and support related to conferences and work-related travels. I also extend my thanks to the office secretaries, Claudia Hauschild, Ritva Herranen, and Sandra Schwarz, for their assistance with office-related paperwork.

I wish to express my gratitude to my colleague and friend, Dr. Oguzcan Karagöz from the University of Freiburg, for his help with university matters and friendly conversations. I appreciate my office mate, Isik Su Yazici, for our friendship and shared experiences in our office space. I am also thankful to everyone at DLR who has directly or indirectly supported me over the years.

I extend my appreciation to my friends in Berlin who have not only created wonderful memories but also made Berlin feel like home, and our joyful travels and fun times together are truly unforgettable.

Lastly, I want to convey my heartfelt thanks to my family, including my parents, sisters, and brother-in-law, for their unwavering love and support, which have been a constant source of strength throughout my Ph.D. journey.

TABLE OF CONTENT

LIST OF FIGURES

LIST OF TABLES

LIST OF ABBREVIATIONS

AU	Astronomical Unit
BDRC	Bright and Dark Ray Crater
BRC	Bright Ray Crater
CSFD	Crater Size–Frequency Distribution
DTM	Digital Terrain Model
DHC	Dark Halo Crater
DRC	Dark Ray Crater
ESA	European Space Agency
GALA	Ganymede Laser Altimeter
Ga	Gigaannum or billion years
GEM	Galileo Europa Mission
GIS	Geographic Information System
GMM	Galileo Millenium Mission
ISS	Imaging Science Subsystem
JANUS	Jovis Amorum ac Natorum Undique Scrutator
JCM	Jupiter-family Comet Model
JUICE	JUpiter ICy moons Explorer
LDM	Lunar Derived impact Model
MAJIS	Moons And Jupiter Imaging Spectrometer
NASA	National Aeronautics and Space Administration
NIMS	Near Infrared Mapping Spectrometer
PIC	Polygonal Impact Crater
RIME	Radar for Icy Moons Exploration
SSI	Solid State Imaging

1 Introduction and Motivation

A major focus of planetary exploration is the geoscientific study of the surfaces of planets, moons as well as smaller celestial bodies such as asteroids and comets. Today, the existing technical requirements make it possible to study planetary objects from close up even in the outer regions of our solar system with the help of space probes. For example, on October 18, 1989, the Galileo space probe began its journey into the realm of the largest planet in our solar system. Galileo was the first space probe to observe and explore Jupiter and its moons over a period of around seven years (from 1995 until 2003). The aim of the mission was, among other things, to explore Jupiter's four Galilean moons. This also includes the subject of this study, Ganymede, the largest moon of Jupiter and also of the entire solar system. During the Galileo mission, the Solid State Imaging (SSI) subsystem in particular imaged the surface of Ganymede with the so far highest possible spatial resolution. This has provided new and far-reaching insights into the structure of Ganymede's surface, particularly for the geosciences. It has shown that Ganymede is subject to complex geological and geophysical processes (differentiation, tectonics, impact events, erosion) that have resulted in diverse surface structures (Pappalardo et al., 2004) that also provide scientists with the opportunity to study habitability in unlikely places.

Especially, Ganymede's past tectonic activity together with the existence of a subsurface ocean is of major interest to the scientific community making Ganymede a key object to study geologic activity in our Solar system. Scientific questions that could not be fully answered so far include: 1) What tectonic processes caused the formation of smooth and grooved light terrain on Ganymede? 2) What is the age of the light terrain and how extended was its formation period? 3) What are the relative roles of tectonism and volcanism in shaping the light terrain? 4) Does the light terrain include cryovolcanic deposits? What are the topographic relationships between dark and light terrains?

The answer to these questions might also help to solve others: Was Ganymede's tectonic activity driven by its internal differentiation early in its geologic history, i.e. near the time of accretion? What caused the different interior states of Ganymede and Callisto? Is Ganymede's thermal history characterized by monotonic decline in temperature, or did Ganymede experience a periodical pulse of tidal heating? Did the entrance into the Laplace resonance affect Ganymede's tectonic activity? Is any part of Ganymede's surface still geologically active today?

To answer all these questions is one of the scientific goals of the JUICE mission led by the European Space Agency (ESA). The space probe will reach the Jovian system in 2031 and, with its unique payload, explore the Jovian system, with Ganymede as its major target. In order to prepare for the JUICE mission i.e. constrain the requirements of future observations, this work reviews the current image data base and tools for investigating Ganymede's tectonic evolution.

1.1 Ganymede

Ganymede is, along with Io, Europa and Callisto, one of Jupiter's large Galilean moons. With a diameter of 5262 km it is the largest moon in the solar system and even larger than the planet Mercury. Ganymede completes an orbit around Jupiter in 7.155 Earth days and orbits the Sun along with Jupiter and its other satellites every 11.862615 Earth years (Hussmann et al., 2009). Every time Ganymede orbits Jupiter once, Europa orbits twice, and Io orbits four times. This orbital pattern is called orbital resonance, specifically Laplace resonance (Schubert et al., 2010). Their resonance forces the orbits of these moons to become slightly elliptical. Ganymede and its neighbors are tidally locked, i.e. the same hemisphere always faces Jupiter.

The mass of Ganymede at 1.49×10^{23} kg (Lewis, 1997) is less than that of Mercury. The average density of Ganymede is 1.93x103 kg/m^3, which is nearly the same as that of its outer neighbor Callisto (1.83x103 kg/m^3) but significantly lower than that of the inner Galilean satellites Io and Europa (Lewis, 1997). The low density is already an indicator that Ganymede, like Callisto, consists largely of water ice in addition to rocky material (Fig. 1.1). A second indicator comes from spectroscopic investigations of the surfaces of the Galilean satellites: Prior to spacecraft being sent to Jupiter and beyond, water ice was discovered spectroscopically on Ganymede and other Jovian satellites in the early 1970s (Dalton et al., 2010, and references therein). Therefore, Ganymede as well as other satellites of the four large planets in the outer Solar System were classified as a new type of planetary bodies termed icy satellites (e.g., Johnson, 1998).

The increasing proportion of water ice with increasing distance from Jupiter is related to a temperature gradient at the time of the moons' formation, analogous to that of the solar primordial nebula, from which the planets of the solar system formed (Lunine & Stevenson, 1982; Lewis, 1997). The current existence of water ice in the Jupiter system is consistent with the assumption that with a distance from the sun of about 5 AU water ice is

geologically stable, i.e. it does not evaporate within the age of our solar system of about 4.6 billion years (Cruikshank et al., 1998). Jupiter's mean distance from the sun is 5.2 AU with a minimum of 4.95 AU. The daytime temperatures on the surface of Ganymede (and Callisto) do not exceed 170 K.

Like Earth, Ganymede is a highly differentiated object with the water ice concentrated in a thick crust, a rocky mantle and a liquid iron core (Schubert et al., 2004, 2010). Ganymede as well as its neighbors Europa and Callisto are believed to hide a salty ocean deep below the surface making it an extremely interesting body for studying possible habitable worlds (Schubert et al., 2004; Sohl et al., 2010). Whereas, on Europa the ocean is believed to lie between a relatively thin icy crust and a rocky mantle, the ocean on Ganymede possibly exists within the thick icy crust between different layers of water ice at a depth of about 150 km (Fig. 1.1). Possible interaction between ocean and surface material are believed to occur on Europa but are still under debate on Ganymede.

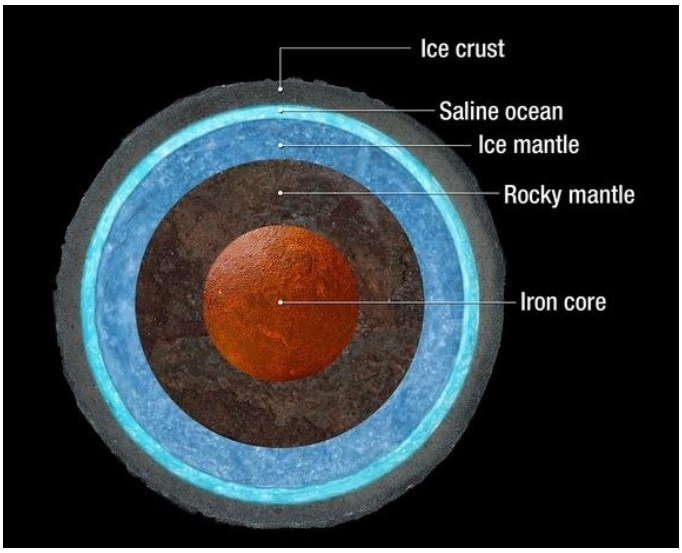

Figure 1.1: Internal structure model of Ganymede (Credit: NASA/ESA/A. Feild).

As different as the Galilean moons are with respect to their interior, they also differ with respect to the processes shaping their surfaces with growing distance from their central planet (Fig. 1.2). The closest moon to Jupiter, Io, mainly a rocky body without ice, is the most volcanically active celestial body in our solar system. At least eight active volcanoes were discovered by Voyager 1 on Io, which exhibited plumes that extended up to 250 km above the surface. Six of them were still active when Voyager 2 flew past Io six months later (Stone & Lane, 1979 a, b). The three outer icy moons can be sorted into three classes or metamorphic grades of icy moons depending of the evolutionary state such as established

by Johnson (1998): (a) **Grade I:** unmodified icy moon such as Callisto, which have remained in a more or less pristine state since ~4 billion years ago and no internal and surface processes other than impact cratering, erosion and surface degradation are active today; (b) **Grade II:** intermediate icy moon such as Ganymede characterized by pristine as well as geologically altered regions, implying geologic activity in the past; and (c) **Grade III:** heavily modified icy moons such as Europa, which have been geologically active (tectonism and/or volcanism) in recent times, or are still active at present. The type of volcanism specific to icy satellites has been termed *ice volcanism* or *cryovolcanism* (Kargel, 1998, and references therein). Thus, Ganymede features old, little evolved areas with a dark albedo and a high density of impact craters – like its outer neighbor Callisto, a Grade I type moon – and younger, bright, tectonically altered areas with a low density of impact craters – as its inner Grade III type neighbor Europa (Smith et al., 1979a, b; Johnson, 1998) making Ganymede the perfect object to study surface evolutions of icy moons in general (Fig. 1.2). Particularly, for the Grade II type satellite Ganymede, it is still an unsolved question what started the tectonic activity and when in the past and for how long intense thermal activity and, hence, geologic activity, have been going on (Schubert et al., 2004; 2010).

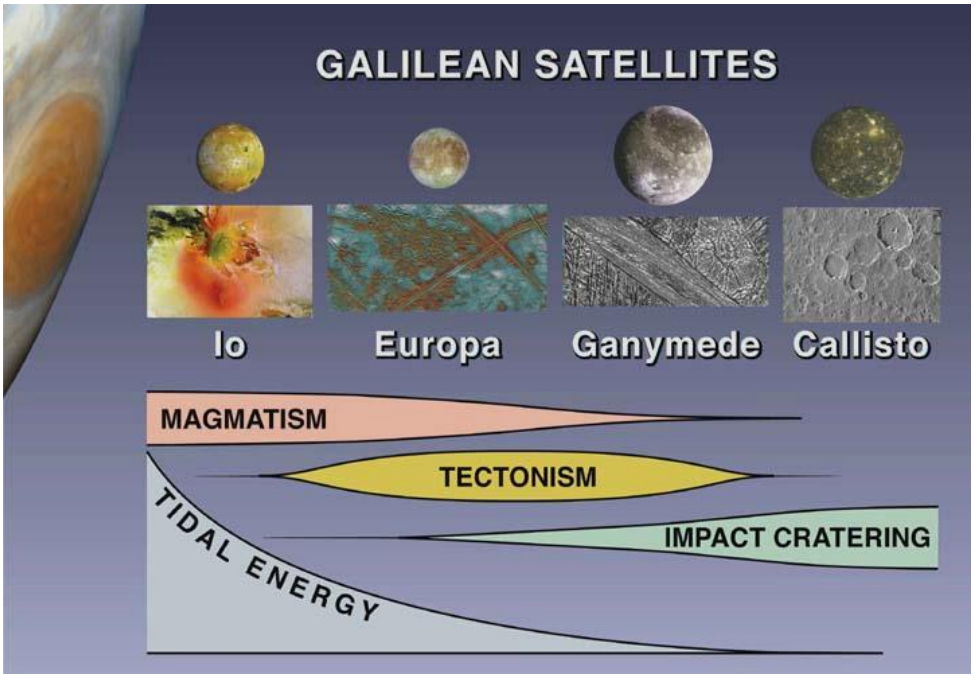

Figure 1.2: Variations in the major surface processes on the Galileo satellites with distance from Jupiter and its tidal forces (from Bagenal et al., 2004).

1.2 Ganymede's Geology

The occurrence of dark and light terrains on Ganymede could be discerned for the first time in very low-resolution photopolarimeter images taken during the Pioneer 10 flyby at Jupiter in December 1973 (Gehrels, 1976). The two Voyager flybys in March and July 1979 eventually revealed in unprecedented detail that Ganymede's surface was predominantly characterized by two types of terrain, dark and light units, and by numerous impact craters in a wide range of crater morphologies not known so far from other planetary bodies (Smith et al., 1979a, b; Shoemaker et al., 1982; McKinnon and Parmentier, 1986). A further important feature of Ganymede's surface is the presence of polar frost deposits (Smith et al., 1979a, b; Shoemaker et al., 1982; McKinnon and Parmentier, 1986; Pappalardo et al., 2004).

1.2.1 Ganymede's dark terrain

About one third of Ganymede's surface is covered by dark terrain units which either form large, hemispherical contiguous regions several hundreds or thousands of kilometers across, or smaller, more or less irregular patches or polygons with straight and/or curved boundaries with respect to the adjacent light terrain (Smith et al., 1979a, b; Shoemaker et al., 1982; McKinnon and Parmentier, 1986). In Ganymede's nomenclature, the large contiguous dark areas are termed *Regiones*. One example is Nicholson Regio shown in Figure 1.3 a.

At Voyager scale, the dark terrain (e.g., Nicholson Regio) features little variation in albedo. Despite a normal visual albedo of ~0.3, Ganymede's dark terrain units are still significantly brighter than the lunar highlands (~0.11), strongly indicating an icy composition and confirming water ice as a major surface constituent (McKinnon and Parmentier, 1986). In addition, non-ice components were found in spectra of the Galileo Galileo Near Infrared Mapping Spectrometer (NIMS) such as hydrated minerals, CO_2, SO_2, or components including CN and CH (Pappalardo et al., 2004, and references therein).

Dark terrain features a high density (or frequency) of impact craters which infers that it dates back to the early history of Ganymede and of the Jovian system, on the order of 4 Ga and higher (Smith et al., 1979a, b; Shoemaker et al., 1982; McKinnon and Parmentier, 1986; Neukum et al., 1998; Zahnle et al., 1998, 2003; Pappalardo et al., 2004; Baby et al., 2023). Ganymede's dark terrain may stem from the same early period as the global dark

terrain unit on the surface of its outer neighbour Callisto which, other than Ganymede, has not undergone significant tectonic resurfacing at later time (Moore et al., 2004).

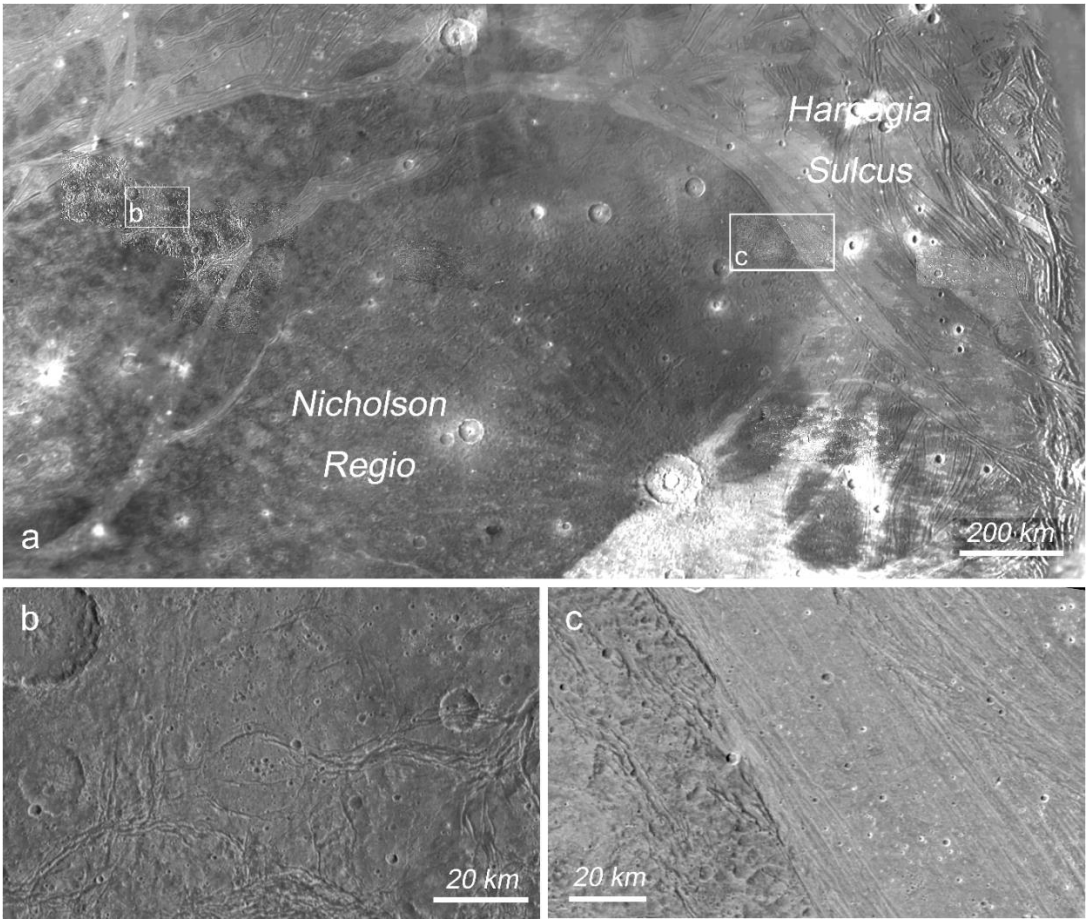

Figure 1.3: Context image of the dark terrain of Nicholson Regio and light terrain of Harpagia Sulcus with the white frames indicating the location of close-up views onto (b) the dark terrain, and c) its transition into the light terrain (adapted from Jaumann et al., 2024).

The large contiguous Regiones, but also some of the smaller dark polygons, display a system of tectonic features termed *furrows* (Smith et al., 1979b). These furrows form large arcuate, sub-concentric, nearly parallel, or longitudinal systems, the latter being more or less perpendicular to the arcuate furrows (Smith et al., 1979b; Shoemaker et al., 1982; McKinnon and Parmentier, 1986). Individual furrows are ~6 to ~20 km wide and up to several hundreds of kilometers or >1000 km long; in the system of arcuate sub-concentric systems, the furrows have a relatively constant spacing of ~50 km (Passey and Shoemaker, 1982; Pappalardo et al., 2004; Prockter et al., 2010). The furrows are bounded by raised rims which are brighter than the dark surrounding terrain. The furrows are comparably old

features, predating most of the >10 km-sized craters superimposed on dark terrain (Passey and Shoemaker, 1982). They most likely represent the remnants of fault-bounded troughs of very old, large multi-ring impact basins formed in an early thin lithosphere. On Callisto, two of such multi-ring basins, Valhalla and Asgard are still preserved, including a bright circular plain at the center (Moore et al., 2004). On Ganymede, these centers are no longer visible due to intense tectonic resurfacing (Passey and Shoemaker, 1982).

In high-resolution Galileo SSI images, dark terrain at local scale is revealed to be much more heterogeneous in albedo and morphology (Prockter et al., 1998; 2010). Topographically high-standing terrain is represented in high-albedo isolated massifs, linear massifs and furrow rims, while dark and intermediate albedo units are either smooth or hummocky, and the darkest units in general are abundant in topographic lows, such as crater and furrow floors. A portion of the dark terrain of Nicholson Regio with dark smooth and hummocky units is shown in Figure 1.3b.

A digital terrain model (DTM) with high-resolution SSI images from a portion (63 x 102 km) of the dark terrain area named Galileo Regio includes the units described in Prockter et al. (1998) and reveals a maximum height difference of ~1500 m (Giese et al., 1998). The bright furrow rims can attain a height of ~900 m above the surrounding dark terrain, and furrow floors are on the order of 500 – 600 m deep (Prockter et al., 1998, 2010; Giese et al., 1998). These results from stereo images agree with previous findings that Ganymede's limb lacks major relief of more than ~1 – 2 kilometers (Smith et al., 1979a).

Examination of SSI high-resolution images (including, where available, stereo DTMs) from Galileo Regio and other dark terrains favor a model that dark material forms a comparatively thin veneer superimposed on relatively clean ice, as shown in Figure 1.4 (Prockter et al., 1998, 2000). Thus, dark material represents a lag deposit, created by processes involving thermal segregation, sublimation, and mass wasting on slopes (Spencer, 1987a, b; Prockter et al., 1998, 2000; Moore et al., 1999; Oberst et al., 1999). On sun-facing slopes, solar insolation causes a sublimation of water ice, leaving a dark refractory layer concentrated on slopes and in topographic lows. The thickness of the dark veneers may be meters or tens of meters at slopes but may be thicker in low-lying areas, such as furrow floors (Pappalardo et al., 2004).

The dark terrain at high resolution features small-scale tectonism in some locations, such as sets of parallel fractures. The dark-light terrain boundary is sharp, with grooves parallel

to the contact, locally characterized by one prominent long, deep groove (Smith et al., 1979a, b; Shoemaker et al., 1982). Some dark-light boundaries display a transition zone ~10 – 20 km wide, with linear scarps parallel to the boundary from the dark terrain into the light grooved terrain, as shown in Figure 1.3 c.

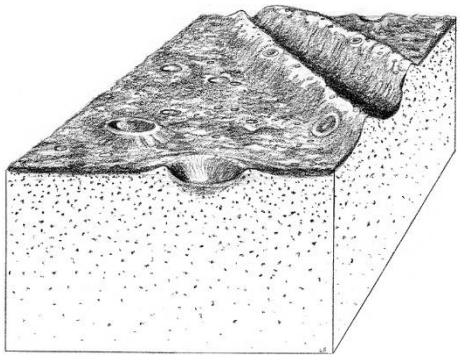

Figure 1.4: Schematic interpretation of dark terrain based on Galileo SSI observations: a thin dark lag deposit overlying cleaner ice that is concentrated in topographic lows (from Prockter et al., 1998).

1.2.2 Ganymede's light terrain

The light (or bright) regions termed *Sulci* cover about two-thirds of the surface of Ganymede (Shoemaker et al., 1982; Collins et al, 2000) and divide the dark terrain of the Regiones into isolated polygons of sizes up to several thousand kilometers. The bright regions consist of a complex network of bright bands that run criss-cross across the surface of Ganymede. The individual bands reach extensions of several tens to hundreds of km, are straight or irregularly shaped, overlap irregularly shaped, overlap each other, are partially interrupted or branch out.

Light terrain occupies kilometers long Sulci interposed between dark terrain units and predominantly shows features termed *grooves* consisting of tens-to-hundreds kilometers wide swaths of parallel, periodically spaced ridges and troughs of different orientation and shape (e.g., Patterson et al., 2010). In addition, bright terrain locally appears more or less smooth at Voyager resolution (Smith et al., 1979a, b; Shoemaker et al., 1982; Pappalardo et al., 2004; Prockter et al., 2010). In total, light terrain has a lower superimposed crater frequency than dark terrain and hence is stratigraphically younger (Smith et al., 1979a, b; Shoemaker et al., 1982). Absolute ages of light terrain formation can be estimated based on impact chronology models (section 1.2.4).

Light terrain was thought to originate by a combination of cryovolcanic and tectonic processes, based on Voyager images (Smith et al., 1979a, b; Shoemaker et al., 1982; McKinnon and Parmentier, 1986). Galileo images, however, showed that cryovolcanism played a minor role in the formation of the bright terrain units compared to tectonic resurfacing (Pappalardo et al., 2004; Prockter et al., 2010). A more detailed discussion of light grooved and smooth terrain formation by tectonism is given in section 1.2.5.

Like dark terrain, light terrain is characterized by a relatively low topography, as inferred from Galileo SSI stereo images and DTMs (Giese et al., 1998, 2001a, b). Wave amplitudes in a high-resolution observation of Uruk Sulcus were found to reach a maximum of only ~500 m. Similar amplitudes were found in Arbela Sulcus (Giese et al., 2001a). In the boundary between light terrain of Harpagia Sulcus and dark terrain of Nicholson Regio, the maximum topography does not exceed ~1 km between the highest point in the dark terrain and the lowest point in the light terrain (Giese et al., 2001b).

1.2.3 Ganymede's impact craters

The Voyager flybys unexpectedly revealed a variety of impact crater morphologies on Ganymede, Callisto, and also on low-cratered Europa, representing the widest range in crater forms ever found on any planet or satellite (Schenk et al., 2004; Hauber and Wagner, 2009). The smallest craters, known as simple craters, exhibit a bowl-shaped profile, similar to those found on Earth's moon. Beyond a certain transition diameter, more complex crater forms emerge, featuring central peaks, pits, and extensive ray systems. A crater form unique to the icy Galilean satellites are flat, bright circular areas with little crater topography termed palimpsests, and craters transitional between complex craters and palimpsests (pene-palimpsests) (Schenk et al., 2004; Hauber and Wagner, 2009).

1.2.3.1 Bright ray craters

Bright ray craters are the most abundant type of least degraded and therefore geologically young impact craters (Pappalardo et al., 2004; Prockter et al., 2010; Collins et al., 2013; Stephan et al., 2021) (Fig 1.5). Their sizes range from a few kilometers up to 100 km and more. They are characterized by bright floors, bright rims, and bright continuous and discontinuous ejecta including rays extending several hundreds of kilometers out from the crater center. One prominent type example is Osiris, shown in Figure 1.5 (a). In a specific

region, the Galileo SSI camera captured numerous clusters of bright secondary craters within Osiris' strewn field at high resolution (detailed description in chapter 2). Bright ray craters are known to be enriched in volatiles such as water ice and CO_2 (Pappalardo et al., 2004; Prockter et al., 2010; Stephan et al., 2021).

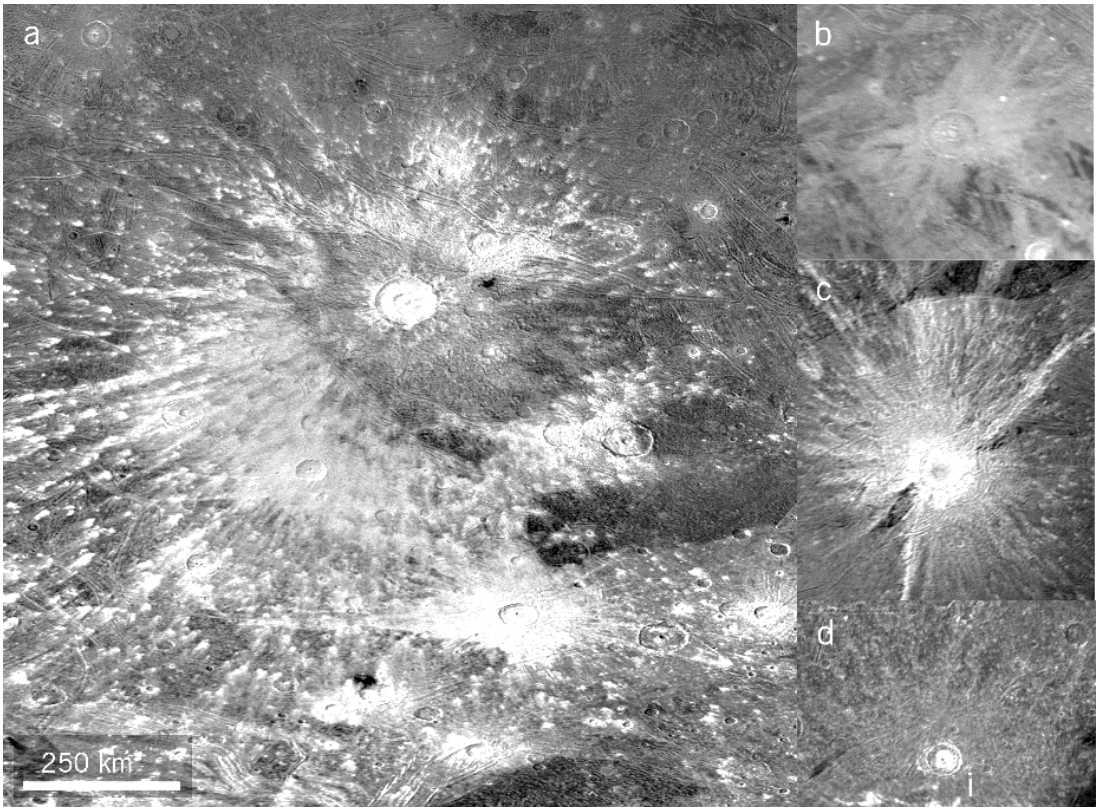

Figure 1.5: Bright ray craters on Ganymede: a) Osiris, b) Amon, c) Tros, d) Laomedon. The scale bar fits to all images.

1.2.3.2 Dark ray and dark halo craters

A unique class of impact features on Ganymede, not observed on other celestial bodies (with some uncertainty regarding Callisto), includes dark ray, dark floor, and dark halo craters (Pappalardo et al., 2004; Prockter et al., 2010; Stephan et al., 2021). Dark floor craters are primarily concentrated in Ganymede's western anti-Jovian hemisphere, notably west of the dark terrain Marius Regio. An example from the sub-Jovian hemisphere is Kittu, shown in Figure 1.6 a. Dark ray craters feature bright floors, bright rims, and a narrow bright zone near the rim, surrounded by dark rays extending outward.

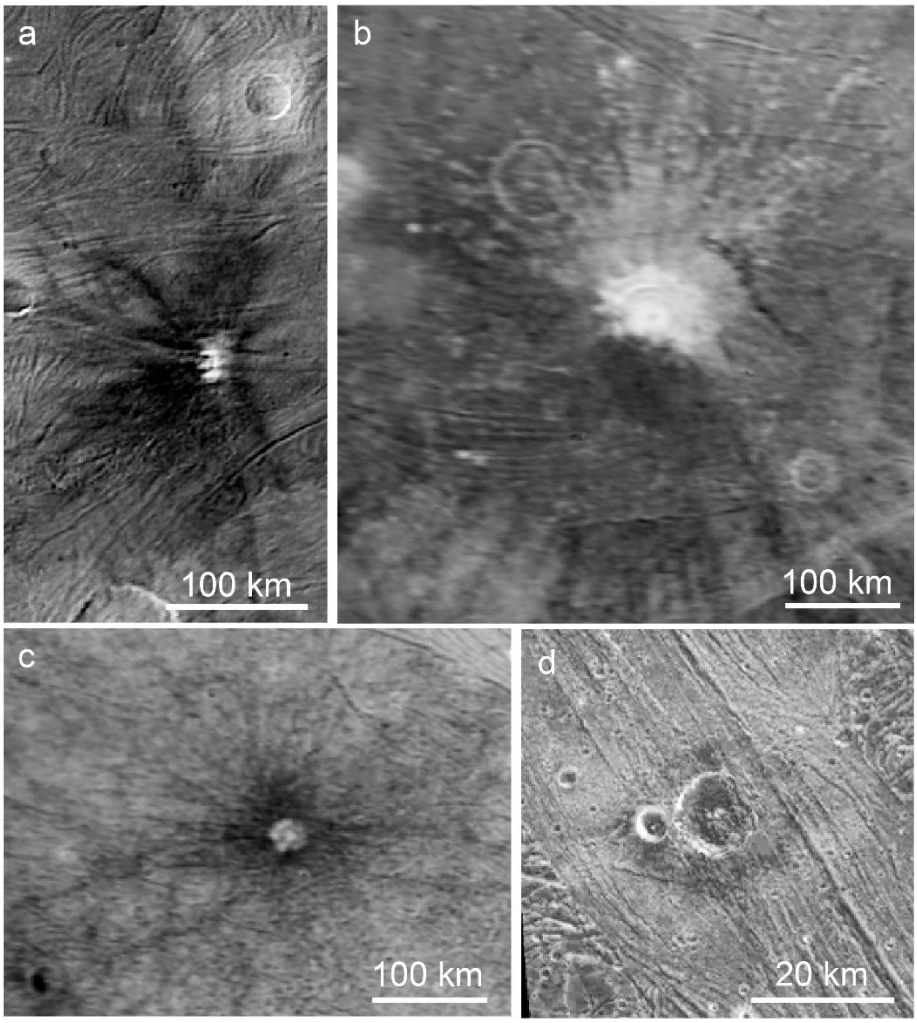

Figure 1.6: Dark ray and halo craters on Ganymede: a) Kittu, b) Tammuz, c) Antum and d) Nergal.

Examples from the anti-Jovian hemisphere include crater Tammuz (Fig. 1.6 b) and Antum (Fig. 1.6 c), with Tammuz displaying a distinctive bimodal ejecta pattern consisting of both bright and dark rays. Dark halo craters, such as Nergal (Fig. 1.6 d) are found exclusively in the light terrain units on Ganymede. These specific crater forms are key features to investigate the subsurface structure (stratification) of Ganymede's icy crust (see chapter 4). The origin and nature of the dark material in these crater forms is not yet fully understood (Stephan et al., 2021, 2024, Hibbitts et al., 2023). Viable models of formation involve the contamination of dark impactor material (Pappalardo et al., 2004; Stephan et al., 2021). All data sets, both in terms of high-resolution imaging as well as mapping spectrometer data are not yet sufficient.

1.2.3.3 Impact basins

Large impact basins several hundreds of kilometers across with bright circular plains in the center, surrounded by numerous concentric rings (ring graben or scarps) only occur on Callisto because they were not resurfaced by later geologic processes on this satellite (Pappalardo et al., 2004; Schenk et al., 2004; Prockter et al., 2010). On Ganymede, only the remnants of this very old basins are found in the dark terrain units in the form of sub-concentric parallel sets of furrows, e.g. in Galileo Regio (see section 1.2.1). Ganymede features only one prominent impact basin named Gilgamesh which is morphogically different from the remnants of the old multi-ringed basins.

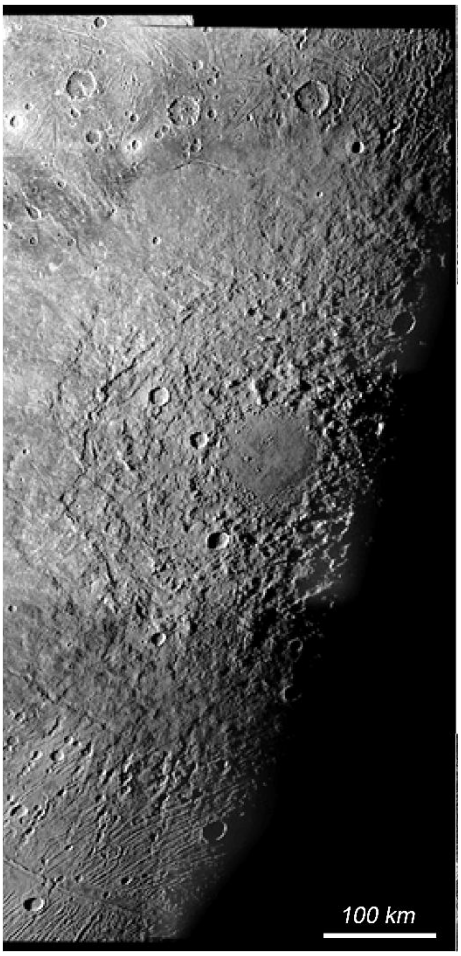

Figure 1.7: Impact basin Gilgamesh

Figure 1.7 shows the Gilgamesh basin taken by Voyager 2 images. Several morphologically different or structural zones can be discerned (Schenk et al., 2004; Prockter et al., 2010): a circular relatively smooth area ~150 km in diameter, surrounded by an annular ~225 km wide hummocky zone, and up to four concentric inward-facing scarps, the latter with a

diameter of ~585 km which is interpreted as the crater rim. Outside this potential crater rim is a 200-km wide zone of mottled terrain most likely representing the continuous ejecta, and beyond this zone chains of secondary craters of the discontinuous ejecta are abundant. Radial secondary chains are prominent in the north and the south of Gilgamesh (Fig. 1.7). The Gilgamesh basin was chosen as the base of a time-stratigraphic system and a chronologic period in Ganymede's geologic history (Collins et al., 2013; see section 1.2.4).

1.2.3.4 Complex craters and palimpsests

The smallest craters on Ganymede exhibit a bowl-shaped profile, akin to simple craters observed on other celestial bodies (Schenk et al., 2004; Hauber and Wagner, 2009). Beyond the so-called simple-to-complex transition diameter, more complex features in impact craters appear. For Ganymede's craters, this transition diameter is at ~3 km, significantly smaller than lunar craters, which typically range from 15 to 25 km in diameter (Schenk et al., 2004; Hauber and Wagner, 2009). The two craters named Chrysor and Aleyn shown in Figure 1.8 are characterized by a central peak. Crater Gula with a diameter of 38 km features a central peak, while crater Achelous (40 km diameter) is characterized by groups of pits instead of a peak. Both craters are so-called pedestal craters, indicated by a smooth or hummocky annulus of continuous ejecta approximately one crater radius in width with a distinct outward-facing scarp (Pappalardo et al., 2004; Prockter et al., 2010). One likely process for pedestal formation is plastic, glacier-like flow or creep in the continuous ejecta that eventually came to a halt (Schenk et al., 2004). In Voyager 1 images taken at higher sun, Achelous is also a prominent bright ray crater in the northern latitudes of the sub-Jovian hemisphere.

With increasing crater diameter (> 10 – 25 km), central peaks in general are replaced by rimmed central pits, and central domes within a rimmed pit (Schenk et al., 2004; Hauber and Wagner, 2009). One example is Melkart (105 km in diameter) (Fig. 1.8). At diameters larger than 35 km, craters with a central pit represent the majority of craters (Schenk et al., 2004).

Ganymede (and also Callisto) are the only planetary bodies featuring a unique impact crater morphology termed *palimpsest*, a term which was coined after examining Voyager 2 images from the anti-Jovian hemisphere (Smith et al., 1979b; Passey and Shoemaker, 1982). These palimpsests are circular, flat pancake-shaped features with an almost complete lack of relief. With the exception of two palimpsests, all of them are superimposed

on dark terrain units. An example, Buto Facula with a diameter of 245 km, from the dark terrain Marius Regio is shown in Figure 1.8. At this higher Galileo SSI resolution remnants of a subdued crater rim and a central pit rim are discernable (Pappalardo et al., 2004; Schenk et al., 2004; Prockter et al., 2010; Stephan et al., 2021). The occurrence of secondary crater chains helps to locate the outer boundary of presumed continuous ejecta and to scale a crater rim and a pit rim diameter (Schenk et al., 2004).

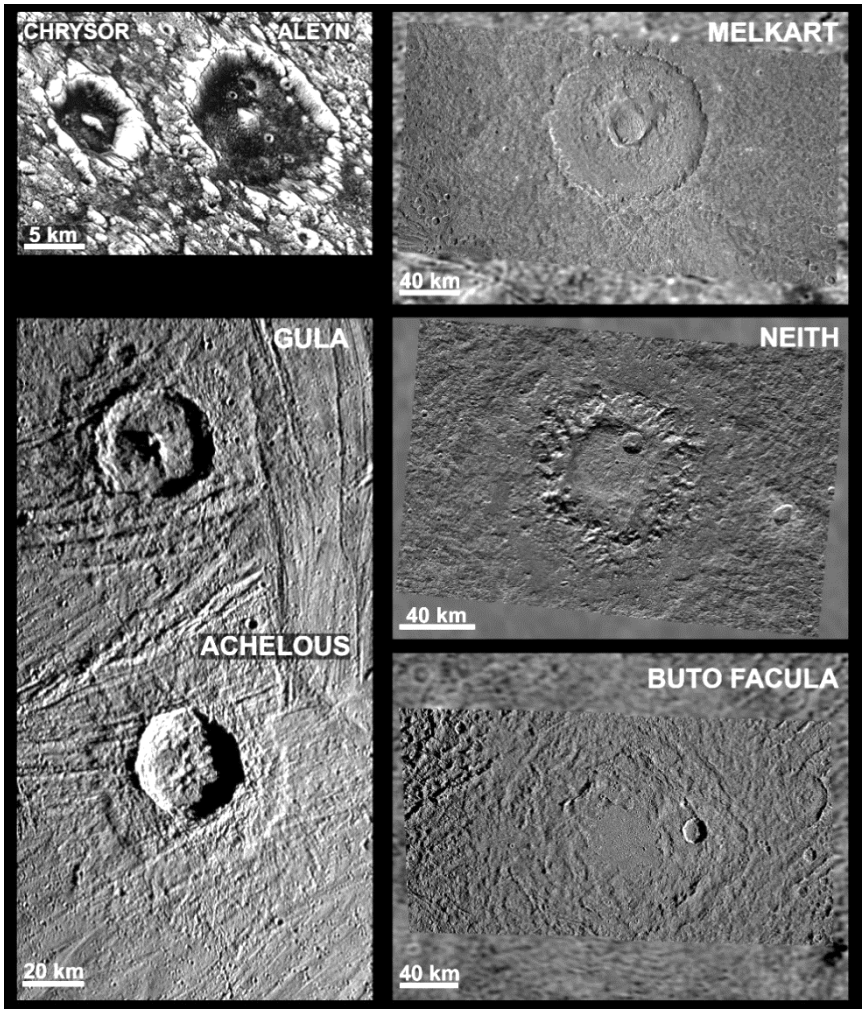

Figure 1.8: Impact crater morphologies on Ganymede with: a) central peak, b) pit, c) dome, d + e) pedestals as well as f) palimpsests (from Stephan et al., 2013).

Two more crater morphologies unique to Ganymede and Callisto are flat crater forms with no prominent or only with a subdued crater rim and a large central dome, surrounded by an annulus of rugged terrain. These craters were named *pene-palimpsests*, suggesting a transition from central pit crater to palimpsests, and *central dome craters* (Passey and

Shoemaker, 1982; Schenk et al., 2004). In Figure 1.8, the central dome crater Neith with a dome approximately 90 km in diameter is depicted.

The formation of palimpsests, pene-palimpsests and central dome craters is still not well understood. Several models of formation were offered for central dome origin (Prockter et al., 2010, and references therein): impact melt refreezing, diapirism subsequent to the impact, or rapid uplift of ductile material during the impact event. Palimpsests could have formed at a time when the heat flow and crustal weakness were higher, thus they represent viscously relaxed craters while pene-palimpsests could represent transitional formed when crustal weakness and the heat flow decreased (Schenk et al., 2004; Prockter et al., 2010). A complete survey of these forms and of their range in morphologies in order to develop models of formation so far is impeded by the lack of global high-resolution image coverage.

1.2.4 Ganymede's Chronology and Time Stratigraphy

The geologic history of Ganymede is based on the global geologic map by Patterson et al. (2010) and Collins et al. (2013). Relative ages of geologic units were derived from cross-cutting relationships and also from measurements of craters size-frequency distributions (CSFDs). Crater frequencies can be translated into absolute model ages (AMAs), based on models of impact cratering chronology (described in detail in chapter 2). Currently, two impact chronologies exist: (1) a lunar-derived model (LDM), based on the preferential impacts of asteroids with a time dependence similar to that observed on the Moon (Neukum et al., 1998), and (2) a model derived from the dominant impacts of Jupiter-family comets (JCM) (Zahnle et al., 2003).

The geologic history of a planet or satellite is based on stratigraphic key horizons, such as those created in prominent resurfacing events by volcanism, tectonism, erosion, or major impacts. Collins et al. (2013) subdivided the geologic history of Ganymede into three time-stratigraphic systems which can be transferred into chronologic periods using impact crater frequencies and their calibration with impact chronology models. This time-stratigraphic scheme and the associated absolute model ages based on the LDM and JCM model is shown in Figure 1.9.

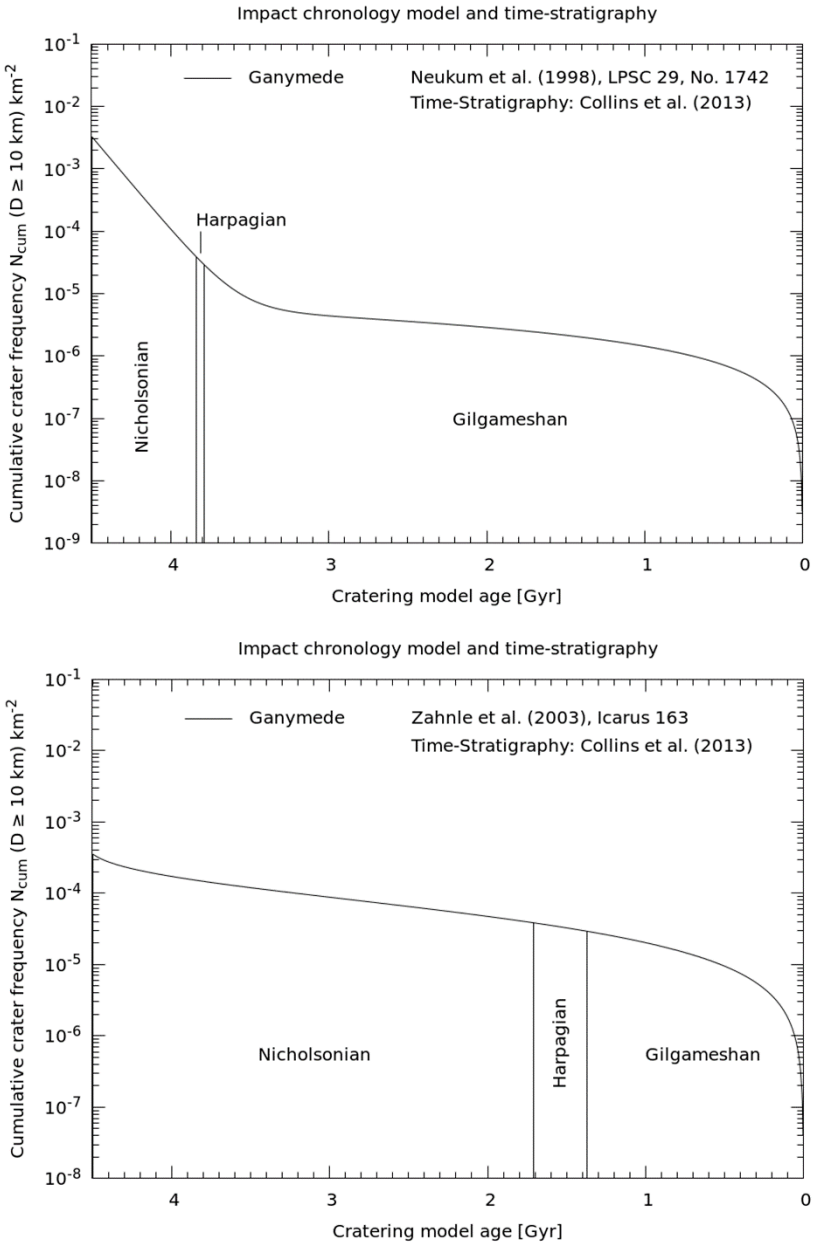

Figure 1.9: Chronologic periods of Ganymede based on the geologic map by Collins et al. (2013) in the two impact chronology models: a) Lunar-derived model (LDM) (Neukum, 1997; Neukum et al., 1998); b) Jupiter family Comet-derived model (LDM) (Zahnle et al., 2003). Both graphs are shown for a cumulative frequency for craters equal to, or greater than, 10 km in diameter (from Jaumann et al., 2024).

The lowest time-stratigraphic system and oldest chronologic period is *Nicholsonian* which encompasses the time since the formation of a solid icy crust until the global resurfacing by light grooved terrain. In this period, most of the old heavily degraded multi-ring basins whose remnants are the sub-concentric furrow systems and the majority of the palimpsests

were formed. The type locality of the Nicholsonian System (Period) is located in the dark terrain of Nicholson Regio (Collins et al., 2013).

Two thirds of the surface of Ganymede were resurfaced in the following *Harpagian* period by intense tectonism which created the light grooved and smooth terrain units. The base of this stratigraphic system is represented by light terrain units in Harpagia Sulcus.

The uppermost time-stratigraphic system and the youngest period *Gilgameshan* is represented by the impact event and its deposits which formed the Gilgamesh basin. Young light terrain units and some of the youngest palimpsests can be grouped into this youngest period in which the heat flow is thought to have decreased significantly (Patterson et al., 2010; Collins et al., 2013).

Figure 1.9 shows that in the LDM model the two periods Harpagian and Gilgameshan are almost not separable based on crater counts and on their associated model ages. On the other hand, Harpagian is at least an approximately 300 Ma long period according to the JCM model. In the LDM model, Gilgamesh is considered to be the so-called marker horizon (formation of the youngest basin), comparable to Orientale on the moon which was formed ~ 3.8 Ga ago (Neukum et al., 1998). According to the JCM model (Zahnle et al., 2003), Gilgamesh represents a major cometary impact ~1.5 Ga ago not related to a potential intense bombardment prior to 3.5 Ga.

1.2.5 Ganymede's tectonic surface processes

Based on numerous studies focusing on geometric and structural analysis, extensional tectonism has been widely accepted as the major process responsible for the light terrain formation (Pappalardo et al., 2004; Collins et al., 1998a, b). But there is less or no corresponding convergence elsewhere (Pappalardo and Collins, 2005; Bland and Showman, 2007). Scenarios presented by Pappalardo et al. (2004) suggest that initial normal faults could have utilized preexisting zones of structural weakness, specifically furrows, in dark terrain for the tectonic resurfacing (Murchie et al. 1986) and newer grooved terrain creating the observed complex array of crosscutting swaths across Ganymede's surface has been formed by resurfacing older light terrain (Fig. 1.10). Horst and graben and domino-style faulting have both been recognized within the grooved light terrain (*e.g.*, Collins et al., 1998b; Pappalardo et al., 1998; Bland and McKinnon, 2015). In domino-style faulting, characterized by a bookshelf pattern, ridges assume triangular to rounded shapes,

and troughs appear narrow and V-shaped in cross-section. In this type of normal faulting, the faults dip in the same direction as the fault motion, leading to back tilting of the surface (Pappalardo et al., 2004). The oldest grooved terrains display horst and graben faulting, while the youngest terrain units exhibit domino-style tilt-block normal faulting (Pappalardo et al., 1998; Collins et al., 1998a, 1998c).

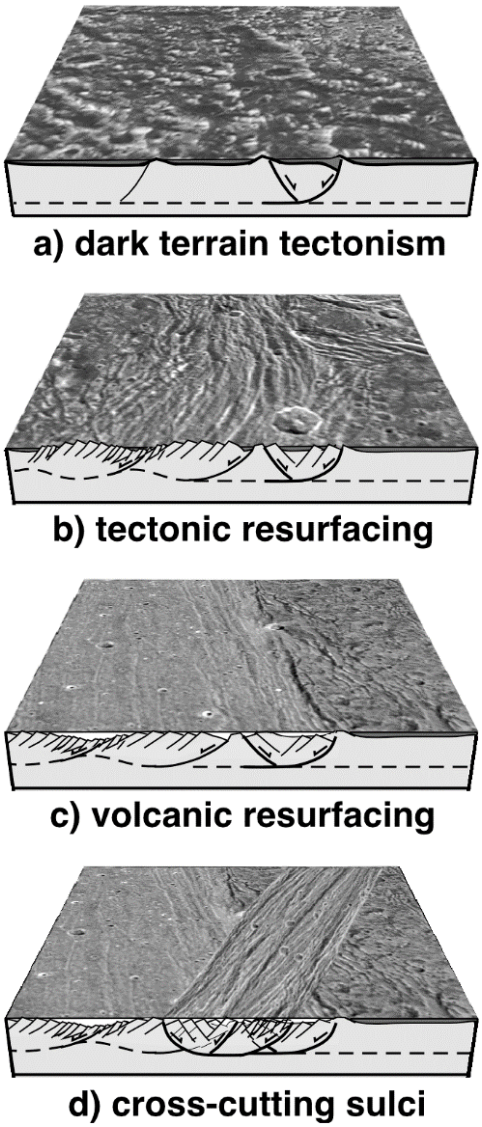

Figure 1.10: Formation model of Ganymede's light terrain: a) reactivated furrows in dark terrain to focus later light terrain deformation; b) grooved light terrain formed by tectonic disruption of the preexisting surface; c) smooth light terrain formed by tectonism combined with cryovolcanism; d) cross-cutting bands (sulci) of light terrain dissecting the preexisting dark terrain into a polygonal patchwork (Pappalardo et al., 2004).

At the same time, the occurrence of strike-slip faulting has been observed, with evidence of dextral shear along the sulci (*e.g.*, Pappalardo et al., 1998; Cameron et al., 2016). Strike-

slip indicators, such as en echelon structures, strike-slip duplexes, laterally offset preexisting features, and strained craters, have been observed in various locations across Ganymede, including Nun Sulci, Dardanus Sulcus, Tiamat Sulcus, Uruk Sulcus, and Arbela Sulcus, as well as Nippur and Philus Sulci, Byblus Sulcus, Anshar Sulcus, and the Transitional Terrain of Northern Marius Regio (Cameron et al., 2018). In Galileo Regio, an early stage of extension followed by strike-slip shear is observed (Rossi et al., 2023). Rossi et al. (2018) observed both compression and extension within a dextral transpressional framework in the Uruk Sulcus region. Whereas, grooved light terrain may be form by tectonic disruption of the preexisting surface, it is still in discussion that smooth portions of light terrain might be formed by a combination of tectonism and icy volcanism which brightens and smooths the surface. Based on Voyager images, suggests that ancient dark terrains were downfaulted, subsequently flooded with low-viscosity cryo-lava, and then faulted to create the light terrains (Parmentier et al., 1982). Initial Voyager images indicated that smooth areas were solely a result of cryovolcanism (Allison and Clifford, 1987). However, subsequent Galileo data revealed that these seemingly smooth areas, such as the light subdued terrains, are not actually smooth but feature fine-scale ridges and troughs (Collins et al., 1998a; Hiesinger et al., 1998; Head et al., 2002). Extensional necking is often described as a process in which a stretched lithosphere could evolve into a series of pinches and swells, giving rise to a tilt-block style of grooved terrains (Collins et al., 1998a; Dombard and McKinnon, 2001).

More recent studies discuss an alternative perspective with two different modes of extension associated with the two different major terrain units of Ganymede's sulci such as 1) spreading forming the smooth light terrain and 2) rifting dominating the formation of the grooved light terrain (Pizzi et al., 2017).

1.2.5.1 Spreading

A model of lithospheric spreading for Ganymede's light terrain was originally suggested based on Voyager observations (Lucchitta 1980). So far, only little evidence has been found for features resembling central ridges and regions of apparent axial symmetry within the grooved terrain as can be observed on Ganymede's inner neighbor Europa (McKinnon and Parmentier 1986; Pappalardo et al., 2004). Nevertheless, detailed structural analyses indicate that Earth-like oceanic spreading centers are possibly widespread on Ganymede implying that spreading could have played a major role in the tectonic evolution of

Ganymede (Collins, 2009; Pizzi et al., 2017), as also hypothesized for other icy satellites such as Europa (*e.g.*, Sullivan et al., 1998; Prockter et al., 2002).

Particularly, smooth light terrain is believed to constitute spreading centers between two dark or two grooved light terrains, similar to the oceanic spreading centers on Earth (Fig. 1.11 a). Here extension is primarily accommodated by crustal accretion of newly formed icy crust. Spreading centers are zones, where post break-up extension between two diverging terrain plates is mainly accommodated by the accretion of newly formed icy crust (total resurfacing) through warm upwelling icy material and/or liquid water dike intrusion through extensional (tensile) fractures. Along spreading centers, it is possible to restore the original configuration of the deformed area matching complementary terrain boundaries and piercing points.

1.2.5.2 Rifting

In the second mode, dark terrain extension is mainly accommodated by swaths of normal fault systems analogous to Earth's continental crustal rifts (Fig. 1.11 b). The sulcus represents a crustal rift dominated by tectonic normal fault systems, stretching the dark terrain crust without its break-up. Faults are represented by closely-spaced, hundreds of kilometers long rectilinear grooves which significantly displaced pre-deformed morphological features such as craters and furrows. In this case, piercing points on each side of the sulcus are not observed.

Restoration of boundaries between dark terrain blocks in various locations, such as Perrine Regio, Arbela Sulcus, and Anshar Sulcus regions, indicates that sulci formation results from either the spreading or rifting mode of extension (Pizzi et al., 2017; Fabi et al., 2022). The reasons for some areas developing through spreading and others through rifting remain uncertain, likely influenced by crustal heterogeneities, including internal melt and ocean distribution (Pizzi et al., 2017). Based on numerical simulations of ice I under extension, the formation of light grooved and subdued terrain depends on the strength of the lithosphere. Smooth bands typically develop in areas with thin, weak lithosphere, requiring high strains. In contrast, groove lanes form in regions with stronger, thicker lithosphere, low strains, and minimal thermal gradients (Howell and Pappalardo, 2018). No one, however, explains how smooth and grooved portions of light terrain can be formed close and/or in direct contact to each other.

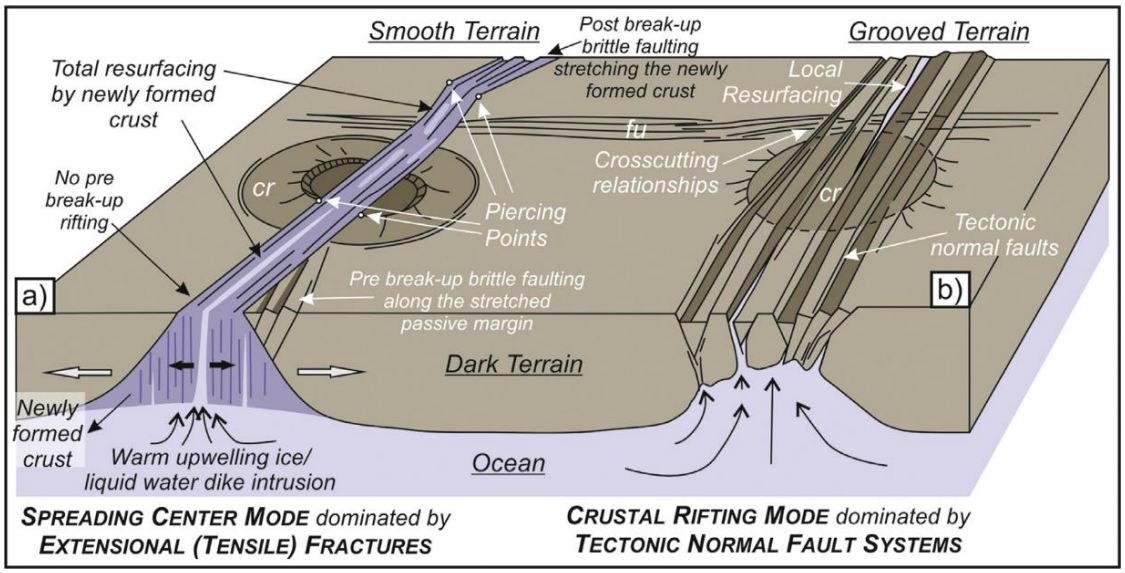

Figure 1.11: Block diagram (not to scale) illustrating different structural scenarios for Ganymede sulci related to the two modes of extension. a) Spreading center mode and b) crustal rifting mode (From Pizzi et al., 2017).

1.2.5.3 Formation scenarios of light terrain formation

Different processes and models are in discussion to explain the origin of extension on Ganymede. In particular, global expansion has been considered as the result of either differentiation (Squyres, 1980; Mueller and McKinnon, 1988) or the passage through one or more Laplace resonances by Ganymede and the other Galilean satellites during their orbital evolution, in combination with tidal heating (Showman et al., 1997; Bland et al., 2009). The time-variation of internal heating, both tidal and radiogenic, has likely produced global volume changes during the melting/freezing of the outer ice I shell and a high-pressure ice layer at the base of the subsurface ocean (Showman and Malhotra, 1997; Showman et al., 1997; Bland et al., 2009). Episodes of increasing internal heating (*e.g.*, tidal heating) produce internal melting and a subsequent decrease in the thickness of the outer ice I layer and high-pressure ice layer. On the other hand, during the cooling of the interior (*e.g.*, secular cooling) the outer ice I layer and high-pressure ice layer freeze, increasing their thickness. By adopting different models, the estimated amount of areal expansion ranges from 1–2% (Golombek, 1982; Showman et al., 1997; Bland et al., 2009) or up to 6% (Squyres, 1980; Mueller and McKinnon, 1988), while Collins (2009) suggests a larger global surface area expansion of up to ~20%. Neither of these models were able to fully explain the mapped distribution of the light terrain. Additional detailed investigations

of Ganymede's light terrain units, deeper insights into the subsurface properties and resurfacing mechanisms of the dark terrain as well as the surface ages of dark and light terrain, but also the time frame of the formation of different units of the light terrain with respect to each other are necessary to solve the details of the light terrain formation. The understanding of Ganymede's light terrain formation, its time, duration and the trigger and nature of deformation processes is also an important factor for understanding the differences in the geologic evolution of the three icy Galilean moons including the possible mechanisms of interaction between surface and subsurface ocean (Jaumann et al., 2024). Understanding the exact trigger of tectonic activity is also essential for modeling interior processes and the geothermal and chemical evolution of Ganymede, especially in comparison to its outer neighbor Callisto, which shares similar dimensions, densities, and environment (Cassen et al., 1980). Despite these similarities, it remains unknown so far why Callisto did not experience any tectonic activity, while Ganymede shows evidence of intense past activity.

1.3 Planetary image data and processing

The studies in this manuscript primarily utilize images from two space missions: The Voyager flybys at Jupiter and the Galilean satellites in 1979, as well as the Galileo Jupiter orbiter from 1995 to 2003. Voyager 1 and 2 conducted their closest flybys of Ganymede on March 5 and July 9, 1979, respectively (Smith et al., 1979a, b). Both Voyager spacecraft were equipped with Mariner Mission-type Vidicon cameras, which is a wide-angle (WA) camera with a 55.6 x 55.6 mrad field-of-view (FOV) and a narrow-angle (NA) camera with a 7.5 x 7.5 mrad FOV, allowing varying flyby distances and dimensions of the observed target bodies (Smith et al., 1977). Both cameras were provided with various color filters from the ultraviolet (minimum wavelength 310 nm, NA camera) to red/orange (maximum wavelength 670 nm, WA camera), and a broadband (panchromatic) CLEAR filter with a wavelength range from 290 nm (minimum, NA camera) to 670 nm (maximum, WA camera). In these studies, only images of the CLEAR filter were used.

During the Voyager 1 flyby, Ganymede was approached at its closest point, ~ 114,710 km from its center, yielding images with a maximum resolution of ~ 1 km/pxl (NA camera) (Smith et al., 1979a). Voyager 2 achieved an even closer distance, coming within 62,130 km of Ganymede and attaining a maximum spatial resolution of about 0.47 km/pxl (NA)

(Smith et al., 1979b; Kersten et al., 2021). These two flybys captured distinct hemispheres, with Voyager 1 focusing on the sub-Jovian hemisphere and Voyager 2 on the anti-Jovian hemisphere of Ganymede (Smith et al., 1979a, b). Unfortunately, the leading and trailing hemispheres were only captured at relatively low spatial resolutions, less than ~ 10 km/pxl. These Voyager gaps were subsequently filled by images from the Galileo Jupiter orbiter's SSI camera.

Before the Voyager missions to Jupiter and its moons, NASA had been planning a new Jupiter mission that included both an orbiter and an atmospheric probe. This mission was named Galileo in honor of Galileo Galilei, who discovered the four Galilean satellites in 1610. The images used in this thesis were captured using the Solid State Imaging Subsystem (SSI) camera aboard the Galileo orbiter (Tab. 1.1), which introduced the charge-coupled device (CCD) technique to planetary missions (Klaasen et al., 1984; Belton et al., 1992). In comparison to the Voyager cameras, the SSI camera boasts approximately 100 times higher sensitivity and approximately double the spectral coverage. The SSI camera's optical system is derived from the Voyager narrow-angle camera, featuring a focal length of 1500 mm (Belton et al., 1992). Unlike the two Voyager cameras, the SSI optical system exhibits negligible geometric distortion.

The SSI sensor, a Silicon Virtual Phase CCD with an FOV of 8.1 mrad, has an active CCD area of 12.19 x 12.19 mm (Klaasen et al., 1984; Belton et al., 1992). Each SSI frame has 800 lines and 800 samples (as had the Voyager cameras), but modifications are possible since the SSI camera can be operated in four modes (Klaasen et al., 1984). The SSI camera encompassed seven color filters from violet (VLT filter; 404 nm) to the near-infrared (NIR; 986 nm). A panchromatic filter was implemented with a range from 360 nm to ~1000 nm. This eight-position filter wheel was also inherited from the Voyager cameras (Belton et al., 1992, and references therein). The SSI images used in this study were exclusively taken through the panchromatic or clear (CLR) filter.

In April 1992, the Galileo science teams agreed on an orbit tour around Jupiter known as 92-14A (Carr et al., 1995). Table 1.2 provides all the relevant information for each Galileo orbit. During the initial two years of the Galileo Prime or Nominal Mission, 11 orbits around Jupiter were completed. In each of these orbits, one of the Galilean satellites was targeted for a close flyby, while others underwent non-targeted flybys at greater distances. Some of the smaller Jovian satellites were also included as non-targeted objects.

Orbit	Date	Targeted	Spatial res. [km/pxl]	Nontargeted	Spatial res. [km/pxl]
Galileo Prime Mission					
G1	June 27, 1996	**Ganymede**	13 - 0.011	Europa	1.6
G2	Sep. 6, 1996	**Ganymede**	0.228 - 0.045	Callisto Europa	17 - 4.3 6.9
C3	Nov. 4, 1996	Callisto	10 - 0.029	Europa Io	0.85 - 0.43 4.1 - 2.5
E4	Dec. 19, 1996	Europa	1.2 - 0.021	(none)	
E6	Feb. 20, 1997	Europa	1.7 - 0.022	**Ganymede** Callisto	14.4 - 3.6 9.4
G7	Apr. 5, 1997	**Ganymede**	0.554 - 0.145	Europa Callisto	3.2 - 0.388 6.4
G8	May 7, 1997	**Ganymede**	0.936 - 0.143	Callisto	2.32 - 0.678
C9	June 25, 1997	Callisto	1.1 - 0.14	**Ganymede** Europa	4.0 - 0.84 12.6
C10	Sep. 17, 1997	Callisto	0.428 - 0.089	Europa **Ganymede**	14.7 - 7.3 17
E11	Nov. 6, 1997	Europa	0.289 - 0.033	Callisto	13.9
Galileo Europa Mission (GEM)					
E12	Dec. 16, 1997	Europa	1.4 - 0.006	**Ganymede**	0.16
E14	Mar. 29, 1998	Europa	1.4 - 0.02	**Ganymede** Io	18.7 - 9.3 2.3
E15	May 15, 1998	Europa	0.245 - 0.028	(none)	
E16	July 21, 1998	*Saving event !*			
E17	Sep. 26, 1998	Europa	4.1 - 0.039	(none)	
E18	Nov. 22, 1998	*Saving event !*			
E19	Feb. 1, 1999	Europa	0.9 - 0.063	(none)	
C20	May 5, 1999	Callisto	0.6 - 0.10	**Ganymede**	9.0
C21	June 30, 1999	Callisto	0.015	Io	3.7 - 1.3
C22	Aug. 14, 1999	*(none)*		Amalthea	5.9 - 5.4
I24	Oct. 11, 1999	Io	> 5 - 0.009	(none)	
I25	Nov. 26, 1999	Io	0.26 - 0.15	Europa Amalthea	0.9 - 0.09 3.78
Galileo Millenium Mission (GMM)					
E26	Jan. 4, 2000	Europa	0.109 - 0.011	Io Amalthea Thebe Metis	4 - 3.4 2.56 1.93 2.93
I27	Feb. 22, 2000	Io	> 3 - 0.01	(none)	
G28	May 21, 2000	**Ganymede**	0.56 - 0.015	Europa	18.4 - 13.6
G29	Dec. 29, 2000	**Ganymede**	0.78 - 0.68	(none)	
C30	May 25, 2001	Callisto	11.6 - 0.005	**Ganymede** Io	12.2 - 3.6 4.0 - 3.6

Table 1.1: Galileo orbits in the Prime Mission and mission extensions GEM and GMM that included targeted and non-targeted Ganymede observations.

SSI observation ID	Center lat./lon. (East)	Footprint	Resolution [km/pxl]	SSI filters	Inc / Emi / Pha angles	Observation details	Chapter / section in thesis
G1GSGLOBAL01	-6.7 / 204	1x1	6.7	clr	30 / 0 / 30	Geodetic control; global color (with G1GSGLOBAL02) of anti-jovian hem.	
G1GSGLOBAL02	-6.7 / 204	1x1	13.5	vio, grn, 756nm, 889nm, 968nm	30 / 0 / 30	Global color (with G1GSGLOBAL01) of anti-jovian hemisphere	
G1GSURUSUL01	11 / 192	2x2	0.075	clr	13 / 23 / 16	Light terrain of Uruk Sulcus; stereo with G2GSURUKSL01	
G1GSGREGIO01	18 / 212	2x2	0.08	clr	30 / 48 / 21	Dark terrain of Galileo Regio; stereo with G2GSGLLREG01	
G1GSMEMPHI01	15 / 226	1x8	0.065	clr	39 / 49 / 17	Transect across palimpsest Memphis Facula in dark terrain of Galileo Regio	
G1GSSULCUS01	30 / 270	1x4	0.011	clr	83 / 9 / 76	High-resolution transect across light terrain of Xibalba Sulcus	
G2GSTRANST01	32 / 173	2x2	0.18	clr	39 / 34 / 30	Tectonic disruption of dark terrain by throughgoing grooves in NW Uruk Sulcus	Chap. 2 / section 2.5.1.3
G2GSCRATER01	1 / 207	1x1	0.22	vio, grn, 756nm, 968nm	11 / 48 / 39	Composition and origin of dark floor crater Khensu	Chap. 4 / section 4.4.3.3.1
G2GSNIPPUR01	49 / 156	3x1	0.1	clr	59 / 49 / 26	Stratigraphy of complex light grooved terrain	Chap. 2 / section 2.5.1.2
G2GSGRVLNS01	39 / 159	1x2	0.08	clr	53 / 39 / 26	Light smooth and grooved terrain of Byblus Sulcus; dark halo crater Nergal	Chap. 2 / section 2.5.1.1
G2GSGLLREG02	18 / 211	1x1	0.1	clr	25 / 54 / 41	Dark terrain of Galileo Regio; stereo with G1GSGREGIO01	
G2GSPLMPST01	22 / 180	1x13	0.09	clr	32 / 15 / 35	Transect across palimpsest Epigeus superimposed on light terrain of Uruk Sulcus with secondary crater chains	

G2GSURUKSL01	11 / 192	2x1	0.04	clr	14 / 36 / 47	High-resolution stereo of light terrain in Uruk Sulcus with G1GSURUSUL01	
G2GSLTDKBD01	60 / 190	1x16	0.05	clr	59 / 52 /33	Transect across high-latitude dark-light terrain boundary	
E6GSCOLOR_01	-0.1 / 36	1x1	14.4	vio, grn, 756nm, 889nm, 968nm	37 / 0 / 37	Global color; Voyager gap fill of trailing hemisphere	
E6GSGLOBAL01	1.2 / 54	1x1	7.5	grn	2.8 / 0 / 2.8	Low-phase photometry	
E6GSGLOBAL02	2.8 / 96	1x1	3.6	clr	62 / 0.7 / 62	Voyager gap fill of trailing hemisphere	
G7GSPALIMP01	31 / 26	1x1	0.48	clr	49 / 37 / 66	Palimpsest Zakar in light terrain	
G7GSCATENA01	38 / 346	1x1	0.57	clr	81 / 34 / 66	Crater chain Enki Catena	
G7GSNICHOL01	-13 / 9	1x3	0.18	clr	58 / 32 / 73	Dark terrain of Nicholson Regio; mosaicking with 28GSARBELA02	Chap. 2 / section 2.5.2.1
G7GSACHELS01	63 / 348	1x2	0.178	clr	82 / 55 / 70	Craters Gula and Achelous (pedestal and bright ray crater) at high latitudes of subjovian hemisphere	Chap. 3 / section 3.4.1.1 // Chap. 4 / section 4.4.3.3.2
G7GSNUNSUL01	45 / 42	1x2	0.23	clr	50 / 57 / 76	Potential shear zone in light terrain of Nun Sulci in subjovian hemisphere	
G7GSNEITH_01	29 / 353	2x2	0.14	clr	72 / 15 / 73	Large dome crater Neith on dark terrain east of Perrine Regio	
G7GSKITTU_01	0.6 / 25	1x1	0.15	grn	37 / 44 / 80	Dark ray crater Kittu on light terrain of Mysia Sulci north of Nicholson Regio (dark terrain)	Chap. 3 / section 3.4.1.2 // Chap. 4 / section 4.4.3.1.3
G7GSKITTU_02	0.6 / 25	1x1	0.3	vio, 756nm, 968nm	37 / 45 / 80	Dark ray crater Kittu; color observation with G7GSKITTU_01	

G8GSREGCON01	40 / 167	1x1	0.95	clr	79 / 44 / 62	Regional context for observations G2GSNIPPUR01, G2GSGRVLNS01, and G2GSTRANST01	
G8GSTIAMAT01	0 / 155	1x1	0.49	clr	84 / 21 / 63	Light grooved terrain of Tiamat Sulcus; low-sun observation	
G8GSMARIUS01	-18 / 204	1x1	0.3	clr	37 / 41 / 70	Detail of dark terrain in Marius Regio with light grooved lane Lagash Sulcus	
G8GSRNGBAS01	-27 / 210	1x2	0.3	clr	35 / 57 / 73	Heavily degraded multi-ring basin in southeastern Marius Regio (dark terrain) and Sippar Sulcus (light terrain)	
G8GSBUTOFC01	13 / 157	1x2	0.19	clr	80 / 15 / 69	Ancient palimpsest in dark terrain of Marius Regio	
G8GSMELKRT01	-10 / 174	1x2	0.18	clr	62 / 19 / 72	Dome crater Melkart in dark terrain of Marius Regio	Chap. 4 / sec. 4.4.3.4.2
G8GSCALDRA01	-30 / 175	2x3	0.18	clr	60 / 41 / 73	Potential cryovolcanic calderas (Musa, Natrun and Rum Patera) in reticulate and smooth light terrains of Sippar Sulcus	Chap. 2 / section 2.5.4.2
G8GSFRACDK01	8 / 203	1x1	0.16	clr	35 / 44 / 78	Fractured light terrain at Galileo Regio (dark terrain) and Uruk Sulcus (light terrain) boundary	
G8GSANSHAR01	12 / 168	1x2	0.15	clr	68 / 10 / 74	Origin of light grooved lane Anshar Sulcus in dark terrain of Marius Regio	
G8GSPITCRA01	24 / 166	1x1	0.14	clr	73 / 22 / 73	Pit crater Lugalmeslam on boundary of light and dark terrain (Uruk Sulcus / Marius Regio)	
G8GSERECH_01	-15 / 182	1x2	0.15	clr	55 / 34 / 77	Deformation style and T-relationship in light terrain of Erech and Sippar Sulcus	Chap. 2 / section 2.5.4.1
C9GSSULCUS01	29 / 275	1x4	0.85	clr	31 / 36 / 33	Transect of Xibalba Sulcus light terrain between Galileo and Perrine Regio dark terrain; context for G1GSSULCUS01	

C9GSGLOBAL01	0 / 270	1x3 + 1x4	2.0	clr	(66 / 25 / 87) (variable)	Voyager gap fill of leading hemisphere	
10GSGLOCOL01	0 / 343	1x1	34.0	vlt, grn, 756nm, 889nm, 989nm	0 / 0 / 0	Global color and low-phase photometry; sub-jovian hemisphere	
12GSGLGMSH01	-57 / 234	4x1	0.16	clr	62 / 64 / 8	Transect of impact basin Gilgamesh	
14GSGLOBAL01	0 / 54	1x1	9.0	vlt, grn, 889nm	10 / 0 / 10	Trailing and sub-jovian hemisphere; investigate global shape, color, and presence of surface frost	
20GSGEOGAP01	0.5 / 90	1x1	9.0	clr	25 / 0 / 25	Improve geodetic control net; trailing hemisphere	
28GSSMOOTH01	-16 / 50	1x4	0.016	clr	50 / 66 / 17	High-resolution transect of smooth light terrain in Harpagia Sulcus (context in 28GSSMOOTH02); cryovolcanic versus tectonic formation hypotheses	
28GSBRTDRK01	-14 / 41	1x5	0.02	clr	58 / 21 / 78	High-resolution transect of dark-light terrain boundary in Nicholson Regio and Harpagia Sulcus (context in 28GSBRTDRK02)	
28GSNICHOL01	-15 / 23	1x4	0.027	clr	42 / 40 / 79	High-resolution transect of dark terrain in Nicholson Regio; small-scale geologic processes and impact cratering (context in 28GSNICHOL02)	
28GSARBELA01	-15 / 13	1x4	0.035	clr	33 / 45 / 74	High-resolution transect of light smooth lane Arbela Sulcus in Nicholson Regio; shear-tectonism versus cryovolcanic origin (context in 28GSARBELA02)	
28GSCALDRA01	-34 / 42	1x4	0.043	clr	62 / 30 / 40	Hi-res transect of light terrain with potential cryovolcanic caldera(s) Hammamat Patera; secondaries from dome crater Enkidu (context in	

						28GSCALDRA02)	
28GSSMOOTH02	-11 / 55	1x2	0.12	clr	73 / 50 / 23	Light smooth and grooved terrain in Harpagia Sulcus; context for 28GSSMOOTH01	Chap. 2 / section 2.5.3.3
28GSBRTDRK02	-10 / 46	1x2	0.12	clr	63 / 39 / 24	Dark-light terrain boundary of Nicholson Regio and Harpagia Sulcus; context for 28GSBRTDRK01 with stereo	Chap. 2 / section 2.5.3.1
28GSNICHOL02	-15 / 22	1x2	0.125	clr	41 / 18 / 27	Dark terrain of Nicholson Regio; context for 28GSNICHOL01 with stereo	Chap. 2 / section 2.5.2.1
28GSARBELA02	-11 / 18	3x2	0.13	clr	37 / 11 / 28	Light smooth lane of Arbela Sulcus through dark terrain of Nicholson Regio; context for 28GSARBELA01 with stereo	Chap. 2 / section 2.5.2.1
28GSCALDRA02	-20 / 47	1x2	0.165	clr	66 / 46 / 22	Potential cryovolcanic calderas (Hammamat Patera) in light terrain; secondary crater clusters from dome crater Enkidu; context for 28GSCALDRA01 with stereo	Chap. 2 / section 2.5.3.2
29GSCAPCOL01	34 / 330	1x2 + 1x3	0.7	vlt, grn	35 / 37 / 2	Dark terrain of Perrine Regio and light terrain at mid- and high latitudes	
29GSDARDAN01	-25 / 339	1x3	0.78	clr	32 / 32 / 2	Strike-slip fault in light terrain of Dardanus Sulcus	
30GSTRMMAP01	0 / 100	1x2	3.6	grn	n/a	Near-terminator mapping in trailing hem.	
30GSGLOCOL01	0 / 110	1x1	9.1	vlt, grn, 756nm, 889nm	30 / 0 / 30	Global color; completion of global imaging for cartographic control	

Table 1.2: Observations of Ganymede by the Solid State Imaging Subystem (SSI) during the Galileo mission. Observations included in this study are indicated.

The orbits were numbered and identified by the targeted encounter body: Orbits G1, G2, G7, and G8 for Ganymede, Orbits E4, E6, and E11 for Europa, and Orbits C3, C9, and C10 for Callisto (Carr et al., 1995). Due to solar conjunction, no images were captured during Orbit E5. Io was only planned for a single targeted flyby in the orbit referred to as J0 following the Jupiter orbit insertion (JOI) in December 1995.

The Galileo mission underwent two extensions. The first, known as the Galileo Europa Mission (GEM), primarily focused on observing Europa through targeted flybys. However, the other three Galilean satellites could also be considered as target bodies. Notably, Io was chosen as a major target to compensate for the loss of data from the J0 close flyby. GEM encompassed orbits E12 to I25, with no SSI images taken in orbits E13, C22, and C23. The third and final mission extension was named the Galileo Millennium Mission (GMM), spanning orbits E26 to A34. Unfortunately, no imaging was planned during the last close flyby at the smaller moon Amalthea. Instead, this final orbit was used to prepare for and execute a controlled impact of the Galileo orbiter into Jupiter's atmosphere on September 21, 2003, as part of the End-Of-Mission (EOM) scenario. This approach was chosen for planetary protection to prevent any accidental impact of Galileo on Europa, which could introduce terrestrial microorganisms and potentially contaminate Europa's subsurface ocean, where traces of life may exist.

1.4 Objectives

The objective of this thesis is to gain more insight into the formation of Ganymede's light terrain. Among the studies that have been conducted regarding the light terrain, no general conclusion has been reached when its formation started and how long it lasted with respect to Ganymede's geologic evolution. Previous works concentrated on the global or regional structural analysis of Ganymede's linear features in the dark and light terrain (Cameron et al., 2018; Rossi et al., 2020) and their implication for which processes could be responsible to trigger this activity (Bland et al., 2009). In order to complement previous studies and to further our knowledge about the formation of Ganymede's light terrain and to provide better constraints for future modeling work, this thesis aims to answer the following research questions:

i. What is the position of the light terrain and its subunits within the stratigraphy of Ganymede's geologic units?

ii. Is there any evidence that changes in tectonic style of different light terrain units, such as smooth and grooved light terrain, happen with time?

iii. What is the geologic age of the light terrain and how extended was its formation period with respect to Ganymede's geologic evolution?

iv. Can the formation of the light terrain be associated to a specific global process of Ganymede's geologic evolution, such as global expansion?

v. Are the current data base and available cratering chronology models for deriving the absolute age of the geologic units on Ganymede's surface sufficient to define the time and duration of the light terrain formation?

vi. What can impact craters, that have been tectonically affected, such as polygonal craters, reveal about Ganymede's tectonic past?

vii. How do polygonal impact craters along with tectonic linear structures, such as ridges, grooves, indicate a past period of intense tectonic activity on Ganymede in comparison to other icy bodies?

viii. Can Ganymede's impact craters depending on their location, size and depth of excavation of different kind of ejecta material be used to investigate and compare the vertical subsurface stratigraphy of both dark and light terrain and the tectonic processes that formed the light terrain and/or resurfaced the older dark terrain?

ix. What types of extensional tectonism, including spreading and rifting modes, are favorable in different locations across Ganymede?

2 Stratigraphy, Crater Size–Frequency Distribution, and Chronology of Selected Areas of Ganymede's Light and Dark Terrains

This chapter has been published as peer-reviewed article as:

N. R. Baby, R.J. Wagner, K. Stephan and T. Kenkmann (2023) Planetary Science Journal, **4,** 162, **DOI:**10.3847/PSJ/acebed.

2.1 Abstract

The stratigraphy of the largest natural satellite of our solar system, Ganymede, is investigated using available global mosaic (basemap) and high-resolution images. We are focusing on the reconstruction of the formation and tectonic evolution of selected areas of dark and light terrain units and investigate their morphological characteristics and relative ages at a local scale using high-resolution images from the sub-Jovian and anti-Jovian hemispheres. For this, geological maps and crater size–frequency distributions for each of the terrain units were prepared, and relative as well as absolute ages were derived by applying the currently available lunar-derived impact chronology model and the Jupiter-family comet chronology model. The relative ages obtained from the cross-cutting relationships of terrain units are not always consistent with the ages derived from the crater size–frequency distributions. Some regions are influenced by secondary and sesquinary craters and tectonic resurfacing activities. Independent of the applied model, the derived crater size–frequency distribution showed that the light terrain started to form soon after the completion of dark terrain formation.

2.2 Introduction

The Jovian satellite Ganymede, the major target of ESA's upcoming JUICE (JUpiter ICy moons Explorer) mission (Grasset et al. 2013; The JUICE Science Working Team 2014), exhibits a complex geology. The surface of Ganymede is dominated by two major geologic units. Approximately 35% of the surface is covered by so-called dark terrain, which is heavily cratered and represents the oldest preserved surface on Ganymede (Pappalardo et al. 2004). The dark terrain is cross-cut by a somewhat younger, so-called "light" terrain that shows strong indications for tectonic resurfacing (Pappalardo et al. 2004; Jaumann et al. 2022). It forms a complex network, surrounds and cross-cuts the dark terrains and builds

up about 65% of Ganymede's surface. The tectonic pattern of the light terrain is a major key for understanding Ganymede's formation and geologic evolution.

In order to prepare for the JUICE mission (Grasset et al. 2013) and to refine the science questions and the requirements for the observations made by the Jovis, Amorum ac Natorum Undique Scrutator (JANUS) camera (Palumbo et al. 2014), as well as to evaluate the currently available methods and models for investigating Ganymede's geologic history, we reinvestigate the stratigraphic relationships of Ganymede's geologic terrains and particularly the light terrain units on the local scale at those locations on Ganymede's surface for which high-resolution imagery is available. We use cross-cutting relationships and crater-counting tools to derive the local geological history. The regions chosen for this study are strongly tectonized light terrains composed of different subunits. This study complements the work of Patterson et al. (2010) and Collins et al. (2013) at the local scale. The goal is to deepen our knowledge on the local formation processes of the light terrain, to evaluate changes in tectonic style through time across Ganymede, and/or to identify possible differences and similarities of the light terrain at different locations, but also various degrees of resurfacing. Further, we evaluate the currently available methods of deriving surface ages by crater size–frequency distribution measurements in order to verify previous estimations of the geologic age of Ganymede's light terrain units and the time of their formation with respect to Ganymede's evolution.

2.3 Database, Data Processing, and Selection of Study Areas

2.3.1 The Voyager and Galileo Missions and a Description of Their Imaging Instruments

In 1979, Voyagers 1 and 2 observed the surface of Ganymede at spatial resolutions up to 470 m pixel^{-1}, with an average of 1–2 km pixel^{-1} (Smith et al. 1977, 1979a, 1979b; Kersten et al. 2021). The Voyager Imaging Experiment encompassed a narrow angle (NA) and a wide angle (WA) Vidicon camera on each Voyager spacecraft. Both cameras could take images through several color filters ranging from 346 nm (UV) to ~600 nm (red/orange), including a panchromatic (broadband) or clear filter (Smith et al. 1977). Prior to the first Voyager flybys, NASA had been planning a mission with a Jupiter orbiter and an atmospheric probe, which was called Galileo. Images could be taken with an NA camera through eight color filters ranging from ~400 nm (violet) to 968 nm (near-infrared) including a panchromatic or clear filter. Galileo was inserted into Jupiter orbit in 1995

December and performed 34 orbits until it was set on an impact course with Jupiter's atmosphere in 2003 September. Orbits were increasingly numbered and designated according to the main satellite target chosen for a close flyby (G: Ganymede, C: Callisto, E: Europa, and I: Io). During the Galileo Prime Mission (orbits G1 through E11) Ganymede was selected for a close flyby in orbits G1, G2, G7, and G8. The gaps at the leading and trailing hemisphere left by Voyager could be filled in orbits E6 and C9, but only at spatial resolutions comparable to Voyager (C9), or even less (E6). In the two mission extensions, Galileo Europa Mission (GEM; orbits E12–I25) and Galileo Millennium Mission (GMM; orbits E26–A34, i.e., Amalthea flyby, no images taken), Ganymede was chosen in orbits G28 and G29 for two further close flybys.

Despite 34 orbits the loss of the High Gain Antenna (HGA) resulted in a significantly incomplete imaging at regional (100–300 m pixel^{-1}) and especially high ($\ll$100 m pixel^{-1}) resolution of Ganymede's surface, often resulting in mostly spatially isolated high-resolution images, which complicates efforts to derive an overall picture of Ganymede's geology, in terms of the extent of geologic units, measurements of their superimposed crater size–frequency distributions, and styles of tectonic deformations. Nevertheless, we could define four study areas (Regions A to D, Section 2.3.3) that are covered by up to three sets of 1 × 2, 2 × 2, or 2 × 3 Galileo Solid State Imaging (SSI) footprints (Figure 2.1 and Table 2.1). These regions cover light terrains that range from narrow bands to extensively resurfaced portions and a complex network of light terrains. Each region offers a view into the direct contact between the light and adjacent ancient dark terrains.

2.3.2 Data Processing

Geologic mapping, measurements of crater size–frequency distributions, and tectonic analyses are based on image mosaics exclusively produced at the DLR Institute of Planetary Research, Berlin. Mostly, the processing of images was carried out using the Video Image Communication and Retrieval (VICAR) program package developed by the Multi-Mission Image Processing Laboratory (MIPL) at JPL. For specific tasks, programs of the Integrated Software for Images and Spectrometers (ISIS) program package developed at the U. S. Geological Survey were used alternatively.

To generate image mosaics, several steps of systematic processing are necessary. In the first step, errors in data transfer, dark currents, and blemishes are corrected and a radiometrically calibrated image is produced. Calibration files and VICAR or ISIS

programs are project and camera specific (Smith et al. 1977; Benesh & Jepsen 1978; Danielson et al. 1981; Klaasen et al. 1984; Belton et al. 1992). For the Voyager cameras an additional processing step is needed to correct distortions of the camera telescopes and of the Vidicon tubes geometrically (Smith et al. 1977; Benesh & Jepsen 1978). The second step is the map projection of images, based on a Voyager-derived control net (Davies & Katayama 1981), and on camera pointing information from the Navigation Ancillary Information Facility (NAIF) at JPL for the Galileo SSI images (Davies et al. 1998). From the map-projected images, local mosaics or a global image basemap can be created.

In this work we used a controlled global basemap, based on updated Ganymede radii and a new set of control points (Archinal et al. 2011; Zubarev et al. 2015, 2016; Kersten et al. 2021). The basemap also provides an essential planning tool for Ganymede imaging with the JANUS camera aboard the upcoming ESA JUICE Mission to Ganymede and the Galilean satellites (Grasset et al. 2013; Stephan et al. 2021). In agreement with the JUICE Task Group for the satellite coordinate systems, cartography, and nomenclature, east longitudes are used. The map resolution is 128 pixels degree^{-1}, corresponding to a map scale of 358.774 2 m pixel^{-1} (Kersten et al. 2021).

Since most of the areas of interest we selected for this work were imaged at spatial resolutions much higher than 358 m pixel^{-1}, we created local context mosaics. For this task, the basemap was zoomed up to the original map scale of each selected SSI target area, and the SSI frames from each area were registered manually onto the basemap. In addition, we applied high-pass filters to enhance the contrast and small-scale details in the Galileo SSI images. Depending on the geographic location of each target area, each context mosaic was reprojected into either a Mercator projection for locations in equatorial latitudes (±22°), or Lambert conformal with two standard parallels for the midlatitudes (±31° to ±66°).

2.3.3 Study Areas

Region A lies in the northern portion of Ganymede's anti-Jovian hemisphere, where Nippur Sulcus adjoins the dark terrain of Marius Regio with the Regio cross-cut by narrow bands of light material such as Byblus Sulcus (Fig. 2.1 b). Three high-resolution SSI observation sequences (50–300 m pixel^{-1}) cover several parts of this region (G2GSNIPPUR01, G2GSGRLVNS01, and G2GSTRANST01) with G8GSREGCON01 (936 m pixel^{-1}) offering the context of these SSI observations.

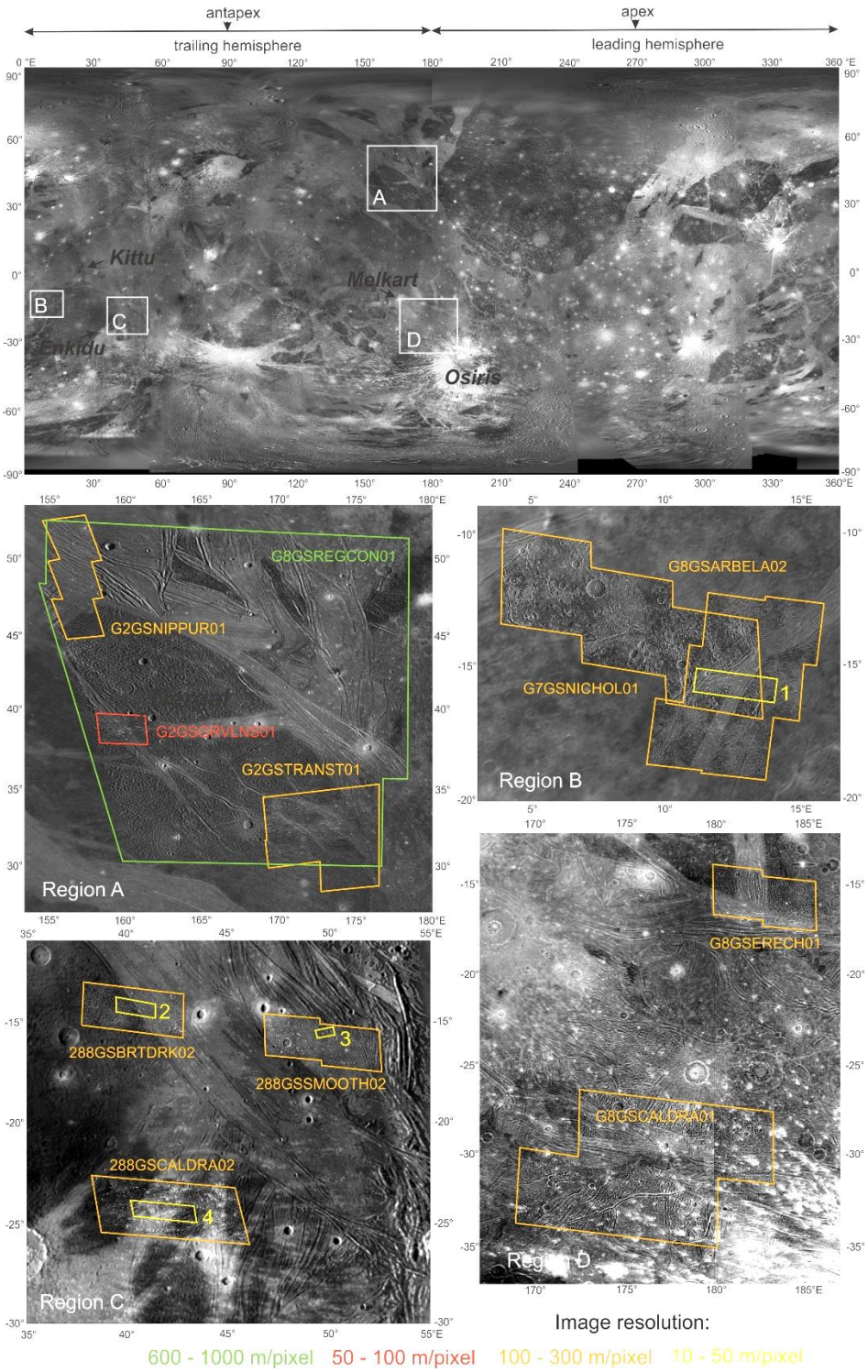

Figure 2.1: Overview of the studied regions: (a) global basemap of Ganymede (from Kersten et al. 2021) showing the location and distribution of the region of interests with subsets of each region such as (b) Region A—Byblus and Nippur Sulcus, (c) Regio Region B – Arbela Sulcus, (d) Region C – Harpagia Sulcus, and (e) Region D – Mummu and Sippar Sulci and Erech Sulcus, with the frames indicating the areas observed by Galileo SSI (Table 2.1) at high resolution. The highest-resolution images indicated by numbers are (1) 28GSARBELA01 (34 m pixel $^{-1}$), (2) 28GSBRTDRK01 (20 m pixel^{-1}, (3) 28GSSMOOTH01 (16 m pixel^{-1}), and (4) 28GSCALDRA01 (43 m pixel^{-1}). For the location of the local features see Figures 2.5 – 2.21.

Reg.	Sequences	No. of Images	Center Coord. (latitude, W longitude)	Apex distance D_A [°]	Resolution [m/pxl]	p/i/e	Covered Regions
A	G2GSNIPPUR01	3	49, 204	105.2	99	26/ 59/ 49	Nippur Sulcus in contact with Marius Regio
	G2GSGRLVNS01	2	40, 202	105.4	86	26/ 53/ 39	Byblus Sulcus within Marius Regio
	G2GSTRANST01	4	32, 188	95.5	188	30/ 39/ 34	Transitional terrains in contact with Marius Regio
	G8GSREGCON01	1	40, 193	(97.6; no counts)	936	62/ 79/ 44	Byblus Sulcus, Philus Sulcus and transitional terrains in contact with Marius Regio
B	28GSARBELA02	6	-15, 347	101.5	133	28/ 37/ 11	Arbela Sulcus within Nicholson Regio
	G7GSNICHOL01	3	-13, 351	99.7	181	73/ 58/ 32	Nicholson Regio in contact with Arbela Sulcus
C	28GSBRTDRK02	2	-14, 337	129.5	121	24/ 63/ 39	Harpagia Sulcus in contact with Nicholson Regio
	28GSSMOOTH02	2	-16, 310	137.4	116	23/ 73/ 50	Harpagia Sulcus
	28GSCALDRA02	2	-24, 318	127.7	150	22/ 66/ 46	Harpagia Sulcus in contact with Nicholson Regio
D	G8GSERECH01	2	-16, 177	87.1	143	77/ 55/ 34	Erech and Sippar Sulcus in contact with Marius Regio
	G8GSCALDRA01	5	-31, 184	93.4	179	73/ 60/ 41	Mummu and Sippar Sulci

Table 2.1: Observation parameters of the high-resolution Galileo SSI observations used in this study including the distances DA in degrees to the apex point of Ganymede's orbital motion (0° N / 270° E), measured for the center of the SSI target areas (see section A.1.2.3 in Appendix). Note that 'p', 'i' and 'e' represent the phase, incidence and emission angle of the corresponding observation sequence, respectively.

In contrast, Region B (Fig. 2.1 c) and C (Fig. 2.1 d) cover parts of Ganymede's sub-Jovian southern hemisphere. Region B is fully located within the dark ancient terrain of Nicholson Regio and cross-cut by the narrow but extended band of Arbela Sulcus. Region C, on the other hand, combines high-resolution observations that cover parts of Harpagia Sulcus. The Sulcus adjoins Nicholson Regio at its eastern border and represents an extended heavily resurfaced light terrain. Whereas Region B was observed by two sequences of SSI observations (G7GSNICHOL01 and 28GSARBELA02, 100–300 m pixel^{-1}) combined in two image mosaics, Harpagia Sulcus in Region C was imaged with high resolution between 100 and 300 m pixel^{-1} at three different locations (28GSBRTDRK02, 28GSSMOOTH02,

and 28GSCALDRA02). Portions of Regions B and C were also imaged at very high resolution better than 50 m pixel^{-1} (Fig. 2.1, SSI observations: 28GSARBELA01, 28GSBRTDRK01, 28GSSMOOTH01, and 28GSCALDRA01). Although these images were not analyzed in detail, they were considered in the geologic mapping procedure (see Section 2.4.1).

Like Region A, Region D (Fig. 2.1 e) is situated on Ganymede's anti-Jovian hemisphere, but in the southern hemisphere. It covers portions of Mummu, Sippar, and Erech Sulcus with the latter adjoining Marius Regio at its southern border. Mummu Sulcus is covered by a sequence of SSI observations (G8GSCALDRA01, 100–300 m pixel^{-1}), whereas Sippar and Erech Sulcus are imaged by two overlapping SSI images (100–300 m pixel^{-1}) of the G8GSERECH01 observation sequence.

2.4 Methodology

2.4.1 Mapping Procedure

Geologic mapping was performed for each of the high-resolution Galileo SSI images covering the study areas (Fig. 2.1). Mapping units and their formation are defined by (i) their albedo characteristics, i.e., from light to dark; (ii) morphological surface characteristics, such as numbers and appearance of superimposed impact craters; (iii) the degree of erosion; and (iv) the occurrence of linear features, including their frequency and orientation, particularly in the light terrain. In order to be consistent with previous geologic mapping done for Ganymede, we followed the scheme and naming convention developed by Patterson et al. (2010) and Collins et al. (2013). This global geological map of Ganymede was produced directly from the digital image mosaic of the satellite's surface released by the USGS (Becker et al. 2001) with the included Galileo and Voyager images resampled at a resolution of 1 km pixel^{-1}. Since our study focuses on a more local scale, geologic units presented in the global map of Collins et al. (2013) were refined or additional subunits were added if necessary. The simple but powerful geological principle of superposition was used to derive details of the stratigraphic relationship between the mapped units. These data were compared with the results of the crater size–frequency measurements, which are described in Section 2.4.2.

According to Patterson et al. (2010) and Collins et al. (2013) the geological terrains in Ganymede are mainly divided into two broad categories: (1) the ancient, heavily cratered

dark terrain (d) and (2) the less heavily cratered and thus presumably younger and strongly resurfaced light terrain (l). The dark terrain is classified as cratered (dc) and lineated (dl), whereas the light terrain is classified as grooved (lg), subdued (ls), and irregular (li). Reticulate terrain (r) appears to be transitional between dark terrain and light terrain. Terrain units whose morphological characteristics are unknown due to very low resolution are classified as undivided (Patterson et al. 2010). The term "sulcus" refers to a type of geological feature on Ganymede, a tectonic groove or furrow known as "sulci" in their plural form, and has been adopted as a designator by the IAU Planetary Nomenclature Committee.

About two thirds of Ganymede's surface area is covered by light terrain (Pappalardo et al. 2004). The light terrain contains a large number of parallel, subparallel, and curvilinear ridges and troughs, which extend for long distances (Shoemaker et al. 1982). Light grooved terrain (lg) has grooves that can form horst-and-graben-like structures, with their widths varying (e.g., Pappalardo et al. 2004). Grooves can be linear to curvilinear, equally to subequally spaced, parallel to subparallel in nature. Light subdued terrain (ls) is characterized by a moderate to high albedo and a smooth appearance, where grooves are mostly absent or not prominent enough to be characterized under lg. They are usually found associated with the light grooved and light irregular terrains. Satellite imagery with a high resolution of 10–50 m $pixel^{-1}$, however, shows that even this unit contains minor ridges and grooves. The light subdued terrain (ls) also shows caldera-like depressions that are interpreted as cryovolcanic features (Head et al. 1998; Kay & Head 1999; Spaun et al. 2001). However, the role of cryovolcanism and the formation of caldera-like features are not yet fully understood. Light irregular terrain (li) is characterized by irregularly spaced and oriented ridges and grooves, often seen as some portions of grooves and smooth regions within a single terrain unit. These terrains possess a moderate to high albedo and are usually found associated with lg and ls. These terrains are less common than other light terrains. Reticulate terrain is mesh-like in appearance, with many crisscross fractures or grooves, and is usually found adjacent to dark terrain. However, the grooves are not well developed. It has been suggested that block rotations within shear zones led to the formation of reticulate terrains (Murchie & Head 1988). Each of these light terrain units are further classified into three main categories based on the principle of cross-cutting relationships. Category 1 (lg_1, ls_1, and li_1) contains light terrain units which are cross-cut by all other light terrain units. Category 3 (lg_3, lg_3, and li_3) contains those light terrain units which cross-cut

all adjacent light terrains. Category 2 (lg_2, ls_2, and li_2) contains those light terrain units which cross-cut Category 1 units and, in turn, are cross-cut by Category 3 units (Patterson et al. 2010).

Dark terrains are commonly seen as polygons with a distinct boundary, which are surrounded or cross-cut by the light terrains. They are always of low albedo due to surface ice contaminants, with the proportion of contaminants ranging from less than 10% (Clark 1980) to about 45% (Spencer 1987). Processes like tectonic deformation, cratering, sublimation, and mass wasting lead to local variations in albedo (Prockter et al. 1998; Moore et al. 1999). The terrain unit dl is inherently similar to dc except for the presence of straight, sinuous, or curvilinear lineaments or fractures. Like dc, it also has low albedo (Pappalardo et al. 2004).

About two thirds of Ganymede's surface area is covered by light terrain (Pappalardo et al. 2004). The light terrain contains a large number of parallel, subparallel, and curvilinear ridges and troughs, which extend for long distances (Shoemaker et al. 1982). Light grooved terrain (lg) has grooves that can form horst-and-graben-like structures, with their widths varying (e.g., Pappalardo et al. 2004). Grooves can be linear to curvilinear, equally to subequally spaced, parallel to subparallel in nature. Light subdued terrain (ls) is characterized by a moderate to high albedo and a smooth appearance, where grooves are mostly absent or not prominent enough to be characterized under lg. They are usually found associated with the light grooved and light irregular terrains. Satellite imagery with a high resolution of 10–50 m $pixel^{-1}$, however, shows that even this unit contains minor ridges and grooves. The light subdued terrain (ls) also shows caldera-like depressions that are interpreted as cryovolcanic features (Head et al. 1998; Kay & Head 1999; Spaun et al. 2001). However, the role of cryovolcanism and the formation of caldera-like features are not yet fully understood. Light irregular terrain (li) is characterized by irregularly spaced and oriented ridges and grooves, often seen as some portions of grooves and smooth regions within a single terrain unit. These terrains possess a moderate to high albedo and are usually found associated with lg and ls. These terrains are less common than other light terrains. Reticulate terrain is mesh-like in appearance, with many crisscross fractures or grooves, and is usually found adjacent to dark terrain. However, the grooves are not well developed. It has been suggested that block rotations within shear zones led to the formation of reticulate terrains (Murchie & Head 1988). Each of these light terrain units are further classified into three main categories based on the principle of cross-cutting relationships.

Category 1 (lg_1, ls_1, and li_1) contains light terrain units which are cross-cut by all other light terrain units. Category 3 (lg_3, lg_3, and li_3) contains those light terrain units which cross-cut all adjacent light terrains. Category 2 (lg_2, ls_2, and li_2) contains those light terrain units which cross-cut Category 1 units and, in turn, are cross-cut by Category 3 units (Patterson et al. 2010).

2.4.2 Crater Size–Frequency Measurements

2.4.2.1 Size–Frequency Distributions of Impact Craters and Surface Ages

Crater size–frequency distributions (henceforth abbreviated CSFDs, or crater SFDs) are used to determine the relative ages of geological units. Deriving surface ages from crater SFDs superimposed on geologic units is based on the correlation between the frequency (or density) of impact craters and time: the higher the frequency of craters, the older the surface (e.g., Öpik 1960; Chapman & McKinnon 1986; Neukum & Ivanov 1994; Neukum et al. 2001; Werner & Ivanov 2015). Therefore, differences in crater frequencies generally reflect differences in the relative ages of surface units.

The absolute ages of surface units are obtained by using the two currently available impact chronology models. Both are subject to high degrees of uncertainties. Nevertheless, we will use such models in this study to compare and discuss the derived absolute ages and their uncertainties, as described in the following subsections, with respect to possible implications of geologic activities on Ganymede in the past. We introduce here the basics of how CSFDs are measured and used for extracting relative and absolute surface ages. A more thorough description of the methodology and the procedure of deriving ages from crater counts is described in Appendix 2.A.1.

2.4.2.2 Crater Production Function

In our study, we prefer to use the cumulative CSFD when plotting crater counts. In the ideal case, a crater SFD represents an image of the SFD of the members of a projectile family impacting a surface over time. In this case a CSFD is termed a production distribution; a crater formed by the impact of an external projectile is termed a primary crater (e.g., Neukum & Ivanov 1994; Werner & Ivanov 2015). Numerous studies on lunar, terrestrial planet, or asteroid surface units and also on the icy satellites of Jupiter have shown that the CSFDs on these bodies can be approximated by a (body-specific) production function

(henceforth abbreviated as PF)—representing the production distribution of craters—as a polynomial of at least tenth or eleventh degree from the smallest measurable crater diameter (meters or tens of meters) to the largest diameter (impact basins of several hundreds of kilometers; e.g., Neukum & Ivanov 1994; Neukum et al. 1998, 2001; Werner & Ivanov 2015; Hiesinger et al. 2016). The lunar PF polynomial is shown in Figure 2.2 (black curve).

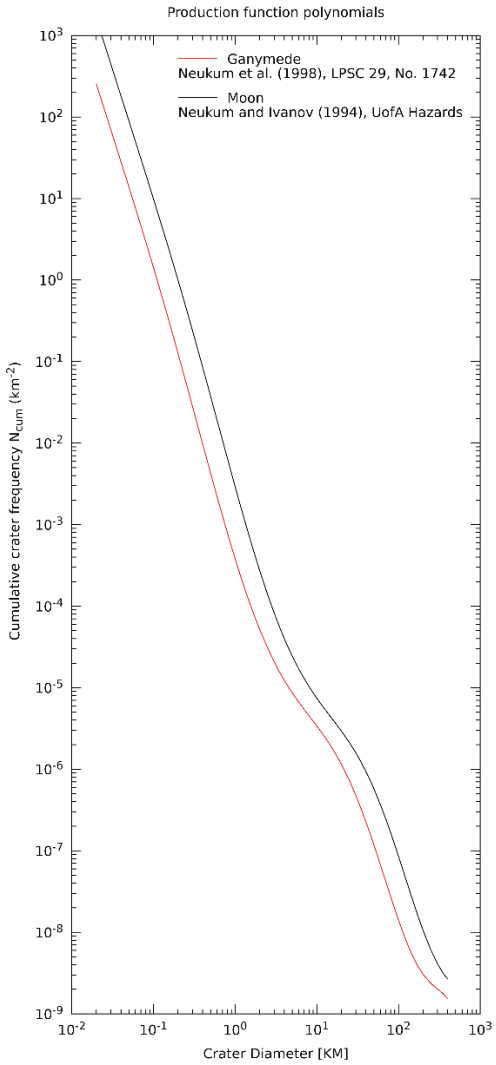

Figure 2.2: The PF polynomial of eleventh degree for Ganymede (Neukum et al. 1998; red), compared to the lunar PF (Neukum & Ivanov 1994; black) shown in a cumulative CSFD diagram.

Based on their CSFD measurements from Voyager images and, later, from Galileo SSI images, Neukum et al. (1998 and references therein) found a remarkable similarity between, e.g., lunar CSFDs and those from the icy Galilean satellites of Jupiter. Therefore, they derived a Ganymede-specific PF by shifting the lunar PF laterally in log(D) (see

Appendix 2.A.1.1). This PF derived for Ganymede is shown in comparison with the lunar PF in Figure 2.2 (red curve). Coefficients of the lunar and Ganymede PFs are listed in Table 2.A1 in Appendix 2.A.1.1.

2.4.2.3 Processes Affecting and Changing the Production CSFDs

In many cases the CSFDs are no longer pristine production distributions, but were subject to several processes affecting their shapes, which have to be considered in interpreting CSFD measurements. Among these are (a) saturation/equilibrium, (b) secondary craters and/or other sources, and (c) geologic processes. We briefly discuss these potential influences on our measurements, but we emphasize that these issues are still being intensely debated and are not fully solved. Also, a thorough discussion of crater scaling laws that link the size (or mass) of an impactor to the size of the crater it forms via specific impact conditions is beyond the scope of this paper (see, e.g., Werner & Ivanov 2015 as a reference).

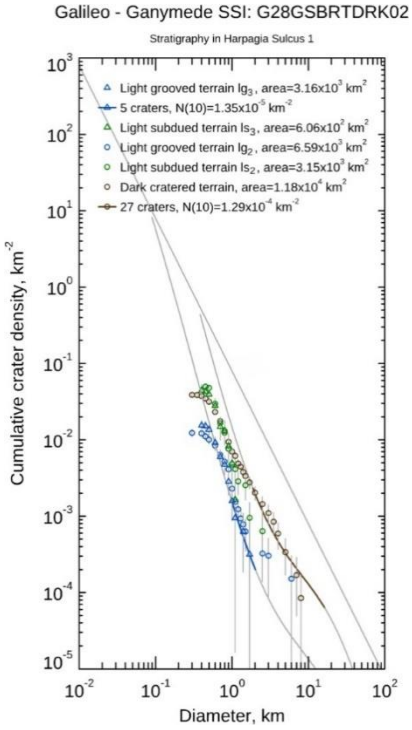

Figure 2.3: CSFDs measured in several light terrain units and in dark terrain (Galileo SSI target area 28GSBRTDRK02) with the Ganymede PF (Neukum et al. 1998) fitted to the data, and the equilibrium distribution with a cumulative slope of −2 (Neukum & Ivanov, 1994). The graph demonstrates that the CSFDs on Ganymede are well below saturation/equilibrium for small craters down to ~500 m diameter even in the old dark densely cratered terrains. See text for further explanation.

2.4.2.3.1 Saturation/Equilibrium versus Production Distributions

If a surface is impacted long enough that each newly formed crater obliterates preexisting craters the CSFD is termed to have reached saturation or equilibrium (e.g., Woronow 1978; Hartmann 1984; Chapman & McKinnon 1986; Neukum & Ivanov 1994; Richardson 2009; Werner & Ivanov 2015). Saturation/equilibrium is represented by a straight line with a cumulative slope of −2, which is achieved for CSFDs with slopes of −3 or steeper reaching equilibrium if subsequent impacts of small craters erase preexisting ones (e.g., Chapman & McKinnon 1986; Neukum & Ivanov 1994).

There is no consensus whether the most densely cratered regions such as, e.g., the lunar highlands, show equilibrium CSFDs (e.g., Richardson 2009) or not (e.g., Neukum & Ivanov 1994). As shown in Figure 2.3, we found that the CSFDs measured in both light and dark terrains on Ganymede in general are lower than a saturation/equilibrium distribution and therefore represent production distributions down to ~500 m crater diameter in the examples shown in the graph.

2.4.2.3.2 Secondary and Sesquinary Craters

Blocky material, which is ejected when a primary crater is formed, creates smaller satellite craters around the primary, termed secondary craters (e.g., Werner & Ivanov 2015 and references therein). These craters are different in morphology than primaries, characterized by less pronounced crater rims and more shallow floors, by more irregularly shaped rims, and by their occurrence in clusters or rays pointing radially away from the center of the for an example of suspected secondary craters). They generally form at lower velocities than primary craters. Secondary craters can also form at great distances from their parent crater by blocks ejected at high velocities close to the impact contact point, and thus they resemble primary craters, making them indistinguishable from each other (e.g., Bierhaus et al. 2005). It has been suggested that small craters (several kilometers and smaller) are predominantly of secondary origin and, therefore, are practically useless for dating surfaces at these crater sizes (e.g., McEwen et al. 2005). However, this issue is still under discussion.

Small craters on the Jovian satellites (and on other satellites in the outer solar system) could be almost exclusively of secondary origin if these bodies are mainly bombarded by projectiles derived from the Kuiper Belt, e.g., by ecliptic comets (ECs) since this impactor family is characterized by a deficit of small bodies (e.g., Dones et al. 2009; Kirchoff et al.

2018; Singer et al. 2019; Kirchoff et al. 2022). Such a scenario has been inferred by Bierhaus et al. (2001) for Europa, but a more recent work (Bierhaus et al. 2018) showed that local, target-specific effects of primary versus secondary cratering have to be considered on these satellites.

Material can be ejected and accelerated beyond the escape velocity of the satellite, impacting other satellites in the system, or even the satellite of origin again. This type of craters is termed sesquinary (e.g., Alvarellos et al. 2002; Zahnle et al. 2008). Sesquinary craters and/or long-traveling secondaries smaller than ∼2 km are practically indistinguishable from primary craters and may contribute to a measured CSFD with some uncertainty for craters smaller than this size (e.g., Singer et al. 2013; Kirchoff et al. 2022).

For measurements closely to or within the strewn field of a larger crater we tried to avoid measuring potential secondaries based on their morphological characteristics described above. However, it cannot be completely guaranteed that such secondaries, with these typical morphological characteristics, were excluded in our measurements, especially near primary craters with strewn fields of several 100s or 1000s of kilometers.

2.4.2.3.3 Geologic Resurfacing Processes

Erosion through micrometeoritic bombardment and sublimation, flooding with liquid material, or tectonic events tend to obliterate or completely erase especially smaller craters below a threshold diameter (e.g., Prockter et al. 1998; Moore et al. 1999; Werner & Ivanov 2015). Below this threshold diameter the slope of the CSFD becomes characteristically flatter in a cumulative crater frequency diagram. When this geologic process comes to an end, the surface becomes recratered with a steeper cumulative slope and remains undisturbed unless further geologic processes become active at later times. Such resurfacing events can be identified and even be dated in measured CSFDs (Michael & Neukum 2010). Indeed, resurfacing events have been documented on various celestial bodies, including the Moon, where early studies on resurfacing events in relation to CSFDs were conducted by Neukum & Horn (1976). These events play a significant role on Ganymede.

Previous measurements of impact craters in Ganymede's dark terrain have also revealed that viscous relaxation could have a major effect on impact degradation (Bland et al. 2017), providing a window into Ganymede's thermal history. However, since mainly the depths

of the majority of impact craters are reduced, this process is not expected to have a major influence on the CSFD measurements. The complete relaxation of small craters (<4 km diameter) requires high heat fluxes (150 mW m^{-2}) over long timescales (~1 Gyr) and is difficult to explain by viscous relaxation alone and thus requires an alternative explanation (Bland et al. 2017) such as the resurfacing processes mentioned above.

2.4.2.4 Absolute Ages Based on Impact Chronology Models

In order to reconstruct the geologic history of a planetary surface, crater frequencies representing the relative ages of surface units can be used to derive the absolute ages for these units. Since no radiometric ages of surface materials are available except for the Moon, this can only be done by impact chronology models, based on impact rates of the members of a dominating projectile family. Due to this model dependence of absolute ages from CSFD measurements, the term absolute model age (AMA) is commonly used (see, e.g., Hiesinger et al. 2016). Despite the high uncertainties associated with such models, we concentrate in our study on relative ages when discussing the stratigraphic relationships of the mapped surface units (Section 2.5). Since, however, absolute ages are essential to shed light on the potential timescales of Ganymede's geologic and tectonic activity, we also derived and discussed their absolute ages of using both models (Section 2.6).

The SFDs of craters described by a body-specific crater PF reflects the SFD of projectiles creating craters in a given time (e.g., Chapman & McKinnon 1986; Neukum & Ivanov 1994; Werner & Ivanov 2015 and references therein). The SFDs of craters also reflect the rheological properties of the surface (e.g., Massironi et al. 2009; Le Feuvre & Wieczorek 2011; Marchi et al. 2011). Craters are formed by members of distinct impactor families; on the terrestrial planets and asteroids in the inner solar system, craters were, and are at present, mainly created by impacts of Main Belt asteroids (MBAs), or from near-Earth objects (NEOs), with a contribution of comets being on the order of less than 10% (e.g., Neukum & Ivanov 1994; Neukum et al. 2001; Bottke et al. 2002; Strom et al. 2005; Marchi et al. 2009). For planets and icy satellites in the outer solar system, several potential impactor families are inferable (Shoemaker & Wolfe 1982; Chapman & McKinnon 1986; Neukum et al. 1998; Zahnle et al. 1998, 2003; Schenk et al. 2004; Dones et al. 2009; Werner & Ivanov 2015; Kirchoff et al. 2018; Singer et al. 2019): (a) MBAs, (b) short-period ECs and Centaurs from the Kuiper Belt, (c) long-period, nearly isotropic comets (NICs) from the

Oort cloud, (d) Trojans librating around the L4 and L5 Lagrangian points of Jupiter and Neptune, (e) irregular satellites, and (f) planetocentric material. The major source of impactors has strong implications on the absolute timescales in cratering these surfaces.

Currently, there are two available chronology models for the satellites of Jupiter, which were developed at the time of the early Voyager (late 1970s) and Galileo missions (late 1990s). The lunar-derived model (Neukum et al. 1998), henceforth abbreviated as LDM, is based on the similarities of lunar CSFDs and those on the Galilean satellites, assuming preferential impacts of MBAs on the Galilean satellites with a similar time dependence of crater frequency as in the case of the moon, as Neukum et al. (1998; and references therein) concluded. In this model, the impact rate drops exponentially but smoothly from ~4.3 Ga ago and becomes more or less constant since ~3–3.3 Ga until the present (Fig. 2.4).

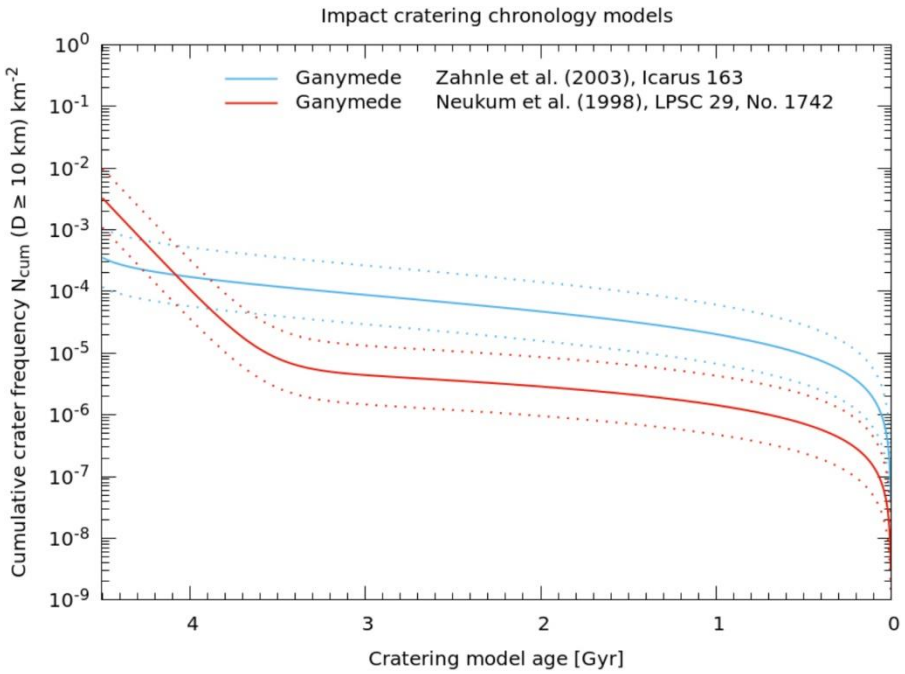

Figure 2.4: Comparison of the impact chronology models by Zahnle et al. (2003; JCM, blue) and Neukum et al. (1998; LDM, red) for a cumulative crater frequency Ncum (D ≥ 10 km). Also shown are the lower and upper model uncertainties (dotted curves; see the text in this section and Section 2.4.2.5). For the parameters (coefficients) and cratering rates of the two model functions we refer to Neukum et al. (1998), Zahnle et al. (2003), and to Appendix 2.A.1.2.1.

The second chronology model for the Jovian satellites is based on the predominant impacts of ECs or Jupiter-family comets (JFCs), henceforth termed JCM. By observing such Jupiter-crossing bodies, Shoemaker et al. (1986) and later Zahnle et al. (1998, 2003)

derived an impact chronology for each satellite with a more or less constant cratering rate from the present time back to ∼4 Ga. Prior to ∼4 Ga, the cratering rate is assumed to increase exponentially due to a $\sim 1/t$ depletion of impactors leaking from the Kuiper Belt with time (t; see the discussion in Zahnle et al. 1998).

Impacts from NICs from the Oort cloud occur much less often than do impactors from ECs (Zahnle et al. 1998). In this study we use the JCM with cratering rates for ECs by Zahnle et al. (2003) with updated cratering rates with respect to Zahnle et al. (1998; Fig. 2.4).

According to Zahnle et al. (2003), the SFD of JFCs for projectiles smaller than 20 km is derived from the crater SFD on Europa, young basins on Ganymede and Callisto, and Triton. In contrast, the SFD of projectiles larger than 50 km is derived from observed Kuiper Belt bodies. To bridge the gap between 20 and 50 km, Zahnle et al. (2003) use interpolation. It is evident that an impactor with a diameter of 20 km creates a crater on Ganymede with a diameter of at least 200–300 km for heliocentric impact velocities. Consequently, Zahnle et al. (2003) infer the impactor SFD from the CSFD for craters with diameters up to 200–300 km, similarly to our approach, but they use a diameter-dependent power-law distribution instead of an eleventh-degree polynomial.

The similarity between CSFDs measured on the surfaces of the moon and of, e.g., Ganymede, reported by Neukum et al. (1998), was never unequivocally explained by them—unless under the premise of mainly asteroidal impacts. Collisional evolution for nonasteroidal impactors dominating the bombardment of the Galilean satellites producing CSFD shapes similar to lunar CSFDs has been suggested (e.g., Wagner et al. 2017). Bottke et al. (2022), eventually, concluded recently that these similarities really exist and are indeed based on the collisional evolution of comets or other potential outer solar system impactors. Therefore, a lunar-derived Ganymede PF can be used to fit CSFDs measured on Ganymede and to derive AMAs from both models, despite different origins of impactors.

The graphs of the two concurring model chronology functions by Neukum et al. (1998; LDM) and Zahnle et al. (2003; JCM) are shown in Figure 2.4. We also included the upper and lower uncertainties of the chronology function graphs (dotted curves). For the JCM, Zahnle and colleagues assume an uncertainty of a factor of 2 in the cratering rate (Zahnle et al. 2003). In the LDM an uncertainty in cratering rate was not specifically given by Neukum et al. (1998). However, studies involving lunar-like chronologies in the inner solar system imply average uncertainties of at least factors of 2–3 (e.g., Neukum et al. 2001)

similar to the case of the JCM, therefore we chose the same uncertainty factor of 3 for the LDM too (see the more detailed description in Section 2.4.2.5). The procedure of how AMAs for both chronology models are obtained is described in more detail in Appendix 2.A.1.2.1.

The relative ages and AMAs from a CSFD measurement are obtained either by a least-squares fit of the Ganymede PF to the crater statistics data, or by a procedure termed Poisson timing analysis (PTA) (Michael et al. 2016). In this latter improved approach, an impact chronology model is exactly evaluated on the basis of Poisson statistics and a likelihood with an intrinsic uncertainty. The advantage of this procedure over a least-squares fit is that it is also applicable to a surface with no superimposed craters at all, which allows one to estimate the maximum age of a surface by considering the measurement area and the image resolution. For such cases, we assumed the existence of at least one crater with a (bin) diameter (in kilometers) beneath a factor of three times the image resolution (in kilometers per pixel). This procedure has been proven to be useful for the estimation of ages especially of those stratigraphically young craters which, at a given image resolution, are devoid of superimposed craters (e.g., Wagner et al. 2010, 2018, 2019). Therefore, the PTA approach is used for fitting CSFD measurements in our study.

2.4.2.5 Uncertainties in the Relative Ages and AMAs

The uncertainties in our CSFD measurements and derived AMAs are derived following the recommendations in Arvidson et al. (1979), Zahnle et al. (2003), Michael et al. (2016), and Robbins et al. (2018). If the formation of craters on a surface with area A (square kilometers) is assumed to have a Poisson distributed, the uncertainty, or the confidence interval, for n craters equal to, or larger than diameter D in a cumulative distribution is log $[(n \pm \sqrt{n})/A]$ (Arvidson et al. 1979). In general, as implemented in the craterstats 2.0 software package (see Appendix 2.A.1.2.1), measured crater diameters are binned using 18 bin diameters in each decade (semilogarithmic binning; e.g., Neukum & Ivanov 1994), and confidence intervals are calculated and plotted accordingly (Arvidson et al. 1979). Despite being recommended by Arvidson et al. (1979), we do not use a bin width of $\sqrt{2}$ km crater diameters, which is comparably coarse, but prefer the finer semilogarithmic binning instead, similar to studies discussed by others (e.g., Hiesinger et al. 2000; Schenk et al. 2004; Werner & Ivanov 2015).

The error handling of both crater frequencies for a reference crater diameter and associated AMAs in the craterstats 2.0 software tool is currently being reworked, expanded, and improved (G. Michael, personal communication). Therefore, we had to use work-arounds using our own software tools to present the uncertainties for the surface ages and/or to calculate AMAs for the JCM chronology.

Using the PTA approach described above (Michael et al. 2016), an LDM AMA and an associated cumulative frequency for craters ≥1 (or 10) km is obtained, along with upper and lower uncertainty frequencies. These uncertainties in the cumulative frequency are shown in plots of relative ages. However, this procedure does not consider that the chronology has a substantial additional uncertainty in the cratering rate, assumed to be a factor of ~2–3, as shown in Figure 2.4 (Section 2.4.2.4). The total uncertainty in the LDM AMA is therefore higher than from the application of the PTA alone, on the order of ±100–200 Ma for ages older than ~3.5 Ga and up to ~±1 Ga for ages younger than ~3–3.3 Ga.

For JCM AMAs, the upper and lower uncertainties are calculated from the factor of 3 in the cratering rate for ECs (Zahnle et al. 2003), holding the cumulative frequency fixed. Due to the low constant cratering rate, these uncertainties in the AMA are high, approximately ±0.5–1 Ga. The calculation of the (generally smaller) upper and lower uncertainties of the JCM AMA from the uncertainty in the cumulative frequency was not carried out in this study. An implementation to consider the total uncertainty in the craterstats 2.0 tool is in development (G. Michael, personal communication). Despite the high uncertainties in both chronology models, we chose to use two significant figures in the AMA (refer to Tables 2.2 through 2.10) since the units of different ages can be distinguished in cumulative frequencies, and increasing or decreasing trends in ages are inferable.

2.5 Mapping Results

2.5.1 Region A: Byblus and Nippur and Philus Sulci and Transitional Terrain (G8GSREGCON01)

Region A offers a detailed look into the light terrain units of Byblus Sulcus, Nippur, and Philus Sulci and the transitional terrain between Marius Regio and Nippur Sulcus, which surrounds and intersects the extended dark terrain of Marius Regio (Figs. 2.1 b, 2.5, 2.7, and 2.9). The light terrain units comprise grooves/fractures, narrow bands, and extensively resurfaced complex networks. Byblus (Fig. 2.5 a) and Nippur Sulcus (Fig. 2.7a) exhibit a northwest–southeast orientation (Head et al. 1997). Akitu Sulcus connects these two sulci

and has an east–west orientation. The Galileo SSI observation sequence G2GSNIPPUR01 (Fig. 2.7) covers portions of Nippur and Philus Sulci that lie approximately 200 km north of the Byblus Sulcus region (G2GSGRVLNS01, Fig. 2.5). The transitional terrain (G2GSTRANST01, Fig. 2.9) lies approximately 400 km southeast of Byblus Sulcus. The extended portion of Nippur Sulcus and Byblus Sulcus toward its south can be considered as part of transitional terrain.

2.5.1.1 Byblus Sulcus (G2GSGRVLNS01)

i. Geological Mapping

Byblus Sulcus is a narrow band of light terrain located at ~40°N/160°E trending in the northwest–southeast direction and intersecting the adjacent dark terrain of Marius Regio. The mosaic of two Galileo SSI images of G2GSGRVLNS01 having 86 m pixel^{-1} resolution is used for detailed mapping and CSFD estimation (Fig. 2.5 a). The geologic units that could be distinguished in this image include two impact craters (c), light grooved terrain lg_3, light subdued terrain ls_3, light grooved terrain lg_2, furrows (F) and dark cratered terrain (dc; Fig. 2.5 b). From the cross-cutting relationship, lg_3 and ls_3 cross-cut all adjacent terrains and are consequently the youngest terrains. The terrain unit dc is cross-cut by all other light terrains and is the oldest terrain.

The youngest features observed in this region are two morphologically fresh impact craters (possibly the result of a double impact) with the larger one, called Nergal (~8 km diameter), showing a dark halo of about one crater radius extent that is surrounded by light ejecta. These craters are located in the center of Byblus Sulcus and are superimposed on the youngest light grooved terrain lg_3. The light terrain of Byblus Sulcus, in general, shows a parallel and regular array of grooves in its middle part and more irregular grooves adjacent to it. The contact toward dark terrain on the western side is sharp whereas on the eastern side the grooves disappear gradually and two ls_3 terrains are present.

The light subdued terrains ls_3 are very smooth and show only a few indistinct grooves. This terrain has a sharp border separating dc and lg_2, but separation from lg_3 does not show any sharp trough. The light grooved terrain lg_2 is characterized by the presence of a sigmoidally shaped large ridge in the middle part, which has a high albedo and is surrounded by a number of short grooves which are trending obliquely to the main ridge.

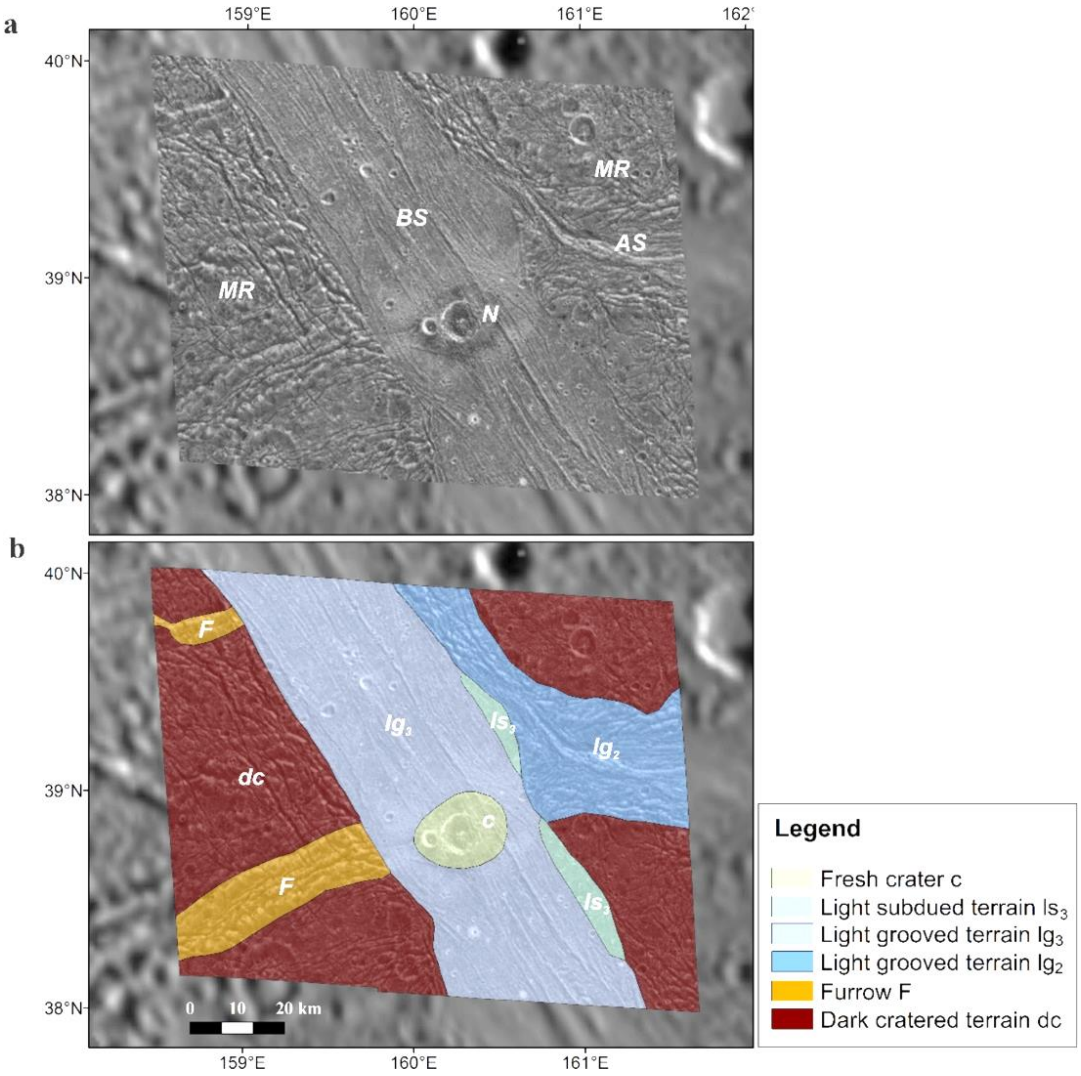

Figure 2.5: Region A/Byblus Sulcus: (a) SSI observation G2GSGRVLNS01 with the location of Byblus (BS) and Akitu Sulcus (AS), Marius Regio (MR), and impact crater Nergal (N) indicated and (b) the associated geologic map produced following the mapping style of Collins et al. (2013).

The dark cratered terrain dc is the oldest unit in G2GSGRVLNS01 (Fig. 2.5). It is not only densely cratered but also highly fractured. Northeast–southwest trending furrows (F) are common geomorphological features in dc. Fractures in between the furrow sets and on either side of lg_2 either run parallel to the trend of lg_3 (northwest–southeast) and seem to be related to the formation of the lg_3 light terrain, or they trend perpendicular to this direction. The furrows usually occur in sets (Smith et al. 1979a, 1979b). The most striking feature of the entire area is the bent Akitu Sulcus with a sigmoidal ridge at its center, mapped as lg_2. This unit suggests that dextral strike-slip may have occurred along the northwest–southeast

direction, which was later formed by the lg_3 and ls_3 units. This suspected shearing led to drag folding of unit lg_2 (Cameron et al. 2018).

Region A	Terrain unit	N (10) [km^{-2}]	N (1) [km^{-2}]	LDM [Ga]	JCM [Ga]	Area [km^2]	No. of craters counted
G2GSGRLVNS01 (**Byblus Sulcus**)	lg_3	2.61e-5±5.38e-6	2.94e-3±6.06e-4	$3.77^{+0.038}_{-0.044}$	$1.25^{+1.57}_{-0.79}$	4027.26	156
	ls_3	3.95e-5±1.95e-5	4.45e-3±2.20e-3	$3.83^{+0.083}_{-0.12}$	$1.62^{+1.72}_{-1.0}$	209.806	20
	lg_2	3.11e-5±1.03e-5	3.51e-3±1.16e-3	$3.80^{+0.055}_{-0.067}$	$1.41^{+1.65}_{-0.88}$	1223.04	9
	dc	9.89e-5±1.67e-4, 3.38e-4±1.18e-4	1.11e-2±1.88e-2, 3.81e-2±1.33e-2	$3.99^{+0.024}_{-0.029}$ $4.17^{+0.057}_{-0.066}$	$3.28^{+1.18}_{-1.71}$ $4.46^{+0.1}_{-1.16}$	4064.55	324

Table 2.2: Measured CSFDs (cumulative frequencies for 10 km (N (10)) and and 1 km (N (1)) craters) for all mapped terrain units in the Byblus Sulcus region, including LDM and JCM age estimates, terrain unit area, and the number of craters counted.

ii. CSFDs

The youngest terrains in Byblus Sulcus (Fig. 2.5), based on mapping, ls_3 and lg_3, have CSFDs of $3.95 \times 10^{-5} \pm 1.95 \times 10^{-5}$ km^{-2} and $2.61 \times 10^{-5} \pm 5.38 \times 10^{-6}$ km^{-2} (Tab. 2.2). Note that in the following we use *N* (10) values as a CSFD. Since they do not have considerable variation in their CSFD and no clear borders separating these terrains both seem to be cogenetic (Fig. 2.6). The second youngest terrain known from mapping results, lg_2, has a CSFD of $3.11 \times 10^{-5} \pm 1.03 \times 10^{-5}$ km^{-2}, which is in the range of ls_3 and lg_3. This suggests that the relative chronology is constrained solely by cross-cutting relationships, as the crater-counting technique alone cannot distinguish between these units. The similar CSFDs of ls_3, lg_3, and lg_2 imply similar ages and a formation in a short period. The relatively low number of craters on lg_2 may indicate some resurfacing activity.

Terrain unit dc has the highest CSFD among all mapped terrain units, consistent with our mapping results. Two possible CSFDs are identified as $9.89 \times 10^{-5} \pm 1.67 \times 10^{-4}$ km^{-2} and $3.38 \times 10^{-4} \pm 1.18 \times 10^{-4}$ km^{-2}. The lower CSFD indicates resurfacing activity which could have erased some craters.

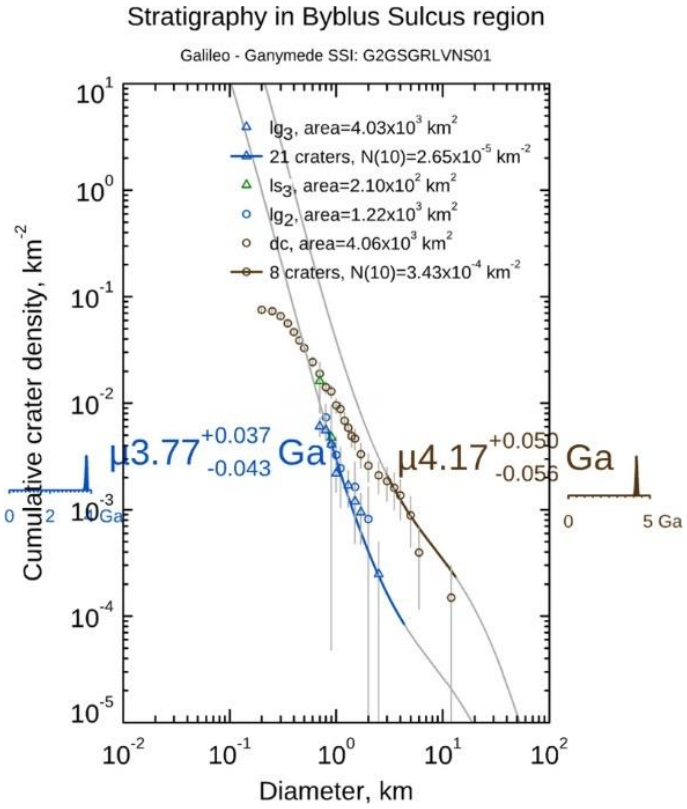

Figure 2.6: Comparison of the relative ages of different terrain units in Byblus Sulcus (SSI observation G2GSGRVLNS01) based on CSFDs. The plot displayed here represents ages derived from LDM. For ages based on JCM, refer to Table 2.2.

2.5.1.2 Nippur and Philus Sulcus (G2GSNIPPUR01)

i. Geological Mapping

Nippur and Philus Sulcus represent extended areas of intense resurfacing. Both sulci surround Marius Regio in the north and east (Fig. 2.7 a). Nippur Sulcus has an overall trend in the northwest–southeast direction while Philus Sulcus has a trend in the northeast–southwest direction. The Galileo SSI observation sequence G2GSNIPPUR01 comprising three images with a spatial resolution of 99 m pixel^{-1} is used for detailed mapping and CSFD measurements. The geology in this region includes various light terrain units of different ages and minor dark terrain (Fig. 2.7 b). Among these, ls_3, lg_2, and lg_1 build Nippur

Sulcus, and lg_2 (2), ls_2, and li_1 form Philus Sulcus. In general, Nippur Sulcus is younger as it cross-cuts Philus Sulcus. From the cross-cutting relationships, the smooth light unit ls_3 is the youngest terrain unit.

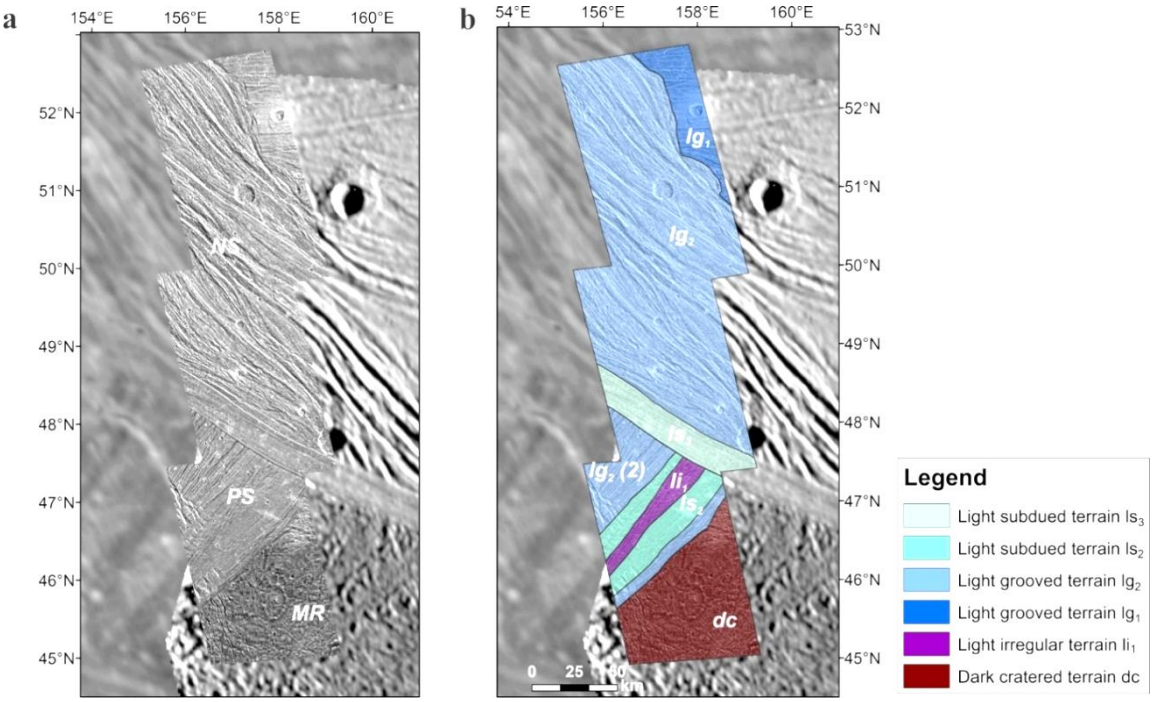

Figure 2.7: Region A/Nippur Sulcus: (a) SSI observation G2GSNIPPUR01 with the location of Philus (PS), Nippur Sulcus (NS), and Marius Regio (MR) indicated and (b) the associated geologic map produced following the mapping style of Collins et al. (2013).

The subdued terrain ls_3 is a narrow band ~15 km wide of northwest–southeast trending smooth terrain. It has two sharp ridges and a trough at the border to the adjacent terrains on its either side. Subdued lineaments mostly trend parallel to the borders. The light grooved terrain lg_2 is a broad band of ~144 km wide northwest–southeast trending grooved terrain with ridges and graben-like depressions. Its contact with ls_3 is long and sharp while its contact with lg_1 consists of many short curvilinear lineaments. The unit contains densely packed linear to sigmoidal-shaped ridges. The spindle-like arrangement of the ridges leads to frequent low-angle unconformities with adjacent straight lineaments.

The light grooved terrain lg_1 is the oldest one among the light terrains of Nippur Sulcus. Unlike ls_3 and lg_2 terrain units, its lineaments trend in the west–east direction and are parallel to subparallel to each other. The lineaments are not strongly grooved as the lineaments of lg_2. The average spacing between the ridges is less than 1 km. It has a 7 km diameter crater located in the center. The contact to lg_2 is a sudden high-angle unconformity

with parallel fractures. The terrain units lg_2 (2), ls_2, and li_1 of Philus Sulcus follow a northeast–southwest trend perpendicular to the orientation of ls_3 and lg_2. Thus, Nippur Sulcus (ls_3) sharply truncates these units. The lineaments of lg_2 (2) are equally spaced, parallel to subparallel to each other and also to its borders. There are some younger fractures that cut the lineaments of lg_2 (2) and reach into ls_2, and further east into the dark terrain. The unit ls_2 appears somewhat smoother, but generally gradational transitions occur here between lg_2 (2), ls_2, and li_1. We mapped a region of light irregular terrain li_1 as it appears more rugged than the surrounding terrain. It appears that the li_1 terrain is being resurfaced by ls_2 and the trend of the lineaments in li_1 and ls_2 are different. The li_1 terrain comprises many closed-spaced minor ridges at low angle to the general trending, but most of them are destroyed by smaller craters. The dark cratered terrain dc has an overall rugged topography with many dominating north–south trending fractures. Sharp grooves separate dc from lg_2. The terrain is more fractured than cratered. An unnamed crater is strongly strained to an ellipse with an aspect ratio of ∼2, with the long axis in the north–south direction.

Mapping of Nippur and Philus Sulci indicates that the relatively smooth terrain ls_3 formed latest. The previously formed wrinkly lg_2 unit with sigmoidal-shaped ridges suggests a contribution of strike-slip tectonics active at the time of formation. We also observed that a small section of the exposed dark terrain has experienced significant tectonic deformation, as evidenced by the strained crater (Pappalardo & Collins 2005; Cameron et al. 2018).

ii. CSFDs

At Nippur Sulcus (Fig. 2.7), lg_1, has a CSFD of $6.44 \times 10^{-5} \pm 5.48 \times 10^{-6}$ km^{-2} followed by lg_2 having a a CSFD of $5.54 \times 10^{-5} \pm 3.01 \times 10^{-6}$ km^{-2} and ls_3 with a CSFD of $4.44 \times 10^{-5} \pm 4.26 \times 10^{-6}$ km^{-2} (Tab. 2.3). Although the cross-cutting relationship infers that lg_2 is older than ls_3, the intervals for CSFD values of lg_2 and ls_3 overlap. However, for lg_1, there are large error bars. At Philus Sulcus, li_1 has a CSFD of $3.34 \times 10^{-5} \pm 4.79 \times 10^{-6}$ km^{-2}, which is slightly older than that of ls_2 ($2.05 \times 10^{-5} \pm 2.13 \times 10^{-6}$ km^{-2}) and lg_2 (2) ($1.64 \times 10^{-5} \pm 3.61 \times 10^{-6}$ km^{-2}), respectively.

The relative age between Nippur Sulcus and Philus Sulcus remains unclear because the ls_3, lg_2, and lg_1 terrain units of Nippur Sulcus shows higher CSFDs than the li_1, ls_2, and lg_2 (2) terrain units of Philus Sulcus. This is in contrast to the cross-cutting relationship, where Nippur Sulcus cross-cuts Philus Sulcus. Nevertheless, from our crater-counting results, we found that the oldest terrain in overall Nippur and Philus Sulcus region is lg_1 (Fig. 2.8).

Terrain unit dc has a CSFD of $4.14 \times 10^{-5} \pm 1.98 \times 10^{-6}$ km^{-2}, lower than those of lg_2 and lg_1, which is also in discrepancy with the mapping. Possible reasons for the lower CSFD of Philus Sulcus compared to Nippur Sulcus may be due to more intense tectonic deformation or resurfacing activities in these regions, or a counting bias. The relatively low CSFD obtained for the dark terrain is an effect of intense fracturing and deformation obliterating preexisting craters. Evidence for this is the presence of deformed ridges and a large strained crater.

Region A	**Terrain unit**	**N (10) [km^{-2}]**	**N (1) [km^{-2}]**	**LDM [Ga]**	**JCM [Ga]**	**Area [km^2]**	**No. of craters counted**
G2GSNIPPUR01 (**Nippur Sulcus**)	ls_3	4.44e-5 ±4.26e-6	5.00e-3 ±4.8e-4	$3.85^{+0.020}_{-0.023}$	$1.90^{+1.76}_{-1.15}$	1675.80	291
	lg_2	5.54e-5 ±3.01e-6	6.25e-3 ±3.39e-4	$3.90^{+0.084}_{-0.089}$	$2.32^{+1.70}_{-1.36}$	15352.3	1624
	lg_2 (2)	1.64e-5 ±3.61e-6	1.85e-3 ±4.07e-4	$3.68^{+0.039}_{-0.055}$	$0.83^{+1.23}_{-0.53}$	4970.65	240
	ls_2	2.05e-5 ±2.13e-6	2.31e-3 ±2.4e-4	$3.72^{+0.019}_{-0.022}$	$1.01^{+1.40}_{-0.64}$	2670.53	217
	lg_1	6.44e-5 ±5.48e-6	7.26e-3 ±6.18e-4	$3.92^{+0.013}_{-0.014}$	$2.46^{+1.66}_{-1.42}$	1576.71	303
	li_1	3.34e-5 ±4.79e-6	3.77e-3 ±5.4e-4	$3.81^{+0.024}_{-0.028}$	$1.96^{+1.76}_{-1.18}$	808.295	95
	dc	4.14e-5 ±1.98e-6	4.67e-3 ±2.23e-4	$3.85^{+0.0077}_{-0.0081}$	$1.81^{+1.75}_{-1.10}$	4781.27	924

Table 2.3: Measured CSFDs (N (10) and N (1)) for all mapped terrain units in the Nippur and Philus sulcus region, including LDM and JCM age estimates, terrain unit area, and the number of craters counted.

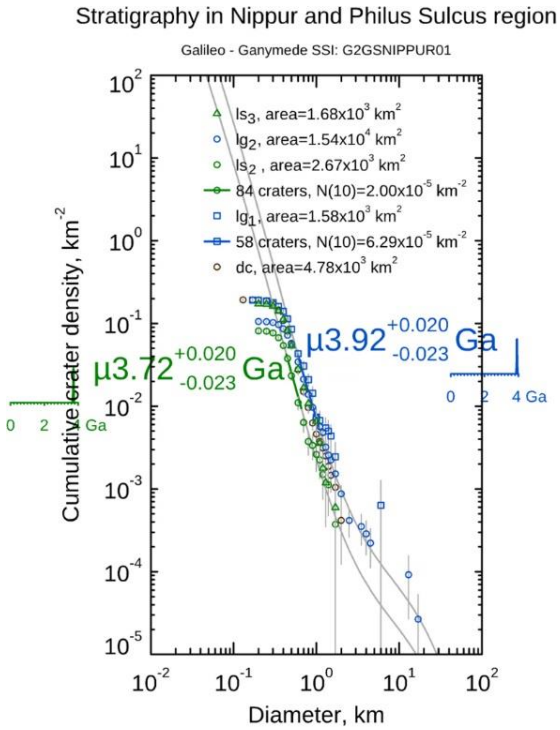

Figure 2.8: Comparison of the relative ages of the different terrain units in Nippur and Philus Sulcus (SSI observation G2GSNIPPUR01) based on CSFDs. The plot displayed here represents ages derived from LDM. For ages based on JCM, refer to Table 2.3.

2.5.1.3 Transitional Terrain (G2GSTRANST01)

i. Geological Mapping

Light terrain units that extend from Nippur Sulcus into Marius Regio comprise the so-called "transitional terrain" observed during the G2GSTRANST01 SSI observation sequence (Figs. 2.1 b and 2.9). The Galileo SSI images having ~188 m pixel^{-1} resolution are used for this study area (Fig. 2.9 a). Overall, the light terrains and the fractures within the dark terrain dc trend in the northwest–southeast direction. The geological units in transitional terrain includes superimposed generations of grooved and subdued light terrain (Fig. 2.9 b). The units li_1, ls_3, and lg_3 are part of Nippur Sulcus. From the cross-cutting relationship, the lg_3 and ls_3 terrains are found to be the youngest ones since they cross-cut adjacent terrains.

The light grooved terrain ls_3 is the youngest terrain in this region. It has a northwest–southeast trend, like ls_3 of Nippur Sulcus. Apart from a few lineaments, the terrain appears mostly very smooth. It has a single groove close to two craters with diameters of 7 and 4 km. The most striking features of the area are sigmoidal-shaped light subdued terrains mapped as ls_2, which are surrounded by grooved and irregular terrains (lg_1 and lg_2). Some

of the minor lineaments inside of these sigmoidal-shaped block units are curved like their borders. But most of the lineaments' spacing and orientation are not clear from this resolution image and the terrain appears mostly smooth. A small portion of dc is found inside unit ls_2.The light grooved terrains lg_2 form narrow and elongated, vein-like zones, which constitute parallel to subparallel sets of ridges trending in the northwest–southeast direction. Their borders to the dark terrain dc are very sharp and are marked by ridges. The elevation of lg_2 seems to be lower than the surrounding dark terrain. A large, 37 km diameter crater of the neighboring dark terrain is being cut by one of the light terrain veins. The southern half of the crater is absent, suggesting either a large strike-slip offset or submergence beneath ice. The light grooved terrain lg_1 also belongs to the network of ls_2, but is somewhat younger as it is terminated by lg_2. The unit ls_1 surrounds the sigmoidal-shaped ls_2 units in a vein-like network. The ridges of lg_1 are intensely grooved, linear to curvilinear in shape and produce a rough topography. The light irregular terrain li_1 is one of the oldest terrains in this region. It has irregular sets of lineaments with different orientation. It appears that li_1 is partly resurfaced by ls_2 and ls_3, and it is also cut by the veins lg_1.

As everywhere else the dark cratered terrain is the oldest unit. It appears strongly fractured. The fractures have overall trend in the northwest–southeast and in the west-southwest–east-northeast directions like lg_2 and lg_1. The orientation of lg_2 including the fractures within dc indicates that these are conjugate shear fractures. Indeed, the sigmoidal shape of ls_2 (reminiscent to SC fabrics) and the presence of a half crater cut by lg_2 demonstrate the importance of the conjugate shearing localized in lg_2 and lg_1.

ii. CSFDs

The youngest mapped units in the transitional terrain (Fig. 2.9) i.e., lg_3 and ls_3, which were believed to be geologically cogenetic, have quite different CSFDs, which are precisely $5.17 \times 10^{-5} \pm 1.53 \times 10^{-5}$ km^{-2} and $1.72 \times 10^{-4} \pm 4.85 \times 10^{-5}$ km^{-2}, respectively (Tab. 2.4). The second youngest terrain, lg_2, lg_2 (2), and ls_2 are found to have similar CSFDs of $6.01 \times 10^{-5} \pm 9.76 \times 10^{-6}$ km^{-2}, $8.37 \times 10^{-5} \pm 1.61 \times 10^{-5}$ km^{-2}, and $6.40 \times 10^{-5} \pm 8.1 \times 10^{-6}$ km^{-2}, respectively. Mapping and crater counting match here. The oldest light terrains, lg_1 and li_1, have CSFDs of $4.06 \times 10^{-5} \pm 1.46 \times 10^{-5}$ km^{-2} and $1.15 \times 10^{-4} \pm 2.04 \times 10^{-5}$ km^{-2}, respectively. Unlike li_1, lg_1 has a lower CSFD than all other terrain units (younger than Category 1 and 2 terrains). In other words, lg_1 was expected to have a much higher CSFD

than all other terrains except for li_1, whose CSFD is similar to the dark terrain. The dark cratered terrain (dc) has a CSFD of $1.23 \times 10^{-4} \pm 1.03 \times 10^{-5}$ km^{-2}, which is in accordance to the geological context.

The high CSFD of ls_3 equivalent to that of dc and the low value for lg_1 is not understood, and disagrees with the relative chronology derived from the cross-cutting relationships (Fig. 2.10). Overall, the higher CSFDs observed in most terrains, as compared to the adjacent Byblus Sulcus, may be attributed to secondaries impinging from the penepalimpsest Epigeus or to the possibility that the light terrain here was formed during an earlier stage, perhaps soon after the formation of the dark terrain.

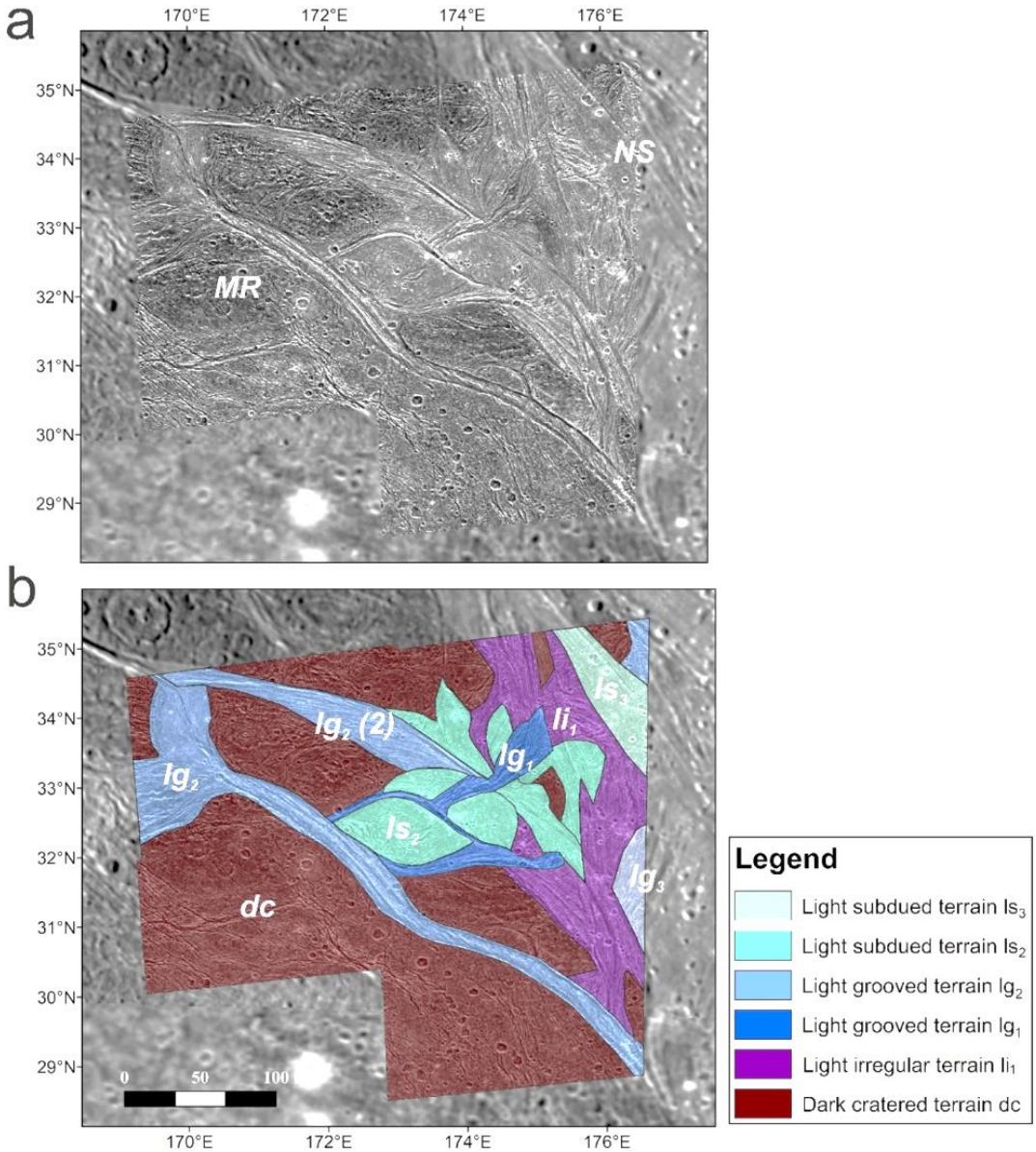

Figure 2.9: Region A/Transitional terrain: (a) SSI observation G2GSTRANST01 with the location of Marius Regio (MR) and Nippur Sulcus (NS) indicated and (b) the associated geologic map produced following the mapping style of Collins et al. (2013).

Region A	Terrain unit	N (10) [km^{-2}]	N (1) [km^{-2}]	LDM [Ga]	JCM [Ga]	Area [km^2]	No. of craters counted
G2GSTRANST01 (**Transitional terrain**)	lg_3	5.17e-5 ±1.53e-5	5.83e-3 ±1.72e-3	$3.88^{+0.041}_{-0.047}$	$2.13^{+1.74}_{-1.37}$	922.337	23
	ls_3	1.72e-4 ±4.85e-5	1.94e-2 ±5.47e-3	$4.07^{+0.037}_{-0.041}$	$4.00^{+0.55}_{-1.71}$	2153.93	49
	lg_2	6.01e-5 ±9.76e-6	6.78e-3 ±1.09e-3	$3.91^{+0.023}_{-0.028}$	$2.37^{+1.69}_{-1.38}$	8243.58	81
	lg_2 (2)	8.37e-5 ±1.61e-5	9.44e-3 ±1.82e-3	$3.96^{+0.027}_{-0.034}$	$2.92^{+1.43}_{-1.60}$	3134.09	41
	ls_2	6.40e-5 ±8.1e-6	7.21e-3 ±9.13e-4	$3.92^{+0.019}_{-0.022}$	$2.47^{+1.65}_{-1.42}$	6365.98	125
	lg_1	4.06e-5 ±1.46e-5	4.58e-3 ±1.65e-3	$3.85^{+0.050}_{-0.059}$	$1.78^{+1.75}_{-1.09}$	4817.12	26
	li_1	1.15e-4 ±2.04e-5	1.30e-2 ±2.30e-3	$4.01^{+0.025}_{-0.030}$	$3.44^{+1.06}_{-1.74}$	9266.77	91
	dc	1.23e-4 ±1.03e-5	1.39e-2 ±1.16e-3	$4.02^{+0.012}_{-0.013}$	$3.54^{+0.97}_{-1.75}$	72876.6	728

Table 2.4: Measured CSFDs (N (10) and N (1)) for all mapped terrain units in the Transitional terrain, including LDM and JCM age estimates, terrain unit area, and the number of craters counted.

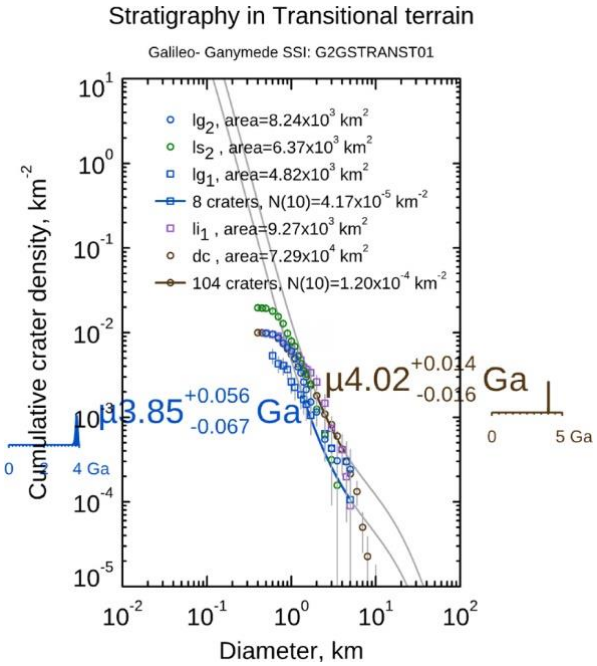

Figure 2.10: Comparison of relative ages of different terrain units in transitional terrain (SSI observation G2GSTRANST01) based on CSFDs. The plot displayed here represents ages derived from LDM. For ages based on JCM, refer to Table 2.4.

2.5.2 Region B: Arbela Sulcus

The narrow band (width ~21 km) of light terrain constituting Arbela Sulcus located at 21.1° S, 10.2° E was selected for Region B (Figs. 2.1 c and 2.11). Arbela Sulcus traverses the dark terrain of Nicholson Regio located in the southern part of Ganymede's sub-Jovian hemisphere. Nicholson Regio is a type locality of the so-called Nicholsonian, the oldest stratigraphic unit or chronological period on Ganymede in the current time–stratigraphic system established by Collins et al. (2013). Unlike Harpagia Sulcus (Region C, Figs. 2.1 d and 2.13), which confines with Nicholson Regio in the north and west, Arbela Sulcus has an overall trend in the northeast–southwest direction and terminates Nicholson Regio in the southeast. The high-resolution images of the Galileo SSI observation sequences 28GSARBELA01+02 and G7GSNICHOL01+02 with spatial resolution between 34 and 133 m pixel^{-1} offer a detailed look into this area (Fig. 2.11 a).

2.5.2.1 Arbela Sulcus (G28GSARBELA02 and G7GSNICHOL01)

i. Geological Mapping

The geological units of Arbela Sulcus from young to old are light subdued terrain ls_3 and light grooved terrain lg_2. They form vein-like systems within dark terrain. The dark lineated (dl) terrain is younger than the dark cratered terrains (dc; Fig. 2.11 b). The light subdued terrain ls_3 of Arbela Sulcus forms a narrow, smooth band with straight and parallel boundaries. It trends in the northeast–southwest direction. It has an average width of about 20–30 km but it narrows down to less than 15 km in its north. It has sharp troughs at its borders which separates it from the other units. It has parallel ridges and troughs but unlike lg_2, it appears striated only in some areas. ls_3 is topographically lower than lg_2 and the dark terrains dl and dc (Giese et al. 2001). The light grooved terrain lg_2 is strongly grooved with densely packed sets of lineaments. Like ls_3, it trends in the northeast–southwest direction. It has an average width of about 30–40 km. A sharp border to the dark terrain is not observed but uneven sets of lineaments form its borders. The ridges and grooves have a curvilinear appearance. These grooves are interconnected with the grooves of dl. The length of ridges varies from a few kilometers to 50 km. The average spacing between the ridges is less than 1 km.

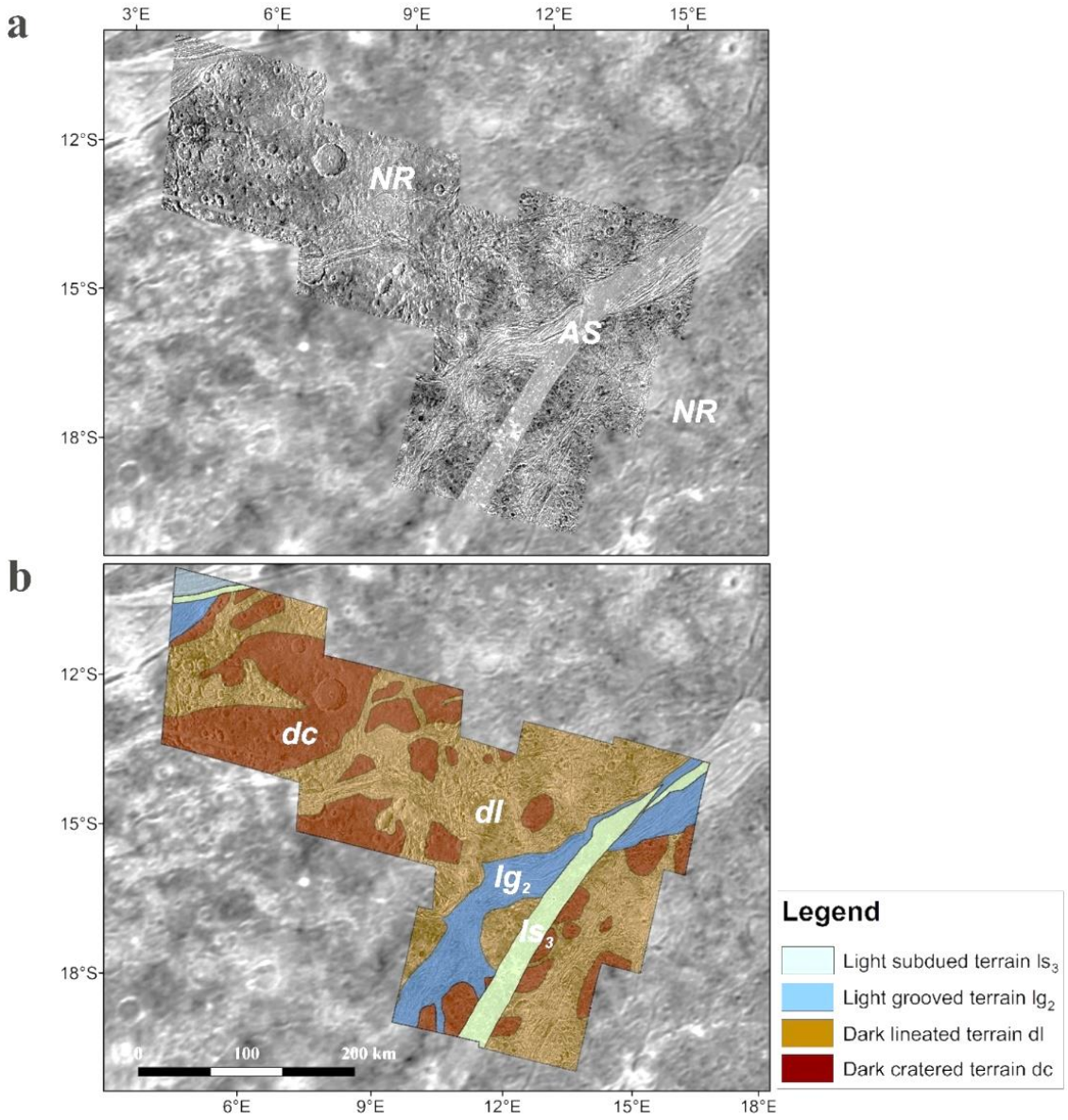

Figure 2.11: Region B/Arbela Sulcus: (a) SSI mosaic combining observations 28GSARBELA02 and G7GSNICHOL01 with the location of Arbela Sulcus (AR) and Nicholson Regio (NR) and (b) the associated geologic map produced following the mapping style of Collins et al. (2013).

The dark lineated terrain dl shows abundant lineaments. The lineaments are unevenly spaced and are parallel to subparallel to each other within each set. Compared to lg_2, the lineaments in dl are widely spaced. The spacing between the lineaments in most cases is ~1 km. The lineaments are connected to each other and also connected to lg_2. But there are some lineaments that on one side of dl do not have counterparts on the other side. The lineaments east of lg_2 mostly trend in the northeast–southwest direction, but west of lg_2 lineament sets perpendicular to lg_2 exist. There are many craters being cut by lineaments

or fractures, distorting them from their actual circular shape. For instance, the crater west to ls_3 and lg_2 is separated by dl at its center by a distance of about 21 km. The dark cratered terrain dc is an intensely cratered terrain. It is unevenly distributed within dl and there is no distinctive border between them. It appears as patches embedded in dl.

The cross-cutting relationships and orientations of all terrains suggest that evident tectonic reworking has taken place in this region. lg_2 is interpreted as a result of shearing which includes ~65 km of left-lateral strike-slip movement followed by ~25 km of crustal separation creating ls_3 and ~4° counterclockwise relative rotation of the eastern side of lg_2 (Head et al. 2002). The intermediate age of dl between that of dark cratered terrain and light terrains would be indicative of a gradual transition from dark terrain to light terrain.

ii. CSFDs

The two light terrains ls_3 and lg_2 in Arbela Sulcus (Fig. 2.11), whose CSFDs are $2.95 \times 10^{-5} \pm 4.73 \times 10^{-6}$ km^{-2} and $2.00 \times 10^{-5} \pm 2.89 \times 10^{-6}$ km^{-2}, respectively (Table 2.5), have lower CSFDs than dl ($6.02 \times 10^{-5} \pm 1.17 \times 10^{-5}$ km^{-2}) and dc ($1.78 \times 10^{-4} \pm 3.64 \times 10^{-5}$ km^{-2}), which are all consistent with the geological mapping. The minor difference in the CSFDs between ls_3 and lg_2 indicates formation within a short period (Fig. 2.12).

Region B	Terrain unit	N (10) [km^{-2}]	N (1) [km^{-2}]	LDM [Ga]	JCM [Ga]	Area [km^2]	No. of craters counted
28GSARBELA02/ G7GSNICHOL01 **(Arbela Sulcus)**	ls_3	2.95e-5 ±4.73e-6	3.33e-3 ±5.33e-4	$3.79^{+0.026}_{-0.031}$	$1.37^{+1.63}_{-0.86}$	7086.41	85
	lg_2	2.00e-5 ±2.89e-6	2.25e-3 ±3.26e-4	$3.72^{+0.026}_{-0.031}$	$0.99^{+1.38}_{-0.63}$	12872.1	137
	Dl	6.02e-5 ±1.17e-5	6.79e-3 ±1.32e-3	$3.91^{+0.028}_{-0.035}$	$2.60^{+1.60}_{-1.48}$	20781.0	468
	Dc	1.78e-4 ±3.64e-5	2.01e-2 ±4.13e-3	$4.08^{+0.028}_{-0.034}$	$4.04^{+0.52}_{-1.69}$	7380.38	1,062

Table 2.5: Measured CSFDs (N (10) and N (1)) for All Mapped Terrain Units in the Arbela Sulcus Region, Including LDM and JCM Age Estimates, Terrain Unit Areas, and the Number of Craters Counted.

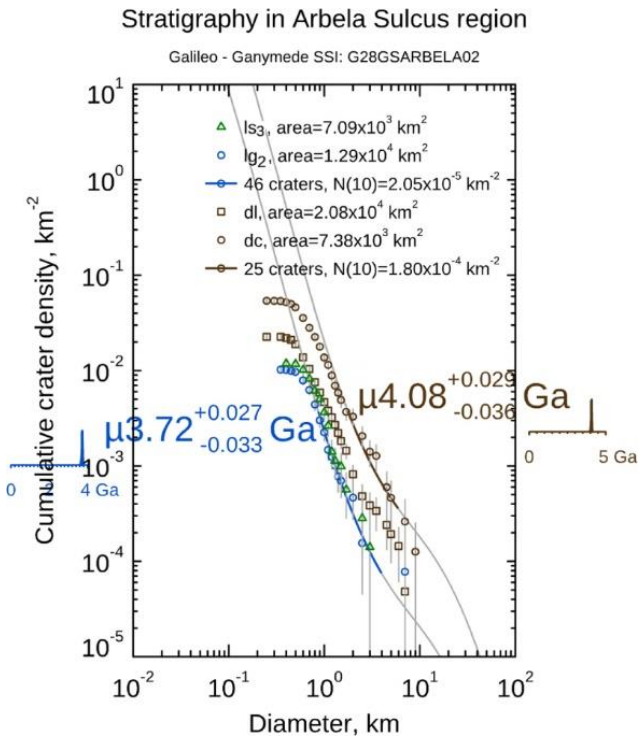

Figure 2.12: Comparison of relative ages of different terrain units from Region B based on CSFDs: Arbela Sulcus—SSI observation 28GSARBELA02. The plot displayed here represents ages derived from LDM. For ages based on JCM, refer to Table 2.5.

2.5.3. Region C: Harpagia Sulcus

Harpagia Sulcus (Region C, Figs. 2.1 d and 2.13, 2.15, and 2.17), an extensively resurfaced portion of Ganymede's light terrain is situated at southern near-equatorial latitudes of the sub-Jovian hemisphere. It confines the northern and western border of Nicholson Regio. The high-resolution images 28GSBRTDRK02 (Fig. 2.13) and 28GSCALDRA02 (Fig. 2.15) allow us to study the direct contact of Harpagia Sulcus with the dark terrain of Nicholson Regio, while 28GSSMOOTH02 (Fig. 2.17) is completely enclosed within the sulcus.

2.5.3.1. Harpagia Sulcus I (28GSBRTDRK02)

i. Geological Mapping

The given image shows a part of Harpagia Sulcus and Nicholson Regio located in the sub-Jovian hemisphere at ~14°S, 40°S, with a spatial resolution of 121 m pixel^{-1} (Fig. 2.13 a). The various light terrain units of Harpagia Sulcus trend northwest–southeast and cross-cut the dark terrain of Nicholson Regio. The geological subdivision is shown in Figure 2.13 b. The light terrain units are aligned parallel to each other except for the youngest units, ls_3

and lg_3, which branch off from this trend obliquely like a railroad switch. It has an average width of about 13 km. The light grooved terrain lg_3 borders ls_3 on both sides. The light subdued terrain ls_2 is a narrow, smooth terrain unit within lg_2. It trends in the northwest–southeast direction like its adjacent terrains. It has an average width of about 25 km. The eastern light grooved terrain lg_2 is obliquely cut by the younger unit lg_3. The western lg_2 occurrence has a sharp grooved contact to the dark terrain of Nicholson Regio, which is characterized by predominantly deeply incised, roughly 20 km long grooves that trend in northwest direction, and many impact craters as large as 33 km in diameter. From these cross-cutting relationships we could infer that lg_3 and ls_3 were formed later than lg_2 and ls_2. But among these terrains, it is unclear whether lg or ls is younger.

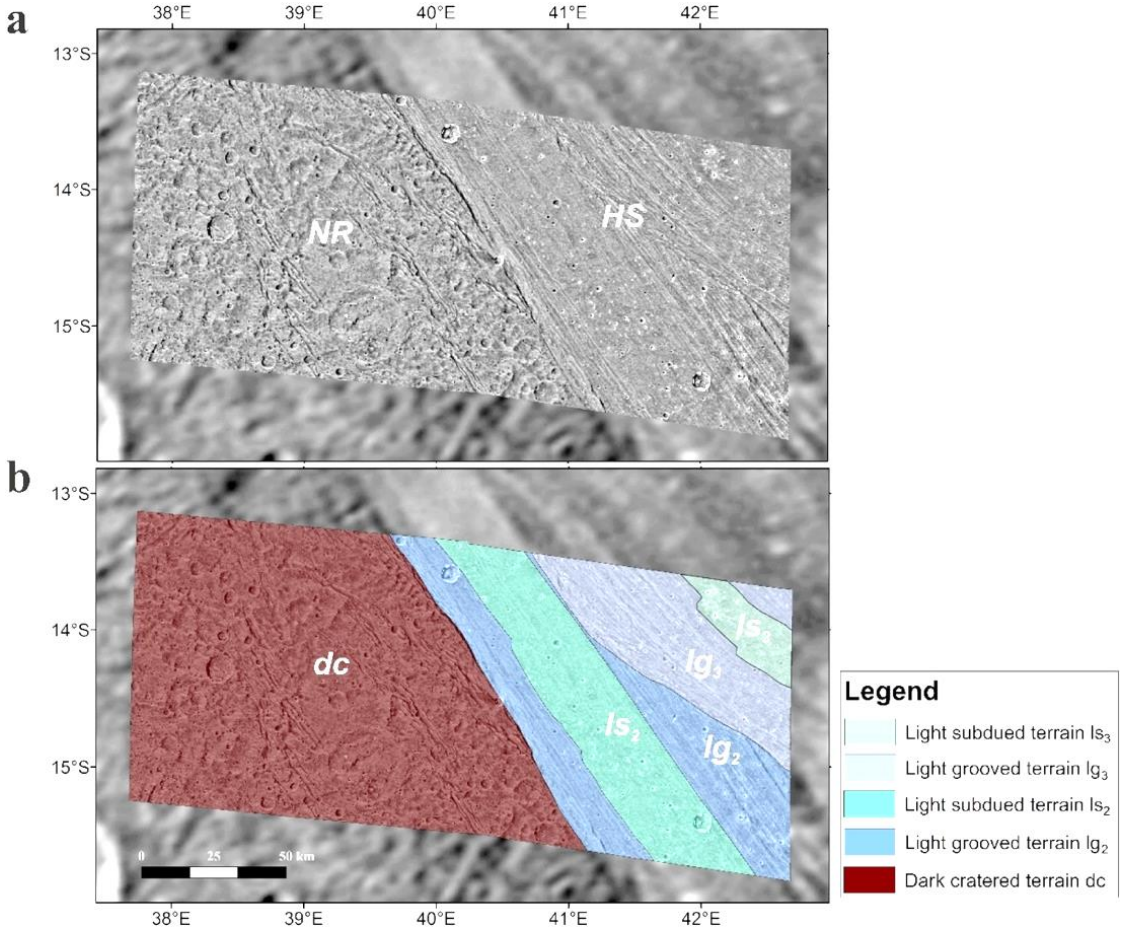

Figure 2.13: Region C/Harpagia Sulcus I: (a) SSI observation 28GSBRTDRK01/02 with the location of Nicholson Regio (NR) and Harpagia Sulcus (HS) indicated and (b) the associated geologic map produced following the mapping style of Collins et al. (2013).

ii. CSFDs

The light terrain units, lg_3 and ls_3, have CSFDs of $1.31 \times 10^{-5} \pm 2.31 \times 10^{-6}$ km^{-2} and $4.20 \times 10^{-5} \pm 1.12 \times 10^{-5}$ km^{-2}, respectively (Table 2.6). The large difference between these units and the high value of the CSFD for ls_3 are remarkable, as both units belong to the same category. A similar trend can be observed for lg_2 ($2.00 \times 10^{-5} \pm 3.53 \times 10^{-6}$ km^{-2}) and ls_2 ($4.18 \times 10^{-5} \pm 4.0 \times 10^{-6}$ km^{-2}). One reason for such a discrepancy between lg and ls is that either the smooth ls terrains are indeed older than lg, suggesting a real difference in age, or both ls units are cogenetic. Alternatively, the nature of the smooth terrain makes it highly unlikely to miss craters, whereas the high relief grooved terrain makes it highly likely to miss craters on the slopes, and hence the identification of craters is subject to a non-zero error. As geologically expected the dark cratered terrain (dc; $1.47 \times 10^{-4} \pm 3.34 \times 10^{-5}$ km^{-2}) has the highest CSFD among other terrain units (Fig. 2.14).

Region C	Terrain unit	N (10) [km^{-2}]	N (1) [km^{-2}]	LDM [Ga]	JCM [Ga]	Area [km^2]	No. of craters counted
28GSBRTDRK02 (**Harpagia Sulcus I**)	lg_3	1.31e-5 ±2.31e-6	1.48e-3 ±2.6e-4	$3.63^{+0.036}_{-0.048}$	$0.67^{+1.06}_{-0.44}$	3163.81	49
	ls_3	4.20e-5 ±1.12e-5	4.74e-3 ±1.26e-3	$3.85^{+0.038}_{-0.043}$	$1.83^{+1.75}_{-1.11}$	606.372	27
	lg_2	2.00e-5 ±3.53e-6	2.26e-3 ±3.98e-4	$3.72^{+0.030}_{-0.039}$	$0.99^{+1.38}_{-0.63}$	6587.83	81
	ls_2	4.18e-5 ±4.0e-6	4.71e-3 ±4.51e-4	$3.85^{+0.015}_{-0.017}$	$1.82^{+1.75}_{-1.11}$	3145.05	166
	dc	1.47e-4 ±3.34e-5	1.66e-2 ±3.76e-3	$4.05^{+0.030}_{-0.039}$	$3.80^{+0.74}_{-1.75}$	11802.6	458

Table 2.6: Measured CSFDs (N (10) and N (1)) for All Mapped Terrain Units in the Harpagia Sulcus I Region, Including LDM and JCM Age Estimates, Terrain Unit Areas, and the Number of Craters Counted.

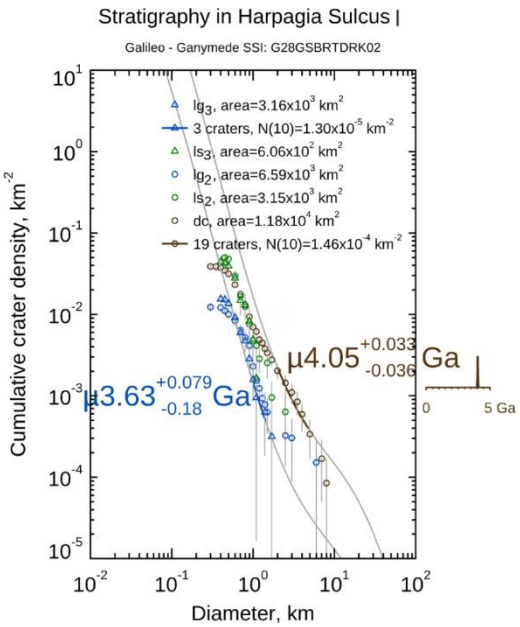

Figure 2.14: Comparison of the relative ages of different terrain units from Harpagia Sulcus I (SSI observation G28GSBRTDRK02) based on CSFDs. The plot displayed here represents ages derived from LDM. For ages based on JCM, refer to Table 2.6.

2.5.3.2 Harpagia Sulcus II (28GSCALDRA02)

i. Geological Mapping

This region lies roughly 300 km south of Harpagia Sulcus I. It includes a part of Harpagia Sulcus located near the prominent impact crater Enkidu (~26.6°S, ~34.9°E). The two Galileo contextual images, 28GSCALDRA02 have a spatial resolution of 147 m pixel^{-1} and the four high-resolution images, 28GSCALDRA01, have a spatial resolution of 42 m pixel^{-1} (Fig. 2.15 a). The region comprises various light terrains, dark terrains (dc and dl), and two caldera-like depressional features (Fig. 2.15 b). The subdued light terrains (ls_1 and ls_1 (2)) are found to be the youngest terrains that cross-cut the dark terrains. The lineated dark terrain dl is found to be intermediate in age as it cross-cuts the dark cratered terrain. All of these terrains are aligned northwest–southeast parallel to each other. The western border between light and dark terrains is very sharp, while gradual transitions occur with the dark lineated terrain. Specific structures are two caldera-like features like the Hammamat Patera (HP; Fig. 2.15 a), which are formed within the ls_1 terrain. Spaun et al. (2001) observed that caldera-like features have an inward-facing scarp. The scarps are high standing, and the interiors of the caldera-like features are depressed with a very smooth appearance. From the cross-cutting relationships, caldera-like features are found to be the lately formed ones. Previous studies have suggested that these features are only present on

light terrains, and may serve as source vents for icy volcanism (Lucchita 1980; Schenk & Moore 1998; Kay & Head 1999; McKinnon et al. 2001; Spaun et al. 2001).

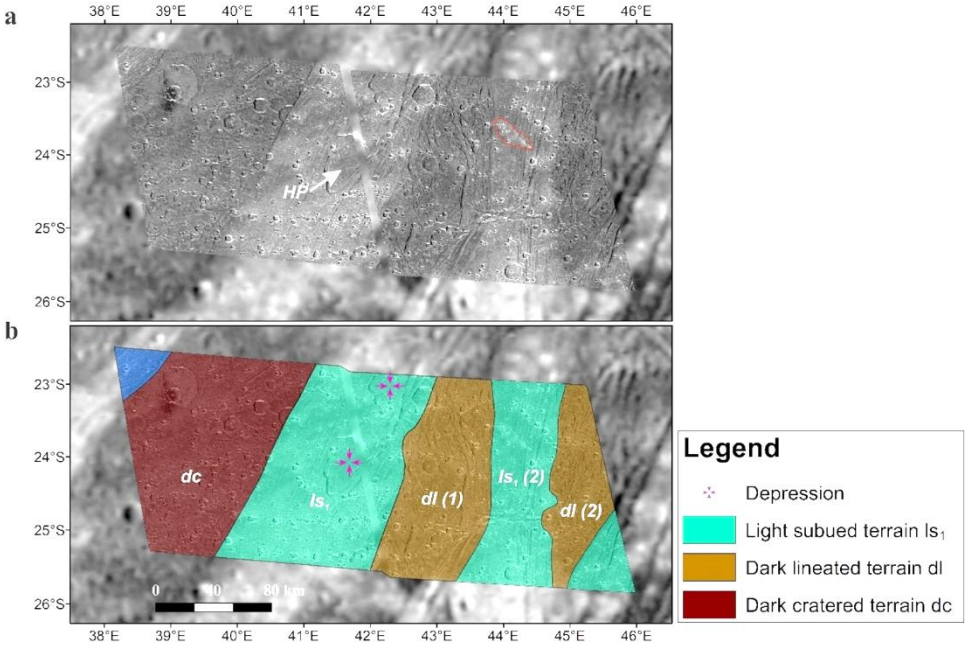

Figure 2.15: Region C/Harpagia Sulcus II: (a) SSI observation 28GSCALDRA01/02 indicating the location of HP. The red polygon represents an example of suspected secondary craters. (b) The associated geologic map produced following the mapping style of Collins et al. (2013).

The dark lineated terrains dl (1 + 2) are separated by ls_1 (2). The terrain unit dl (1) contains some sinuous lineaments that also extends into ls_1 (2). In contrast, the dark cratered terrain dc shows very few lineaments, but is highly cratered. Along the sharp border to the light terrain, there is a crater that is exactly cut into half. The missing half is not exposed. The light terrain ls_1 shows a polygonal crater, whose straight rim segment is defined by a lineament.

ii. CSFDs

The two light terrain units, ls_1 and ls_1 (2), have CSFDs of $2.09 \times 10^{-4} \pm 2.26 \times 10^{-5}$ km^{-2} and $1.63 \times 10^{-4} \pm 4.17 \times 10^{-5}$ km^{-2}, respectively (Table 2.7). The two dark lineated terrains, dl (1) and dl (2), have CSFDs of $1.83 \times 10^{-4} \pm 4.67 \times 10^{-5}$ km^{-2} and $1.61 \times 10^{-4} \pm 3.81 \times 10^{-5}$ km^{-2}. Their CSFDs are similar among each other and also with regard to the ls units (Fig. 2.16). However, according to their cross-cutting relationships, the lineated dark terrain unit dl is expected to have higher CSFDs than ls terrains. As expected, the dark

cratered terrain (dc) has the highest CSFD of $3.94 \times 10^{-4} \pm 3.48 \times 10^{-5}$ km^{-2}. Possible explanations for the counterintuitive CSFDs of dl and ls are a number of potential secondary craters on these terrains formed by the Enkidu crater or some degree of resurfacing.

Region C	Terrain unit	N (10) [km^{-2}]	N (1) [km^{-2}]	LDM [Ga]	JCM [Ga]	Area [km^2]	No. of craters counted
28GSCALDRA02 (**Harpagia Sulcus II**)	ls_1	2.09e-4 ±2.26e-5	2.36e-2 ±2.55e-3	$4.10^{+0.015}_{-0.017}$	$4.20^{+0.36}_{-1.59}$	10725.9	174
	ls_1 (2)	1.63e-4 ±4.17e-5	1.84e-2 ±4.7e-3	$4.06^{+0.034}_{-0.037}$	$3.93^{+0.61}_{-1.73}$	5423.41	116
	dl (1)	1.83e-4 ±4.67e-5	2.06e-2 ±5.26e-3	$4.08^{+0.034}_{-0.037}$	$4.06^{+0.49}_{-1.68}$	6815.56	116
	dl (2)	1.61e-4 ±3.81e-5	1.82e-2 ±4.29e-3	$4.06^{+0.031}_{-0.037}$	$3.93^{+0.62}_{-1.73}$	3400.43	82
	dc	3.94e-4 ±3.48e-5	4.44e-2 ±3.92e-3	$4.19^{+0.012}_{-0.014}$	$4.52^{+0.04}_{-0.88}$	10194.2	255

Table 2.7: Measured CSFDs (N (10) and N (1)) for All Mapped Terrain Units in the Harpagia Sulcus II Region, Including LDM and JCM Age Estimates, Terrain Unit Areas, and the Number of Craters Counted.

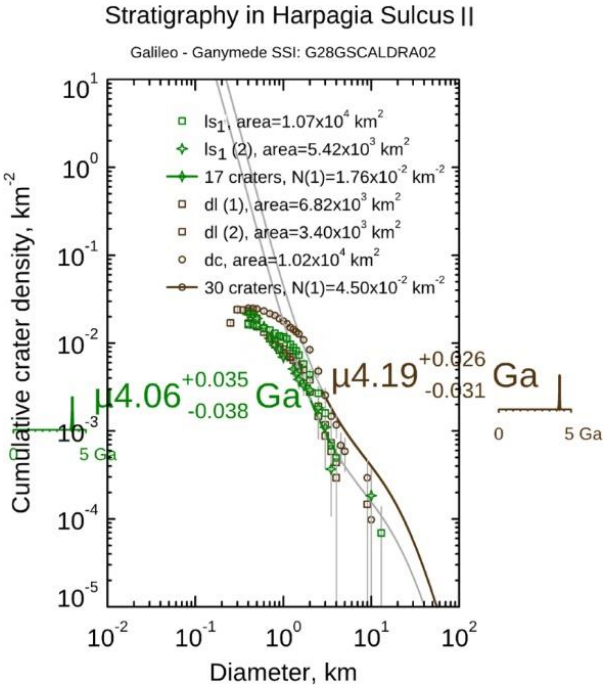

Figure 2.16: Comparison of the relative ages of the different terrain units from Harpagia Sulcus II (SSI observation 28GSCALDRA02) based on CSFDs. The plot displayed here represents ages derived from LDM. For ages based on JCM, refer to Table 2.7.

2.5.3.3. Harpagia Sulcus III (28GSSMOOTH02)

i. Geological Mapping

At a distance of about 180 km east of Harpagia Sulcus I (Fig. 2.13 a), there lies the SSI observation sequence 28GSSMOOTH02 (Fig. 2.17 a). The two images have a spatial resolution of about 116 m pixel^{-1}. This portion is located at ~16°S, 50 °E completely within Harpagia Sulcus and comprises an area of about 24,649 km^2. The four high-resolution 16 m pixel^{-1} images provide a more detailed view of the contact between the light subdued terrain ls_2 and the light grooved terrain lg_2 (Fig. 2.17 b). The exposed subdued and grooved terrains all belong to the light terrains (Fig. 2.17 c). The cross-cutting relationships allows us to derive a relative chronology from lg_3 (youngest) via ls_2 and lg_2 to ls_1 (oldest). All light terrain units are characterized by different orientations of their lineaments, with typical form unconformity angles of ~30° at the border of adjacent terrains. In contrast to previous case studies, lg_3 is the youngest terrain unit that has a strongly grooved surface while the older unit ls_1 is relatively smooth with subdued lineaments. This unit hosts the largest impact structure of the scene whose continuous ejecta blanket is clearly visible. The crater has a diameter of about 19 km with a small central pit. While the light grooved terrains lg_3, lg_2, and ls_1 contain long, parallel, and equally spaced ridges and troughs, the undivided terrain (undiv) differs from the other grooved terrains for the presence of strongly curved lineaments that are cross-cut by lg_3.

ii. CSFDs

The youngest terrain units, $lg_3$and lg_3 (2), have CSFDs of $1.66 \times 10^{-5} \pm 2.87 \times 10^{-6}$ km^{-2} and $2.87 \times 10^{-5} \pm 1.64 \times 10^{-5}$ km^{-2} (Table 2.8). These CSFDs are similar to the terrains lg_2 and ls_2, with CSFDs of $1.23 \times 10^{-5} \pm 1.96 \times 10^{-6}$ km^{-2} and $2.81 \times 10^{-5} \pm 2.98 \times 10^{-6}$ km^{-2}, respectively. Consistent with the geological findings, the light terrain ls_1 shows a slightly higher CSFD than the other terrain units (Fig. 2.18). We measured two possible CSFDs of $7.97 \times 10^{-5} \pm 3.02 \times 10^{-5}$ km^{-2} and $1.93 \times 10^{-5} \pm 1.91 \times 10^{-6}$ km^{-2}. The two CSFD values are due to two cumulative curves that best fit the data points. Such an uneven CSFD within ls_1 may indicate the imprint of secondaries or local resurfacing. The formation time differences between lg_3 and lg_3(2) may be real, as they are not directly connected to each other. The low CSFD measured in the undiv light terrain suggests that deformation has erased some craters.

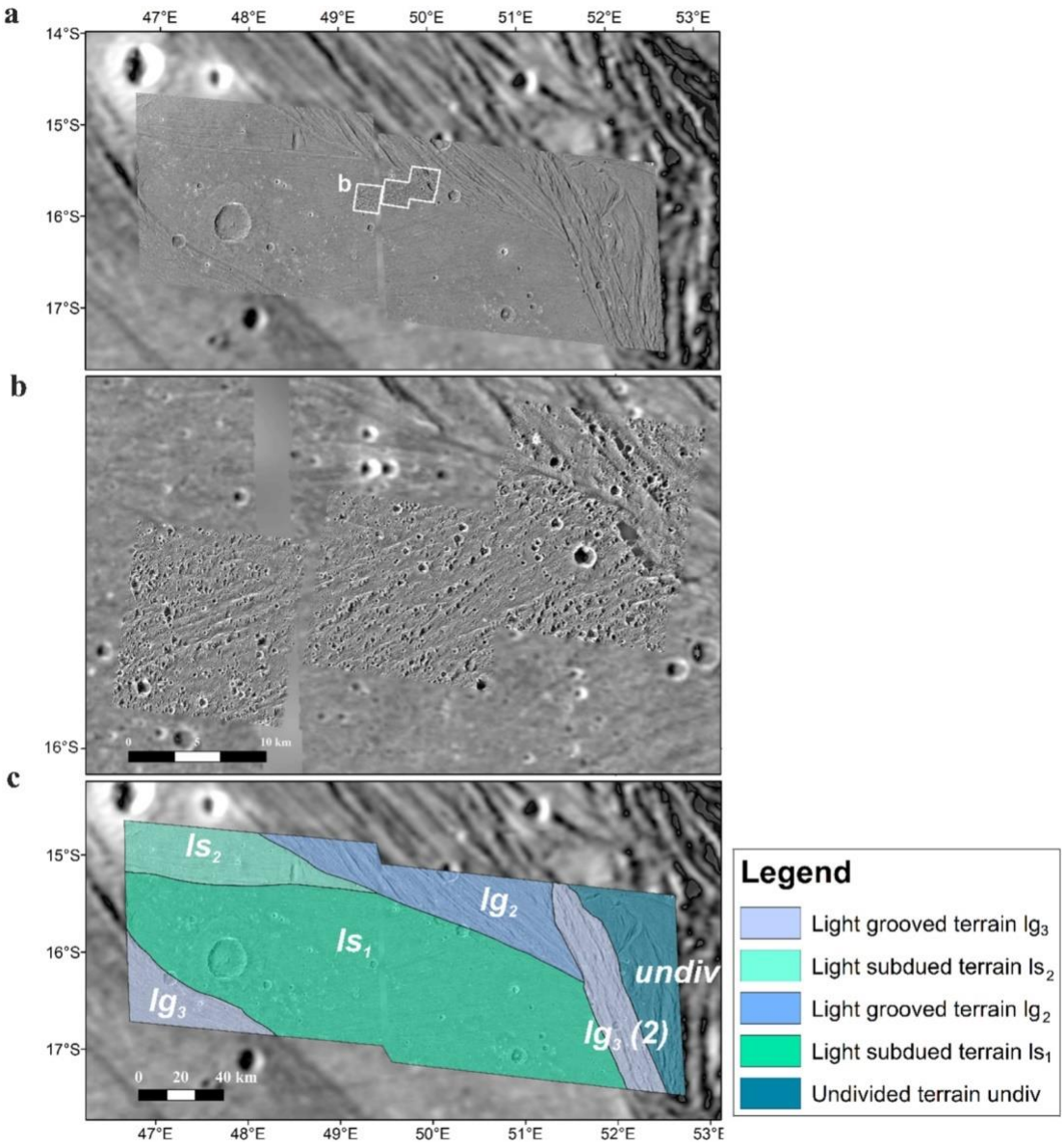

Figure 2.17: Region C/Harpagia Sulcus III: (a) SSI observation 28GSSMOOTH02; (b) the highest-resolution image sequence 28GSSMOOTH01, and (c) the associated geological map of panel (a) following the mapping style of Collins et al. (2013).

Region C	Terrain unit	N (10) [km^{-2}]	N (1) [km^{-2}]	LDM [Ga]	JCM [Ga]	Area [km^2]	No. of craters counted
28GSSMOOTH02 **(Harpagia Sulcus III)**	lg_3	1.66e-5 ±2.87e-6	1.87e-3 ±3.23e-4	$3.68^{+0.032}_{-0.041}$	$0.84^{+1.24}_{-0.54}$	1303.16	51
	lg_3 (2)	2.87e-5 ±1.64e-5	3.23e-3 ±1.85e-3	$3.79^{+0.076}_{-0.11}$	$1.35^{+1.62}_{-0.84}$	1825.55	15
	lg_2	1.23e-5 ±1.96e-6	1.39e-3 ±2.21e-4	$3.61^{+0.034}_{-0.045}$	$0.64^{+1.02}_{-0.41}$	3107.27	62
	ls_1	7.97e-5 ±3.02e-5, 1.93e-5 ±1.91e-6	8.98e-3 ±3.4e-3, 2.18e-3 ±2.15e-4	$3.95^{+0.049}_{-0.057}$ $3.71^{+0.012}_{-0.013}$	$0.96^{+1.36}_{-0.62}$ $2.83^{+1.48}_{-1.52}$	13832.8	404
	ls_2	2.81e-5 ±2.98e-6	3.16e-3 ±3.36e-4	$3.78^{+0.018}_{-0.020}$	$1.32^{+1.60}_{-0.83}$	2190.27	103
	Undiv	1.60e-5 ±2.17e-6	1.80e-3 ±2.45e-4	$3.67^{+0.026}_{-0.032}$	$0.81^{+1.21}_{-0.52}$	2438.51	65

Table 2.8: Measured CSFDs (N (10) and N (1)) for all Mapped Terrain Units in the Harpagia Sulcus III Region, Including LDM and JCM age Estimates, Terrain Unit area, and the Number of Craters Counted.

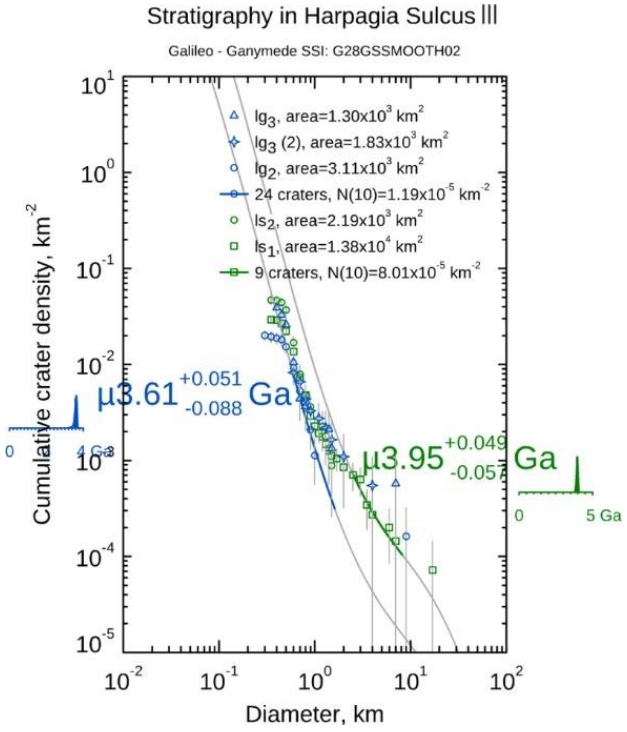

Figure 2.18: Comparison of relative ages of different terrain units from Harpagia Sulcus II (SSI observation 28GSSMOOTH02) based on CSFDs. The plot displayed here represents ages derived from LDM. For ages based on JCM, refer to Table 2.8.

2.5.4 Region D: Erech, Sippar, and Mummu Sulci

The portions of Erech, Mummu, and Sippar Sulci observed by Galileo SSI selected for Region D constitute extended light terrain units located in the southern near-equatorial and midlatitudes of Ganymede's anti-Jovian hemisphere, northwest to Osiris crater (Figs. 2.1 a and e). Mostly Mummu and Sippar Sulci consist of terrain units trending in an east–west direction, while Erech Sulcus lies perpendicular to it (Figs. 2.19 and 2.21). These Sulci form the southern margin of the dark terrain Marius Regio. The region observed in G8GSCALDRA01 constituting Mummu and Sippar Sulcus lies approximately 480 km south of Erech Sulcus (G8GSERECH01), in which Erech Sulcus is being cross-cut by Sippar Sulcus. The light terrain (lg_2) of Erech Sulcus decreases in width toward the north, where it is cross-cut by Uruk Sulcus.

2.5.4.1 Erech Sulcus (G8GSERECH01)

i. Geological Mapping

Erech Sulcus is a 75–85 km wide band of light terrain (lg_2), located in the anti-Jovian hemisphere at ~16°S, 177°W trending in a north–south direction and cutting through the dark terrain of Marius Regio. The terrain extends for approximately 900 km in the northward direction. The Galileo image mosaic has a resolution of 143 m pixel^{-1} (Fig. 2.19 a). Erech Sulcus has a pronounced relief caused by parallel to subparallel grooves and partly spindle-like ridges. Erech Sulcus is cut by the east–west trending younger Sippar Sulcus (ls_3). This Sulcus is adjacent to the large crater named Melkart. The mapped terrains of Sippar Sulcus are subdivided according to superposition and surface properties (Fig. 2.19 b). The terrain ls_3 is a narrow band of ~9 km width bifurcating westward. This unit has a smooth and only weakly lineated surface. Although it is the youngest unit, the terrain shows a large number of craters. The proximity of Melkart crater may be the factor contributing to the large number of craters in the area. The borders of the terrain are sharp with all its adjacent terrains.

The light irregular terrain unit li_1 is a small triangular-shaped area between the two bifurcating arms of ls_3 with differently oriented lineaments. To the west, it borders with a sharp trough to the light subdued terrain ls_1, whose surface appears smooth, except for a few distinct grooves. The outer shape and the internal lineament structure of the light

subdued terrain ls_2 are remarkably curved. This is in stark contrast to the light grooved terrain lg_1 whose long ridges are straight and parallel and exceed a length of 70 km. This unit is separated from the adjacent terrains by means of oblique contacts. The dark cratered terrain dc has a high crater density and many northwest–southeast trending fractures. Its borders with the light terrains are sharp and the terrain seems to be slightly elevated with respect to lg_2 and ls_3. At 16.5° S, 175.5°W lies a half-circular feature whose classification as either a crater or caldera cannot be determined with certainty.

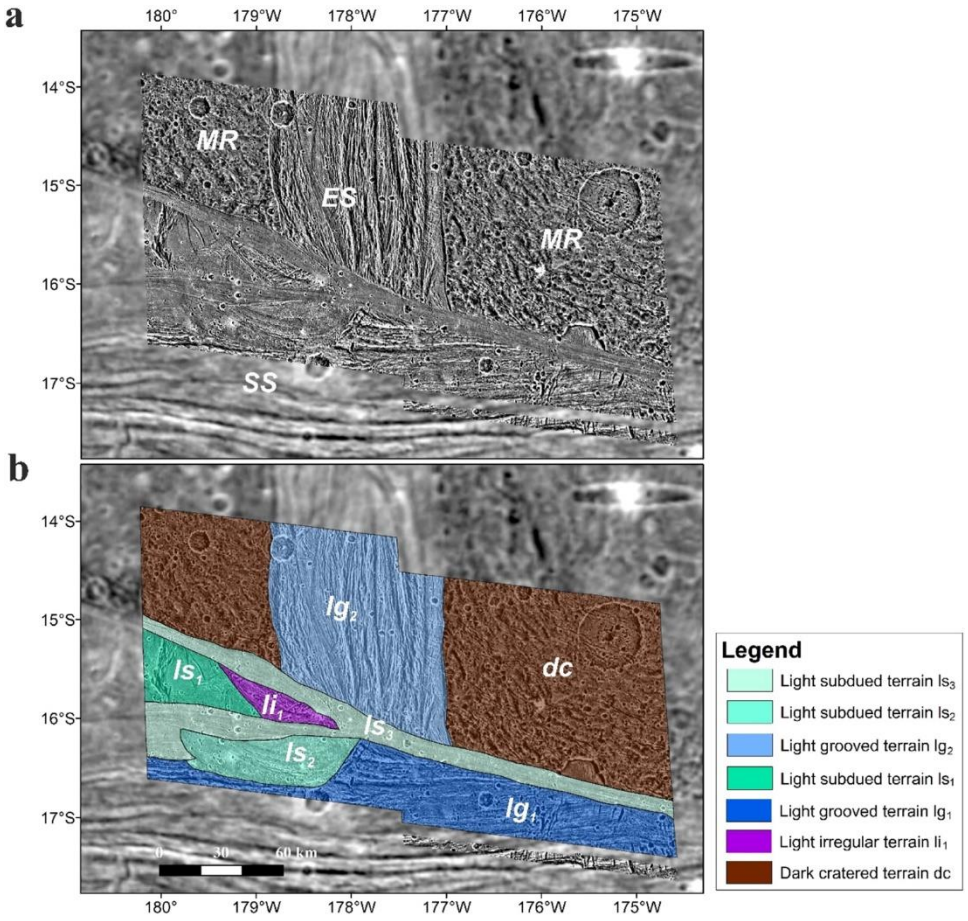

Figure 2.19: Region D/Erech Sulcus: (a) SSI observation G8GSERECH01 with the main surface features Erech Sulcus (ES), Sippar Sulcus (SS), and Marius Regio (MR) indicated and (b) the associated geologic map produced following the mapping style of Collins et al. (2013).

ii. CSFDs

The youngest terrain known from cross-cutting relationship, ls_3, has a CSFD of $7.52 \times 10^{-5} \pm 1.3 \times 10^{-5}$ which is very similar to the CSFDs obtained for the other light terrains of this

studied area (Table 2.9). The minimum value was found for lg_2 ($5.65 \times 10^{-5} \pm 1.45 \times 10^{-5}$). The oldest light terrains outlined in the geological maps, i.e., ls_1, lg_1, and li_1, have CSFDs of $7.39 \times 10^{-5} \pm 2.02 \times 10^{-5}$, $9.93 \times 10^{-5} \pm 1.93 \times 10^{-5}$, and $7.56 \times 10^{-5} \pm 2.87 \times 10^{-5}$, respectively. The dark terrain dc has a CSFD of $1.49 \times 10^{-4} \pm 1.39 \times 10^{-5}$, which, unlike what is observed in the other regions, is only slightly higher than the light terrains (Fig. 2.20).

To conclude, we found that the CSFDs of all terrains are very similar and also the difference between the light and dark terrains is minimal. In other words, the CSFDs of light terrains are much higher than the CSFDs in other regions. We propose that secondary craters formed by material ejected from Melkart crater (which is ~340 km away from this study area) may have masked and modified the original CSFDs. The secondaries covering all the studied terrains of this area were then wrongly marked as primaries.

Region D	Terrain unit	N (10) [km^{-2}]	N (1) [km^{-2}]	LDM [Ga]	JCM [Ga]	Area [km^2]	No. of craters counted
G8GSERECH_01 (**Erech Sulcus**)	ls_3	7.52e-5 ±1.3e-5	8.48e-3 ±1.46e-3	$3.94^{+0.024}_{-0.030}$	$2.74^{+1.53}_{-1.54}$	3101.21	54
	lg_2	5.65e-5 ±1.45e-5	6.37e-3 ±1.63e-3	$3.90^{+0.036}_{-0.040}$	$2.27^{+1.71}_{-1.33}$	6280.42	49
	ls_2	7.90e-5 ±1.97e-5	8.91e-3 ±2.22e-3	$3.95^{+0.034}_{-0.038}$	$2.82^{+1.49}_{-1.57}$	1476.20	39
	lg_1	9.93e-5 ±1.93e-5	1.12e-2 ±2.18e-3	$3.99^{+0.027}_{-0.033}$	$3.21^{+1.23}_{-1.69}$	4550.63	106
	ls_1	7.39e-5 ±2.02e-5	8.33e-3 ±2.28e-3	$3.94^{+0.037}_{-0.041}$	$2.71^{+1.55}_{-1.52}$	1145.05	55
	li_1	7.56e-5 ±2.87e-5	8.52e-3 ±3.23e-3	$3.95^{+0.049}_{-0.057}$	$2.74^{+1.53}_{-1.54}$	488.008	23
	Dc	1.49e-4 ±1.39e-5	1.68e-2 ±1.57e-3	$4.05^{+0.013}_{-0.015}$	$3.82^{+0.72}_{-1.75}$	12248.7	298

Table 2.9: Measured CSFDs (N (10) and N (1)) for All Mapped Terrain Units in the Erech Sulcus Region, Including LDM and JCM Age Estimates, Terrain Unit Areas, and the Number of Craters Counted.

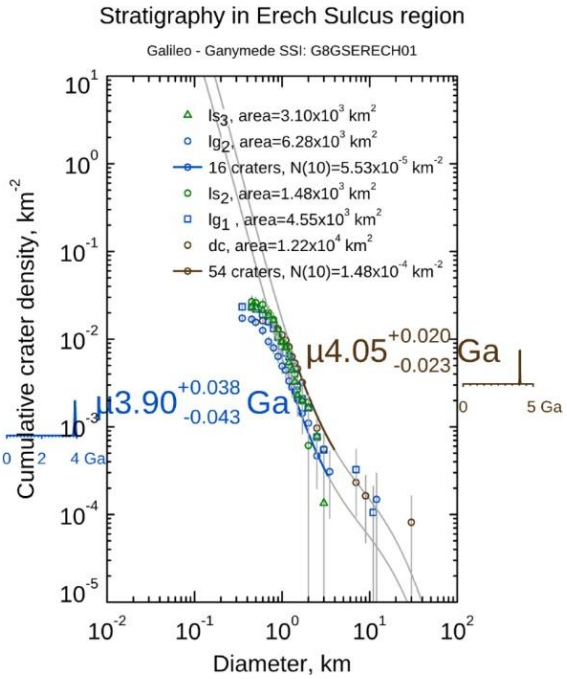

Figure 2.20: Comparison of the relative ages of the different terrain units from Erech Sulcus (SSI observation G8GSERECH01) based on CSFDs. The plot displayed here represents ages derived from LDM. For ages based on JCM, refer to Table 2.9.

2.5.4.2 Mummu and Sippar Sulcus (G8GSCALDRA01)

i. Geological Mapping

Mummu and Sippar Sulcus are located on the anti-Jovian hemisphere at ~39°S, 180° E (Figs. 2.1 e and 2.21). The images acquired during the sequence G8GSCALDRA01 have a resolution of 179 m pixel^{-1} (Fig. 2.21 a). The mosaic shows a complex pattern of cross-cutting relationships of 28 light terrain units. The terrain types observed include three superimposed generations of light grooved terrains (lg_1, lg_2, and lg_3), light subdued terrains (ls_1, ls_2, and ls_3), light irregular terrains (li_1, li_2, and li_3), plus reticulate terrains (Fig. 2.21 b). The most striking features are seven caldera-like depressions. The light subdued terrain ls_3 is a narrow, smooth, and subdued terrain bifurcating in the west and has a width of ~25 km. Like in most of the previous study areas, the smoothest terrain is the youngest. Six of the seven caldera-like features are cross-cut by the youngest terrain ls_3 or merge with it. The calderas are always asymmetric with a steep inward-facing fault scarp. This fault scarp shows indentations. The low-lying caldera interiors contain smooth material that seems to have flown out on one side toward the ls_3 unit.

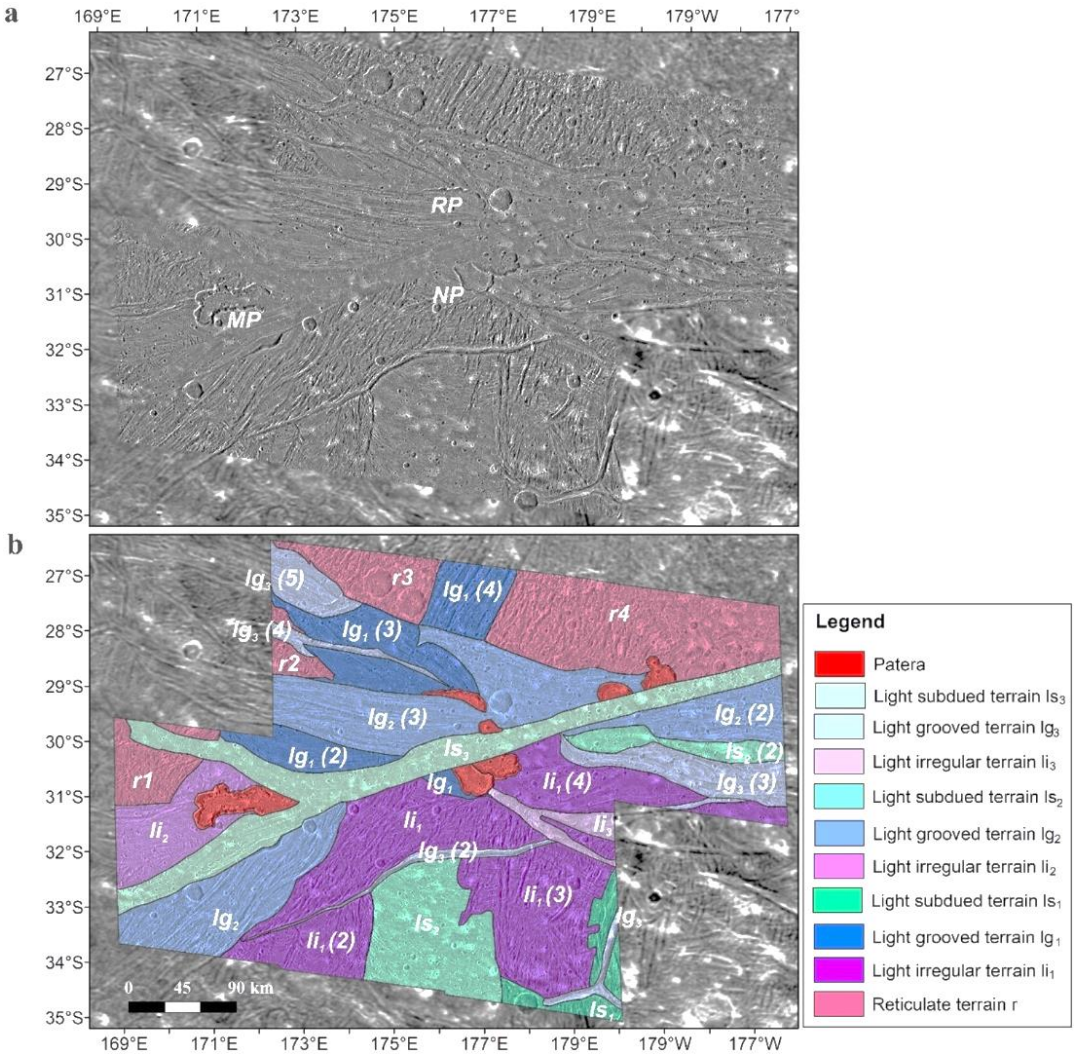

Figure 2.21: Region D/Mummu and Sippar Sulci: (a) SSI observation sequence G8GSCALDRA01 with the location of Musa (MP), Natrum (NP), and Rum Patera (RP) indicated and (b) the associated geologic map produced following the mapping style of Collins et al. (2013).

Light terrains are more frequent than reticulate terrains, which are found to be the oldest terrain type in this area. This region is a good example because all types of grooves and ridges exist, ranging from sharp edged (grooved and irregular terrains) to faint ones (subdued terrains; Baby et al. 2022). Clusters of irregular craters often found on the subdued terrains are interpreted as secondary craters, which radiate from the large Osiris crater (38° S, 193.69° E; Fig. 2.1 a), which is ~440 km away from the study area.

The light grooved terrains, lg_3, lg_3 (2), lg_3 (3), lg_3 (4), and lg_3 (5), form narrow and deep troughs just a few kilometers wide. Their borders with adjacent terrains are usually sharp. In contrast, the light subdued terrains, ls_2 and ls_2 (2), are much broader, showing a smooth

relief. The light grooved terrains lg_2, lg_2 (2), and lg_2 (3) are broader than the younger lg_3 generation. However, the lineaments in lg_2 (2) have a trend in the east–west direction, while those in lg_2 (3) have a trend in the northwest–southeast direction. The light grooved terrains, lg_1, lg_1 (2), lg_1 (3), and lg_1 (4), are broad and grooved. Their borders separating them from adjacent terrains are sharp. The lineaments they contain appear to have similar widths, lengths, spacings, and orientations.

The light irregular terrains li_1, li_1 (2), li_1 (3), and li_1 (4) have very rough surface morphologies with lineaments occurring in various directions. Mummu and Sippar Sulci are examples of the complex tectonic processes imprinting one over the other in which the dark terrain is completely erased by the formation of light terrain. The light terrains intersect and cut across one another, sometimes leaving only a small portion of a particular type of terrain visible. Earlier studies suggested that a combination of cryovolcanism and tectonic activities played an important role in shaping the present light terrains (Schenk et al. 2001; Showman et al. 2004).

ii. CSFDs

The youngest terrains known from cross-cutting relationships, ls_3, lg_3, and li_3, have CSFDs that lie in the range from 3.45×10^{-5} to 1.416×10^{-4} km^{-2} (when considering the upper and lower error bars of the uncertainty values; Tab. 2.10, Fig. 2.22). Among these, lg_3 and lg_3 (4) have similar CSFDs of $4.75 \times 10^{-5} \pm 1.3 \times 10^{-5}$ km^{-2} and $5.23 \times 10^{-5} \pm 7.42 \times 10^{-6}$ km^{-2}, respectively, which are lower in comparison to those of other terrains. Apart from lg_3 and lg_3 (4), the other studied terrains are characterized by CSFDs with values similar to each other and to any typical dark terrain. The second youngest terrains inferred from mapping results, ls_2, lg_2, and li_2, have CSFDs that lie in the range from 6.3296×10^{-5} to 3.059×10^{-4} km^{-2} (when considering the upper and lower error bars of the uncertainty values). This range overlaps with that of the younger ones. The oldest light terrains inferred from the mapping results, ls_1, lg_1, and li_1, as well as the reticulate terrain, have CSFDs that lie in the range from 2.14×10^{-5} to 1.687×10^{-4} km^{-2} (when considering the upper and lower error bars of the uncertainty values; Fig. 2.22). Again, this shows a complete overlap between the CSFDs of the oldest and youngest light terrain units. Overall, the CSFDs are quite high, comparable to those of the dark terrains found in other locations.

To summarize, the CSFDs of the light terrains are much higher than the CSFDs in other study regions and show only small differences between the various light terrain units, which

are often in contraposition to geological observations. Like for Erech Sulcus, the reasons for such similar CSFDs could be the superposition with secondary craters, which formed by the material ejected by Osiris crater (~440 km east from this study area). The secondaries have evenly disturbed all the terrains, and were mistaken as primaries due to the close similarity in shape between the two sets of landforms. Overprinting with secondaries prevents us from correctly constraining the period of light terrain formation. Hence, geological interpretation by the cross-cutting relationship is the better method here to derive a relative chronology.

Region D	Terrain unit	N (10) [km^{-2}]	N (1) [km^{-2}]	LDM [Ga]	JCM [Ga]	Area [km^2]	No. of craters counted
G8GSCALDRA01 (**Mummu and Sippar Sulcus**)	lg_3	4.75e-5 ±1.3e-5	5.35e-3 ±1.47e-3	$3.87^{+0.039}_{-0.044}$	$2.00^{+1.75}_{-1.20}$	869.719	20
	$lg_3(2)$	1.05e-4 ±3.53e-5	1.18e-2 ±3.98e-3	$4.00^{+0.044}_{-0.050}$	$3.29^{+1.17}_{-1.71}$	1225.49	21
	$lg_3(3)$	1.99e-4 ±2.92e-5	2.24e-2 ±3.29e-3	$4.09^{+0.020}_{-0.024}$	$4.15^{+0.40}_{-1.63}$	4917.89	165
	$lg_3(4)$	5.23e-5 ±7.42e-6	5.90e-2 ±8.36e-4	$3.89^{+0.021}_{-0.025}$	$2.14^{+1.74}_{-1.28}$	2489.43	43
	$lg_3(5)$	1.06e-4 ±3.59e-4	1.19e-2 ±4.05e-3	$4.00^{+0.055}_{-0.064}$	$3.31^{+1.16}_{-1.71}$	998.227	75
	ls_3	9.67e-5 ±7.9e-6	1.09e-2 ±8.91e-4	$3.98^{+0.012}_{-0.013}$	$3.16^{+1.27}_{-1.68}$	13428.0	355
	li_3	2.41e-4 ±5.55e-5	2.72e-2 ±6.26e-3	$4.12^{+0.033}_{-0.035}$	$4.32^{+0.24}_{-1.47}$	1930	41
	lg_2	9.67e-5 ±9.93e-6	1.09e-2 ±1.12e-3	$3.98^{+0.015}_{-0.017}$	$3.16^{+1.27}_{-1.68}$	8894.42	238
	$lg_2(2)$	2.60e-4 ±4.39e-5	2.93e-2 ±4.95e-3	$4.13^{+0.023}_{-0.027}$	$4.37^{+0.19}_{-1.29}$	4976.44	130
	$lg_2(3)$	7.03e-5 ±7.04e-6	7.93e-3 ±7.94e-4	$3.93^{+0.015}_{-0.017}$	$2.62^{+1.59}_{-1.49}$	8044.88	250
	$lg_2(4)$	1.50e-4 ±2.03e-5	1.69e-2 ±2.29e-3	$4.05^{+0.019}_{-0.022}$	$3.83^{+0.71}_{-1.75}$	5955.69	201

	ls_2	2.39e-4 ±7.03e-5	2.70e-2 ±7.92e-3	$4.12^{+0.038}_{-0.042}$	$4.31^{+0.25}_{-1.48}$	4709.82	103
	$ls_2(2)$	2.00e-4 ±3.1e-5	2.26e-2 ±3.49e-3	$4.09^{+0.021}_{-0.025}$	$4.17^{+0.39}_{-1.62}$	2637.59	94
	li_2	1.21e-4 ±1.3e-5	1.36e-2 ±1.47e-3	$4.02^{+0.015}_{-0.017}$	$3.50^{+1.00}_{-1.74}$	5626.47	164
	lg_1	3.26e-5 ±1.12e-5	3.68e-3 ±1.26e-3	$3.81^{+0.049}_{-0.058}$	$1.50^{+1.68}_{-0.93}$	495.831	88
	$lg_1(2)$	6.97e-5 ±1.51e-5	7.86e-3 ±1.7e-3	$3.93^{+0.030}_{-0.039}$	$2.61^{+1.59}_{-1.48}$	2928.20	270
	$lg_1(3)$	1.10e-4 ±1.03e-5	1.24e-2 ±1.16e-3	$4.00^{+0.014}_{-0.015}$	$3.37^{+1.11}_{-1.72}$	6647.43	124
	$lg_1(4)$	1.38e-4 ±1.91e-5	1.56e-2 ±2.15e-3	$4.04^{+0.019}_{-0.022}$	$3.71^{+0.82}_{-1.76}$	3524.41	13
	ls_1	8.20e-5 ±1.53e-5	9.25e-3 ±1.73e-3	$3.96^{+0.026}_{-0.032}$	$2.88^{+1.45}_{-1.59}$	2954.11	86
	li_1	4.50e-5 ±8.46e-6	5.07e-3±9.54e-4	$3.86^{+0.028}_{-0.035}$	$1.92^{+1.76}_{-1.16}$	10748.0	134
	$li_1(2)$	5.51e-5 ±9.85e-6	6.21e-3 ±1.11e-3	$3.90^{+0.026}_{-0.032}$	$2.23^{+1.72}_{-1.32}$	4784.35	168
	$li_1(3)$	6.69e-5 ±7.33e-6	7.54e-3 ±8.26e-4	$3.93^{+0.016}_{-0.018}$	$2.54^{+1.62}_{-1.46}$	10973.1	70
	$li_1(4)$	1.52e-4 ±1.69e-5	1.71e-2 ±1.91e-3	$4.05^{+0.016}_{-0.018}$	$3.84^{+0.70}_{-1.74}$	6707.67	190
	r	6.96e-5 ±9.58e-6	7.85e-3 ±1.08e-3	$3.93^{+0.020}_{-0.023}$	$2.61^{+1.59}_{-1.48}$	3484.79	95
	r (2)	7.55e-5 ±2.0e-5	8.51e-3 ±2.25e-3	$3.94^{+0.036}_{-0.040}$	$2.74^{+1.53}_{-1.54}$	1288.93	34
	r (3)	5.94e-5 ±1.69e-5	6.70e-3 ±1.9e-3	$3.91^{+0.039}_{-0.044}$	$2.35^{+1.69}_{-1.37}$	616.277	120
	r (4)	1.20e-4 ±1.2e-5	1.35e-2 ±1.35e-3	$4.02^{+0.014}_{-0.016}$	$3.50^{+1.00}_{-1.74}$	10948.2	285

Table 2.10: Measured CSFDs (N (10) and N (1)) for All Mapped Terrain Units in the Mummu and Sippar Sulcus Region, Including LDM and JCM Age Estimates, Terrain Unit Areas, and the Number of Craters Counted.

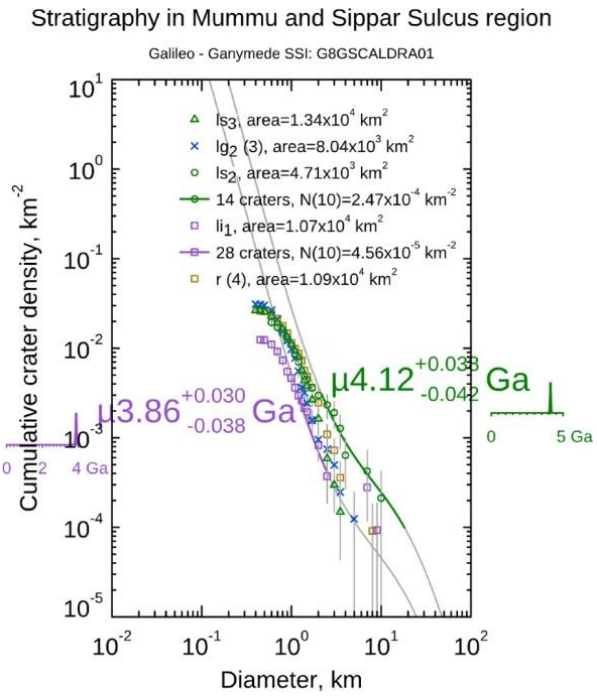

Figure 2.22: Comparison of the relative ages of the different terrain units from Mummu and Sippar Sulcus (SSI observation G8GSCALDRA01) based on CSFDs. The plot displayed here represents ages derived from LDM. For ages based on JCM, refer to Table 2.10.

2.6 AMAs of the Mapped Terrain Units

Despite the uncertainties in determining the absolute ages of Ganymede's geologic units, we applied impact crater chronology models to understand better and constrain the formation period of the light terrains and to shed some light into Ganymede's geologic evolution. Additionally, we aimed to constrain the prerequisites that should be implemented and/or improved when using these models before the JUICE spacecraft will arrive in the Jovian system.

Region A

In Byblus Sulcus, the youngest unit is the fresh crater Nergal (Figs. 2.1 b and 2.5 a), whose model age ranges between ~1.2 and ~2.7 Ga (LDM; ±1 Ga) and ~0.1 to ~0.4 Ga (JCM), and acts as a stratigraphic marker (Fig. 2.23 a). Among all the terrain units in Region A, the transitional region shows a higher CSFD than the various units of Byblus and Nippur Sulcus. Moreover, the range of ages in the ls and li terrain units of the transitional region is high. In contrast, the CSFDs and hence the period of formation of Byblus and Nippur Sulcus suggest a rather short period of formation. The formation period of all light terrains

units lies between ~3.68 Ga and ~4.07 Ga (LDM; ±0.1–0.2 Ga) or ~0.83 Ga and ~4 Ga (JCM). The model ages of the dark terrains of Marius Regio range between ~3.85 and ~4.17 Ga (LDM; ±0.1–0.2 Ga) or ~1.81 to ~4.46 Ga (JCM). Thus, using LDM the light terrain could have formed immediately after the dark terrain. In JCM, the formation period of light terrains lasts considerably longer.

Region B

In Arbela Sulcus, the youngest unit is the fresh crater Enkidu (Fig. 2.1 a), which seems to have formed shortly after the light terrain (Fig. 2.23 b). The light terrains have formation ages of ~3.72 to ~3.79 Ga (LDM; ±0.1–0.2 Ga) or ~0.99 to ~1.37 Ga (JCM). The dark terrains (dc and dl) of Nicholson Regio formed between ~3.91 and ~4.08 Ga (LDM; ±0.1–0.2 Ga) or ~2.60 to ~4.04 (JCM). Thus, the dark terrain is somewhat older in comparison to Region A. There is a possible hiatus between the dark and light terrain formation. However, Region B is less well explored than the other regions.

Region C

In Harpagia Sulcus, the youngest unit is crater Kittu (Fig. 2.1 a), which is younger than Enkidu and the light terrain units (Fig. 2.23 c). Its model age ranges between ~0.2 and ~1.5 Ga (LDM; ±1.0 Ga) or less than ~0.1 Ga (JCM). The light terrain of Region C spans a period between ~3.61 Ga and ~4.10 Ga (LDM; ±0.1–0.2 Ga) or ~0.64 to ~4.20 Ga (JCM). Within this range, the smooth light terrains ls generally have higher CSFDs than the grooved light terrain units lg. Whether this reflects older ages is questionable. A selective increase of the CSFD of the smooth terrain by bombardment with secondaries is only reasonable if the crater-forming event happened prior to the formation of the grooved terrain and after the formation of the smooth terrain. Enkidu may be the origin of secondary craters. The extensive secondary field of Enkidu spans about 600 km around the crater, and, since our study regions lie within this field, it can potentially cause a bias in the counted primary craters. The dark terrain formation that belongs to Nicholson Regio happened between ~4.05 and 4.19 Ga (LDM; ±0.1–0.2 Ga) or ~3.80 to ~4.52 Ga (JCM). To summarize, the time gap between the formation of the dark terrain units and the light terrains appears to be short using both chronologies.

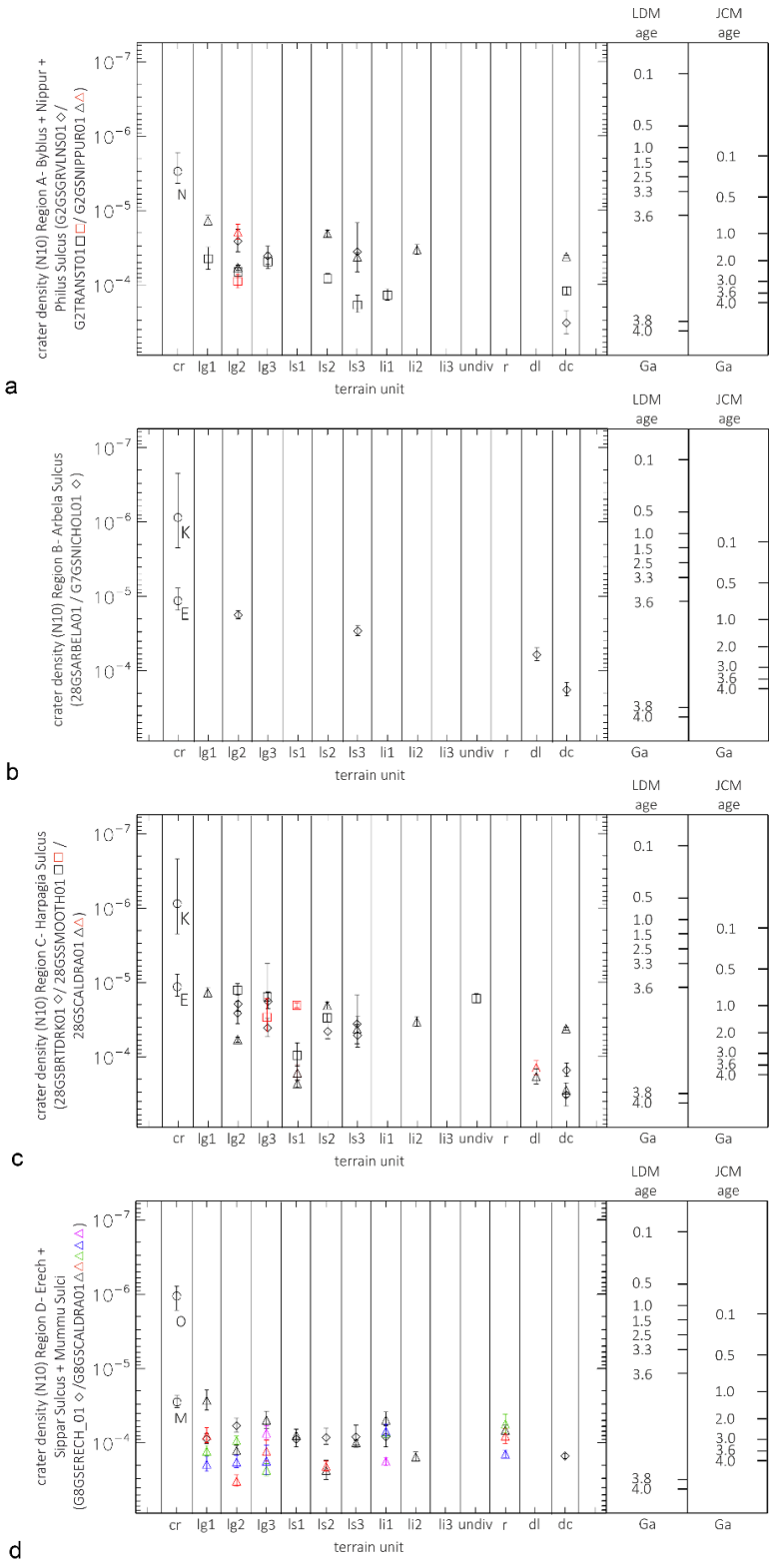

Figure 2.23: N (10) values derived for Regions (a) A, (b) B, (c) C, and (d) D. Please note that the N (10) values derived for fresh impact craters (cr) Kittu (K) and Enkidu (E), which are located near Regions B and C as well as Melkart (M) and Osiris (O), located near Region D, have been included as stratigraphic markers for the youngest period in the specific region. Also, note that different colors indicate various facies of a particular type of terrain.

Region D

In Region D, the youngest feature, Osiris crater (Fig. 2.1 a), has a model age of ~0.5 to ~1 Ga (LDM; ±1.0 Ga) or less than ~0.1 Ga (JCM) (Fig. 2.23 d). The CSFD of Melkart crater is slightly lower than that of the light terrains, whose age corresponds to ~3.63 Ga (LDM; ±0.1–0.2 Ga) or ~1.5 Ga (JCM). Unlike Regions A, B, and C, the light terrains in region D have generally high CSFDs, which is similar to that of the dark terrain. In Erech Sulcus, as well as in Mummu and Sippar Sulci, no large differences in the CSFDs could be detected between the various light terrains and the dark terrains. As outlined before, secondary craters, likely radiating from the Osiris and Melkart craters, superposed the original CSFDs, and therefore they hampered a genuine/realistic age determination of the geological units.

2.6.1 Summary of Results

First, from the above discussion about the relative age relationships of the different terrains, it is clear that the dc units feature higher CSFDs. Also, they possess comparatively higher AMAs than the light terrains and exhibit a similar age in all regions (Fig. 2.23). Unlike the case of the light terrains, the ages estimated for the dark terrains from both models also equally suggest dc to have formed very early in Ganymede's evolution. This implies that they belong to the Nicholsonian era. But dc in Nippur and Philus Sulcus has a lower CSFD value like that of the light terrains. This is an exceptional case because dark terrain has usually undergone tectonic deformation, resulting in the presence of many fractures cutting through it and a large crater having strained to a great extent. The dl terrains have slightly lower CSFD values than dc and their values are similar to that of the light terrains. As a rule, dl is formed when dc undergoes intense fracturing.

Second, the nearest youngest impact craters belonging to the Gilgameshan era are considered in each study regions since they represent the latest prominent impact events and act as stratigraphic markers in these regions. They are found to have formed completely after the tectonic events forming the light terrains. So, their ages would lie above the ages of the light terrains. Also, their model ages in comparison with the model ages of the old dark terrains would help to derive the relative ages for the light terrains. A comparatively older impact crater from our study regions is Melkart, having a CSFD value of $2.80e-5\,^{+0.49}_{-0.55}$ km^{-2} and the youngest impact crater is Kittu having CSFD value of $8.67e-7^{+13.4}_{-6.48}$ km^{-2} (Fig. 2.23). Except for Melkart and Enkidu, which have similar

CSFDs compared to those of some light terrain units, other large craters such as Nergal, Kittu, and Osiris have lower CSFDs than all light terrains. Therefore, the young impact craters stand as a stratigraphic marker, in which the light terrain formation has ended before such impact events happened.

Furthermore, the model ages derived for the light terrains belonging to the Harpagian era are found to be more complicated than the model ages of the dark terrains and young impact craters. According to LDM, the ages of the different light terrains range between ~3.6 Ga and ~4 Ga. The ages given by this model are very old compared to JCM. The range infers that there is no large time gap between the formation periods of the different light terrains. In other words, the different light terrains formed simultaneously and/or subsequently one after the other. According to JCM, however, the ages of the different light terrains range between ~0.7 Ga and ~4.3 Ga. The ages given by this model for most of the light terrains are much younger. This range implies that there is a very large time gap between the formation periods of the different light terrains. This means that the different light terrain formations could have taken place gradually and that the tectonic activities responsible for the light terrain formation have lasted over a long time, or several periods of tectonic activity occurred. Nevertheless, their ages when compared with the JCM ages of the dark terrain shows that the light terrain formation took place shortly after the dark terrain formation ended.

Finally, between all of the individual terrains investigated so far, we found more grooved and subdued terrains than irregular ones. The irregular terrains are mostly comparably old ones since they were cross-cut by adjacent terrain units. But an older li_1 not always exhibits higher CSFD values. For instance, the li_1 terrains in Mummu and Sippar Sulci shows lower CSFD values than the more lately formed terrains. In Regions A, B, and D we have a similar number of lately formed grooved and subdued terrains. In Harpagia Sulcus III, we found that the older ls_1 terrain, which is being cross-cut by adjacent terrains, has a higher CSFD value. Therefore, the CSFD values for most of the regions (Regions A, C, and D) do not always follow the same relative age relationships that we obtained from their cross-cutting relationships. But the CSFD values of the terrains in Arbela Sulcus follow the relative age relationships inferred from their cross-cutting relationships.

In general, in most of the regions, the ls terrain unit accumulated higher CSFDs than lg and li terrain units. The smoother the terrains are (with fewer grooves), the higher the CSFDs found on them are. This is in exception to Mummu and Sippar Sulci, where almost all the

terrains are highly cratered and no relative age relationships could be obtained from the CSFD measurements alone. In regions like Nippur, Philus Sulcus, and Harpagia Sulcus I, the younger ls_3 terrains display higher CSFD values than the lg_2 and lg_3 terrains. If these ls_3 terrains had accumulated secondaries from large impact craters causing the CSFD to increase to higher values, then it remains unknown why the neighboring lg_3 and lg_2 have lower CSFDs than it. The possible reason behind this would be that the light grooved terrains may have undergone resurfacing activities while Ganymede was tectonically active. Besides, Ganymede's surface may have initially formed as smooth terrain (i.e., ls terrain), which later underwent faulting, resulting in the creation of the lg and li terrains. This could explain why the ls terrains have higher CSFD values than the lg and li terrains. Therefore, the light terrain on Ganymede would have undergone tectonic processes and evolved into morphologically different terrains from its initial formation until the moon's active stage. In addition, their complex cross-cutting relationships with each other point toward a complex tectonism and subsurface activities of Ganymede responsible for the formation of the morphologically different terrains.

2.7 Discussion

2.7.1 Stratigraphic Analysis of the Terrain Units in the Different Regions

In general, the stratigraphic relationships of the terrain units investigated in this study support the results of the earlier works of Patterson et al. (2010) and Collins et al. (2013). They showed that the dark cratered terrains are the geologically oldest and the light terrains are the relatively youngest terrains, whereas the dark lineated terrains and reticulate terrains have intermediate ages between them. Thus, a dark lineated terrain represents a dark cratered terrain with subsequent tectonic resurfacing (Pappalardo et al. 2004). The reticulate terrains examined in Mummu and Sippar Sulci show that they formed shortly before the light terrain formation had started, because they are being cross-cut by light terrain and have slightly higher CSFDs with respect to the light terrain. Therefore, our result supports earlier studies on reticulate terrains by Guest et al. (1988), Wilhelms (1997), Schenk et al. (2001), Patterson et al. (2010), and Collins et al. (2013).

In our study, we investigated whether the distances of the target areas relative to the apex could significantly influence our findings. For each of our study areas, we calculated the apex distance using the center of each Galileo SSI observation. Table 2.1 reports these

distances (see the fifth column). Regions A, B, and D have distances ranging from approximately 80° to 110°, situated halfway between the apex and antapex. According to Xu et al. (2017), frequencies between a 80° and 110° apex distance differ by a factor of 1.5–2, which is comparable to the average measurement uncertainties in the cumulative frequencies for diameters of 1 km and 10 km. Consequently, we deduce that, in terms of apex distance, the frequencies and ages measured in these three regions are comparable from a stratigraphic perspective. The three study areas in Region C (Harpagia Sulcus I, II, and III) have a greater distance to the apex, ranging from 120° to 140°. On average, the cumulative frequencies in these areas are approximately 2 times lower than the frequency obtained in a unit at a 90° distance, similarly to the findings of Xu et al. (2017) for light terrains. Therefore, it is essential to consider that the cumulative frequencies measured in Harpagia Sulcus I to III, which are lower than the average frequencies in Regions A, B, or D, could actually indicate a similar age or even older than the units in Regions A, B, and D. Comparing the different study regions, we could find a consistent relative age relationship between the light terrains lg, ls, and li. In some of the selected areas, the smooth, light subdued terrain forms the youngest stratigraphic unit, which indicates tectonic extension in spreading mode.

We have not observed a significant variation in the CSFDs (and, consequently, the absolute ages derived from both models) with respect to an increment in area for any specific type of terrain (for a more detailed explanation, please refer to Appendix B). Due to the cross-cutting relationships of the geological units, a relative chronology could be derived from geological mapping. This is not always congruent with the age determination derived from the CSFD measurement. In the following, we are going to explain both such deviations and the possible reasons for their occurrence. First, we defined that the degree of matching between both methods is expressed in percentages. For example, if five different chronological units are inferred from mapping, matching is 80% when four of the five units show the same sequence in crater counting. In brief, in Byblus Sulcus (Region A) the two light terrains are of similar age from the crater counts while lg_3 is younger than lg_2 from the cross-cutting relationships. In the Nippur and Philus Sulcus region, the terrains of Nippur Sulcus have an older age than Philus Sulcus from the crater counts. This is in contrast to the mapping result of this area where Nippur Sulcus cross-cuts Philus Sulcus. This may indicate a short period between the formation of these terrains. To conclude, the matching in Region A between geological mapping and crater counting is 60%. In the case of Region

B (Arbela Sulcus), we found that the age relationship of the two light terrains and two dark terrains agrees with the relative age inferred from the cross-cutting relationships. The matching is 80%. In Region C, the light subdued terrains have a comparatively higher age than the light grooved terrains. In these regions, we hypothesized that the light subdued terrains formed earlier and subsequent faulting could have developed into light grooved terrains at a later stage. The region constituting Harpagia Sulcus II (28GSCALDRA02) is inferred to be older based on its cross-cutting relationships and CSFDs compared to the regions containing Harpagia Sulcus III (28GSSMOOTH02) and Harpagia Sulcus I (28GSBRTDRK02). The overall matching of Region C is 60%. In Region D, the terrains are highly contaminated by secondary craters from the Osiris and Melkart craters. There is no significant difference of the crater-counting-derived ages between the studied terrains, but the related cross-cutting relationships clearly suggest subsequent formations. Nevertheless, a saturation of craters or the short period between the formation of different terrains could be possible reasons for such a disagreement. The derived CSFDs and ages from such regions should be taken with caution. Due to the superposition with secondaries the matching between the relative chronology derived from geological mapping and crater counting is only 40%.

2.7.2 Discrepancies of Crater Chronology Models

The usage of JCM and the obtained age interpretation is difficult in older regions since this model uses the present cometary fluxes to infer the dynamical motion of these bodies in the past. Therefore, such extrapolation results in ages older than the solar system caused by highly uncertain conditions in a planetary migration period prior to ~3.6 Gyr with a possible exponentially decaying impactor flux versus mainly constant flux.

On the contrary, LDM is based on a lunar-like model with its assumption that the craters on Ganymede were mainly created by asteroidal impacts, like those on the Moon. Although this might be unrealistic for the bombarding flux on Ganymede, recent studies (Bottke et al. 2022) supported a similar SFD between comets and asteroids, i.e., both groups of impactors represent a collisionally evolved impactor family showing similar crater distributions, such as, e.g., asteroidal impacts on the Moon. Possibly different impactor families existed through time with preferentially asteroids prior to ~3.6 Gyr and preferentially JFCs at later time to the present (G. Neukum, personal communication;

Schenk et al. 2004). However, the projectile SFD can be similar; the result of an impact (i.e., the crater SFD) can be different due to the distinct surfaces of the Moon and Ganymede and the variation in impact velocities.

2.7.3 Formation Scenarios for the Light Terrain on Ganymede

The variations of the SFDs of impact craters on different terrains are not always coherent with geological observations. The moderate variations of CSFDs suggest that the range of formation ages is not large. Knowledge of the absolute ages of the light terrain units, however, is essential to solve which processes or conditions could be responsible for the tectonic activity in Ganymede's past and the light terrain formation. The following formation scenarios have been discussed in recent studies.

(A) Global Volume Expansion Through Internal Differentiation

A global expansion through differentiation early in Ganymede's history (Squyres 1980; Schubert et al. 1981; Zuber & Parmentier 1984; Mueller & McKinnon 1988; Bland et al. 2009) would be most likely a continuous process that is associated with a continuous formation of the different light terrains. So different light terrains were formed via extension of the lithosphere once differentiation started. Under such circumstances, the light terrains would have likely formed shortly one after the other or contemporarily with the tectonic style (grooved or subdued) depending on the local surface properties. Light terrain formation might have stopped once the differentiation process and associated thermal expansion has been completed.

Light terrains could have already started developing through lithospheric extension, when the Ganymede surface was made up by a thin ice shell (Nimmo 2004), as evidenced from its low thermal gradient at present and high thermal gradient in the past (Pappalardo et al. 2004). Although the depth to diameter ratios of craters that formed after the grooved terrains suggest an ice shell thickness of at least 60 km (Schenk 2002), the ancient palimpsests suggest instead a much lower ice shell thickness in the past (Bland et al. 2009).

Our results support that the light terrains started to form soon after dark terrain formation. However, although, using LDM, the derived ages imply a light terrain formation in a short period early in Ganymede's evolution, when applying JCM, an unrealistically large time span is often observed because of the model's large overlapping error bars.

(B) Laplace Resonance and Orbital Recession—Tidal Heating

It is estimated that Ganymede's eccentricity (presently e = 0.0013) is currently too low to cause prominent tidal heating effects (Mckinnon & Parmentier 1986) and subsequent tectonic resurfacing activities (Bland et al. 2009). Nevertheless, an orbital eccentricity originated by periods of Laplace-like resonances with Europa and Io in the past could have triggered periods of tidal heating and internal melting, which, in turn, would have led to enhanced differentiation and geologic activity (Showman et al. 1997). In such a scenario, the light terrains could have resulted from Ganymede's past high eccentricity and higher tidal dissipation (Showman & Malhotra 1997), if the Laplace resonance has a major effect in generating tectonism.

The CSFDs of different terrain units show that the period between the end of dark terrain formation and beginning of light terrain formation is generally small if LDM is used. In this case, eccentricity-induced tidal heating would have taken place soon after dark terrain formation. The morphological characteristics distinguishing light terrain into grooved, subdued, and irregular terrains could have reflected changes in the internal dynamics of the outer ice shell. The reason for such changes, as suggested by Choblet et al. (2017), is the chemical transfer of melt or liquid water from the surface of a silicate core or high-pressure ice mantle layer. Such transport through heat pipes could have taken place up to at least 500 Myr ago and may have affected the history of ocean crystallization. This theory is contradicted by the surface ages estimated by using LDM, but is supported by JCM because this model assumes ages of ~ 1 Ga for some terrains and suggest larger formation period for light terrains.

(C) Nonsynchronous Rotation

The tectonic activity in Ganymede's past could have taken place in a time of nonsynchronous rotation. At present Ganymede's synodic rotation around Jupiter is synchronous. Studies, however, showed that Ganymede could have rotated nonsynchronously in the past (Nimmo & Pappalardo 2004; Cameron et al. 2019, 2020). Past nonsynchronous motion could have produced diurnal and tidal stresses, which would have induced shear failure giving rise to strike-slip faulting within light terrains (Cameron et al. 2019). If nonsynchronous rotation is the cause of the formation of the light terrain then the time of completion of the light terrain would help to constrain the time of the gradual transition toward synchronous rotation. If we consider nonsynchronous rotation to

represent the main reason responsible for light terrain formation, then LDM is somewhat unlikely as it suggests a short formation period for light terrains. In contrast, JCM, which implies a rather long formation for light terrain formation, would better fit to such a scenario. In that case, light terrain formation has ended ~1 Ga ago and Ganymede would have successively entered a synchronous state.

(D) Large Impacts in Ganymede's *Early History*

Could the formation of the light terrain have been initiated by intense impact cratering? Large impact basins, like Gilgamesh basin (62.8° S, 125° W; 600 km diameter) on Ganymede, are believed to have been formed early in the history of Ganymede, likely during the light terrain formation, when there was an intense bombardment by large projectiles, whose diameters were several tens of kilometers. Gilgamesh basin was emplaced into the light terrain at a later time than the degraded basins in the dark terrain (Schenk et al. 2004). These older impact events could have generated significant thermal anomalies in the mantle. The heat generated could alter the mantle's buoyancy enough to create upwellings and to drive tectonic activity. The effect would be stronger if Ganymede had an uneven thickness of its lithosphere during that time. Large impacts could have also added heat to the differentiation process. Moreover, large impact events could cause the onset of synchronous rotation. According to Murchie & Head's (1986) findings, the large impacts led to a global reorientation of Ganymede's rotational axis by approximately 15°. However, observing impact craters on Ganymede's neighbor Callisto raises doubt whether large impact events can trigger tectonism of light terrains. Callisto is probably a partially differentiated body (e.g., Sohl et al. 2002; Nagel et al. 2004), having a heavily cratered surface and containing the largest multiring impact basin in the solar system, Valhalla. However, it does not have any tectonically resurfaced terrains.

2.8 Conclusions

We analyzed selected regions on Ganymede for which high-resolution remote sensing data are available. The combination of geologic mapping and CSFD measurements was a useful tool to explore the stratigraphic relationships of each investigated individual terrain unit in the studied regions. However, we often found a mismatch in the relative ages derived from cross-cutting relationships and crater statistics. Dark cratered terrains are found to be the

oldest terrains, and light terrains are the youngest ones, whereas the dark lineated and reticulate terrains have intermediate ages, all of which agree with earlier studies. Light subdued terrains from the sub-Jovian hemisphere are older and those from the anti-Jovian hemisphere are younger. Tectonic resurfacing of the dark cratered terrains has led to the formation of dark lineated terrains. Prolonged tectonic resurfacing in the form of normal and strike-slip faulting gradationally has transformed the dark lineated terrain into new light terrains. The early stage of evolution of Ganymede is represented by dark cratered terrains, which are simply densely cratered and lacking lineaments. Its intermediate stage (when dark lineated terrains have started to evolve) is recorded by lineaments that are mostly widely spaced. The morphology of light grooved, light subdued, and light irregular terrains represents lately formed geological units within which the light irregular terrains are usually cross-cut by the light grooved and light subdued terrains. Younger light subdued terrains appear as narrower stripes, while older light subdued terrains appear as broader areas. In most cases, light grooved and light subdued terrains are found adjacent to each other. The formation of light grooved terrains can occur via extensive faulting within light subdued terrains. Therefore, a clear understanding of overall tectonic processes would be possible with wider coverage and better resolution of images and digital terrain models.

The two chronology models, LDM and JCM, correlate crater statistics with absolute ages. Both models lead to considerably different results. On one hand, according to LDM, the age derived for light terrain units (~3.6 Ga–4 Ga) is not much younger than the ancient dark terrains (~3.7 Ga–4.2 Ga). On the other hand, JCM-derived ages point to a longer formation period for light terrain units (~0.7 Ga to >4 Ga), which ended around 1 Ga ago, unlike the case of dark terrain (~3.5 to >4 Ga). Based on the CSFDs and the models, light terrain formation may have begun soon after dark terrain formation, with a time gap of ~0.2 Ga. However, as shown in this study, a complete understanding is far from being reached, due to the limits of the chronology models and the currently available restricted spatial resolution of Ganymede's surface. In addition to the significant differences in the model ages of the light terrain units, the estimated errors of both models are often too large to distinguish the ages between individual tectonic units of the light terrains. Therefore, improvements of these models are necessary. Updated chronologies should enable us to constrain the errors through a better description of how and when the planets changed their orbits in the past.

This study supports the JUICE mission. Particularly, the images acquired by the JANUS camera will enable thorough analyses of Ganymede's entire surface at unprecedented spatial resolutions and thus to investigate further and comprehend its relative and/or geologic age, tectonic processes, and relationships to its complex internal dynamics. Nevertheless, resolving model age-related issues on Ganymede (and the other icy moons) in the long-term future requires the collection of samples at landing sites to obtain absolute radiometric ages accurately. The optimal landing site for calibrating CSFDs with radiometric ages would be located in light terrain areas with minimal saturation due to craters, while avoiding large ray crater strewn fields.

2.9 Acknowledgments

We acknowledge the support of the DLR-DAAD PhD fellowship from the German Aerospace Center and the German Academic Exchange Service. We thank the editor, Edgard G. Rivera-Valentín, and two anonymous reviewers for their detailed comments and suggestions, which greatly contributed to the improvement of this manuscript.

2. A Appendix A: CSFDs and Ages

2.A.1. CSFDs and Surface Ages

2.A.1.1. The Crater PF Polynomial of the Moon and Ganymede

As described in Section 2.4.2.2, polynomials of eleventh degree were adopted to fit the crater PF of a planet, satellite, or asteroid (e.g., Neukum & Ivanov 1994; Neukum et al. 2001; Werner & Ivanov 2015; Hiesinger et al. 2016). The PF of Ganymede is derived from the lunar PF, as shown in Fig. 2.2 (regular section). This polynomial can fit measured CSFDs.

At small crater sizes (less than ~1 km), the lunar PF (and any lunar-derived PF) has a cumulative slope of ~−3. For craters larger than several kilometers to the largest sizes of 100s of kilometers, the slope changes between ~−3 and ~−1. This characteristic shape reflects the shape of the impactor SFD, derived from collisional evolution of these bodies with time (e.g., Ivanov et al. 2002). For inner solar system bodies, the correlation of CSFDs

with the SFDs of asteroids that created the majority of craters is straightforward (e.g., Neukum & Ivanov 1994; Neukum et al. 2001; Ivanov et al. 2002; Werner & Ivanov 2015). The Ganymede PF and its polynomial coefficients (Table 2.A.1) is obtained by a lateral shift of the lunar PF in log(D) (Section 2.4.2.2). This empirical method, however, is subjective and dependent of the interpreter: the lunar PF is shifted in log(D) until a specific Ganymede PF is found which best fits the CSFDs (e.g., Neukum et al. 1998). Similarly, the same methodology was applied to derive the PFs for Europa and Callisto (Neukum et al. 1998).

Coefficent a_k	Ganymede PF	Lunar PF
a_0	-3. 181	-2.5339
a_1	-3.2491	-3.6269
a_2	1.0307	0.4366
a_3	0.6933	0.7935
a_4	-0.2916	0.0865
a_5	-0.3061	-0.2648
a_6	0.0171	-0.0664
a_7	0.0533	0.0379
a_8	4.018e-3	0.0106
a_9	3.43e-3	-2.25e-3
a_{10}	4.065e-4	5.18e-4
a_{11}	3.97e-5	3.97e-5

Table 2.A.1: Coefficients of the Ganymede PF Polynomial in Comparison with the Lunar PF. ***Note:*** *The Ganymede PF is from Neukum et al. (1998) and the lunar PF is from Neukum & Ivanov (1994).*

Although it is not explicitly said, such a shift of the PF is related to the specific impact condition of each body, for example the (average) impact velocity or the (average) frequency of impactors. A derivation of a Ganymede PF from crater scaling laws, like for Mars, is possible but this did not produce good results because of many unknowns in the crater scaling parameters. Using a single PF polynomial for CSFDs measured in surface units of different ages tacitly assumes that the PF did not change its shape over time. Whether a PF is time independent is subject to debate, however. Several groups of investigators concluded from their measurements of terrestrial planets that the shape has changed with time due to a change in the impactor SFD (e.g., Strom et al. 2005, 2018;

Kirchoff et al. 2022 and references therein). Other studies supported instead that any changes are within a factor of, or lower than, 2, and therefore an eventual variation in time of the PF would not have affected the inferred age in comparison to other errors (e.g., Neukum et al. 2001).

The PF polynomial coefficients listed in Table 2.A.1 (Neukum & Ivanov 1994; Neukum et al. 2001) are used to calculate the cumulative frequency N_{cum} for a crater equal to, or larger than, a diameter D (in km) according to:

$$\log N_{cum}(D) = \sum_{k=0}^{k=11} a_k \cdot [\log (D)]^k \qquad \text{(Eq 2.A.1)}$$

The lunar polynomial is valid in the diameter range of 10 m–300 km (Neukum & Ivanov 1994; Neukum et al. 2001). The term a_0 reflects the time dependence of the measured CSFD. For the lunar PF, the value $a_0 = -2.5339$ (similarly $a_0 = -3.4181$ for Ganymede) is correlated to a unit which is 1 Ga old in the LDM chronology (e.g., Neukum & Ivanov 1994). By shifting (fitting) the PF vertically in $\log(N_{cum})$ to a CSFD, the relative age of a unit can be determined by changing the term a_0 alone, holding the values a_1 to a_{11} fixed because of the (assumed) time-independent CSFD polynomial. This procedure is described in the following section.

2.A.1.2. Derivation of Surface Ages from Crater Counts

2.A.1.2.1. The Software Tool craterstats 2.0

We used ESRI/ArcGIS to map geologic units and to carry out crater counts. The toolbar CraterTools is an ArcGIS plug-in specifically developed for crater measurements, and provided by the Planetology Group at the Free University of Berlin (Kneissl et al. 2011). The software can be accessed and downloaded at the following URL: CraterTools • Planetary Sciences and Remote Sensing • Department of Earth Sciences (fu-berlin.de). In this study, we preferentially used images or mosaics in conformal map projections in which craters are represented as circles. The toolbar, however, is independent of map projections and accounts for any distortions caused by different map types (Kneissl et al. 2011). Two ArcGIS shape files are created, one for the area, another for the craters. After a measurement has been completed, the craters are exported into a spatial crater count (scc) file. Since a significant fraction of a crater can lie outside the measurement area and since

large craters tend to obliterate smaller craters, several improved methods of the crater-counting technique have been developed for such cases (Kneissl et al. 2015, 2016; Riedel et al. 2018): (1) the traditional crater-counting approach takes only those craters into account whose centers lie within the measurement area boundary; (2) the buffered crater-counting approach also uses the fractions of those craters whose rims overlap the area boundary but whose centers lie outside the measurement area; the measurement area is enlarged by a buffer size of at least one crater radius for each one of these craters; (3) on densely cratered surfaces the impacts of large craters cause a depletion in small preexisting craters which affect the shape of the measured distribution; this can be corrected by the nonsparseness approach, removing the crater and ejecta area emplaced by the most pristine large impact craters, specified in an average obliteration factor; and last (4) the buffered nonsparseness approach which combines methods (2) and (3) (see detailed descriptions of all four methods in Kneissl et al. 2015, 2016; Riedel et al. 2018). Since the measurements presented in this study were carried out on high-resolution images in a comparably small diameter range (in general <10 km), we selected the buffered crater-counting approach.

Following the recommendations given by the Crater Analysis Techniques Working Group (1979; Arvidson et al. 1979), CSFDs—and, similarly, projectile SFDs—are plotted in diagrams with double-logarithmic (base 10) axes at the same scale, with the logarithm of crater frequency per square kilometer versus the logarithm of crater diameter in kilometers. Several plotting techniques can be used, i.e., (a) cumulative, (b) differential, and (c) relative crater size–frequency. The analysis and age dating of crater size–frequency measurements are performed in the separate software tool, craterstats 2.0. This software, provided freely by the Planetology group at the Free University of Berlin (Michael & Neukum 2008), operates within the framework of the IDL Virtual Machine, which is also available at no cost. The *craterstats2* software can be accessed and downloaded at the following URL: Craterstats • Planetary Sciences and Remote Sensing • Department of Earth Sciences (fu-berlin.de). The tool can plot the crater statistics in the graphical presentation modes introduced by Arvidson et al. (1979). The cumulative crater frequency N_{cum}, which we preferred in this study, represents the number of craters in an area of diameters greater than, or equal to, the diameter of a specific crater. We use reference diameters of 1 and 10 km since the two chronology models are based on cratering rates for either 1 km or 10 km craters., which we preferred in this study, represents the number of craters in an area of diameters greater than, or equal to, the diameter of a specific crater. We use reference

diameters of 1 and 10 km since the two chronology models are based on cratering rates for either 1 km or 10 km craters.

To obtain relative ages from a specific measurement, the Ganymede PF is approximated to the measured CSFD with the PTA method (Michael et al. 2016) by selecting an upper and lower boundary crater diameter. Like finding a PF polynomial for, e.g., Ganymede, this method is subjective: an interpreter tests different diameter boundaries until a "best" fit of the curve to the data is found visually (see the examples in Figs. 2.6, 2.8, 2.10, etc.). When this procedure is carried out in the craterstats 2.0 software tool, the cumulative frequency for a crater equal to, or larger than 1 km (default), is directly obtained from the curve, and this value is used to represent the relative age of the unit and included in tables (see Tables 2.2 – 2.10). In this study, we also used a reference diameter of 10 km since the JCM chronology by Zahnle et al. (2003) is based on the cratering rate for 10 km craters. In the PF polynomial (assumed as time invariant), the factor between the (cumulative) frequencies of any two specific crater diameters is always constant and can be used to transfer a chronology function to any crater diameter (here, N_{cum} (D ≥ 1 km)/N_{cum} (D ≥ 10 km) = 112.74). The AMAs of the LDM chronology are obtained in craterstats 2.0 according to the equation (Neukum & Ivanov 1994; Neukum et al. 1998):

$$N_{cum}\ (D \geq 1\ km) = p_1 \times \left[e^{(p_2 \times t)} - 1\right] + p_3 \times t \qquad \text{(Eq 2.A.2)}$$

The AMA *t* (in Ga) is numerically calculated from the cumulative frequency N_{cum} for craters larger than, or equal to 1 km. The three coefficients p_1, p_2 and p_3 of the Ganymede LDM chronology are listed in Table 2.A.2 in comparison with the lunar coefficients. The equation consists of two summands: the left summand (coefficients p_1 and p_2) represents the part of the chronology dominated by an exponentially declining cratering rate prior to ~3 – 3.3 Ga, while the right summand (coefficient p_3) is dominated by the constant cratering rate. For AMAs younger than ~3 – 3.3 Ga the exponential term becomes negligible.

Coefficient *p*	Ganymede	Moon
p_1	1.055e-14	5.44e-14
p_2	6.93	6.93
p_3	1.625e-4	8.38e-4

Table 2.A.2: Coeffcients p1, p2 and p3 of the LDM chronology for Ganymede (Neukum et al., 1998) in comparison with the one for the moon (Neukum and Ivanov, 1994).

Currently, the JCM chronology has not yet been implemented in craterstats 2.0. JCM AMAs therefore are calculated in a separate program (*jcmchronage*, written in ANSI C by Roland Wagner) according to the formula (Zahnle et al. 1998, 2003):

$$t' = \frac{N_{cum}}{\dot{C}} \qquad \text{(Eq 2.A.3)}$$

,with N_{cum} representing the cumulative frequency for crater diameters equal to, or greater than, 10 km. $\dot{C}$ is the constant cratering rate for craters $D \geq 10$ km and t' is the temporary model age in Ga for a constant cratering rate (Zahnle et al. 1998, 2003). We adopted the cratering rate of $\dot{C} = 1.8 \times 10^{-14}$ for Ganymede from Zahnle et al. (2003). Using a constant cratering rate for dating the oldest surfaces on Ganymede would yield AMAs considerably older than the age of the solar system of $T = 4.56$ Ga. Zahnle et al. (1998; and references therein) introduced a term $1/t$ to account for secular variations in the cratering rate, and the "true" JCM AMA t in Ga then is calculated according to:

$$t = T \times [1 - e^{\left(-\frac{t'}{T}\right)}] \qquad \text{(Eq 2.A.4)}$$

This term was not further discussed in the Zahnle et al. (2003) paper but is still held valid in their updated JCM chronology (K. Zahnle, personal communication). However, we found that the oldest units in the dark terrains, with LDM AMAs of ~4 Ga, are dated about ~4.56 Ga if using JCM AMAs, which thus suggests an unrealistic high age (larger than the solar system one).

2. A.1.2.2. Potential Variations of CSFDs with Distance from the Apex Point of Orbital Motion

ECs are heliocentric bodies impacting a synchronously rotating satellite asymmetrically with respect to distance to the apex of orbital motion (0° N latitude, 270° E longitude; Shoemaker & Wolfe 1982, Horedt & Neukum 1984a, 1984b; Zahnle et al. 1998, 2003; Schenk et al. 2004; Xu et al. 2017; Kirchoff et al. 2022). A theoretically derived pronounced asymmetry of a factor of 20–60 in the cratering rates at the apex with respect to the antapex point has not been observed on both Jovian (Galilean) or Saturnian satellites, however (Schenk et al. 2004 and references therein). These authors reported a ~4 factor difference in crater frequencies in light terrain, much lower than the theoretically predicted values. In

a more recent study, Xu et al. (2017) found apex–antapex asymmetries of only a factor of ~2 in CSFDs on dark terrains and ~3 in those on light terrains, for all measured crater diameters. Bright ray craters, predominantly those on light terrain, however, show a pronounced asymmetry with respect to the distance from the apex. Nonsynchronous rotation, possibly episodic, polar wander, and, much less likely, saturation equilibrium were offered as explanations for this little pronounced apex–antapex asymmetry (e.g., Schenk et al. 2004; Xu et al. 2017; Kirchoff et al. 2022 and references therein).

2.A.1.2.3. Summary: CSFDs and Surface Ages

1. To obtain relative ages and AMAs from crater counts, we used the buffered crater-counting approach for a CSFD measured in a mapped surface unit, based on Cratertool in ArcGIS (Kneissl et al. 2015, 2016; Riedel et al. 2018).
2. A polynomial PF for Ganymede derived from the lunar PF can be used to fit measured CSFDs independently of the SFD of impactors since collisional evolution produced similar shapes of CSFDs on the moon and on icy satellites of, e.g., Jupiter (Bottke et al. 2022).
3. The Ganymede PF is fit to a CSFD using the PTA procedure with the tool craterstats 2.0 (Michael et al. 2016) to obtain the relative age of a unit which is represented by the cumulative frequency for a 1 km or 10 km crater.
4. In the same procedural step, an AMA for LDM can be derived. The AMA for JCM is calculated in a separate software tool written by one of us (Wagner), based on the cumulative frequency for a 10 km crater.
5. The error handling in AMA for both models is still incompletely implemented in craterstats 2.0 but this task may be completed in the near term (G. Michael, personal communication).
6. Taking a potential uncertainty factor of 3 in the cratering rate into account for each of the two chronology models, the errors in the AMAs are on the order of ~0.1–0.2 Ga for LDM ages older than ~3.3 Ga, and considerably higher (~ 0.5–1 Ga or even more) for LDM ages less than ~3.3 Ga, or JCM ages less than ~4 Ga.

7. Secondary craters may affect a measurement, especially near large ray craters, thus the "true" age could be lower.
8. Variations in the crater frequencies due to the distance to the apex point of orbital motion of a study area are less significant since, with the exception of two areas, most are within a comparable distance to the apex.

2.B Appendix B:

2.B.1 Effect of the Crater Counting Area on the CSFDs

The crater-counting methodology and the obtained model ages may critically depend on (i) the minimum area for crater counting, (ii) resurfacing in the light terrains, (iii) the presence of secondary craters, (iv) sesquinaries, and (v) recent large craters obliterating preexisting craters. We carefully avoided crater cluster or aligned crater chains that are indicative of secondary cratering. In order to assess the influence of the given crater counting areas on the obtained results, we systematically tested the dependency of the *N* values on the area used for the crater counting. The test was performed on the SSI images covering Mummu Sulci and Sippar Sulcus (Fig. 2.B1). We systematically varied the area of investigation from small to large values for the same region and recorded the variation in the *N* (10) values. We considered four different terrains: (a) reticulate terrain (r), (b) light grooved terrain lg_2, (c) light subdued terrain ls_3, and (d) light irregular terrain li_1.

For the four different terrains we varied the area of investigation in six steps. We started our test using a 800 km^2 area and enlarged the areas in each step by 800 km^2. So, the test areas are: test 1: 800, test 2: 1600, test 3: 2400, test 4: 3200, test 5: 4000, and test 6: 4800 km^2. In the reticulate terrain (Fig. 2.B.2 a), test 1 (800 km^2) has the lowest CSFD of 7.19×10^{-5} and test 2 (1600 km^2) has highest CSFD of 1.15×10^{-4}, and CSFDs of the other test areas fall between these two curves. From this, it is understood that there is no considerable variation in the CSFDs of larger areas and smaller areas. In lg_2 (Fig. 2.B.2 b), test 2 (of 1600 km^2) has the lowest CSFD of 6.23×10^{-5} and test 6 (4800 km^2) has six tests values are very similar.

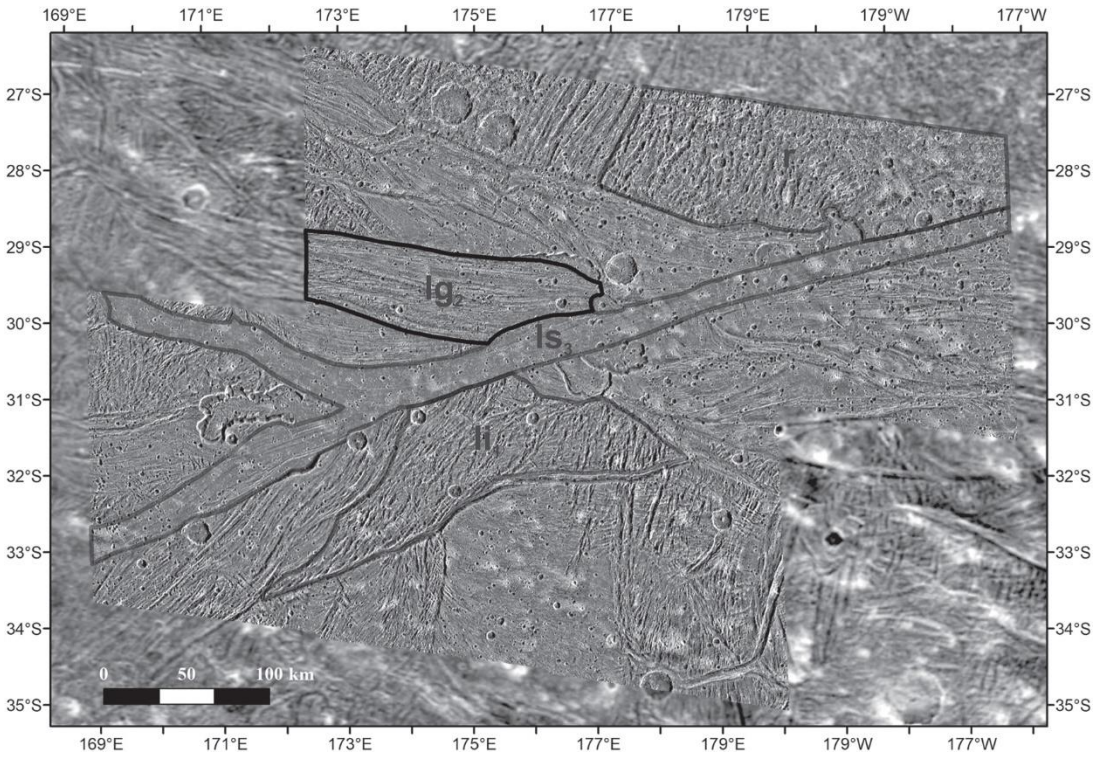

Figure 2.B.1: Test areas selected from Region D/Mummu and Sippar Sulcus (see Figure 13). Four different types of terrain units are used for the test, which have four different morphologies: reticulate terrain (r), light grooved terrain lg_2, light subdued terrain ls_3, and light irregular terrain li_1.

In ls_3 (Fig. 2.B.2 c), the curves of all test areas fall into a single curve and there is almost no variation in their CSFDs. The lowest CSFDs noted is 1.69×10^{-4} of test 5 (4000 km^2) and the highest is 1.82×10^{-4} of test 2 (1600 km^2). In li_1 (Fig. 2.B.2 d), the highest CSFD of 7.77×10^{-5}, and the CSFDs of other test areas fall between these two curves. Thus, all test 1 (of 800 km^2) has the lowest CSFD of 1.99×10^{-5} and test 5 (of 4800 km^2) has the highest CSFD of 2.80×10^{-5}. To conclude there is no systematic area effect recognizable in the data sets. We, therefore, infer that the obtained CSFDs are independent of the investigated respective areas. Of course, this also means that the absolute ages derived from LDM and JCM are independent of area.

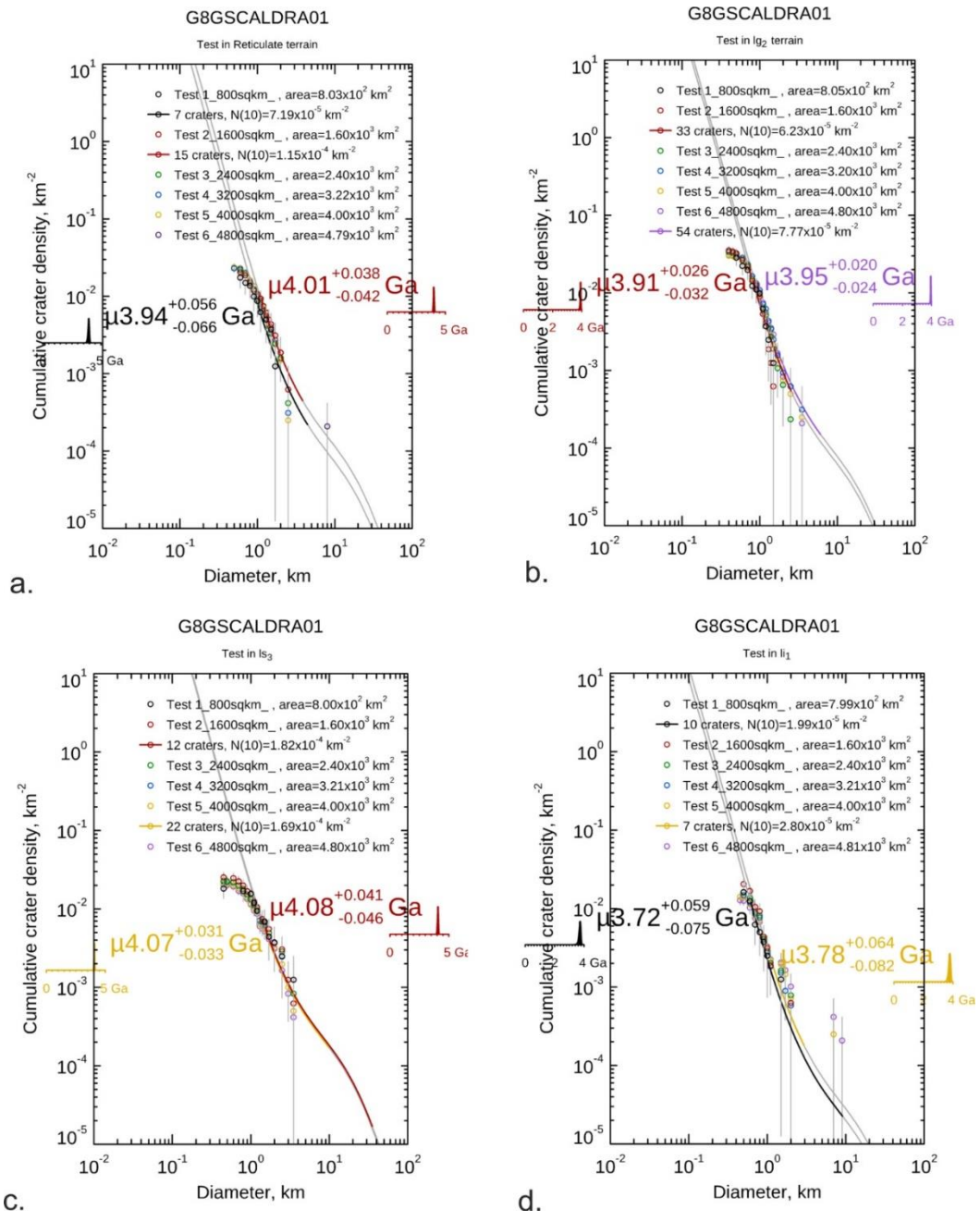

Figure 2.B.2: Histograms showing crater counts, CSFDs, and best curve fits for four different types of terrain units: (a) reticulate terrain (r), (b) light grooved terrain lg_2, (c) light subdued terrain ls_3, and (d) light irregular terrain li_1. In each of these individual terrain units, we consider six test areas: test 1 of 800 (black), test 2 of 1600 (red), test 3 of 2400 (green), test 4 of 3200 (blue), test 5 of 4000 (yellow), and test 6 of 4800 (violet) km^2. Two best-fit curves within each plot represents the test areas which have the lowest and highest crater CSFDs.

2.10 References

Alvarellos, J. L., Zahnle, K. J., Dobrovolskis, A. R., Hamill, P., 2002. Orbital evolution of impact ejecta from Ganymede. Icarus 160, 108–123.

Archinal, B. A., A'Hearn, M. F., Bowell, E., Conrad, A., Consolmagno, G. J., Courtin, R., Fukushima, T., Hestroffer, D., Hilton, J. L., Krasinsky, G. A., Neumann, G., Oberst, J., Seidelmann, P. K., Stooke, P., Tholen, D. J., Thomas, P. C., Williams, I. P., 2011. Report of the IAU Working Group on cartographic coordinates and rotational elements: 2009. Celestial Mech. Dyn. Astron. 109, 101–135. https://doi.org/10.1007/s10569-010-9320-4.

Arvidson, R., Guinness, E., & Lee, S., 1979. Differential aeolian redistribution rates on Mars. Nature, 278(5704), 533-535.

Baby, N. R., Stephan, K., Wagner, R., Kenkmann, T., Collins, G. C., Hauber, E., & Jaumann, R., 2022. Stratigraphic relationships of different terrain units on Ganymede and possible implications towards their evolution. No. EPSC2022-1016, Copernicus Meetings.

Becker, T., Archinal, B., Colvin, T., Davies, M., Gitlin, A., Kirk, R. L., Weller, L., 2001. Final digital global maps of Ganymede, Europa, and Callisto. Lunar Planet. Sci. Conf. XXXII, abstr. No. 2009.

Belton, M. J. S., Klaasen, K. P., Clary, M. C., Anderson, J. L., Anger, C. D., Carr, M. H., Chapman, C. R., Davies, M. E., Greeley, R., Anderson, D., Bolef, L. K., Townsend, T. E., Greenberg, R., Head, J. W. III, Neukum, G., Pilcher, C. B., Veverka, J., Gierasch, P. J., Fanale, F. P., Ingersoll, A. P., Masursky, H., Morrison, D., Pollack, J. B., 1992. The Galileo Solid-State Imaging experiment. Space Sci. Rev. 60, 413 – 455.

Benesh M., Jepsen, P. L.,1978. Voyager imaging science subsystem calibration report. Jet Propul. Lab., Pasadena, Ca.

Bierhaus, E. B., Chapman, C. R., & Merline, W. J., 2005. Secondary craters on Europa and implications for cratered surfaces. Nature, 437(7062), 1125-1127.

Bierhaus, E. B., Chapman, C. R., Merline, W. J., Brooks, S. M., Asphaug, E., 2001. Pwyll secondaries and other small craters on Europa. Icarus 153, 264–276.

Bierhaus, E. B., McEwen, A. S., Robbins, S. J., Singer, K. N., Dones L, Kirchoff, M. R., Williams, J.-P., 2018. Secondary craters and ejecta across the solar system: Populations and effects on impact-crater-based chronologies. Meteor. Planet. Sci. 53 (4), 638–671.

Bland, M. T., Showman, A. P., & Tobie, G., 2009. The orbital–thermal evolution and global expansion of Ganymede. Icarus, 200(1), 207-221.

Bland, M. T., Singer, K. N., McKinnon, W. B., & Schenk, P. M., 2017. Viscous relaxation of Ganymede's impact craters: Constraints on heat flux. Icarus, 296, 275-288.

Bottke, W. F., Marschall, F., Vokrouhlický, D., Nesvorný, D., Morbidelli, A., Deienno, R., Kirchoff, M., Marchi, S., Levison, H., 2022. Collisional evolution of the primordial Kuiper Belt, scattered disk, and Trojan populations. Lunar Planet. Sci. Conf. LIII, abstr. No. 2638.

Bottke, W. F., Morbidelli, A., Jedicke, R., Petit, J.-M., Levison, H. F., Michel, P., Metcalfe, T. S., 2002. Debiased orbital and absolute magnitude distribution of the near-Earth objects. Icarus 156, 399–433.

Cameron, M. E., Smith-Konter, B. R., Burkhard, L., Collins, G. C., Seifert, F., & Pappalardo, R. T., 2018. Morphological mapping of Ganymede: Investigating the role of strike-slip tectonics in the evolution of terrain types. Icarus, 315, 92-114.

Cameron, M. E., Smith-Konter, B. R., Collins, G. C., Patthoff, D. A., & Pappalardo, R. T., 2019. Tidal stress modeling of Ganymede: Strike-slip tectonism and Coulomb failure. Icarus, 319, 99-120.

Cameron, M. E., Smith-Konter, B. R., Collins, G. C., Patthoff, D. A., & Pappalardo, R. T., 2020. Ganymede, then and now: How past eccentricity may have altered tidally driven Coulomb failure. Journal of Geophysical Research: Planets, 125(7), e2019JE005995.

Chapman, C. R., & McKinnon, W.B., 1986. Cratering of planetary satellites. In IAU Colloq. 77: Some background about satellites, pp. 492-580.

Choblet, G., Tobie, G., Sotin, C., Kalousova, K., & Grasset, O., 2017. Heat transport in the high-pressure ice mantle of large icy moons. Icarus, 285, 252-262.

Clark, R. N., 1980. Ganymede, Europa, Callisto, and Saturn's rings: Compositional analysis from reflectance spectroscopy. Icarus, 44(2), 388-409.

Collins, G. C., Patterson, G. W., Head, J. W., Prockter, L., Pappalardo, R. T., Lucchitta, B. K., & Kay, J. P., 2013. Global geologic map of Ganymede (p. 3237). US Department of the Interior, US Geological Survey.

Crater Analysis Techniques Working Group., 1979. Standard techniques for presentation and analysis of crater size-frequency data. Icarus, 37(2), 467-474.

Danielson, G. E., Kupferman, P. N., Johnson, T. V., Soderblom, L. A., 1981. Radiometric performance of the Voyager cameras. J. Geophys. Res. 86 (A10), 8683 – 8689.

Davies, M. E., Colvin, T. R., Oberst, J., Zeitler, W., Schuster, P., Neukum, G., ... & Schubert, G., 1998. The control networks of the Galilean satellites and implications for global shape. Icarus, 135(1), 372-376.

Davies, M. E., Katayama, F. Y., 1981. Coordinates of features on the Galilean satellites. J. Geophys. Res. 86 (A10), 8635 – 8657.

Dones, L., Chapman, C. R., McKinnon, W. B., Melosh, H. J., Kirchoff, M. R., Neukum, G., Zahnle, K. J., 2009. Icy satellites of Saturn: Impact cratering and age determination. In: Dougherty, M. K., Esposito, L. W., Krimigis, S. M. (Eds.), Saturn from Cassini-Huygens. Springer Publ., Dordrecht, Netherlands, pp. 613–635.

ESA JUICE definition study report /Red Book, E. S., 2014. JUICE Jupiter ICy moons Explorer 10 Exploring the emergence of habitable worlds around gas giants, no. ESA/SRE (2014)1.

Giese, B., Wagner, R., Neukum, G., Pappalardo, R., Head, J. W., & Team, G. I., 2001. The topography of Ganymede's Arbela Sulcus. Lunar and Planetary Science XXXII, 32, abstract 1743.

Grasset, O., Dougherty, M. K., Coustenis, A., Bunce, E. J., Erd, C., Titov, D., Blanc, M., Coates, A., Drossart, P., Fletcher, L. N., Hussmann, H., Jaumann, R., Krupp, N., Lebreton, J.-P., Prieto-Ballesteros, O., Tortora, P., Tosi, F., Van Hoolst, T., 2013. JUpiter ICy moon Explorer (JUICE): an ESA mission to orbit Ganymede and to characterise the Jupiter system. Planet. Space Sci. 78, 1–21. https://doi.org/10.1016/S0032063312003777.

Guest, J. E., Bianchi, R., & Greeley, R., 1988. Geologic map of the Uruk Sulcus quadrangle of Ganymede. US Geological Survey Report, 1934.

Hartmann, W. K., 1984. Does crater „saturation equilibrium“ exist in the solar system ? Icarus 60, 56–74.

Head, J. W., Pappalardo, R. T., Collins, G., Greeley, R., & Galileo IMAGING Team., 1997, March. Tectonic resurfacing on Ganymede and its role in the formation of grooved terrain. In Lunar and Planetary Science Conference, Vol. 28, p. 535.

Head, J. W., Pappalardo, R. T., Kay, J., Collins, G., Prockter, L., Greeley, R., ... & Team, G. I., 1998, March. Cryovolcanism on Ganymede: Evidence in bright terrain from Galileo solid state imaging data. In Lunar and Planetary Science Conference, No. 1666, p. 1666.

Head, J., Pappalardo, R., Collins, G., Belton, M. J., Giese, B., Wagner, R., ... & Moore, J., 2002. Evidence for Europa-like tectonic resurfacing styles on Ganymede. Geophysical Research Letters, 29(24), 4-1.

Hiesinger, H., Jaumann, R., Neukum, G., & Head III, J. W., 2000. Ages of mare basalts on the lunar nearside. Journal of Geophysical Research: Planets, 105(E12), 29239-29275.

Hiesinger, H., Marchi, S., Schmedemann, N., Schenk, P., Pasckert, J. H., Neesemann, A., O'Brien, D. P., Kneissl, T., Ermakov, A. I., Fu, R. R., Bland, M. T., Nathues, A., Platz, T., Williams, D. A., Jaumann, R., Castillo-Rogez, J. C., Ruesch, O., Schmidt, B., Park, R. S., Preusker, F., Buczkowski, D. L., Russell, C. T., Raymond, C. A., 2016. Cratering on Ceres: Implications for its crust and avolution. Science 353, doi:10./1126/science.aaf4759.

Ivanov, B. A., Neukum, G., Bottke Jr., W. F., Hartmann, W. K., 2002. The comparison of size-frequency distributions of impact craters and asteroids and the planetary cratering rate. In: Bottke Jr., W. F., Cellino, A., Paolicchi, P., Binzel, R. P. (Eds.), Asteroids III. Univ. of Arizona Press, Tucson, Az., pp. 89–101.

Jaumann, R., Stephan, K., Wagner, R., Hussmann, H., Palumbo, P., Lucchetti, A., Postberg, F., Roatsch, T., Stark, A., 2024. Ganymede's stratigraphy and geologic evolution. In: Volwerk, M., McGrath, M., Xianzhe, J., Spohn, T. (Eds.), Ganymede. Cambridge University Press, in press.

Kay, J. E., & Head III, J. W., 1999, March. Geologic mapping of the Ganymede G8 calderas region: Evidence for cryovolcanism. In Lunar and Planetary Science Conference, p. 1103.

Kersten, E., Zubarev, A. E., Roatsch, T. Matz, K.-D., 2021.Controlled global Ganymede mosaic from Voyager and Galileo images. Planet. Space Sci. 206, https://doi.org/10.1016/j.pss.2021.105310.

Kirchoff, M. R., Barr, A., Bland, M., Bray, V., Rivera-Valentin, R. G., Schenk, P., 2024. The cratering record of Ganymede: Surface ages, impactor populations, and evolution history. In: Volwerk, M., McGrath, M., Xianzhe, J., Spohn, T. (Eds.), Ganymede. Cambridge University Press, in press.

Kirchoff, M. R., Bierhaus, E. B., Dones, L., Robbins, S. J., Singer, K. N., Wagner, R. J., Zahnle, K. J., 2018. Cratering histories in the Saturnian system. In: Schenk, P. M., Clark, R. N., Howett, C. J. A., Verbiscer, A. J., Waite, J. H. (Eds.), Enceladus and the icy moons of Saturn. Univ. of Arizona Press, Tucson, Az., pp. 267–284.

Klaasen, K. P., Clary, M. C., Janesick, J. R., 1984. Charged-coupled device television camera for NASA's Galileo mission to Jupiter. Opt. Eng. 23 (3), 334 – 342.

Kneissl, T., Michael, G. G., & Schmedemann, N., 2016. Treatment of non-sparse cratering in planetary surface dating. Icarus, 277, 187-195.

Kneissl, T., Michael, G. G., Platz, T., & Walter, S. H. G., 2015. Age determination of linear surface features using the Buffered Crater Counting approach–Case studies of the Sirenum and Fortuna Fossae graben systems on Mars. Icarus, 250, 384-394.

Kneissl, T., van Gasselt, S., & Neukum, G., 2011. Map-projection-independent crater size-frequency determination in GIS environments—New software tool for ArcGIS. Planetary and Space Science, 59(11-12), 1243-1254.

Le Feuvre, M., & Wieczorek, M. A., 2011. Nonuniform cratering of the Moon and a revised crater chronology of the inner Solar System. Icarus, 214(1), 1-20.

Lucchita, B. K., 1980. Grooved terrain on Ganymede. Icarus, 44(2), 481-501.

Marchi, S., Massironi, M., Cremonese, G., Martellato, E., Giacomini, L., & Prockter, L., 2011. The effects of the target material properties and layering on the crater chronology: The case of Raditladi and Rachmaninoff basins on Mercury. Planetary and Space Science, 59(15), 1968-1980.

Marchi, S., Mottola, S., Cremonese, Martellato, E., 2009. A new chronology for the Moon and Mercury. Astron. J. 137, 4936–4048.

Massironi, M., Cremonese, G., Marchi, S., Martellato, E., Mottola, S., & Wagner, R. J., 2009. Mercury's geochronology revised by applying Model Production Function to Mariner 10 data: Geological implications. Geophysical Research Letters, 36(21).

McEwen, A. S., Preblich, B. S., Turtle, E. P., Artemieva, N. A., Golombek, M. P., Hurst, M., ... & Christensen, P. R., 2005. The rayed crater Zunil and interpretations of small impact craters on Mars. Icarus, 176(2), 351-381.

Mckinnon, W. B., and E. M. Parmentier., 1986. Ganymede and Callisto In Satellites (J. A. Burns and M. S. Matthews, Eds.), pp. 718–763. Univ. of Arizona Press, Tucson.

McKinnon, W.B., Schenk, P.M., & Moore, J.M., 2001. Topographic and Morphologic Evidence for Flooding of Ganymede's Resurfaced Terrains by Low-Viscosity Water-Ice Lavas. Lunar and Planetary Science XXXII.

Michael, G. G., Kneissl, T., & Neesemann, A., 2016. Planetary surface dating from crater size-frequency distribution measurements: Poisson timing analysis. Icarus, 277, 279-285.

Michael, G. G., Neukum, G., 2010. Planetary surface dating from crater size-frequency distribution measurements: Partial resurfacing events and statistical uncertainty. Earth Planet. Sci. Lett. 294, 223–229.

Michael, G., & Neukum, G., 2008, March. Surface dating: Software tool for analysing crater size-frequency distributions including those showing partial resurfacing events. In 39th Annual Lunar and Planetary Science Conference, No. 1391, p. 1780.

Moore, J. M., Asphaug, E., Morrison, D., Spencer, J. R., Chapman, C. R., Bierhaus, B., ... & Pilcher, C. B., 1999. Mass movement and landform degradation on the icy Galilean satellites: Results of the Galileo nominal mission. Icarus, 140(2), 294-312.

Mueller, S., & McKinnon, W. B., 1988. Three-layered models of Ganymede and Callisto: Compositions, structures, and aspects of evolution. Icarus, 76(3), 437-464.

Murchie, S. L., & Head III, J. W., 1986. Global reorientation and its effect on tectonic patterns on Ganymede. Geophysical Research Letters, 13(4), 345-348.

Murchie, S. L., & Head, J. W., 1988. Possible breakup of dark terrain on Ganymede by large-scale shear faulting. Journal of Geophysical Research: Solid Earth, 93(B8), 8795-8824.

Nagel, K., Breuer, D., & Spohn, T., 2004. A model for the interior structure, evolution, and differentiation of Callisto. Icarus, 169(2), 402-412.

Neukum, G., & Horn, P., 1976. Effects of lava flows on lunar crater populations. The Moon, 15(3-4), 205-222.

Neukum, G., Ivanov, B. A., 1994. Crater size distributions and impact probabilities on Earth from lunar, terrestrial-type planets, and asteroid cratering data. In: Gehrels, T. (Ed.), Hazards due to comets and asteroids. Univ. of Arizona Press, Tucson, Az., pp. 359–416.

Neukum, G., Ivanov, B. A., Hartmann, W. K., 2001. Cratering records in the inner solar system in relation to the lunar reference system. Space Sci. Rev. 96, 55–86.

Neukum, G., Wagner, R., Wolf, U., Head III, J. W., Pappalardo, R. T., Klemaszewski, J. E., Greeley, R., Belton, M. J. S., Galileo SSI Team, 1998. Cratering chronology in the Jovian system and derivation of absolute ages. Lunar Planet. Sci. Conf. XXIX, abstr. No. 1742.

Nimmo, F., 2004. Dynamics of rifting and modes of extension on icy satellites. Journal of Geophysical Research: Planets, 109(E1).

Nimmo, F., & Pappalardo, R. T., 2004. Furrow flexure and ancient heat flux on Ganymede. Geophysical research letters, 31(19).

Öpik, E. J., 1960. The lunar surface as an impact counter. Monthly Notices of the Royal Astronomical Society, 120(5), 404-411.

Palumbo, P., Jaumann, R., Cremonese, G., Hoffmann, H., Debei, S., Della Corte, V., ... & Wagner, R., 2014. JANUS: the visible camera onboard the ESA JUICE mission to the Jovian system.

Pappalardo, R. T., & Collins, G. C., 2005. Strained craters on Ganymede. Journal of structural geology, 27(5), 827-838.

Pappalardo, R. T., Collins, G. C., Head, J. W. III, Helfenstein, P., McCord, T. B., Moore, J. M., Prockter, L. M., Schenk, P. M., Spencer, J. R., 2004. Ganymede. In: Bagenal, F., Dowling, T. E., McKinnon, W. B. (Eds.), Jupiter. The Planet, Satellites, and Magnetosphere. Cambridge Univ. Press, Cambridge, pp. 363-396.

Patterson, G. W., Collins, G.C., Head, J. W., Pappalardo, R. T., Prockter, L.M., Lucchitta, B. K., & Kay, J. P., 2010. Global geological mapping of Ganymede. Icarus, 207(2), 845-867.

Prockter, L. M., Head, J. W., Pappalardo, R. T., Senske, D. A., Neukum, G., Wagner, R., ... & Belton, M. J., 1998. Dark terrain on Ganymede: Geological mapping and interpretation of Galileo Regio at high resolution. Icarus, 135(1), 317-344.

Richardson, J. E., 2009. Cratering saturation and equilibrium: a new model looks at an old problem. Icarus 204, 697–715.

Riedel, C., Michael, G., Kneissl, T., Orgel, C., Hiesinger, H., & van der Bogert, C. H., 2018. A new tool to account for crater obliteration effects in crater size-frequency distribution measurements. Earth and Space Science, 5(6), 258-267.

Robbins, S. J., Riggs, J. D., Weaver, B. P., Bierhaus, E. B., Chapman, C. R., Kirchoff, M. R., ... & Gaddis, L. R., 2018. Revised recommended methods for analyzing crater size-frequency distributions. Meteoritics & Planetary Science, 53(4), 891-931.

Schenk, P. M., 2002. Thickness constraints on the icy shells of the Galilean satellites from a comparison of crater shapes. Nature, 417(6887), 419-421.

Schenk, P. M., & Moore, J. M., 1998. Geologic landforms and processes on icy satellites. In Solar System Ices, pp. 551-578. Springer, Dordrecht.

Schenk, P. M., Chapman, C. R., Zahnle, K., Moore, J. M., 2004. Ages and interiors: the cratering record of the Galilean satellites. In: Bagenal, F., Dowling, T. E., McKinnon, W. B. (Eds.), Jupiter. The planet, satellites, and magnetosphere. Cambridge Univ. Press, Cambridge, pp. 427–456.

Schenk, P. M., McKinnon, W. B., Gwynn, D., & Moore, J. M., 2001. Flooding of Ganymede's bright terrains by low-viscosity water-ice lavas. Nature, 410(6824), 57-60.

Schubert, G., Stevenson, D. J., & Ellsworth, K., 1981. Internal structures of the Galilean satellites. Icarus, 47(1), 46-59.

Shoemaker, E. M., Lucchitta, B. K., Wilhelms, D. E., Plescia, J. B., & Squyres, S. W.,1982. The geology of Ganymede. Satellites of Jupiter, 435-520.

Shoemaker, E. M., Wolfe, R. F., & Shoemaker, C. S., 1986, March. Extinct Jupiter-family comets and cratering rates on the Galilean satellites. In Lunar and Planetary Science Conference, Vol. 17, pp. 799-800.

Shoemaker, E. Wolfe, R. F., 1982. Cratering time scales for the Galilean satellites. In: Morrison, D. (Ed.), Satellites of Jupiter. Univ. of Arizona Press, Tucson, Az., pp. 277–339.

Showman, A. P., & Malhotra, R., 1997. Tidal evolution into the Laplace resonance and the resurfacing of Ganymede. Icarus, 127(1), 93-111.

Showman, A. P., Mosqueira, I., & Head III, J. W., 2004. On the resurfacing of Ganymede by liquid–water volcanism. Icarus, 172(2), 625-640.

Showman, A. P., Stevenson, D. J., & Malhotra, R., 1997. Coupled orbital and thermal evolution of Ganymede. Icarus, 129(2), 367-383.

Singer, K. N., McKinnon, W. B., Gladman, B., Greenstreet, S., Bierhaus, E. B., Stern, S. A., Parker, A. H., Robbins, S. J., Schenk, P. M., Grundy, W. M., Bray, V. J., Beyer, R. A., Binzel, R. P., Weaver, H. A., Young, L. A., Spencer, J. R., Kavelaars, J. J., Moore, J. M., Zangari, A. M., Olkin, C. B., Lauer, T. R., Lisse, C. M., Ennico, K., New Horizons Geol., Geophys. and Imaging Sci. Theme Team, New Horizons Surface Comp. Sci. Theme Team, New Horizons Ralph and LORRI Teams, 2019. Impact craters on Pluto and Charon indicate a deficit of small Kuiper belt objects. Science 363, 955–959.

Singer, K. N., McKinnon, W.B., & Nowicki, L. T., 2013. Secondary craters from large impacts on Europa and Ganymede: Ejecta size–velocity distributions on icy worlds, and the scaling of ejected blocks. Icarus, 226(1), 865-884.

Smith, B. A., Briggs, G. A., Danielson, G. E., Cook, A. F., Davies, M. E., Hunt, G. E., ... & Suomi, V. E., 1977. Voyager imaging experiment. Space Science Reviews, 21(2), 103-127.

Smith, B.A., Soderblom, L.A., Beebe, R., Joyce, J., Briggs, G., Carr, M., Collins, S.A., Cook II, A.F., Danielson, G.E., Davies, M.E., Hunt, G.E., Ingersoll, A., Johnson, T.V., Masursky, H., Morrison, D., Owen, T., Sagan, C., Shoemaker, E.M., Veverka, J., 1979b. The Galilean satellites and Jupiter – Voyager 2 imaging results. Science 206, 927–950.

Smith, B.A., Soderblom, L.A., Johnson, T.V., Ingersoll, A.P., Collins, S.A., Shoemaker, E.M., Hunt, G.E., Masursky, H., Carr, M.H., Davies, M.E., Cook, A.F., Boyce, J.M., Owen, T., Danielson, G.E., Sagan, C., Beebe, R.F., Veverka, J., McCauley, J.F., Strom, R.G., Morrison, D., Briggs, G.A., Suomi, V.E., 1979a. The Jupiter system through the eyes of Voyager 1. Science 204, 951–957.

Sohl, F., Spohn, T., Breuer, D., & Nagel, K., 2002. Implications from Galileo observations on the interior structure and chemistry of the Galilean satellites. Icarus, 157(1), 104-119.

Spaun, N. A., Head III, J. W., Pappalardo, R. T., & Galileo SSI Team., 2001, March. Scalloped depressions on Ganymede from Galileo (G28) very high-resolution imaging. In Lunar and Planetary Science Conference, p. 1448.

Spencer, J. R., 1987. Icy Galilean satellite reflectance spectra: Less ice on Ganymede and Callisto?. Icarus, 70(1), 99-110.

Squyres, S. W., 1980. Volume changes in Ganymede and Callisto and the origin of grooved terrain. Geophysical Research Letters, 7(8), 593-596.

Stephan, K., Roatsch, T., Tosi, F., Matz, K.-D., Kersten, E., Wagner, R., Palumbo, P., Poulet, F., Hussmann, H., Barabash, S., Bruzzone, L., Dougherty, M., Gladstone, R., Gurvits, L. I., Hartogh, P., Less, L., Wahlund, J.-E., Wurz, P., Witasse, O., Grasset, O., Altobelli, N., Carter, J., d'Aversa, E., Della Corte, V., Filacchione, G., Galli, A., Galluzzi, V., Gwinner, K., Hauber, E., Jaumann, R., Langevin, Y., Lucchetti, A., Migliorini, A., Piccioni, G., Solomonidou, A., Stark, A., Tobie, G., Vallat, C., van Hoolst, T., JUICE SWT Team, 2021. Regions of interest on Ganymede's and Callisto's surface as potential targets for ESA's JUICE mission. Planet. Space Sci. 208, https://doi.org/10.1016/j.pss.2021.105324.

Strom, R. G., Malhotra, R., Ito, T., Yoshida, F., Kring, D. A., 2005. The origin of planetary impactors in the inner solar system. Science 309, 1847–1850.

Strom, R. G., Marchi, S., & Malhotra, R., 2018. Ceres and the terrestrial planets impact cratering record. Icarus, 302, 104-108.

Wagner, R. J., Schmedemann, N., Werner, S. C., Head, J. W., Stephan, K., Krohn, K., ... & Palumbo, P., 2019, January. Ray Craters as Stratigraphic Markers in Ganymede's Geologic History. In Geophysical Research Abstracts, Vol. 21.

Wagner, R. J., Schmedemann, N., Werner, S. C., Ivanov, B. A., Stephan, K., Jaumann, R., Palumbo, P., 2017. The cratering record of Ganymede and the origin of potential impactors: open issues. Europ. Planet. Sci. Congr. 2017, abstr. No. EPSC2017-470.

Wagner, R., Head III, J. W., Wolf, U., Neukum, G., 2010. Lunar red spots: Stratigraphic sequence and ages of domes and plains in the Hansteen and Helmet regions on the lunar nearside. J. Geophys. Res. 115, doi:10.1029/2009JE003359.

Wagner, R., Stephan, K., Schmedemann, N., Werner, S. C., Hoffmann, H., Roatsch, T., ... & Palumbo, P., 2018. The large bright ray crater Osiris on Ganymede: its age, role as a potential time-stratigraphic marker, and target for detailed imaging by the JUICE/JANUS Camera. EPSC2018-855.

Werner, S. C., Ivanov, B. A., 2015. Exogenic dynamics, cratering, and surface ages. In: T. Spohn (Ed.), Treatise on Geophysics, Vol. 10 – Planets and Moons. Elsevier B. V., Amsterdam/NL, pp. 327–365.

Wilhelms, D. E., 1997. Geologic map of the Osiris (Jg-12) and Apsu Sulci (Jg-13) Quadrangles of Ganymede, No. 2442.

Woronow, A., 1978. A general cratering-history model and its implications for the lunar highlands. Icarus, 34(1), 76-88.

Xu, L., Hirata, N., Miyamoto, H., 2017. Ray craters on Ganymede: Implications for cratering apex-antapex asymmetry and surface modification processes. Icarus 295. 140-148.

Zahnle, K., Alvarellos, J. L., Dobrovolskis, A., Hamill, P., 2008. Secondary and sesquinary craters on Europa. Icarus 194, 660–674.

Zahnle, K., Dones, L., Levison, H. F., 1998. Cratering ages on the Galilean satellites. Icarus 136, 202–222.

Zahnle, K., Schenk, P., Levison, H., Dones, L., 2003. Cratering rates in the outer Solar System. Icarus 163, 263–289.

Zubarev, A. E., Nadezhdina, I. E., Brusnikin, E. S., Karachevtseva, I. P., Oberst, J., 2016. A technique for processing planetary images with heterogeneous characteristics for estimating geodetic parameters of celestial bodies with the example of Ganymede. Sol. Syst. Res. 50 (5), 352 – 360. https://doi.org/10.1134/S0038094616050087.

Zubarev, A., Nadezhdina, I., Oberst, J., Hussman, H., Stark, A., 2015. New Ganymede control point network and global shape model. Planet. Space Sci. 117, 246–249. https://doi.org/10.1016/S0032063314002007.

Zuber, M. T., & Parmentier, E. M., 1984. A geometric analysis of surface deformation: Implications for the tectonic evolution of Ganymede. Icarus, 60(1), 200.

3 Polygonal impact craters on Ganymede

This chapter has been accepted to be published as peer-reviewed article as:

N. R. Baby, T. Kenkmann, K. Stephan, R.J. Wagner (2024): Polygonal impact craters on Ganymede. Meteoritics and Planetary Science.

3.1 Abstract

Polygonal impact craters (PICs) are unique geological features observed on various planetary bodies, and constitute a small percentage of the impact crater population. This study focuses on PICs on Ganymede, where no such craters have been investigated so far. Here we present the distribution of PICs, examine their morphological characteristics, investigate the causes for their polygonal shapes, and discuss the factors that support their formation. We identified and analyzed 459 PICs on Ganymede with complex crater morphologies. They are widely distributed across the moon, and occur on both dark and light terrain. Our analysis revealed that the majority of orientations of straight rim segments align parallel or subparallel to adjacent tectonic linear features. There is at least one tectonic linear orientation adjacent to PICs, even in dark cratered terrains. Based on the comparison of the number of PICs and tectonic linear features Ganymede is believed to have undergone more intense tectonic activity than other icy bodies like Ceres and Dione, where PICs where described. The presence of numerous PICs on Ganymede suggests that surface lineations and grooves are expressions of fractures that form zones of weakness in the ice crust that got reactivated during impact cratering.

3.2 Introduction

3.2.1 Ganymede's geology

Ganymede, the largest planetary satellite of the Solar System is a differentiated icy moon with an inner rocky core, an icy mantle with different layers that are believed to be liquid and an icy crust. The bulk composition of Ganymede is comprised of approximately 60% rock and 40% ice (Pappalardo et al., 2004). Approximately 35% of the surface is densely cratered, low albedo area, known as dark terrain. It is considered to represent the oldest preserved surface. This terrain is crosscut by tectonically active, younger, brighter, and less densely cratered terrain called light terrain, which constitutes approximately 65% of the surface (Shoemaker et al., 1982, Collins et al., 2000, Schenk et al., 2001). The light terrain is sculptured by grooves and ridges to various degrees. The aligned features are believed to

represent fault scarps of normal faults and graben structures but some have been formed by strike-slip transpressional and transtensional faulting. Lineated light terrain may also have formed by some sort of spreading (Collins et al., 1998). Owing to its relief the light terrain can be subdivided into several subunits with slightly different crater densities (Baby et al., 2023). Dark terrain is mainly found as cratered terrain while at some regions it is also highly lineated. These dark lineated terrains have intermediate ages between those of the dark cratered terrain and the light terrain and may indicate the beginning of extensional faulting and break-up of the dark terrain (Patterson et al., 2010; Baby et al., 2023). The major tectonic features observed on dark terrain are furrows, which are interpreted as remnants from large impact events, (Schenk and McKinnon, 1987; Zuber and Parmentier, 1984, Hirata et al., 2020) and minor tectonic features in the form of fractures (Rossi et al. 2022). It is believed that a large number of impact craters were destroyed during resurfacing activities on Ganymede.

3.2.2 Polygonal impact craters (PICs)

Polygonal impact craters (PICs) have at least one straight rim segment in planform (Beddingfield et al., 2016, Beddingfield and Cartwright, 2020). Studies distinguishing PICs from circular impact craters go back to the 1960s. PICs constitute a small fraction of all impact craters and they exist on both rocky and icy planetary bodies of the solar system (Öhman, 2010). For example, on Earth, 208 impact craters were discovered and confirmed so far (Gottwald et al. 2020; Kenkmann, 2021). Among those, 14 craters or 7% were identified as PICs including the well-known quadrangular Meteor Crater of Arizona (Shoemaker et al., 1963; Kumar and Kring, 2008; Poelchau et al. 2009) and the hexagonal Söderfjärden crater of Finland (Talvitie et al. 1975; Abels 2003; Gottwald et al. 2020).

3.2.3 PICs on icy bodies in the asteroid belt and outer solar system

PICs have been reported from the asteroid Ceres and many icy bodies of the outer solar system (e.g., Buczkowski et al., 2016; Porco et al., 2005). Ceres has a low albedo surface that is enriched in ammoniated phyllosilicates, salts and organics (De Sanctis et al., 2015; Stephan et al., 2019) and is assumed to host significant amounts of water ice in its subsurface (Prettyman et al., 2017). Ceres shows a larger number of PICs at its northern hemisphere in comparison to the southern latitudes (Otto et al., 2016). PICs on Ceres mainly have hexagonal shapes with their adjacent straight rim segments subtending an

average angle of about 121.99º (Zeilnhofer and Barlow, 2020). During the Voyager missions, PICs were identified on numerous icy moons in the outer solar system. A detailed study on PICs was done during Galileo and Cassini missions. Of the Jovian satellites, Callisto shows small craters with diameters of 7 km and less that have polygonal shapes in planform. They exhibit a range of degradation states starting from simple-bowl shaped fresh craters, which often have high-albedo ejecta to highly eroded craters with discontinuous rims and lack of ejecta blanket (Greeley et al., 2000). On Europa, the largest and youngest crater, Amergin of the trailing hemisphere has a polygonal shape that is controlled by preexisting tectonic linear features in that area (Figueredo and Greeley, 2004). To our knowledge PICs have not been reported from Ganymede so far.

Fresh craters of the Saturnian moon Rhea were identified to have strong polygonal outlines (Smith et al., 1981, Moore et al., 1985). PICs on Tethys show the highest concentration in/near Ithaca Chasma, which is indicative of a high degree of subsurface fracturing (Ferguson et al., 2020). On Dione, many of the craters identified from Voyager data have polygonal rims (Moore, 1984). A detailed study by Beddingfield et al. (2016) showed that PICs are abundant both within the wispy and non-wispy terrains, where in the non-wispy terrain a lesser number of fractures were found. PICs were also identified on Iapetus (Porco et al., 2005; Denk et al. 2005; Singer and McKinnon, 2011). In case of Titan, the Selk crater appears polygonal in outline and its two straight rim segments have azimuths that align parallel to the planes of weakness that existed in the crust prior to the existence of the crater (Soderblom et al., 2010). On Enceladus, square-shaped PICs (2 km in diameter) were observed in subdued cratered plains of the north polar region, where the subdued troughs align parallel with straight rim segments of these PICs (Crow-Willard and Pappalardo, 2015). Through examination of Mima's global mosaic, PICs were identified, though they remain unstudied to date.

On the Uranian moon Miranda, 14 PICs were confirmed and identified as an important indicator of subtle and non-visible fracture systems (Beddingfield and Cartwright, 2020). On Ariel, many of craters are polygonal in outline and their straight segments trend parallels the major structural trends (Plescia, 1987). On Oberon, many of the craters with diameters of less than 100 km were identified as polygonal in shape (e.g., the large crater Hamlet) (Plescia, 1987). The lack of sufficient data for Umbriel and Titania limited detailed studies on them. However, since both are highly cratered and contain lineated features like the other Uranian moons the chances for finding PICs are not negligible. On Charon, Pluto´s companion, PICs are present within the fractured and rilled terrain of Vulcan Planitia, as

well as to the north and south, in close proximity to Clark Montes. Additionally, PICs have been identified to the east of Kubrick Mons, where the straight rim segments run parallel to the fracture systems in that area (Beddingfield et al., 2020). All the above examples suggest that PICs are common on most of the celestial bodies of Outer Solar system.

3.2.4 Possible models for PIC formation

Deviations from circular shape for any impact crater depend on either the angle of impact, the velocity of the impacting body, the size and shape of the impacting body and/or target body heterogeneity (Eppler et al., 1983). Additionally, topography of target body, particularly, impacting into slope can give rise to asymmetrical craters (Aschauer and Kenkmann, 2017).

3.2.4.1 Earlier works on formation mechanism for PICs

Ideally, vertical impacts of spherical object into homogenous target body would give rise to circular craters (Öpik, 1969). However, cratering tests conducted by Darling (1948) on basalt found that a joint fabric of the parent rock had control on the development of straight rim segments for crater. Similarly, cratering experiments conducted on Buckboard Mesa at the Nevada Test Site into basaltic rocks resulted in PIC formation (Johnson, 1962). Later, experiment conducted by Gault et al. (1968) at the NASA Ames Vertical Gun Range showed that crater impacted into a target with two perpendicular joint sets would give rise to square-shaped or hexagonal shaped PIC, where its diagonals run parallel to the joints. All these laboratory experiments show that already existing linear features of rock influence the rims of the crater when it is emplaced.

The effect of projectile shape on the final crater morphology is negligible compared to other factors such as impact angle, velocity, and target properties (Anderson et al., 2003; Pierazzo & Collins, 2004). For simple craters, the crater rim attains the straight rim segments during the excavation stage (Schultz, 1976; Eppler et al., 1983; Poelchau et al., 2009; Watters et al., 2011; Beddingfield et al., 2016). Poelchau et al. (2009) found that it is roughly 1.4 times easier to excavate a crater parallel to the joints than at 45° angle to the joint planes. This enlarges the transient cavity along the zones of weakness that trend along the diagonals of a quadrangular crater such as Meteor crater. The straight rim segments of such simple craters thus trend at 45° to the zones of weakness. In contrast for complex craters, the crater rim attains straight segments during the modification stage via slumping or normal faulting

along the pre-existing fractures within crater wall (Eppler et al., 1983; Schultz, 1976; Beddingfield et al., 2016). Thus, the straight rim segments trend parallel to the crustal zones (joints, faults) of weakness. Due to the reduced spatial resolution of remote sensed data on Ganymede, almost all described PICs belong to the group of complex craters so that the polygonality should be governed by the crater modification stage rather than crater excavation.

Here we report on polygonal craters on Ganymede that have been discovered on both light and dark terrains. The presence of polygonal impact craters (PICs) is studied in relation to the linear features on the dark and light terrain. We will present the distribution of PICs across Ganymede, describe their morphological characteristics and their genetic relationship with tectonic linear features. The formation of PICs is discussed in the light of target material characteristics and gravitational influences.

3.3 Methodology

3.3.1 Data

For mapping PICs on the entire Ganymede surface, we used the new global mosaic, which combines the best high-resolution images from Voyager 1, Voyager 2, Galileo, and Juno spacecrafts (Kersten et al., 2022). Juno images were obtained on 7th June 2021 during Juno's closest approach with Ganymede at an altitude of 1044 km at the perijove 34 using wide-angle camera (Ravine et al., 2022; Hansen et al., 2022). JunoCam captured comparatively better illuminated and slightly higher resolution images between longitudes 40°W and 25°E (1 km/pxl), than those obtained from Voyager 1+2 and Galileo spacecrafts (Hansen et al., 2022). So, the available global mosaic has integrated images with spatial resolutions starting from 100 m/pxl to 10 km/pxl (Kersten et al., 2021). We find that resolutions coarser 5 km/pxl are not sufficient to identify or digitize PICs. Images with extreme illumination conditions such as emission, incidence and phase angles smaller than 15° and larger than 75° were excluded from this study in order to minimize effects onto the identification of PICs. Although images with relatively large illumination angles causing shadows still enable the identification of straight rims of PICs on Ganymede given the maximum topographic differences of 1 km, particularly, smaller angles significantly reduce topographic image information and thus limit the investigation of characteristics of local surface features (Collins et al., 2013, Stephan et al., 2021).

3.3.2 PIC identification and analysis

We conducted a visual inspection of craters to identify potential straight sides as opposed to arcs within each crater. An edge that appears straight and terminates at a vertex point is deemed a straight rim segment. Therefore, a crater with multiple straight rim segments is characterized by distinct azimuths and separation by vertices. We mapped all the craters that have at least one straight rim segment in plane view. Most of the previous studies considered PICs as those having at least two straight segments with an angle subtended between them (Öhman et al., 2008; Aittola et al., 2010; Weihs et al., 2015; Neidhart et al., 2017; Dasgupta et al., 2019; Zeilnhofer and Barlow, 2020, Weber et al., 2022). But since single straight rim segment of a crater could also reveal the relationship with adjacent linear features, it is unavoidable to map them. This is supported by the studies from Beddingfield et al., (2016, 2020, 2022).

We identified and mapped 459 PICs across Ganymede. Those PICs, which were crosscut by other craters or terrains are not considered for the study. Mapped PICs have diameters ranging from 5 km to 153 km. In regions, where the resolution is larger than 4 km/pxl, PICs identification was restricted to only those craters that have a somewhat larger diameter. PICs with 5 km diameter are mostly taken from the higher resolution images whose resolution is better than 100 m/pxl. The crater rims were mapped manually using ArcGIS 10.7. To ensure accurate diameter measurement and minimize distortion during analysis of straight rim segments, each of the PICs to be analyzed is projected in the center. For PICs in areas poleward of 60°, the global mosaic has been re-projected into stereographic projection and centered into each crater. For the other areas mapping has been carried out in equidistant cylindrical projection (Plate Carree projection). Morphometrical measurements like diameter, perimeter, area, azimuths, number of straight segments and length of straight segments are measured using ArcGIS. Moreover, the orientation of lineations are determined in the vicinity of a crater. These geometrical measurements were obtained to characterize (i) the angularity, (ii) the maximum crater diameter for polygonality, and, (iii) the dependence of straight rim orientation to the orientation of linear features.

Angularity is a measure of how much a polygon deviates from an ideal circular shape. In case of impact craters, angularity refers to the degree to which the shape of PIC deviates from that of an ideal circular impact crater with same area as the polygon. It can be formulated as the following:

$$\text{Angularity} = (P_p/A_p) / (P_c/A_p) \quad \text{(Eq. 3.1)}$$

where, P_p is perimeter of polygonal crater, A_p is area of polygonal crater, P_c is perimeter enclosed if it is a circular crater.

The higher the angularity value, the more angular the polygon is, and hence the more it deviates from the expected circular crater shape. In general, the angularity of PICs depends on the number of sides, the length of each side, and the angles between the straight rim segments.

Rose diagrams were prepared with QGIS to statistically illustrate the orientation distribution of the straight rim segments of PICs. The major trend of straight rim segments of each of PICs are discernible when applying weighting on the length. We utilized a bin count of 16, dividing the 360-degree circle into 16 equal intervals, each spanning 22.5 degrees. In the case of a circular impact crater, the rose diagram also forms a circle, with all directions being nearly equal. But in the case of PICs, straight rim segments and their orientation is analyzed based on the longest directional value.

3.4 Results

3.4.1 Morphology of PICs

Most of the mapped PICs on Ganymede deviate from ideal polygonal shapes. They are mostly seen as imperfect squares, pentagons, hexagons etc. In other cases, some PICs have few numbers of well-developed straight rim segments and rest of the sides appear more rounded in appearance. Figures 3.1 and 3.2 show typical examples of PICs observed on Ganymede and imaged by the Galileo spacecraft.

3.4.1.1 Achelous and Gula

Achelous is a 35 km diameter fresh polygonal pedestal / rampart-like impact crater located at ~62°N, 12°W of north pole side (Fig. 3.1 a). It is impacted on light grooved terrain of Aquarius Sulcus. The availability of a high-resolution image of ~178 m/pxl enabled to study its polygonal morphology in detail. Its fluidized ejecta is radial in shape and has radial extent of ~17 km (Jones et al., 2003; Boyce et al., 2010). Jones et al. (2003) suggested that it has a double-layered morphology with the outer discontinuous ejecta deposited beyond the pedestal deposit. The continuous ejecta corresponds to the margin of a palimpsest. The double layered nature results from the presence of near-surface target volatiles rather than

atmospheric effects (Jones et al., 2003). Achelous has seven straight rim segments (Fig. 3.1 b). Gula is another ~ 35 km diameter crater located north of Achelous. Unlike Achelous, it does not have any visible pedestal deposits surrounding it while it is punctured by secondary craters emanating from Achelous. Gula has two straight rim segments and other parts of the rim appear to be rounded in shape (Fig. 3.1 b). The rose diagrams display the major orientations of their straight rim segments with respect to adjacent linear features.

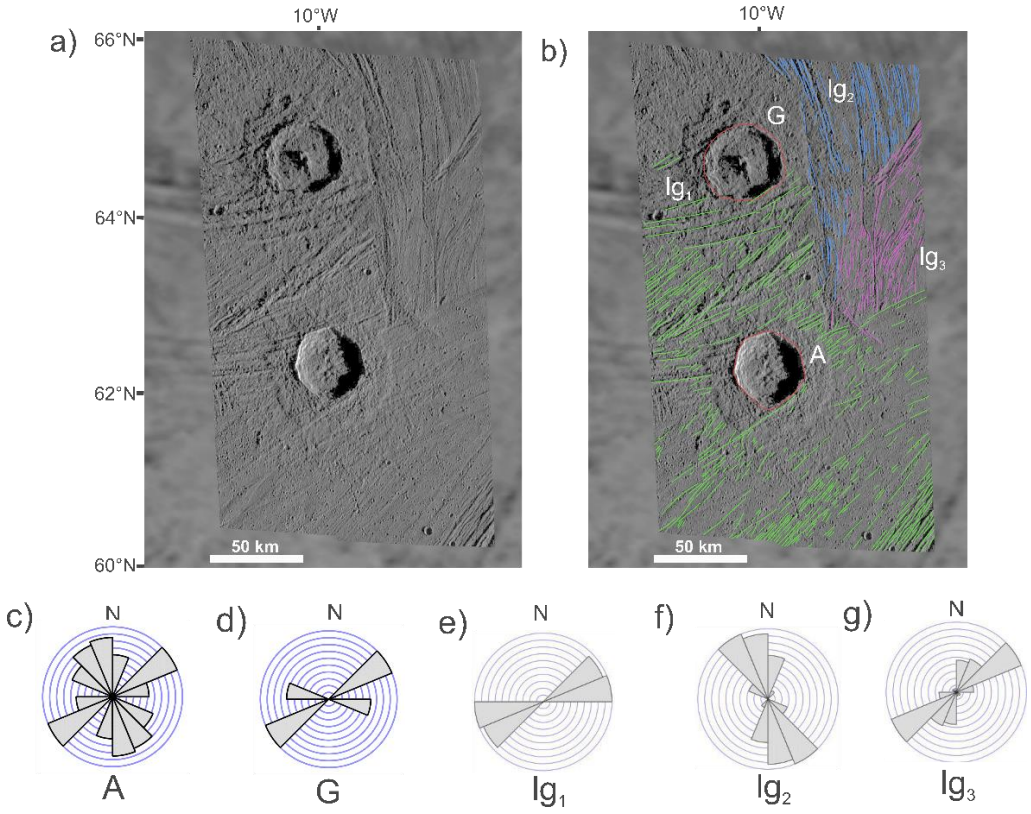

Figure 3.1: (a) SSI observation G7GSACHELS01 showing the PIC Achelous (b) Lineament orientation mapping in the vicinity of PICs Achelous and Gula (red). "A" denotes Achelous and "G" denotes Gula (c) Rose diagrams showing the orientation of straight rim segments of Achelous and, (d) Gula. (e) Rose diagram showing orientation of lineaments in terrain unit lg_1. (f) Rose diagram showing orientation of lineaments in terrain unit lg_2. (g) Rose diagram showing orientation of lineaments in terrain unit lg_3. Note that the names of the terrain units are followed according to the mapping scheme of Patterson et al., 2010.

The dominant orientation of the longest straight rim segments of Achelous and Gula is in E-W direction (Fig. 3.1 c and 3.1 d). Three major light grooved terrains are found in and near Achelous and Gula and they are; older terrain unit lg_1, intermediate aged lg_2 and the youngest lg_3 (the mapping scheme is followed from Patterson et al., 2010). The relative age determination is done based on the principle of cross-cutting relationship. Gula and Achelous are located on the oldest unit lg_1 whose lineaments trends in a single direction,

that is in NE-SW direction (Fig.3.1 e). While the dominant orientation of lg_2 is in NW-SE direction (Fig.3.1 f) and lg_3 is in NE-SW direction (Fig.3.1 g). Among these 7 straight rim segments, 2 of them aligns parallel with the lineaments while the other 5 segments are in ~45° angle with rim segments that parallel the lineaments. Like Achelous, the lineaments adjacent to Gula also trend in NE-SW direction. One of its straight rim segments clearly aligns parallel with the adjacent lineaments.

We found that there is no/negligible influence of lg_2 and lg_3 lineaments in controlling their rim (Fig. 3.1 b). Namely, Gula is located at ~13 km away from the nearest lineament of lg_2, which clearly have not influenced much in development of straight rim segment. In terms of length, the longest ones are those straight rim segments that are parallel with the lineaments. There are no noticeable radial and circumferential fractures associated with PICs. Also, lineaments are found extending into the pedestal ejecta of Achelous, indicating the influence of lineaments.

3.4.1.2 Kittu

Kittu is a ~18 km diameter PIC, located in Ganymede´s trailing hemisphere. The crater has a dark ejecta with a "butterfly wing" pattern extending for a long distance (Fig. 3.2 a) indicating a low impact angle < 10-15°, with respect to the target surface (Melosh, 1989). Earlier studies suggested that it contains subsurface chondritic silicates, which got exposed during the impact event (Hartmann, 1980). From spectral analysis, their dark ejecta was interpreted to contain more non-ice material and a higher concentration of CO_2 (Hibbitts et al., 2003, Hibbitts, 2023, Stephan et al., 2024).

The image of Kittu used for the study has a resolution of 145 m/pxl. Kittu is identified with six straight rim segments (Fig. 3.2 b), whose two longest straight segments have NW-SE orientation (Fig. 3.2 c). Kittu is emplaced at the border of two light grooved terrains lg_1 and lg_2 (mapping scheme followed from Patterson et al., 2010), where a major portion of the crater is placed onto the younger terrain unit lg_2. From this stratigraphic relationship, it is clear that Kittu represents the youngest unit. The lineaments in lg_2 trends in NW-SE direction (Fig. 3.2 d) while lineaments in lg_1 trends in NE-SW direction (Fig. 3.2 e).

The rose diagram of Kittu shows that the longest straight rim segments are the ones that aligned parallel to the lineaments. Since Kittu is at the interface between two differently oriented terrains, we find the rims got aligned parallel with the ridges or grooves of both terrains. Usually for a very oblique impact <15°m measured from the surface, an elliptical crater is formed but, here, where it is incident on grooved terrain, the elongation of crater

rim is obviously suppressed. There are no noticeable radial and circumferential fractures associated with this PIC. Also, secondary craters and bright ejecta restrict further analysis of its surroundings.

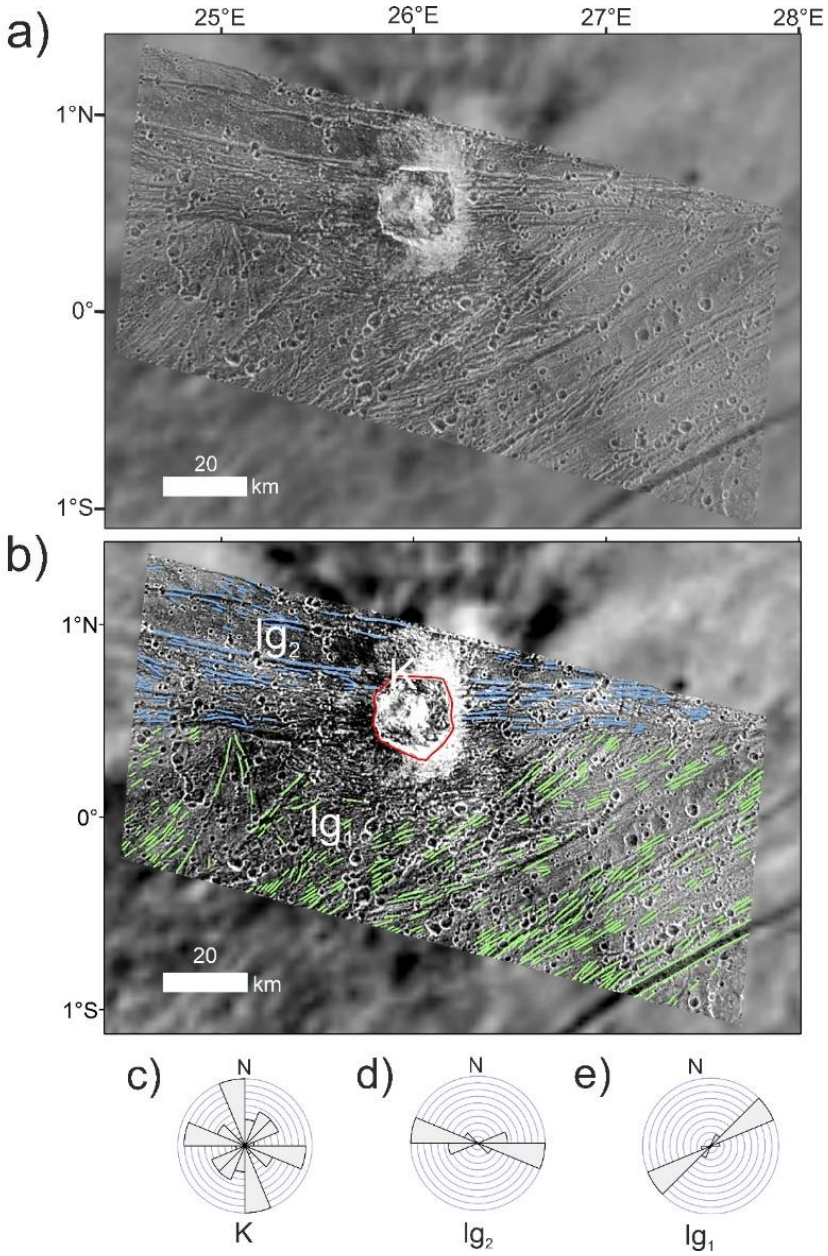

Figure 3.2:(a) SSI observation G7GSKITTU01 showing the PIC Kittu. (b) Lineament orientation mapping in the surrounding of PIC Kittu (K). (c) Rose diagram showing orientation of straight rim segments of Kittu. (d) Rose diagram showing orientation of lineaments in terrain unit lg1. Note that the names of the terrain units are followed according to the mapping scheme of Patterson et al., 2010.

3.4.2 Distribution of different types of PICs across Ganymede

The mapped PICs show an uneven distribution across Ganymede (Fig. 3.3). This is primarily caused by the lack of equally resolved remote sensing data. Because of this, PICs are hardly noticed in regions with resolutions of 5 km/pixel, which is the lowest resolution at which two PICs with diameters of 145 km and 119 km are mapped. For instance, a very few PICs are mapped from regions 60° N and higher and longitudes between 60° E and 140° E (except regions down to 60° S).

Among the 459 PICs identified and mapped, about 215 (47%) were found on dark terrain, 210 on light terrain (46%), 33 bordering between dark and light terrain (7 %) and 1 PIC on reticulate terrain (Fig. 3.4). As the dark terrain covers 35% of Ganymede´s surface the number of PICs on this terrain appears high. However, one has to consider here that the average crater density is higher on dark terrain than on light terrain increasing the absolute number of PICs. With regard to the diameter, those craters between 20 to 40 km diameter are most frequent among PICs and they are equally present on dark and light terrains (Fig. 3.4). This is the same with PICs found at borders between dark and light terrains. The number of PICs gradually decreases with increasing diameters. This, however, also reflects the circumstance that the absolute number of craters decreases with increasing diameter. The relatively low number of PICs with less than 20 km diameter is biased by resolutions of images that ranges from 100 m/pxl to lower than 4 km/pxl (Fig. 3.4).

Most of the PICs identified have either a pit, a peak or a dome as central features and fall in the category of complex craters (Fig. 3.5). Among the 459 PICs identified and mapped, about 157 PICs' have a central peak, 124 of them have a pit, and 5 of them have a central dome. About 26 PICs were marked as 'none' which expresses that any central feature is missing. However, these craters are too large to denote them as simple craters. About 147 PICs were marked as 'unknown' whose central features were not able to be detected as peak, pit or lack any central feature due to insufficient resolution. The maximum number of central peak PICs are found between 10 and 25 km diameters and gradually decreases in number with increasing diameters. In contrast, PICs with a central pit are larger on average, and the maximum number are found between 45 and 85 km crater diameter. Dome PICs are fewer in number and their diameters starts from 110 and larger. For PICs without discernable central feature, the diameters range between 20 and 60 km. The largest detected PIC has a diameter of 153 km and has a dome as central feature. The smallest detected PIC is 5 km in diameter and contains a central peak.

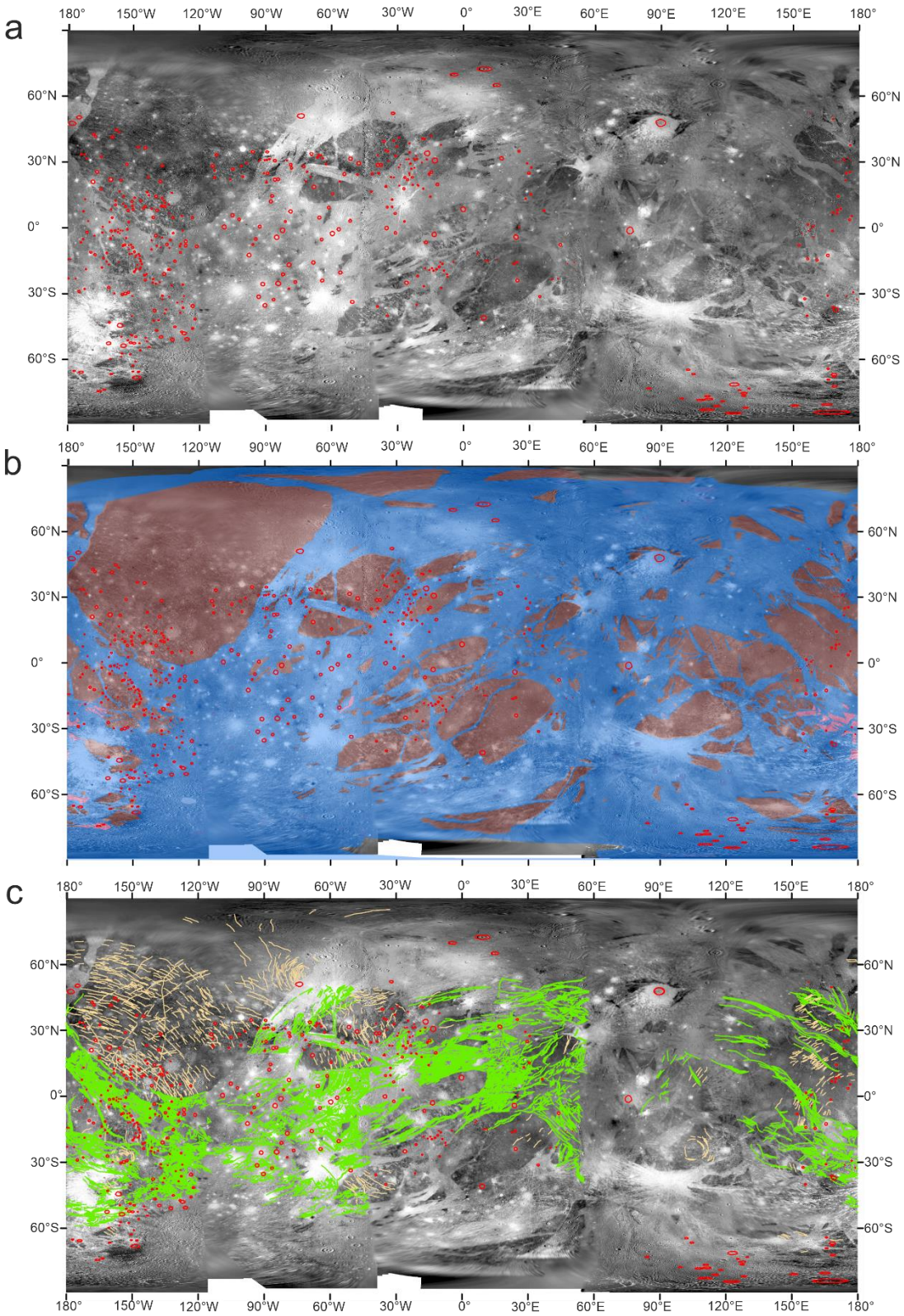

Figure 3.3:(a) Global base map of Ganymede in equidistant cylindrical projection (from Kersten et al., 2022) showing all mapped PICs (red). (b) The categorization of PICs based on the terrain type in which they are found: dark terrain (brown), light terrain (blue), and reticulate terrain (pink), according to the classification by Collins et al., 2013. (c) PICs in association with all the linear features (green and orange). The linear features on light terrain are mainly grooves (green, from Rossi et al., 2020) and linear features on dark terrain are mainly furrows (orange, from Collins et al., 2013).

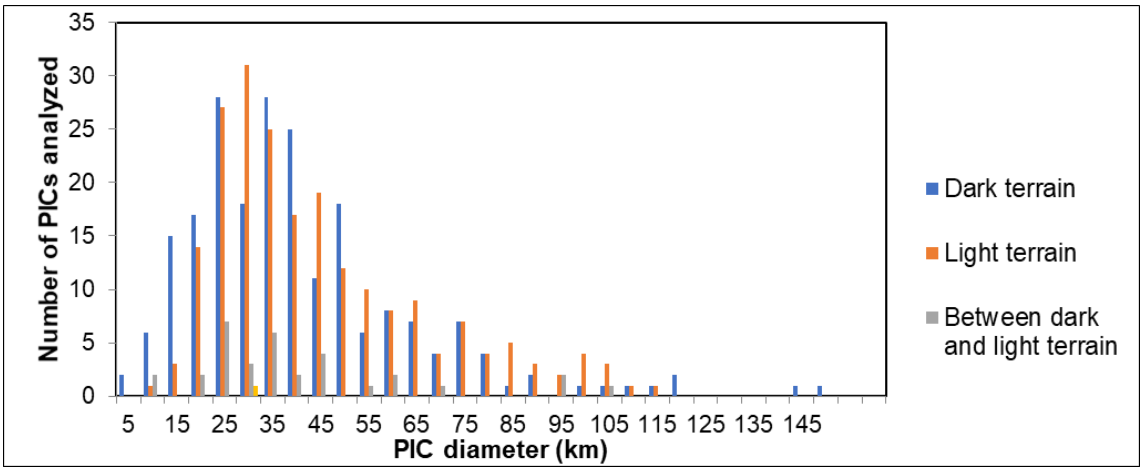

Figure 3.4: Histogram showing the diameter range of PICs in dark terrain, light terrain, reticulate terrain and those located between dark terrain and light terrain.

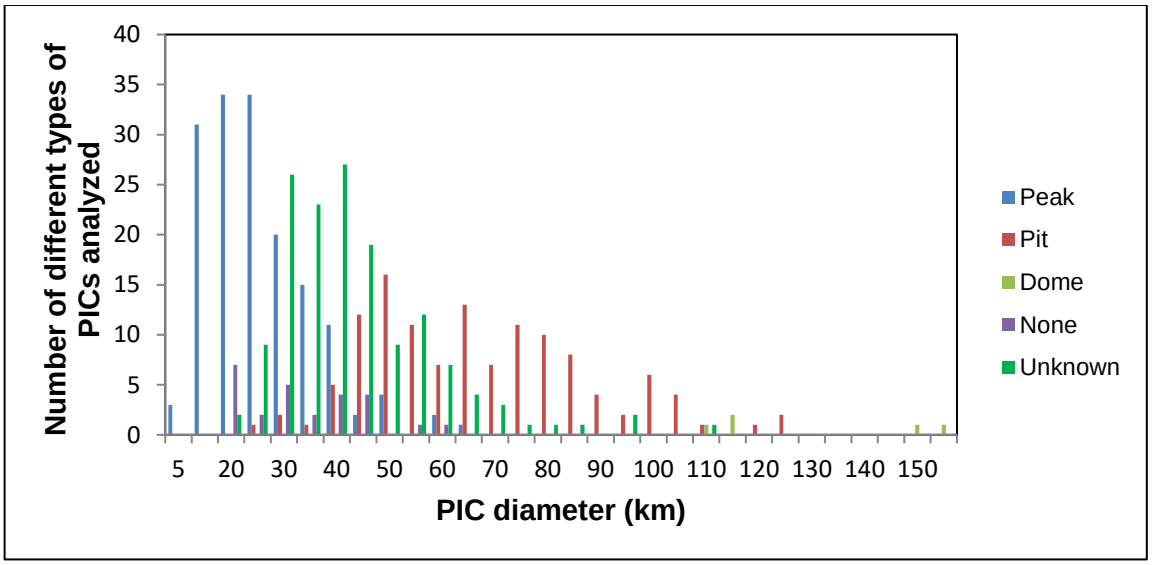

Figure 3.5: Histogram showing the distribution of different types of PICs across Ganymede. 'None' is a category that lacks any central feature and 'unknown' represents a group of craters whose central feature could not be detected due to low resolution.

3.4.3 Number of segments

Figure 3.6 shows the number of straight segments of the analyzed PICs. Polygonal craters with 2 straight segments are most frequent, followed by those with hexagonal shape (6 segments). PICs with just 1 and with 9 linear segments are rare. Some of the analyzed craters have a square, pentagonal, or octagonal shapes while others have few straight segments that alternate with rounded sections of the perimeter.

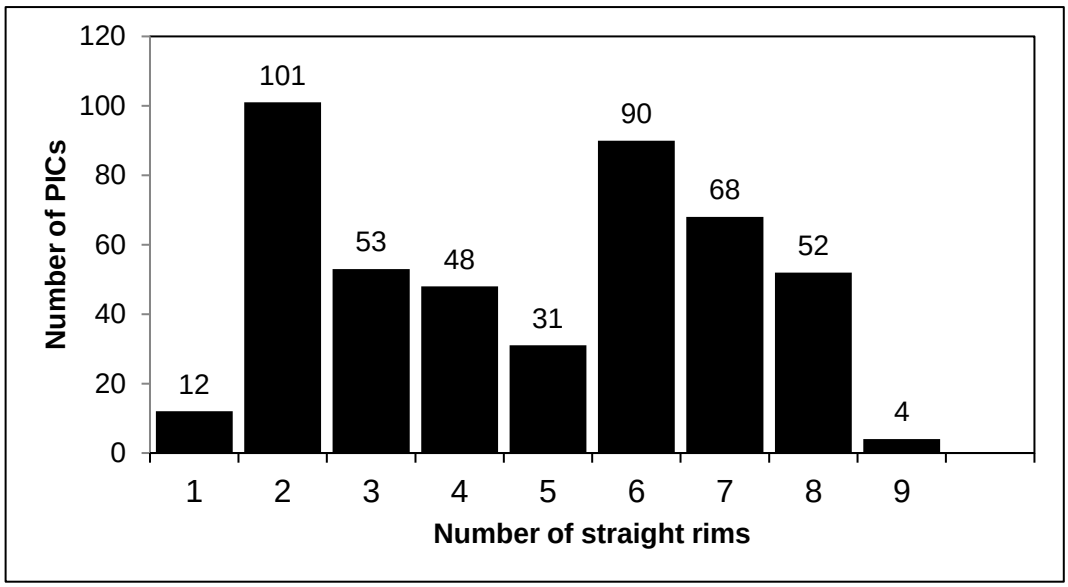

Figure 3.6: Histogram showing the number of straight segments possessed by different number of PICs.

3.4.4 Angularity

The deviation from a circular planform was quantified using an "Angularity" factor. For definition we refer to the Methods section. Figure 3.7 shows the angularity values as a function of the diameter of PICs, subdivided for those identified as having peak, pit, dome, none, and unknown central features. The majority of the angularity values lie between 1.0 and 1.1, followed by values between 1.1 and 1.2, whereas 1.0 represents a circle. The density of points decreases from an angularity value of 1 towards an angularity value of 1.6. PICs that lie close to 1 still possess one or more straight segments, but the overall deviation from circularity is low. An angularity value close to 1.0 does not necessarily mean

that a PIC has one or two straight segments. The highest angularity values were observed for a few PICs with smaller diameters.

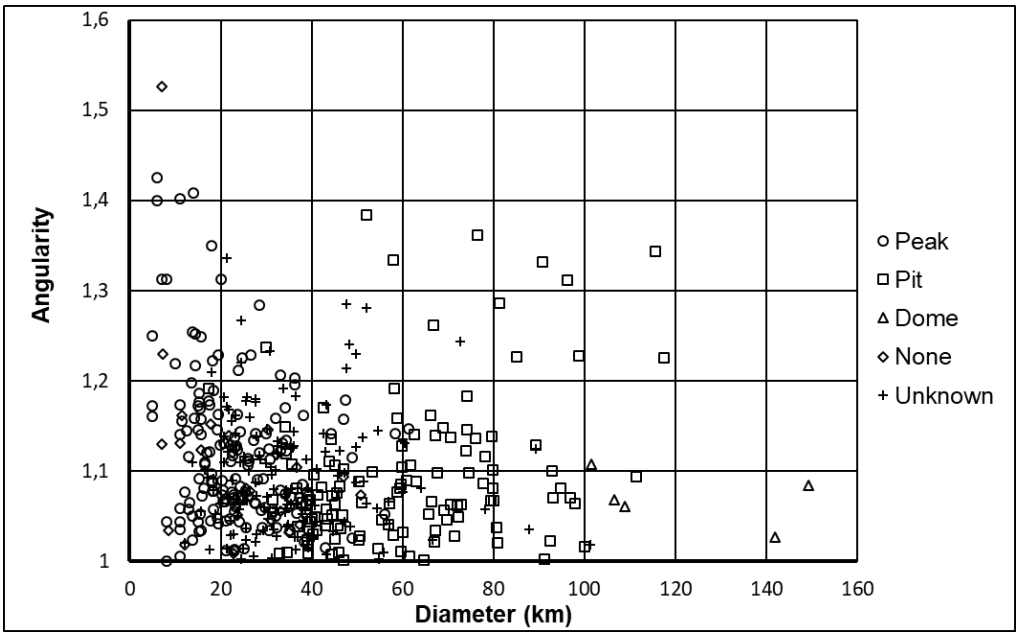

Figure 3.7: The graph displays the relationship between the diameter and angularity of the mapped PICs, whose central features are identified as peak, pit, dome, none and unknown.

3.4.5 Linear features and influence on PICs

Since two thirds of Ganymede's surface are dominated by light terrain (Fig. 3.3 a) (Pappalardo et al., 2004), which consists of ridges and grooves, the influence of these tectonic linear features on the morphology of the craters is obvious. However, as the density of PICs on dark terrain is apparently not less or even higher to that of the light terrain, the structurally controlling factors on dark terrain are likewise investigated. For this, we compare the major orientations of PICs straight segments and tectonic linear features of dark and light terrains from the sub-Jovian and the anti-Jovian hemispheres (Fig. 3.8). We utilize the regional groove system map of light terrain (60°N-60°S) as presented by Rossi et al. (2020) (Fig. 3.3 c). Similarly, to understand the structurally controlling factors on dark terrain, we utilize the global geological map as presented by Collins et al. (2013) in comparison to our mapped PICs.

In the light terrain, the grooves (Fig. 3.3 c) have a preferred orientation and are densely concentrated in regions of younger light terrain (Fig. 3.3 b). The dominant orientation of grooves from sub-Jovian and anti-Jovian hemispheres are in opposite directions: grooves in the sub-Jovian hemisphere have a dominant trend in NE-SW direction while the grooves

in anti-Jovian hemisphere have a dominant trend in NW-SE direction (Rossi et al., 2020). PICs are dominantly found in areas surrounding or within the grooved terrain. Particularly, from the available mapped global distribution of PICs, we find higher PIC density in regions within and around Uruk sulcus region (Fig. 3.3). This region is interpreted to be affected by transpressional strike-slip tectonics (Rossi et al., 2018). Figure 3.8 displays the orientation of a straight rim segments and the orientation of an adjacent linear feature. Data points that fall on the full diagonal line indicate that the orientation of a straight rim segment is parallel to that of nearby grooves. Data points that fall on the dashed diagonals indicate that the straight rim segment is perpendicular to nearby grooves. We found that most of the data points cluster around the diagonal, meaning that azimuths of rim segments are parallel with adjacent linear features for many of these PICs. In case of PICs from light terrain of sub-Jovian hemisphere, we found 52% of straight rim segments aligned parallel with their adjacent linear features. For PICs from light terrain of anti-Jovian hemisphere, we found 65% of straight rim segments aligned parallel with their adjacent linear features.

In the dark terrain, the mapped furrows have curvilinear appearance (Fig. 3.3 c) and are particularly frequent in the SW region of Galileo Regio, the largest coherent dark terrain. The dominant orientation of furrows from sub-Jovian and anti-Jovian hemispheres are NW-SE directions. The dark terrain area with highest number of PICs is located in Galileo Regio, adjacent to Uruk Sulcus (Fig. 3.3). The different types of dark terrain and the major and minor tectonic activities affecting the formation of furrows and fractures on dark terrain are listed in Table 3.1. In case of PICs from dark terrain of the sub-Jovian hemisphere, we found that 71% of straight rim segments aligned parallel with their adjacent linear features. For PICs from dark terrain of anti-Jovian hemisphere, only 39% of straight rim segments aligned parallel with their adjacent linear features.

To conclude the orientation analyses of straight rim segments and adjacent grooves shows that the latter indeed govern the orientation of straight crater rims. Lineaments and grooves are first of all surface features of unknown origin. If they would just sculpture the surface they would cause no effect on crater formation. However, that they indeed lead to a localization of deformation and constrain the position of the crater rim segments during the cratering process gives independent proof that the surface features go deep into the icy crust. The observation is proof that the lineations and groove represent fault scarps and traces of faults. The faults have damaged the crust and thus created planar zones of mechanical weakness. The similar number of PICs on dark and light terrain indicates that both types of terrains behave mechanically similar and contain such faults. However, in

Galileo Regio, Perrine Regio, Melotte Regio and Marius Regio, the major cause for linear features are identified to be furrows from ancient large impact event. In Nicholson Regio, the linear features are due to the development of dark lineated terrain formed via tectonic resurfacing activities (Table 3.1).

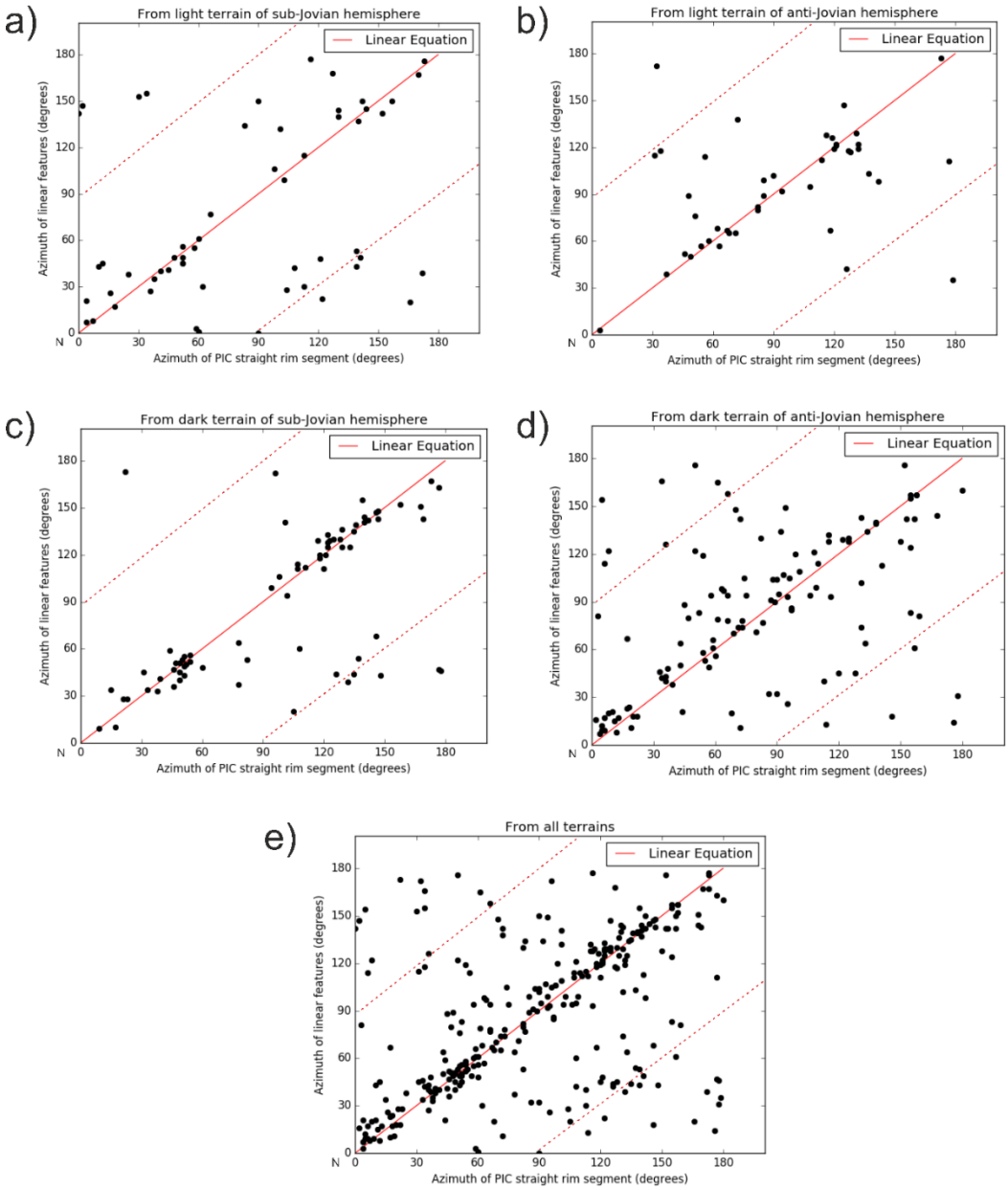

Figure 3.8: Azimuth comparisons of straight rim segments of PICs and adjacent tectonic linear features. (a) from light terrain of sub-Jovian hemisphere; (b) from light terrain of anti-Jovian hemisphere; (c) from dark terrain of sub-Jovian hemisphere; (d) from dark terrain of anti-Jovian hemisphere; (e) Combined analysis from all terrains. Note that the solid red line represents a regression line illustrating similar azimuths. The red dashed lines illustrate perpendicular azimuths.

	Dark terrain	Number of PICs observed	Main linear features influencing PICs	Cause for Main linear features	Minor linear features influencing PICs	Cause for Minor linear features
1	Galileo Regio	139	Lakhmu furrow	Old Impact (Schenk and McKinnon, 1987; Zuber and Paramentier, 1984)	Zu fossae	Strike-slip faulting (Rossi et al 2023)
2	Perrine Regio	33	NW-SE furrows	Large Impact	E-W trending furrow	Impact related
3	Barnard Regio	2	NW-SE furrows	Large Impact	-	-
4	Nicholson Regio	30	NW-SE linear features	Dark lineated terrain formation	NE-SW linear features	Probably related to the impact of Enkidu crater
5	Melotte Regio	2	Concentric fractures	old impact	Unknown (low resolution)	Unknown (low resolution)
6	Marius Regio	29	NE-SW linear features	old impact (Schenk and McKinnon, 1987; Zuber and Paramentier, 1984)	-	-

Table 3.1: The different types of dark terrains and the number of PICs mapped from them are noted. The major and minor form of linear features responsible for determining polygonal shape for the craters emplaced on dark terrains are also listed. In cells which are blank indicate that we do not observe any linear features.

3.4.5.1 PICs in Galileo Regio

Galileo Regio, the largest of the dark terrain, mostly shows concentric furrows (Fig. 3.9 a). The age of dark terrains like Galileo Regio, in general, is estimated to be ~4 Gyr which represents one of the oldest terrains on Ganymede (Neukum, 1997; Zahnle et al., 2003; Baby et al., 2023). The number of PICs in Galileo Regio is largest of all dark terrain and the density of PICs per area (Figs. 3.3 b, 3.9 a) seems to positively correlate with the number

of furrows, although this is only a qualitative statement. The PICs in Galileo Regio have well-developed straight rim segments.

PICs are influenced by furrows of Lakhmu and Zu fossae but are also found within or between furrows. There is a higher number of furrows related to Lakhmu fossae than to Zu fossae. Both of them seem to control the abundance of PICs. The mapped PICs postdate furrow formation. Here straight rim segments of PICs are commonly found to have irregular hexagonal to octagonal shapes (Fig. 3.9 b). The rose diagram of straight rim segments of PICs (Fig. 3.9 c) shows various orientations and a subdued concentration of WNW-ESE and NE-SW directions. While the rose diagram of the furrows (Fig. 3.9 d) has a clear preferred orientation in NW-SE direction. The discrepancy between furrow orientation and straight rim orientation is less obvious but this might be an artefact due to the concentric character of the furrows.

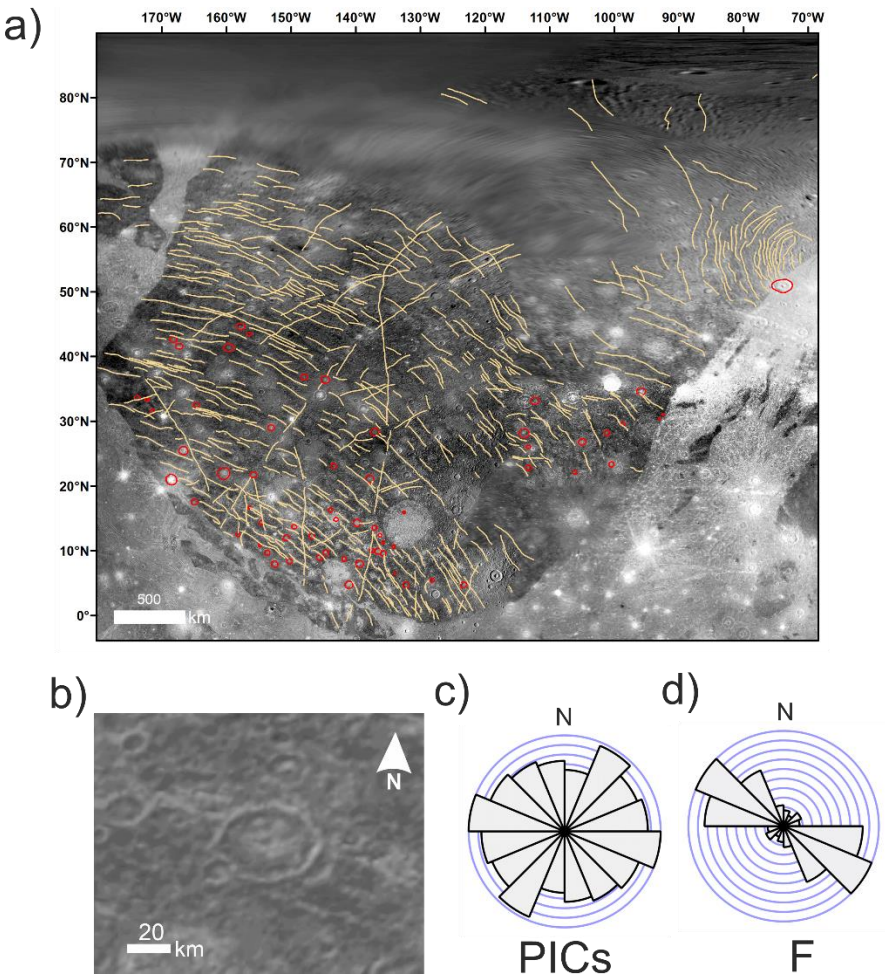

Figure 3.9: (a) Distribution of PICs and lineaments on Galileo Regio. Note that PICs are indicated by red circles and furrows by orange lines (from Collins et al., 2013). (b) Close-up view of a hexagonal shaped PIC in Galileo Regio. (c) Rose diagram showing the orientation of all furrows.

3.5 Discussion

3.5.1 Formation mechanism of PICs on Ganymede

Our analysis revealed that the majority of azimuths of straight rim segments align parallel or subparallel to adjacent tectonic linear features (Fig. 3.8). This observation leads us to infer that the development of polygonal shapes is primarily influenced by deep-rooted faults that represent planes of crustal weaknesses and got reactivated during crater formation. However, we also observed non-parallel or perpendicular relationships between straight rim segments and their adjacent tectonic linear features in some cases, suggesting that these particular straight rim segments might result from surface expressions rather than deep-rooted faults. In addition, ice is known as one of the mechanically most anisotropic crystals (e.g., Duval et al. 2010). If the icy crust of Ganymede has experienced some shearing or flow, crystallographic preferred orientation may form that may result in large scale crustal anisotropies that also can affect the crater forming process.

The dominantly parallel alignment of straight segments of PICs with furrows, grooves, and lineaments suggest at the formation mechanism of PICs' straight rim segments occurred during the modification stage of cratering. The additional presence of straight rims perpendicular to the lineation orientation (Fig. 3.8) is somewhat surprising. For instance, for individual PICs in Galileo Regio, there are at least two straight rim segments within each PICs that are parallel and at perpendicular angles with respect to the furrows. When the crater is emplaced on densely and differently oriented linear features, then the resulting PIC would have the tendency to obtain a greater number of straight segments which in distant view appear more towards circular shape. Thus, the presence of one fault and one straight segment may govern the entire crater collapse process and induces additional straight segments although they are probably not supported by an anisotropic target strength.

On Ganymede, the spatial resolution did not allow to investigate simple craters and their potential polygonality. The simple-to-complex transition diameter on Ganymede is at ~ 5 km diameter (Schenk, 1991). Similarly, the transition diameters from central peak to central pit crater is inversely proportional to surface gravity. The formation of polygonal crater outlines seems to be not affected by these different crater types. The surface temperatures on Ganymede down to ~ 100 K, causes ice that is stronger than the ice on terrestrial planets, but still the static tensile and compressive strength are lower than those of rocks (Durham and Stern, 2001). So, Ganymede's icy crust is sufficiently brittle to allow the formation and

also the preservation of distinct polygonal shapes. Relaxation affects the crater floor and can induce alterations to the crater rim (Singer et al., 2018). Viscous relaxation is wavelength dependent and progresses more rapidly for larger craters, potentially reducing their depths, while it has a lesser effect on smaller craters (Bland et al., 2017; Singer et al., 2018). Numerous craters on Ganymede exhibit some degree of relaxation, primarily attributed to radiogenic heat flow (Bland et al., 2017).

3.5.2 Comparison to Ceres and Dione

A comparison of Ganymede with the dwarf planet Ceres of the asteroid belt and the moon of Saturn, Dione is presented here to assess the influence of linear features, crustal composition temperature and gravity in governing the development of PIC formation. In terms of distance from the sun and surface temperature, Ganymede is located between Ceres and Dione.Ceres has much warmer ice than Ganymede and Dione. The near subsurface temperature is estimated to range from about 180K at the equator to approximately 130K at the poles (Fanale and Salvail, 1989). The acceleration due to gravity is ~ 0.28 m/s^2 (similar to Dione). On Ceres, linear tectonic features in the form of furrows, ridges, troughs and scarps are widely spaced across the surface (Buczkowski et al., 2016). The lower number of linear tectonic features is ascribed to the resurfacing in the form of impacts playing dominant role (Hiesinger et al., 2016). About 3 % of impact craters on Ceres are identified to represent PICs (Zeilnhofer and Barlow, 2021). Most of these PICs are found adjacent to tectonic linear features and the other PICs and suggests extensive subsurface fracturing (Zeilnhofer and Barlow, 2021).

Dione's surface temperature exhibits a lower average compared to celestial bodies such as Ceres and Ganymede. The thermal variations on Dione, ranging from equatorial to polar regions, span an approximate range of 50 to 90 K (Howett et al., 2010). The acceleration due to gravity is 0.232 m/s^2. On Dione, the surface is heavily cratered but in areas like the wispy terrain (found mostly in trailing hemisphere) it contains faults (Smith et al., 1981; Smith et al., 1982). The non-wispy region, which was previously thought to be only cratered does also possess sub-surface fractures due to the presence of PICs found (Beddingfield et al., 2016). Bedingfield et al. (2016) inferred 35% of impact craters of non-wispy terrain to be PICs.

Unlike Ganymede, Ceres and Dione surfaces are densely cratered and visible tectonic linear features are concentrated in few areas globally. However, non-visible linear features due to

subsurface fracturing are reported for Ceres (Otto et al., 2016; Zeilnhofer and Barlow, 2021) and Dione (Beddingfield et al., 2016) based on the presence of PICs. On Ganymede faults and fractures forming grooves and lineations are widespread and visible and there seems to be a correlation of their frequency with the number of PICs. Ganymede's crustal temperature is intermediate between that of Ceres and Dione. The acceleration due to gravity of Ganymede is 1.428 m/s^2. Gravity affects the fault scaling relationship of fault length to fault displacement and fault width (Schultz et al. 2006) Thus for a given fault length the displacement and width is less on a low gravity body. This circumstance may influence the amount of strength degradation due to faulting.

On Ganymede, we found that all of the mapped PICs are situated near to at least one tectonic linear feature. Faults and fractures are not restricted to the light terrain but are also frequent on the dark terrain. Thus, in contrast to Ceres and Dione, faults causing polygonality are surface ruptures. The surface temperatures of Ganymede and Dione are down to ~100 K (Durham and Stern, 2001) suggesting that their crusts behave more brittle than that of Ceres. On Ceres fault obliteration by thermal relaxation and surface degradation seems to be more active.

We do not know the exact ages of these three icy bodies, nor whether they accreted from their present location or were captured into their current resonance (eg., Showman et al., 1997; Sinclair, 1972). Also, we are not certain of the specific combination of processes, such as global volume expansion, Laplace resonance, orbital recession, non-synchronous rotation, and large impacts, that are responsible for initiating tectonic activity on these bodies. However, based on the present-day scenario, Ganymede exhibits less cratering and more pronounced tectonic activity compared to Ceres and Dione, as evidenced by the densely distributed and globally pervasive tectonic linear features on its surface.

3.6 Conclusions

This study is the first report and analysis of PICs on Ganymede:

- PICs occur on both the light and dark terrain. The high number of PICs on dark terrain partly results from the being more densely cratered.
- All of the mapped PICs are complex craters and have either a peak, a pit or a dome as central morphological feature. The PICs attain their final polygonal shape during the modification stage via slumping/ faulting along preexisting fractures and faults planes of weakness.

- Among impact craters of 30 km and larger, PICs constitute 30 % of the crater population present on Ganymede. This is consistent with results of PICs from other icy bodies.
- The comparative analysis of the orientation of PICs straight rim segments and adjacent linear features indicates that there exists genetic relationship between PICs and linear features. This implies that linear features are not only surface markers but act as mechanical anisotropies and zone of crustal weakness This study provides independent proof that grooves and lineations are the traces of faults.
- PICs on Ganymede postdate tectonic activities in the light and dark terrain.
- The abundance of PICs on a planetary body relative to the entire crater population is a measure of the mechanical anisotropy of the particular crust and seems to correlate with the intensity of the tectonic activity of that body.
- Ganymede's icy crust is sufficiently brittle to allow the formation and preservation of distinct polygonal shapes. Relaxation affects the crater floor of many craters but does not degrade their rims. This suggests that relaxation is caused by localized impact-induced thermal anomalies in the crater centers.

3.7 Conflict of interest statement

We declare no conflict of interest.

3.8 Acknowledgement

We gratefully acknowledge the DLR-DAAD PhD fellowship from the German Aerospace Center and the German Academic Exchange Service. Special thanks to Costanza Rossi for sharing Ganymede's regional groove system data. We thank the editor and two anonymous reviewers for their detailed comments and suggestions, which greatly contributed to the improvement of this manuscript.

3.9 References

Abels, A., 2003. Investigation of impact structures in Finland (Söderfjärden, Lumparn, Lappajärvi) by digital integration of multidisciplinary geodata. Inaugural dissertation for attaining the doctoral degree in natural sciences, Westfalian-Wilhelms University, Mü finster, Germany (CD–ROM).

Aittola, M., Öhman, T., Leitner, J. J., Kostama, V. P., & Raitala, J., 2010. The structural control of venusian polygonal impact craters. Icarus, 205(2), 356-363.

Anderson, J. L., Schultz, P. H., & Heineck, J. T., 2003. Asymmetry of ejecta flow during oblique impacts using three-dimensional particle image velocimetry. Journal of Geophysical Research: Planets, 108(E8).

Aschauer, J., & Kenkmann, T., 2017. Impact cratering on slopes. Icarus, 290, 89-95.

Baby, N. R., Wagner, R. J., Stephan, K., & Kenkmann, T., 2023. Stratigraphy, Crater Size–Frequency Distribution, and Chronology of Selected Areas of Ganymede's Light and Dark Terrains. The Planetary Science Journal, 4(9). http://dx.doi.org/10.3847/PSJ/acebed.

Beddingfield, C. B., Burr, D. M., & Tran, L. T., 2016. Polygonal impact craters on Dione: Evidence for tectonic structures outside the wispy terrain. Icarus, 274, 163-194.

Beddingfield, C. B., & Cartwright, R. J., 2020. Hidden tectonism on Miranda's Elsinore Corona revealed by polygonal impact craters. Icarus, 343, 113687.

Beddingfield, C. B., Beyer, R., Cartwright, R. J., Singer, K., Robbins, S., Stern, S. A., ... & Parker, J., 2020. Polygonal impact craters on Charon. Lunar Planet. Sci. Conf., LI, 2326, abstr. 1241.

Beddingfield, C. B., Cartwright, R. J., Patthoff, D. A., Beyer, R., & Moore, J., 2022. Investigating hidden fractures on iapetus using polygonal impact craters. Lunar Planet. Sci. Conf., LIII, 2678, abstr. 1077.

Bland, M. T., Singer, K. N., McKinnon, W. B., & Schenk, P. M., 2017. Viscous relaxation of Ganymede's impact craters: Constraints on heat flux. Icarus, 296, 275-288.

Boyce, J., Barlow, N., MOUGINIS-MARK, P., & Stewart, S., 2010. Rampart craters on Ganymede: Their implications for fluidized ejecta emplacement. Meteoritics & Planetary Science, 45(4), 638-661.

Buczkowski, D. L., Schmidt, B. E., Williams, D. A., Mest, S. C., Scully, J. E. C., Ermakov, A. I., ... & Russell, C. T., 2016. The geomorphology of Ceres. Science, 353(6303), aaf4332.

Collins, G. C., Head, J. W., & Pappalardo, R. T., 1998. Formation of Ganymede grooved terrain by sequential extensional episodes: Implications of Galileo observations for regional stratigraphy. Icarus, 135(1), 345-359.

Collins, G., 2000. Driving Mechanisms for Grooved Terrain Tectonics on Ganymede and Chaotic Terrain Fonnation on Europa: Constraints from Galileo Data, Ph.D. thesis, Brown University.

Collins, G. C., Patterson, G. W., Head, J. W., Prockter, L., Pappalardo, R. T., Lucchitta, B. K., & Kay, J. P., 2013. Global geologic map of Ganymede. US Department of the Interior, US Geological Survey, p. 3237.

Crow-Willard, E. N., & Pappalardo, R. T., 2015. Structural mapping of Enceladus and implications for formation of tectonized regions. Journal of Geophysical Research: Planets, 120(5), 928-950.

Darling, J. A., & Mes, A., 1948. Crater Tests in Basalt. Dept. of Operations and Maintenance, Spec. Engineering Dium. Panama Canal Zone, ICS Memo.

Dasgupta, D., Kundu, A., De, K., & Dasgupta, N., 2019. Polygonal impact craters in the Thaumasia Minor, Mars: role of pre-existing faults in their formation. Journal of the Indian Society of Remote Sensing, 47(2), 257-265.

De Sanctis, M. C., Ammannito, E., Raponi, A., Marchi, S., McCord, T. B., McSween, H. Y., Capaccioni, F., Capria, M. T., Carrozzo, F. G., Ciarniello, M., Longobardo, A., Tosi, F., Fonte, S., Formisano, M., … Russell, C. T., 2015, Ammoniated phyllosilicates with a likely outer Solar System origin on (1) Ceres, Nature, 528, 241-244.

Denk, T., Neukum, G., Helfenstein, P., Thomas, P. C., Turtle, E. P., McEwen, A. S., ... & Porco, C. C., 2005. The first six month of Iapetus observations by the Cassini ISS camera. Lunar Planet. Sci. Conf., XXXVI, 1734, abstr. 2262.

Durham, W. B., & Stern, L. A., 2001. Rheological properties of water ice--applications to satellites of the outer planets. Annual Review of Earth and Planetary Sciences, 29(1), 295-330.

Duval, P., Montagnat, M., Grennerat, F., Weiss, J., Meyssonnier, J., and Philip, A., 2010. Creep and plasticity of glacier ice: a material science perspective. Journal of Glaciology 56, 1059-1068.

Eppler, D.T., Ehrlich, R., Nummedal, D., et al., 1983. Sources of shape variation in lunar impact craters: Fourier shape analysis. Geol. Soc. Am. Bull. 94, 274–291. doi:10.1130/0016-7606.

Fanale, F. P., & Salvail, J. R., 1989. The water regime of asteroid (1) Ceres. Icarus, 82(1), 97-110.

Ferguson, S. N., Rhoden, A. R., & Kirchoff, M. R., 2020. Small impact crater populations on Saturn's moon Tethys and implications for source impactors in the system. Journal of Geophysical Research: Planets, 125(9), e2020JE006400.

Figueredo, P. H., & Greeley, R., 2004. Resurfacing history of Europa from pole-to-pole geological mapping. Icarus, 167(2), 287-312.

Gault, D. E., & VR, Q. W. O., 1968. Impact cratering mechanics and structures. In: French, B.M.,

Short N.M (Eds.), Shock Metamorphism of Natural Materials, 177-189.

Gottwald, M., Kenkmann, T. and Reimold, W.U., 2020. Terrestrial Impact Structures: The TanDEM-X atlas. 608 p, Verlag Dr. Friedrich Pfeil, München.

Greeley, R., Klemaszewski, J. E., & Wagner, R., 2000. Galileo views of the geology of Callisto. Planetary and Space Science, 48(9), 829-853.

Hiesinger, H., Marchi, S., Schmedemann, N., Schenk, P., Pasckert, J. H., Neesemann, A., O'Brien, D. P., Kneissl, T., Ermakov, A. I., Fu, R. R., Bland, M. T., Nathues, A., …, 2016. Cratering on Ceres: Implications for its crust and evolution. Science 353, aaf4759.

Hansen, C. J., Bolton, S., Sulaiman, A. H., Duling, S., Bagenal, F., Brennan, M., ... & Withers, P., 2022. Juno's close encounter with Ganymede—an overview. Geophysical Research Letters, 49(23), e2022GL099285.

Hartman, W. K., 1980. Surface evolution of two-component stone/ice bodies inthe Jupiter region, Icarus,44, 441–453.

Hibbitts, C. A., Pappalardo, R. T., Hansen, G. B., & McCord, T. B., 2003. Carbon dioxide on Ganymede. Journal of Geophysical Research: Planets, 108(E5).

Hirata, N., Suetsugu, R., & Ohtsuki, K., 2020. A global system of furrows on Ganymede indicative of their creation in a single impact event. Icarus,352, 113941.

Howett, C. J. A., Spencer, J. R., Pearl, J., & Segura, M., 2010. Thermal inertia and bolometric Bond albedo values for Mimas, Enceladus, Tethys, Dione, Rhea and Iapetus as derived from Cassini/CIRS measurements. Icarus, 206(2), 573-593.

Johnson, R. B., 1962. Effect of Geologic Factors on Cratering Experiments in Basalt, Buckboard Mesa, Nevada Test Site, Nevada. US Department of the Interior, Geological Survey.

Jones, K. B., Head III, J. W., Pappalardo, R. T., & Moore, J. M., 2003. Morphology and origin of palimpsests on Ganymede based on Galileo observations. Icarus, 164(1), 197-212.

Kenkmann, T., 2021. The terrestrial impact crater record: A statistical analysis of morphologies, structures, ages, lithologies, and more. Meteoritics and Planetary Science 56, Nr 5, 1024–1070. doi: 10.1111/maps.13657

Kersten, E., Zubarev, A. E., Roatsch, T., & Matz, K. D., 2021. Controlled global Ganymede mosaic from voyager and Galileo images. Planetary and Space Science, 206, 105310.

Kersten, E., Zubarev, A. E., Nadezhdina, I. E., Roatsch, T., Matz, K.-D., Szczech, C. C., 2022. Updated Ganymede Mosaic from Juno Perijove 34 Images. EPSC2022-450, https://doi.org/10.5194/epsc2022-450, 2022.

Kumar, P.S., Kring, D.A., 2008. Impact fracturing and structural modification of sedimentary rocks at Meteor crater, Arizona. J. Geophys. Res.-Planets 113, E09009. doi:10.1029/2008JE003115

Melosh, H. J., 1989. Impact cratering: A geologic process. New York: Oxford University Press; Oxford: Clarendon Press.

Moore, J. M., 1984. The tectonic and volcanic history of Dione. Icarus, 59(2), 205-220.

Moore, J. M., Horner, V. M., & Greeley, R., 1985. The geomorphology of Rhea: Implications for geologic history and surface processes. J. Geophys. Res., 90(S02), C785. doi:10.1029/jb090is02p0c785.

Neidhart, T., Leitner, J. J., & Firneis, M. G., 2017. Polygonal impact craters on Rhea, Dione, Tethys, Ceres, and Vesta. Lunar and Planet. Sci. Conf., XLVIII, abstr. 1964, 1625.

Neukum, G., 1997. Bombardment history of the Jovian system. In The Three Galileos: The Man, the Spacecraft, the Telescope. Springer, Dordrecht, 201-212.

Öhman, T., Aittola, M., Kostama, V. P., Raitala, J., & Korteniemi, J., 2008. Polygonal impact craters in Argyre region, Mars: Implications for geology and cratering mechanics. Meteoritics & Planetary Science, 43(10), 1605-1628.

Öhman, T., Aittola, M., Korteniemi, J., Kostama, V. P., & Raitala, J., 2010. Polygonal impact craters in the solar system: Observations and implications.

Öpik, E. J., 1969. The moon's surface. Annual Review of Astronomy and Astrophysics, 7(1), 473-526.

Otto, K. A., Jaumann, R., Krohn, K., Buczkowski, D., von der Gathen, I., Kersten, E., ... & Russell, C. T., 2016. Polygonal impact craters on Ceres: morphology and distribution.

Pappalardo, R. T., Collins, G. C., Head, J. W., Helfenstein, P., McCord, T. B., Moore, J. M., ... & Spencer, J. R., 2004. Geology of ganymede. Jupiter: The Planet, Satellites and Magnetosphere, 2, 363.

Parmentier, E. M., & Head, J. W., 1981. Viscous relaxation of impact craters on icy planetary surfaces: Determination of viscosity variation with depth. Icarus, 47(1), 100-111.

Patterson, G. W., Collins, G. C., Head, J. W., Pappalardo, R. T., Prockter, L. M., Lucchitta, B. K., & Kay, J. P., 2010. Global geological mapping of Ganymede. Icarus, 207(2), 845-867.

Pierazzo, E., & Collins, G., 2004. A brief introduction to hydrocode modeling of impact cratering. Cratering in marine environments and on ice, 323-340.

Plescia, J. B., 1987. Geological terrains and crater frequencies on Ariel. Nature, 327(6119), 201–204. doi:10.1038/327201a0.

Poelchau, M. H., Kenkmann, T., & Kring, D. A., 2009. Rim uplift and crater shape in Meteor Crater: Effects of target heterogeneities and trajectory obliquity. Journal of Geophysical Research: Planets, 114(E1).

Porco, C. C., Baker, E., Barbara, J., Beurle, K., Brahic, A., Burns, J. A., ... & West, R., 2005. Cassini imaging science: Initial results on Phoebe and Iapetus. Science, 307(5713), 1237-1242.

Prettyman, T. H., Yamashita, N., Toplis, M. J., McSween, H. Y., Schörghofer, N., Marchi, S., Feldman, W. C., Castillo-Rogez, J., Forni, O., … & Russell, C. T., 2017. Extensive water ice within Ceres' aqueously altered regolith: Evidence from nuclear spectroscopy, Science, 355(6320), 55-59, doi:10.1126/science.aah6765.

Ravine, M. A., Hansen, C. J., Collins, G. C., Schenk, P. M., Caplinger, M. A., Lipkaman Vittling, L., ... & Bolton, S. J., 2022. Ganymede observations by JunoCam on Juno Perijove 34. Geophysical Research Letters, 49(23), e2022GL099211.

Rossi, C., Cianfarra, P., Salvini, F., Mitri, G., & Massé, M., 2018. Evidence of transpressional tectonics on the Uruk Sulcus region, Ganymede. Tectonophysics, 749, 72-87.

Rossi, C., Cianfarra, P., & Salvini, F., 2020. Structural geology of Ganymede regional groove systems (60° N–60° S). Journal of Maps, 16(2), 6-16.

Rossi, C., Lucchetti, A., Massironi, M., Penasa, L., Pozzobon, R., Munaretto, G., & Pajola, M., 2023. Multi-phase activity on Ganymede's dark terrain: Tectonic evolution of Galileo Regio. Icarus,390, 115305.

Schenk, P. M., & McKinnon, W. B., 1987. Ring geometry on Ganymede and Callisto. Icarus, 72(1), 209-234.

Schenk, P. M., 1991. Ganymede and Callisto: Complex crater formation and planetary crusts. Journal of Geophysical Research: Planets, 96(E1), 15635-15664.

Schenk, P. M., W. B. McKinnon, D. Gwynn, and J. M. Moore, 2001. Flooding of Ganymede's bright terrains by low-viscosity water-ice lavas, Nature 410, 57-60.

Schubert, G., Anderson, J. D., Spohn, T., & McKinnon, W. B., 2004. Interior composition, structure and dynamics of the Galilean satellites. Jupiter: The planet, satellites and magnetosphere, 1, 281-306.

Schultz, P. H., 1976. Moon morphology: Interpretations based on Lunar Orbiter photography. Austin: University of Texas Press.

Schultz, R. A., Okubo, C. H., & Wilkins, S. J., 2006. Displacement-length scaling relations for faults on the terrestrial planets. Journal of Structural Geology, 28(12), 2182-2193.

Shoemaker, E. M., 1963: Impact mechanics at Meteor Crater, Arizona, in Middlehurst, B. M., & Kuiper, G. P. (Eds), The Moon, Meteorites and Comets. The Solar System, IV, Univ. Chicago Press, Chicago, 301-336.

Shoemaker, E. M., B. K. Lucchitta, D. E. Wilhelms, J. B. Plescia, and S. W. Squyres, 1982. The geology of Ganymede, in Satellites of Jupiter, D. Morrison (ed), University of Arizona Press, 435-520.

Showman, A. P., Stevenson, D. J., & Malhotra, R., 1997. Coupled orbital and thermal evolution of Ganymede. Icarus, 129(2), 367-383.

Sinclair, Andrew T., 1972. On the origin of the commensurabilities amongst the satellites of Saturn. Monthly Notices of the Royal Astronomical Society 160, 2, 169-187.

Singer, K. N., & McKinnon, W. B., 2011. Tectonics on Iapetus: Despinning, respinning, or something completely different? Icarus, 216(1), 198-211.

Smith, B. A., L. Soderblom, R. Beebe, J. Boyce, G. Briggs, A. Bunker, S. A. Collins, C. J. Hansen, T. V. Johnson, J. L. Mitchell, R. J. Terrile, M. Carr, A. F. Cook, J. Cuzzi, J. B. Pollack, G. E. Danielson, A. Ingersoll, M. E. Davies, G. E. Hunt, H. Masursky, E. Shoemaker, D. Morrison, T. Owen, C. Sagan, J. Veverka, R. Strom, and V. E. Suomi, 1981. Encounter with Saturn: Voyager 1 imaging science results. Science. 212, 163-191.

Smith, B. A., Soderblom, L., Batson, R., Bridges, P., Inge, J. A. Y., Masursky, H., ... & Suomi, V. E., 1982. A new look at the Saturn system: The Voyager 2 images, Science,215(4532), 504–537.

Soderblom, J. M., Brown, R. H., Soderblom, L. A., Barnes, J. W., Jaumann, R., Le Mouélic, S., ... & Nicholson, P. D., 2010. Geology of the Selk crater region on Titan from Cassini VIMS observations. Icarus, 208(2), 905-912.

Stephan, K., Jaumann, R., Zambon, F., Carrozzo, F. G., Wagner, R., Longobardo, A., Palomba, E., De Sanctis, M. C., Tosi, F., Ammannito, … & Russell, C. T., 2019. Ceres' impact craters - Relationships between surface composition and geology, Icarus, 318, 56-74.

Stephan, K., Roatsch, T., Tosi, F., Matz, K. D., Kersten, E., Wagner, R., ... & Van Hoolst, T., 2021. Regions of interest on Ganymede's and Callisto's surfaces as potential targets for ESA's JUICE mission. Planetary and Space Science, 208, 105324.

Talvitie J., Pernu T., and Raitala J., 1975.The circular Vaasastructure in the Baltic Shield, western Finland.Contribution#59. Finland: Department of Geophysics, University of Oulu. 15 p.

Watters, W. A., Grotzinger, J. P., Bell III, J., Grant, J., Hayes, A. G., Li, R., ... & Zuber, M. T., 2011. Origin of the structure and planform of small impact craters in fractured targets: Endurance Crater at Meridiani Planum, Mars. Icarus 211 (1), 472–497. doi:10.1016/j.icarus.2010.08.030.

Weber, P., Zeilnhofer, M. F., Martorana, M., & Nocera, K., 2022. Regional Investigations of Polygonal Impact Craters on the Moon and Vesta. Research Notes of the AAS, 6(4), 87.

Weihs, G. T., Leitner, J. J., & Firneis, M. G., 2015. Polygonal impact craters on mercury. Planetary and Space Science, 111, 77-82.

Zahnle, K., Schenk, P., Levison, H., & Dones, L., 2003. Cratering rates in the outer Solar System. Icarus, 163(2), 263-289.

Zeilnhofer, M. F., and Barlow, N. G., 2021. The characterization and distribution of polygonal impact craters on Ceres and their implications for the cerean crust. Icarus, 368, 114586.

Zuber, M. T., and Parmentier, E. M., 1984. A geometric analysis of surface deformation: Implications for the tectonic evolution of Ganymede. Icarus, 60(1), 200-210.

4 Ray and Halo impact craters on Ganymede – indicator for subsurface properties of light terrain formation

This chapter has been submitted to Earth and Space Science as:

N. R. Baby, T. Kenkmann, K. Stephan, R.J. Wagner and E. Hauber (submitted 2024): Ray and Halo impact craters on Ganymede – indicator for subsurface properties of light terrain formation. Earth and Space Science.

4.1 Abstract

Impact craters are a unique tool not only for inferring ages of planetary surfaces and examining geological processes, but also for exploring subsurface properties. In this study, we employ ray and halo craters as proxies to obtain insights into the subsurface characteristics and the vertical stratification of Ganymede's icy crust. We investigated 36 prominent ray and halo craters using images acquired during the Voyager, Galileo, and Juno spacecraft missions. These craters exhibit diverse characteristics, including dark rays, bright rays, or their combination, in both continuous and discontinuous patterns as well as dark and bright halos. Craters including dark deposits are generally small, but with dark halo craters exhibiting the smallest, and dark ray craters exhibiting the largest radial extents of their dark ejecta deposits. The excavation depths of the dark ray craters located in dark terrain imply a thin dark layer of less than a 1 km on top of an icy crust. The in-depth analysis of ray and halo craters located in light terrain reveal significant heterogeneity in the uppermost portions of icy crust at various locations. Negligible differences between the subsurface properties of dark and light terrain are apparent for larger impact craters that excavate down to ~ 7 km. In contrast, the presence of at least one layer of subsurface dark material is needed to explain the existence of small dark ray and dark halo craters in the light terrain and their distribution of the dark ejecta deposits with maximum excavation depth of ~ 3 km. Such occurrences of near-surface dark terrain material imply a tectonic rifting mode as responsible for these portions of light terrain, indicating downfaulting of the dark terrain material in these locations.

4.2 Introduction

Ganymede, the largest moon in the solar system, is one of the most interesting celestial bodies in our Solar System due to its complex geological history and its potential

habitability, which now resulted in Ganymede being now the main target of ESA´s current JUICE mission to the Jovian system (Grasset et al., 2013; Stephan et al., 2021). Among its intriguing surface features are a large spectrum of different impact crater morphologies as well as different ejecta materials (Schenk et al., 2004). Here we study impact craters that contain rays or halos composed of either bright icy and/or dark non-ice material (Hibbitts, 2023; Schenk and McKinnon, 1991), which are located in various terrain types such as the dark and light terrains on Ganymede formed due to different surface processes such as impact cratering and tectonic resurfacing, respectively (Pappalardo et al., 2004). These processes, particularly the formation of the light terrain, are still not fully understood and reach from the tectonic resurfacing of the ancient dark terrain to spreading-like formation of new icy crust (Pizzi et al., 2017).

Since the emplacement of ejecta surrounding many of Ganymede's craters is potentially strongly sensitive to the vertical stratigraphy of the subsurface, we use the current understanding of the impact crater process (Kenkmann et al., 2014; Melosh, 1989) and here in particular, the excavation flow field of a hypervelocity impact, to deepen our understanding of the vertical stratification of the Ganymede´s icy crust with implications for the formation processes of the light terrain. Ray craters, which occur on most planetary bodies, are defined as impact craters with a prominent and distant ray system formed by radially to sub-radially oriented streaks of fine, either continuous or discontinuous, ejecta deposits extending outward from the crater rim (Melosh, 1989). Ray craters are usually bright in albedo. On Ganymede, however, some of these craters also exhibit distinct dark rays (Schenk et al., 2004, Stephan et al., 2021, 2024). A halo crater is defined as a crater with an ejecta deposit that is either darker or brighter than its surroundings. The ejecta deposits of a halo crater form a roughly circular to sub-circular area around the crater rim, often featuring a diffuse edge (Melosh, 1989).

Schenk and McKinnon (1985) conducted the first study on Ganymede's dark rays, floor and halo craters using Voyager imagery. In the region of Uruk Sulcus, they found that halo effects were only present in craters with diameters smaller than ~ 12 km. They suggested that the dark material in this region could be buried ~ 1 km below the grooved terrain. Later Schenk and McKinnon (1991) investigated the distribution of dark ray and dark floor craters on various terrains, and found no preference for either dark or light terrains. They interpreted the dark material in these craters to be formed by remnants of the impactors, such as D-group asteroids or comets, rather than being a result of excavation of underlying

stratigraphic units. Spectral investigations of dark ray craters on Ganymede using data from the Galileo Near Infrared Mapping Spectrometer (NIMS) which detected Ganymede's surface composition in the near-infrared wavelengths region between 0.7 and 5.2 µm (Stephan et al. 2020), have led to the assumption that the dark material of dark ray craters could not belong to a single compositional group with a few of them possibly being the result of the excavation of endogenous material or residual of the impactor (Hibbitts, 2023).

During the Galileo mission, in addition to NIMS observations, Ganymede was imaged by the Solid State Imaging (SSI) camera system (Belton et al., 1992). These images show Ganymede's craters in so far unprecedented resolution including some of Ganymede's unique dark ray and dark halo craters. In addition, craters have been observed that were emplaced directly at the border between dark and bright terrain. Studying these crater types in their geologic context in high detail offers the opportunity to investigate their formation mechanisms and the vertical stratigraphy of its subsurface. Therefore, any differences in the subsurface of dark and light terrain could possibly be revealed. Even more, halo and ray craters may shed light on the tectonic formation of light terrain, whether this region is formed by down-faulting and rifting or by spreading and the formation of new icy crust (Pizzi et al., 2017).

4.2.1 Previous studies on ray and halo craters on other bodies

For the near-Earth asteroid Bennu, a detailed analysis of the topography of Bralgah crater using altimetry data indicates that approximately two-thirds of the crater volume is typically excavated during impact, influenced by compaction and uplift near the crater rim (Perry et al., 2022). On the Moon, young craters with 3.8 cm radar-bright halos contain ejecta materials with surface or near-surface rock compositions (Thompson et al., 1981). Craters with dark halos and rays, observed at large phase angles, can also result from surface roughness rather than compositional variance (Kaydash et al., 2014). Mars exhibits crater halos influenced by thicker dust layers and lower elevations, with halo size primarily controlled by impact energy (Bart et al., 2019). Additionally, the dual-toned blast zones on Mars are attributed to the excavation of compositionally different materials from depths of ~ 0.5–1 m, rather than to contributions from impactor material or surficial disturbance (Daubar et al., 2022). Ceres showcases diverse colored deposits, such as the dark material on the Dantu crater floor, due to compositional differences at subsurface levels, indicating heterogeneous crust excavation during impact (Williams et al., 2018). On Vesta, the various

types of crater rays and ejecta materials represent excavation from underlying layers (Krohn et al., 2014; Williams et al., 2014; Yingst et al., 2014). Callisto's dark halo craters reveal subsurface dark layer materials excavated during the impact process, while craters Lofn and Heimdall feature bright ejecta facies with water ice-rich impact melt deposits and more non-ice components excavated from shallower depths (Greeley et al., 2000). Europa exhibits dark, red materials around craters, originating from depths of a few kilometers below the surface, with maximum excavation depths reaching up to 3.6 km (Moore et al., 2001). Dione's ray craters reveal excavation through surface deposits to reach redder materials, characterized by higher IR/UV ratios (Schenk et al., 2011). On Rhea, a study using VIMS data indicates the presence of clean, water-rich ice below the weathered surface, starting at a depth of at least 4 km. This suggests that at least the uppermost crust consists of clean water ice (Stephan et al., 2012).

4.3 Data basis and methods

4.3.1 Voyager and Galileo data

In order to identify and map dark ray and halo craters across Ganymede's entire surface, we utilized a global mosaic formed by merging high-resolution images from Voyager 1, Voyager 2, Galileo, and Juno spacecraft missions (Kersten et al., 2022). Juno's wide-angle camera, JunoCam, captured images during its close approach to Ganymede on June 7, 2021, providing additional images in the region between longitudes 40°W and 25°E (1 km/pxl) with slightly better resolution (1km/pxl) and better illumination compared to Voyager 1+2 and Galileo spacecraft (Hansen et al., 2022). The global mosaic incorporates images with spatial resolutions ranging from 100 m/pxl to 10 km/pxl (Kersten et al., 2021). The detailed geologic study of individual craters and their geologic context was performed based on the best resolved Voyager and Galileo images available.

Several of the studied craters were observed also by Galileo NIMS. If available, we included NIMS-derived information about the varying abundance of water ice and dark non-ice material as well as water ice grains sizes as presented in Stephan et al. (2020). Although, the composition of the dark non-ice material is not yet fully solved, we take the advantage of the work by Stephan et al. (2020) to use NIMS data to identify regions of higher abundance of non-ice material as well as varying ice properties such as the grain size of water ice independent of illumination conditions. Following this work, the water ice absorptions at 1.5 and 2 µm can be used to derive information of the relative abundance of

the water ice and an estimation of variations in the water ice grain size across the study area.

4.3.2 Identification and Mapping of Ray and Halo craters

All studied craters are supposed to be geologically relatively young and did not experience extensive weathering because of their pronounced crater morphology and their bright or dark ejecta which distinctly stand out compared to the surroundings of the crater. The retention time for ray craters on icy satellites of Jupiter were estimated to be on the order of 1 to 2 Ga (Passey and Shoemaker et al., 1982).

We conducted a visual inspection of the global mosaic of Ganymede images to identify ray and halo craters on both light and dark terrains. We traced and mapped the morphologic details of the craters including their inner crater features such as peak, pit or dome, the crater rim as well as the extension of their halos or ray system, as precisely as possible. In order to determine the crater diameter as accurately as possible, we first calculated the area enclosed by the rim of the halo or ray craters. Then, we equated this area to that of a circle and derived the diameter from it. These tasks were carried out using QGIS 3.16.11. Mapping was performed in an equidistant cylindrical projection (Plate Carree projection) to ensure accurate diameter measurements, with each crater being centered for analysis. For areas poleward of 60°, the global mosaic was re-projected into a stereographic projection and centered on each crater. We considered only those craters, whose rays and halos were traceable enough to be accurately mapped and which crater diameters could be measured. Additionally, we documented the geologic context of the mapped crater and whether these craters were located in light or dark terrain or at the boundary between these two terrain types. Based on albedo differences in image data in combination with the geologic context, and differences in albedo and/or abundance of water ice, we identified 4 classes for ray and halo craters:

Bright Ray Craters (BRCs): Bright Ray Craters (BRCs) are characterized by a bright, presumably ice-rich crater and extensive rays of bright icy material. Although, these types of craters make up the majority of impact craters on Ganymede, some of them were emplaced directly at the border between dark and light terrain and are extremely valuable to understand any differences in the subsurface composition of the dark and light terrain.

Dark Ray Craters (DRCs): Dark Ray Craters (DRCs) generally exhibit a bright, presumably ice-rich crater as seen for the BRCs. In contrast, however, their ejecta deposits, which extend as rays over long distances are very dark and presumably composed of non-ice material (Stephan et al., 2024).

Bright and Dark Ray Craters (BDRCs): BDRCs are characterized by one half of their rays having a bright appearance, while the other half displays a dark appearance. Such occurrences are exceptionally rare on planetary bodies.

Dark Halo Craters (DHCs): DHCs are characterized by double concentric zones of differently colored continuous ejecta material with circular to sub-circular diffused edges. These concentric zones consist of alternating dark and light ejecta materials around the crater rim.

4.3.3 Determination of Excavation depths

The excavation flow field can be described by streamlines (Maxwell, 1977). The streamlines of the excavation flow near the point of impact are directed downward and outward, away from the point of impact and lead to the opening of the transient cavity (Kenkmann et al. 2014, Fig. 4.1). Sidewise streamlines radiate outward and gradually bend upward due to the reduced pressure gradient towards the surface, leave the crater, and form an ejecta blanket. It is important to note that only the displaced material of the upper one-third of the cavity depth leaves the crater. According to Melosh et al. (1989), the maximum depth of excavation (D_e) of a crater is roughly 10% of the transient cavity diameter:

$$D_e \approx 1/10^* D_t \quad \text{(Eq. 4.1)}$$

Where, D_t is the parabolically shaped diameter of the transient crater cavity.

To determine the transient diameter (D_t) of a crater with known final crater diameter (D), we employ the equation formulated by Schenk et al. (2004). This equation integrates the transient diameter (D_t), the simple to complex crater transition diameter ($D_{c)}$, and the final crater diameter (D) for complex craters. As all the craters we have mapped exceed 5 km in size, we can apply the Schenk et al. (2004) equation in our analysis. This equation is rooted in the crater scaling equation established by Schmidt and Housen (1987) within a gravity-scaling framework. Therefore, for complex craters:

$$D = D_t^{\varepsilon} \cdot D_c^{1-\varepsilon} \text{ (Schenk et al., 2004)} \quad \text{(Eq. 4.2)}$$

D_c = 2.5 km for Ganymede (Schenk et al., 2004), d and D_t are in kilometers ε ~ 1.13, which accounts for crater slumping (Schenk et al., 2004). Rearranging and substituting values in equation 2 leads to:

$$D_t = 1.111\, D^{0.8849} \qquad \text{(Eq. 4.3)}$$

Equation 3 gives a maximum value of excavation aside of the impacting point.

The radial distance of the ejecta from the crater center gives further hints to the original location and depth of the material prior to the impact (Fig. 4.1). For example, proximal ejecta deposited close to the crater rim originates from a nearby position inside the crater and becomes involved in the excavation flow field only when the transient cavity reached almost its final size (Kenkmann et al. 2014). This ejecta is slow and is usually from a near surface location. In contrast, ejecta that forms a discontinuous blanket and is deposited multiple crater radii away from the source crater is ejected early in the cratering process and stems from a central region of the crater, close to the point, where the projectile came to halt. In analogy to explosion cratering this point is known as the equivalent depth-of-burst (Holsapple 1980). In a simplified version this depth-of-burst *dob* depends on the density contrast between projectile ρ_p and target ρ_t and the diameter D_p of the projectile

$$dob = D_p \sqrt{\rho_p / \rho_t} \qquad \text{(Eq. 4.4)}$$

If carbonaceous chondrites or cometary material are considered as impactors for Ganymede the density ratio to the ice target might be in the order of 1.5. To calculate the diameter of a projectile as a function of crater diameter, scaling laws in the gravity regime are applied (Collins et al. 2005). Solving this for the projectile diameter yield

$$D_p^{-0.78} = 1.161\, D_t^{-1} \left(\rho_p / \rho_t\right)^{1/3} v_p^{0.44}\, g^{-0.22} \quad . \qquad \text{(Eq. 4.5).}$$

where v_p is the mean impact velocity, g, is the gravity of Ganymede. With g = 1.428 ms^{-2}, the mean v_p = 2740 ms^{-1} and, a projectile density of 1500 kgm^{-3}; a target density of 1000 kgm^{-3}, equations 5 is simplified to:

$$D_p = \left(39.95 / D_t \right)^{-1.28} \qquad \text{(Eq.4.6)}$$

For small craters up to 5 km diameter the equivalent depth-of-burst calculation gives similar results as the excavation depth. For larger craters the excavation depth dob exceeds the 10% of the transient cavity size.

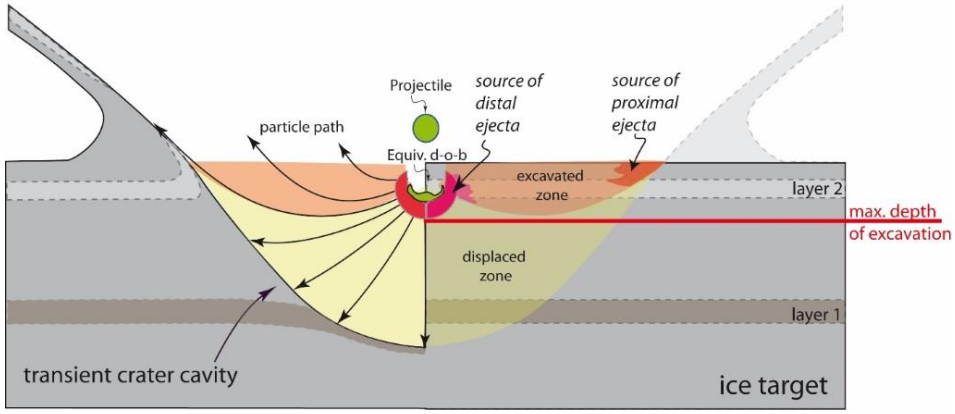

Figure 4.1: Excavation flow field of a hypervelocity impact. The streamlines (left) indicate the displacement of material upon impact. They are bent upwards due to the interaction with the free surface. The red colored area indicates material that leaves the crater cavity, forming an ejecta curtain and ultimately an ejecta blanket. Proximal ejecta contributes to the lower part of the ejecta curtain, has a low speed and is sourced from a shallow region near the edge of the transient cavity. Distal ejecta comes from a shocked aureole that surrounds the equivalent depth-of-burst and from deeper parts of the excavated zone. The red horizontal line indicates the depth below which no excavation takes place. Layer 1 is entirely in the displaced zone. This layer will not be excavated but will cover the lower part of the transient cavity. It can appear at the surface when the transient cavity collapse and forms a central uplift (not shown here). Layer 2 will be excavated and will form a part of the ejecta blanket surrounding the crater.

4.4 Results

4.4.1 Distribution of ray and halo craters on Ganymede

We included 36 impact craters on Ganymede (Fig. 4.2) in this study with 3 of them categorized as dark halo craters (DHCs, Nergal, Khensu and Humbaba) while the remaining craters were classified as ray craters. These 3 DHCs exhibit a unique double-halo configuration, characterized by dark ejecta material surrounded by bright ejecta material. These halo craters have dark crater floors. Double-layered ejecta configurations were not observed in any ray craters, indicating that all ray craters possess single-layered ejecta. Additionally, 5 of the ray craters are DRCs, with 4 located in dark terrain and 1 in light terrain. The ray crater Tammuz (DBRC) is a unique case, displaying half bright and dark ejecta. The 27 ray craters included in this study are BRCs were selected as representative of the majority of Ganymede's craters with respect to their size and location

and geologic context. In detail, 20 are situated in the light terrain, 8 in the dark terrain, and 8 were emplaced along the boundary between light and dark terrain.

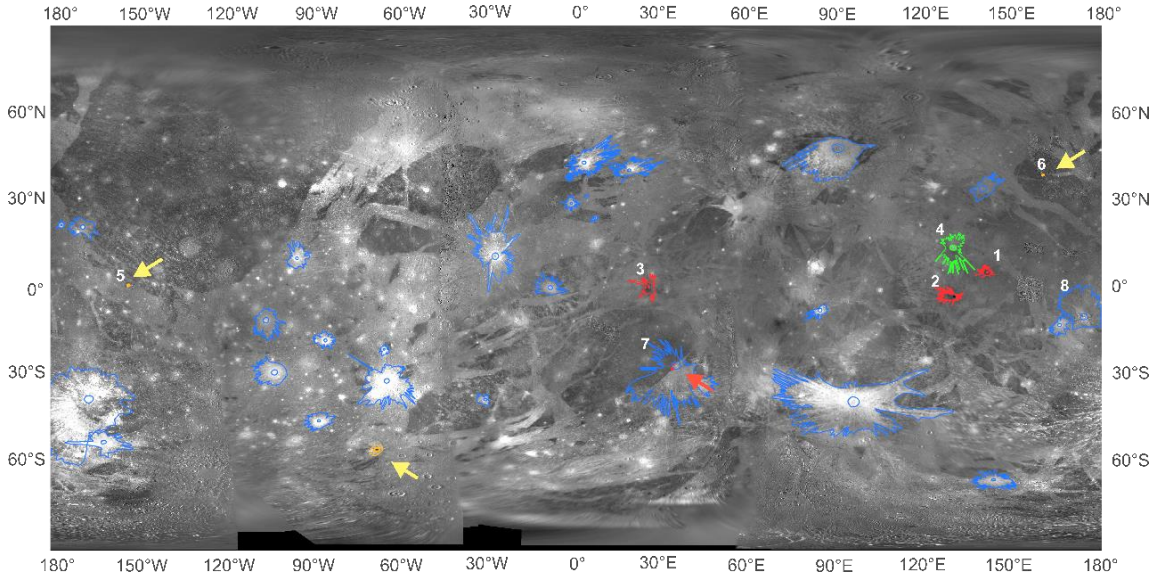

Figure 4.2: The global distribution of BRCs (blue), DRCs (black), BDRCs (green), and DHCs (yellow) on Ganymede. Small craters, which are not easily seen in the image, are indicated by arrows. Crater discussed in detail are indicated by numbers: 1) DRC Antum, 2) DRC Mir, 3) DRC Kittu, 4) BDRC Tammuz, 5) DHC Khensu, 6) DHC Nergal, 7) BRC Enkidu, and 8) BRC Melkart.

4.4.2 Excavation depths of ray and halo craters on Ganymede

Crater parameters derived for the studied craters and discussed in this work are presented in Table 4.1. Figure 4.3 displays the maximum excavation depth versus the final crater diameter separated for (a), the light terrain, (b), the dark terrain, and (c) mixed terrain. The majority of rays and halo craters are situated in the light terrain (Fig. 4.3 a). The observed power law trend in the graph arises reflects Eq. 3 and deviates slightly from a linear trend. The largest excavation depth, 8.5 km, was found for a 135 km final crater diameter, bright ray crater situated in light terrain. All craters with final diameter larger than 75 km excavate material from a maximal depth of 5 km have bright rays. In contrast, the smallest 9 km crater Nergal excavates material from a maximal depth of ~ 0.7 km. DRCs are typically found among the smaller craters. All DHCs are located on light grooved terrain. Nergal, the smallest DHC with a diameter of 9 km, excavates dark material from a maximum depth of approximately 0.77 km. In contrast, Humbaba, the largest DHC, excavates dark material from a maximum depth of about 3 km. (Fig. 4.3 a). DRCs in dark terrain (Fig. 4.3 b), excavate dark material from a maximum depth of ~1.2 km. Larger ray craters located at the borders of light and dark terrain are observed to be bright ray craters (Fig. 4.3 c).

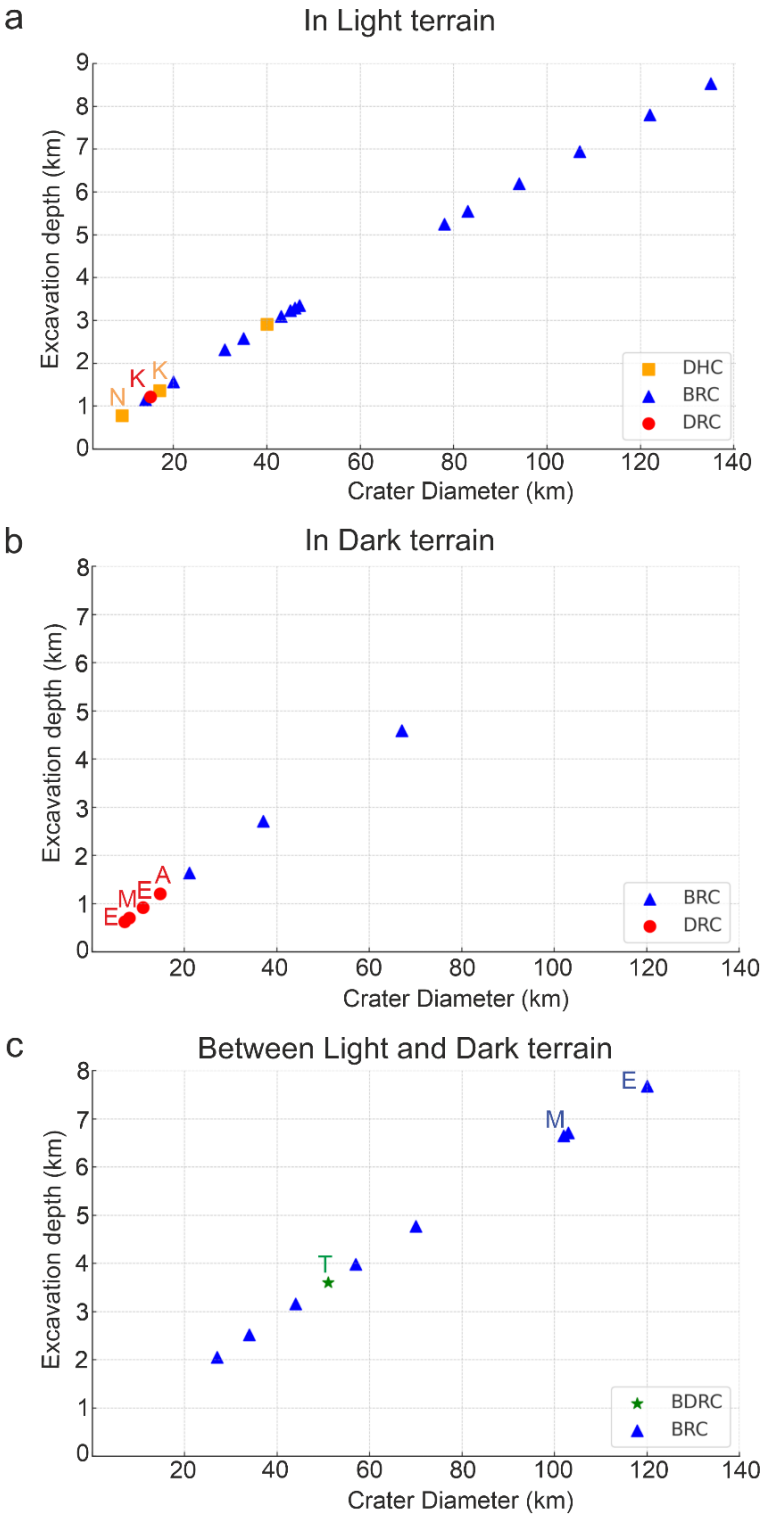

Figure 4.3: Crater diameter vs. excavation depth (km) for various crater types and terrains: a) craters located in light terrain, b) in dark terrain and c) at border between light and dark terrains. The different crater types are distinguished by different colors: DHCs are represented in yellow, DBRCs in green, BRCs in blue, and DRCs in red. Craters studied in detail indicated by letters: Nergal (yellow N), Kittu (red K), Khensu (yellow K), Mir (red M), Antum (red A), Tammuz (green T), Melkart (blue M), Enkidu (blue) and the two dark craters superimposed on Enkidu (red E).

4.4.3 Radial ejecta extent of ray and halo craters on Ganymede

Figure 4.4 displays the variation in the average radial extent of ray and halo craters versus the corresponding standard deviation. The standard deviation indicates the difference between the minimum and the maximum extent of the ejecta deposits from their average. Note that the radii of the ejecta deposits are normalized to the respective crater radii. The resulting graph reveals that the studied crater types can be well separated by their radial extent of the ejecta (rays or halos) and their standard deviation.

DHCs including Nergal (N) and Khensu (K) generally exhibit the smallest ejecta extents (< 5km) and standard deviations (~ 1km). Conversely, the rays of DRCs including Mir (M), Antum (A) and Kittu (K) exhibit the largest radial extents (>15 km) and standard deviations (> 9 km), possibly due to different material properties of the dark non-ice material compared to bright ice. The rays of BRCs exhibit intermediate values for the radial extend of the ejecta deposits. Intriguingly, Tammuz's (BDRC) radial extent with its ejecta composed of dark as well as bright portions is similar to that of other bright ray craters. The same accounts also for the special group of BRCs such as Enkidu (E) and Melkart (M) emplaced at the border between dark and light terrains on Ganymede.

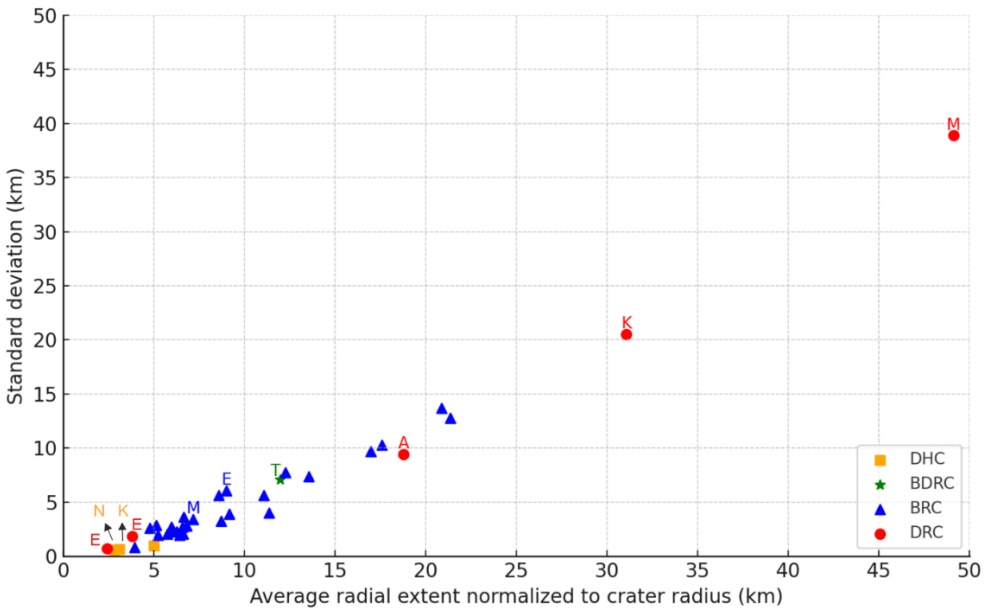

Figure 4.4: The average radial extent normalized to crater radius plotted against the standard deviation for various crater types, with each type represented by a distinct color code: DHC (yellow), BDRC (Tammuz, green), BRC (blue), and DRC (red). Yellow letters 'N' and 'K' represent Nergal and Khensu. Red letters 'K,' 'M,' and 'A' represent Kittu, Mir, and Antum, while 'E' represents Enkidu's neighboring craters. Green letter 'T' represents Tammuz, and blue letters 'M' and 'E' represent Melkart and Enkidu.

N	Crater name	Lat °/ Lon °E	D [km]	D_t [km]	D_e [km]	C_C	Tt	R_{min} [km]	R_{max} [km]	R_A [km]	S [km]
1	Nergal	38.7/160.1	9	7.76	0.77	DRC	L	11	17	3.11	0.66
2	Khensu	1.0/207.1	17	13.63	1.36	DRC	L	19	29	2.82	0.58
3	Tammuz	13.9/129.1	51	36.04	3.60	BDRC	L	124	486	11.96	7.09
4	Antum	5.5/141.1	15	12.02	1.20	DRC	D	69	208	18.77	9.42
5	Kittu	0.5/25.2	15	12.20	1.22	DRC	L	79	387	31.06	20.53
6	Tros	11.1/332.5	94	61.91	6.19	BRC	L	254	785	11.05	5.64
7	Herschef	47.8/89.7	120	76.85	7.68	BRC	L/D	176	854	8.58	5.65
8	Tash-Metum	-38.7/95.1	135	85.29	8.52	BRC	L	305	1351	12.26	7.74
9	n.n.	-12.6/165.6	46	32.89	3.28	BRC	L	85	190	5.97	2.28
10	Amon	34.1/139.4	102	66.55	6.65	BRC	L/D	112	377	4.79	2.59
11	n.n.	20.9/191.5	67	45.88	4.58	BRC	D	111	240	5.23	1.92
12	Nah-Hunte	-17.8/274.5	47	33.52	3.35	BRC	L	107	203	6.59	2.04
13	Cisti	-31.7/295.5	70	47.69	4.76	BRC	L/D	217	731	13.54	7.34
14	n.n.	-28.9/257.0	78	52.49	5.24	BRC	L	151	363	6.58	2.71
15	n.n.	-10.8/254.2	83	55.45	5.54	BRC	L	153	324	5.74	2.06
16	n.n.	-45.6/272.2	35	25.83	2.58	BRC	L	129	269	11.37	4.00
17	n.n.	21.6/184.2	20	15.74	1.57	BRC	L	40	96	6.80	2.80
18	n.n.	10.2/264.7	43	30.99	3.09	BRC	L	113	281	9.16	3.90
19	Enkidu	-26.4/34.5	122	77.98	7.79	BRC	L	179	920	9.00	6.07

20	n.n.	-37.9/328.7	37	27.13	2.71	BRC	D	60	161	5.97	2.72
21	Min	29.2/358.5	31	23.19	2.31	BRC	L	85	185	8.70	3.22
22	Shu	43.1/2.8	44	31.62	3.16	BRC	L/D	160	613	17.56	10.29
23	n.n.	23.9/6.5	21	16.43	1.64	BRC	D	24	84	5.14	2.85
24	Ishkur	0.4/351.4	67	45.88	4.58	BRC	D	150	280	6.41	1.94
25	Apophis	-7.6/83.6	57	39.76	3.97	BRC	L/D	85	293	6.63	3.64
26	n.n.	40.4/18.4	34	25.17	2.51	BRC	L/D	122	588	20.88	13.70
27	n.n.	-20.8/294.6	27	20.53	2.05	BRC	L/D	54	115	6.25	2.25
28	Osiris	-37.8/193.4	107	69.43	6.94	BRC	L	460	1826	21.36	12.76
29	Melkart	-9.7/173.9	103	67.13	6.71	BRC	L/D	194	545	7.17	3.40
30	Mir	-2.9/129.7	8	6.99	0.69	DRC	D	41	352	49.12	38.87
31	Humbaba	-55.2/292.1	40	29.06	2.90	DRC	L	80	120	5.00	1.00
32	n.n.	31.6/3.6	14	11.48	1.14	BRC	L	22	33	3.92	0.78
33	n.n.	-65.4/134.1	29	21.87	2.18	BRC	L	119	334	15.62	7.41
34	Andjeti	-52.6	45	32.26	3.22	BRC	L	164	600	16.97	9.68
35	Enkidu (I)	-27.6/33.0	11	9.27	0.92	DRC	D	11	31	3.81	1.81
36	Enkidu(II)	-25.9/33.7	7	6.21	0.62	DRC	D	6	11	2.42	0.71

Table 4.1: Parameters derived for the craters selected for this study such as: number of crater in this study (N), latitude (lat °) and longitude (lon°) where the crater is located, crater diameter (D), transient crater diameter (Dt), maximum depth of excavation (De), class of crater type (Cc), terrain type (Tt), i.e. dark (DT) or light terrain (LT), or between light and dark terrain (LT/DT), minimum (Rmin), maximum (Rmax) and average radius (R_A) of the ejecta extent together with the standard deviation (S) of the ejecta radii from the average. Note that RA has been normalized to the radius of the corresponding crater. "n.n." is used to denote craters without assigned names.

4.4.4 Individual craters

Several craters have been observed during the Voyager and Galileo missions with sufficient resolution to analysis their characteristics in detail. In the following we present the results of the detailed geologic mapping of these craters, which include various dark ray and halo craters in addition to bright ray craters emplaced at the border between dark and light terrain.

4.4.4.1 Dark Ray Craters (DCRs)

4.4.4.1.1 Antum (~5.5°N/ ~141.1°E)

Antum, a ~ 15 km diameter dark ray crater is positioned close to the equator of Ganymede's trailing hemisphere at ~5.5°N/~141.1°E (Fig. 4.2). The maximum excavation depth reaches up to ~1.2 km (Tab. 1). Antum was only imaged during the Voyager mission with ~ 2 km/pxl, but observed at relatively high resolution by Galileo NIMS (2.1 km/pxl). Antum is fully situated within the extensive dark terrain of Marius Regio.

Several craters have been observed during the Voyager and Galileo mission with sufficient resolution for analysis of their characteristics in detail. In the following we present the results of the detailed geologic mapping of these craters, which include various dark ray and halo craters in addition to bright ray craters emplaced at the border between dark and light terrain.

Antum, a ~ 15 km diameter large dark ray crater is positioned close to the equator of Ganymede's trailing hemisphere at ~5.5°N/~141.1°E (Fig. 4.2). The maximum excavation depth reaches up to ~1.2 km (Tab. 4.1). Antum was only imaged during the Voyager mission with ~ 2 km/pxl, but observed at relatively high resolution by Galileo NIMS (2.1 km/pxl). Antum is entirely situated within the extensive dark terrain of Marius Regio. The main geological units observed are: crater with a distinct floor and rim, bright continuous ejecta, and extended dark rays (Fig. 4.5 a, b). The dark ray materials (discontinuous ejecta) were deposited at a maximum distance of ~ 130 km from the crater center (Tab. 4.1). The crater interior and its outer rim appear predominantly bright. Due to low resolution, it is unclear whether a peak or pit is present. The dark rays represent the discontinuous ejecta and are presumably a very thin layer of dark material on top of the dark terrain of Marius Regio.

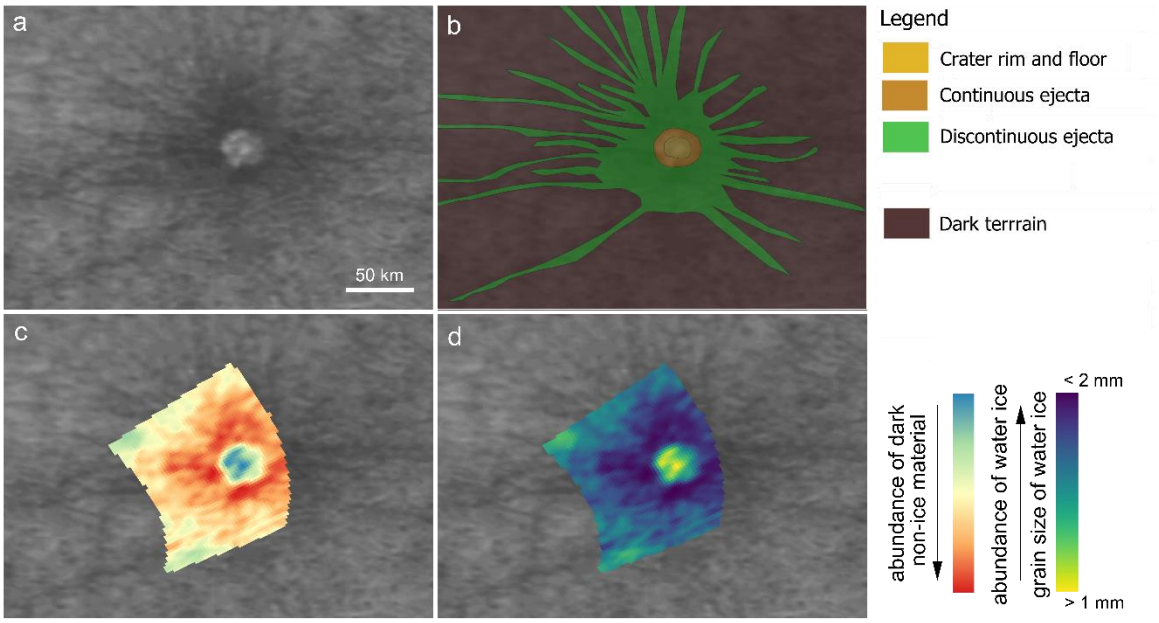

Figure 4.5: Dark ray crater (DRC) Antum: a) Voyager image, b) geologic map, c) relative abundance of water ice/non-ice material and d) grain size of water ice as derived after Stephan et al. (2020) from NIMS data.

NIMS observations support the enrichment of water ice in the crater and dark non-ice material in the ray material (Hibbitts et al., 2023, Stephan et al., 2024) (Fig. 4.5 c, d). Although the differences in ice grain sizes are very small, slightly smaller sizes occur and are associated with the ice rich crater. Generally, ice grain sizes adapt to the local surface temperature with time (Stephan et al. 2020). Slightly smaller grain sizes in the crater could possibly result from a colder crater in comparison to warmer darker regions (Pappalardo et al., 2004).

4.4.4.1.2 Mir (~ 2.9°S/129.7°E)

Mir, a ~ 8 km diameter dark ray crater (DRC) is positioned on the trailing hemisphere at ~ 2.9°S/129.7°E in the southwest of Antum (Fig. 4.2). The maximum excavation depth of Mir could be estimated to be ~ 0.7 km (Tab. 4.1). Our analysis utilized an available image resolution of ~ 2 km/pxl and additional Galileo NIMS data acquired at 3.4 km/pxl. The main geological units identified are a bright crater with a distinct rim and floor and dark rays making up the discontinuous ejecta (Fig. 4.6 a, b). Similar to Antum, the low resolution prevents to identify any peak or pit located in the crater center. The dark rays cross a relatively narrow band of light terrain in the area and extend up to a maximum distance of ~ 160 km from the crater center.

Furthermore, the dark rays appear to be asymmetrically distributed and extend farther to the west than to the east, suggesting an oblique (30-40°) impact from east. Also, two neighboring craters, with one superimposed onto the dark rays of Mir, might have contributed to the dark ejecta. NIMS data support that the ejecta concentrates downrange (west of the crater) with more non-ice material than the surrounding dark terrain, whereas the craters themselves are richer in ice (Fig 4.6 c, d). Similar to Antum, the variations in water ice grains sizes are small and correspond to the global variations in grain sizes related to the surface temperature presented in Stephan et al. (2020). Intriguingly, the dark ejecta and central part (peak) of Mir crater apparently exhibit slightly smaller ice grains than the presumably geologically older and warmer surroundings in the dark terrain of Marius Regio.

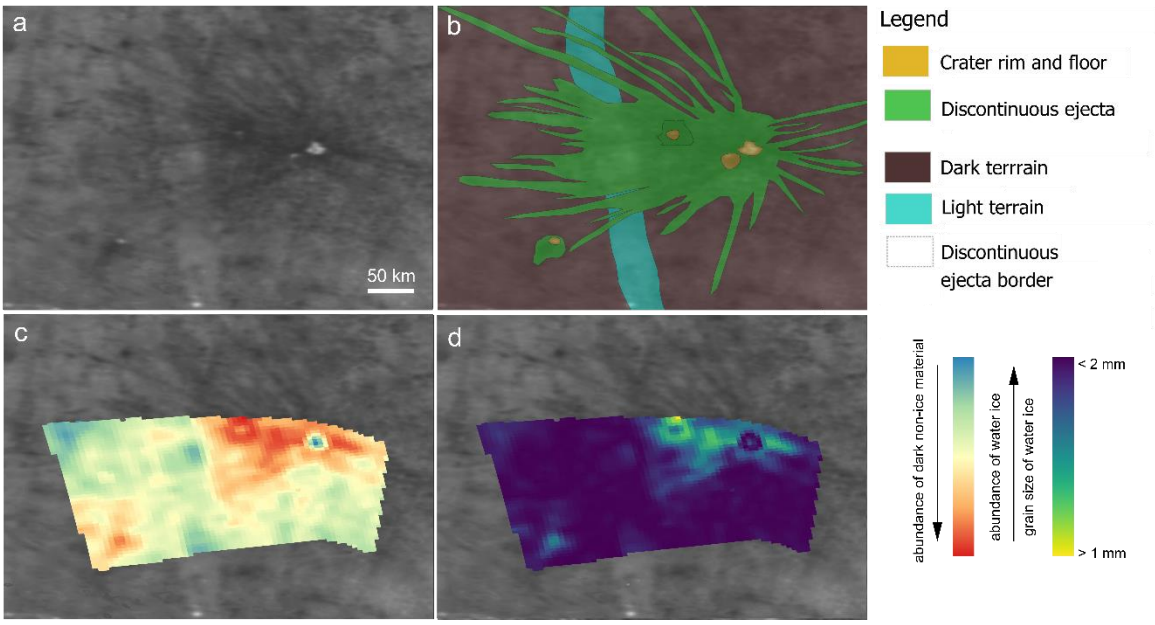

Figure 4.6: Dark ray crater (DRC) Mir: a) Voyager image, b) geologic map, c) relative abundance of water ice/non-ice material and d) grain size of water ice as derived after Stephan et al. (2020) from NIMS data.

4.4.4.1.3 Kittu (0.5°N/25°E)

Kittu, a 15 km diameter dark ray crater, is located on Ganymede's trailing hemisphere at ~ 0.5°N/~ 25°E within two distinct types of extended light grooved terrains (Mysia and Harpagia Sulci) (Fig. 4.2). It is likely that the dark ejected material originated from a depth up to ~ 1.2 km (Tab. 4.1). Kittu is one of the rare surface features on Ganymede that have been imaged at high resolution by Galileo SSI as well as NIMS. Therefore, we were able

to use SSI image and NIMS data with resolutions of 145 m/pxl and 279 m/pxl and ~3 km/pxl, respectively for our analysis.

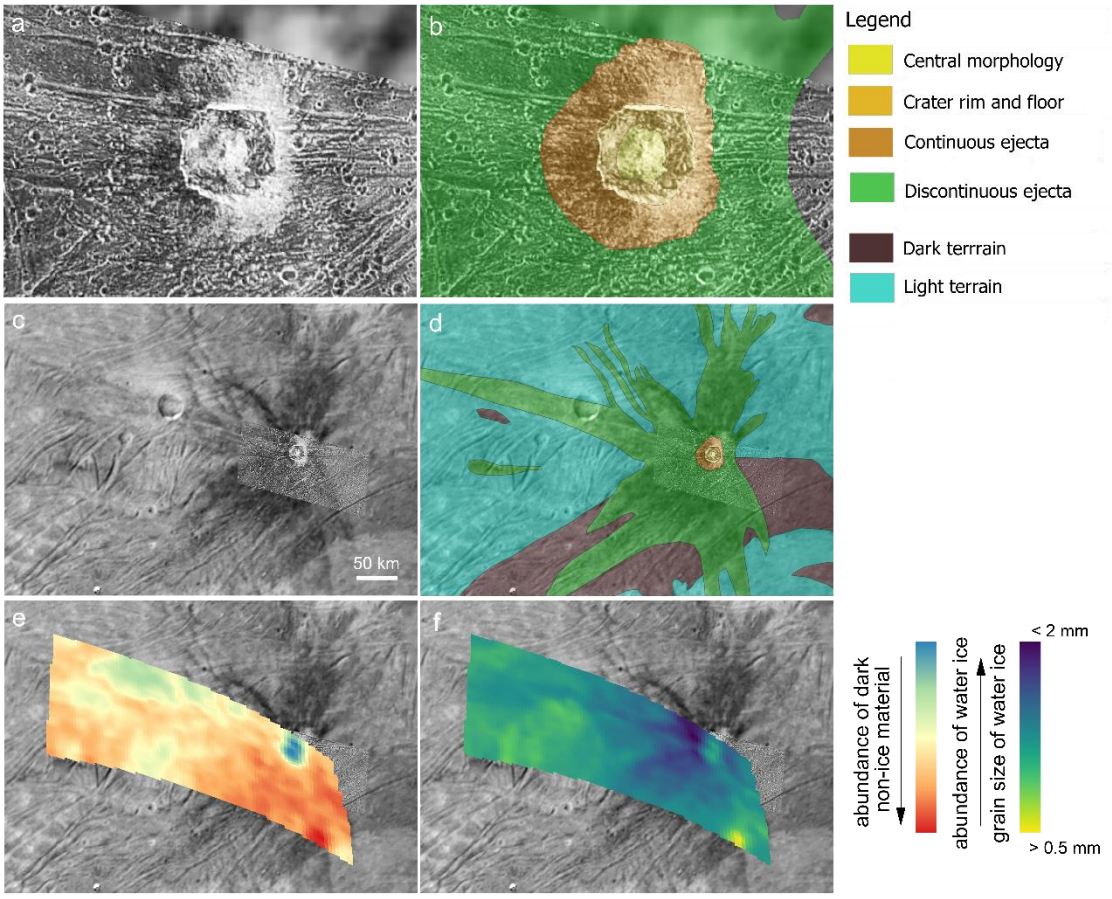

Figure 4.7: Dark ray crater (DRC) Kittu: a) High resolution Galileo observation, b) geologic map of Kittu crater, c) Voyager + Galileo mosaic, d) geologic map, e) relative abundance of water ice/non-ice material and f) grain size of water ice as derived after Stephan et al. (2020) from NIMS data.

The main geological units observed in our study comprise a broad central peak, a bright rim and floor, a continuous bright ejecta blanket extending about one crater radius beyond the crater rim, and discontinuous ejecta of extensive dark rays (Fig. 4.7 a, b, c, d). Kittu displays a butterfly-shaped ejecta blanket comprised of dark ejecta material, suggesting a low-angle impact from east to west (Pierazzo and Melosh, 2000). Up-range forbidden zone, along with ejecta deposition cross-range and downrange, are characteristic features. However, note the polygonal outline of the crater, that is governed by orientation of grooves (Baby et al. 2024). It cannot be excluded that the emplacement of the crater itself within a band of grooves affected the configuration, distribution and orientation of the dark rays.

NIMS supports the dark non-ice material dominating the dark rays and an icier crater as well as icier surroundings (Fig. 4.7 e, f). The darkest portions possibly refer to the piece of dark terrain South of Kittu crater partly covered by the dark rays. NIMS data also imply slightly larger grain sizes for the dark ejecta and smaller grain sizes in the surrounding light terrain and within the crater.

4.4.4.2 Half bright and dark ray crater-Tammuz (~13.9°N/~129.1°E)

Tammuz is a ~ 51 km diameter ray crater located in the North of Antum and Mir at ~13.9°N/~129.1°E in Ganymede's trailing hemisphere (Fig. 4.2). The maximum excavation depth is estimated to be of 3.6 km (Tab. 4.1). Intriguingly, Tammuz exhibits an asymmetrical distribution of its ejecta. Half of the ejecta is dark, while the other half is bright, both radiating in opposite directions. Like Antum and Mir, Tammuz was also imaged only during the Voyager mission with a resolution of 2 km/pxl, but observed by NIMS with 6.2 km/pxl.

The main geological units observed for Tammuz include: a bright crater floor and rim (constituting a major portion of the crater floor and rim), a dark crater floor and rim (constituting only a minor portion of the crater floor and rim), bright continuous ejecta, dark continuous ejecta, bright discontinuous ejecta, and dark discontinuous ejecta (Fig. 4.8). The bright ejecta is predominantly located to the north, stretching from slightly west to slightly east of due North, while the dark ejecta is predominantly situated to the south, extending from slightly west to slightly east of due South. Due to the low resolution, it is challenging to precisely determine the exact position of the dual-colored ejecta. Nevertheless, NIMS data confirm the change in albedo related to the abundance in water ice / dark non-ice material with respect to the ejecta and the crater itself. It is not clear, however, if Tammuz was emplaced within the dark terrain of Marius Regio or the light terrain of Tiamat Sulcus, which crosses the area north of Tammuz from Southeast to Northwest. Possibly, a piece of dark terrain related to Marius Regio reaches up to the southern crater rim of Tammuz, but is covered by its dark ejecta. This is as also indicated in the global geologic map of Ganymede by Collins et al. (2013) favoring a heterogeneous target area, that is most likely composed of light ice in the northeastern half and dark ice in the southwestern half.

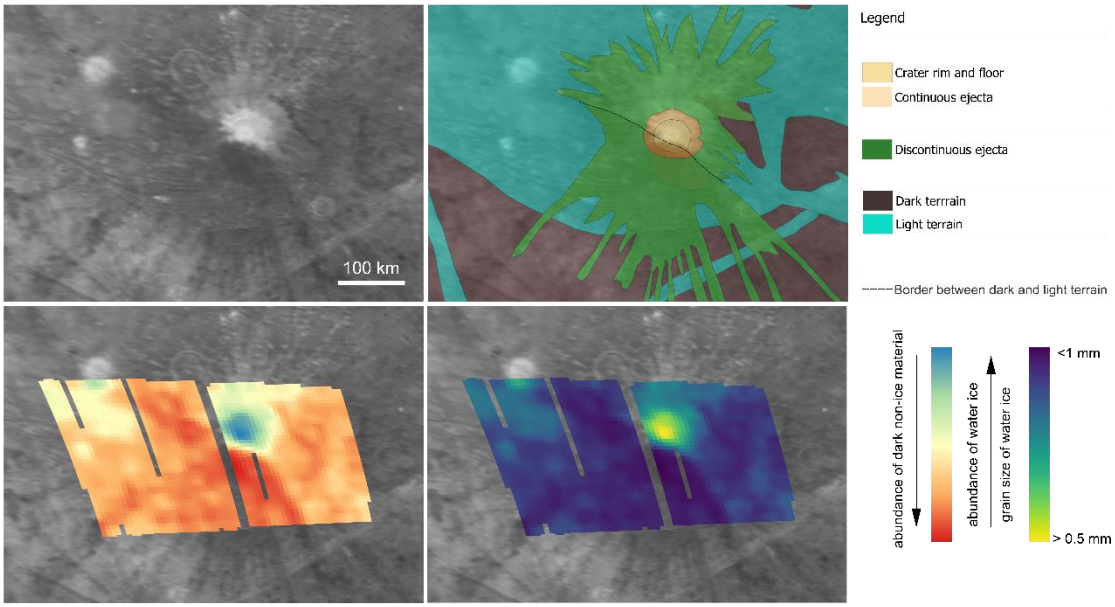

Figure 4.8: Bright and Dark ray crater (BDRC) Tammuz: a) Voyager mosaic, b) geologic map, c) relative abundance of water ice/non-ice material and d) grain size of water ice as derived after Stephan et al. (2020) from NIMS data.

4.4.4.3 Dark halo craters (DHCs)

4.4.3.3.1 Khensu (~1.04°N/207.1°E)

Khensu, a 17 km diameter double halo crater, features a central dark material region encircled by lighter materials. Positioned on the leading hemisphere at ~1.04°N/~207.1°E, it is situated close to the equator. Khensu lies within the light grooved terrain of Uruk Sulcus but relatively close to the border of the dark terrain of Galileo Regio in the North (Fig. 4.2). The presence of double layer ejecta indicates on a body like Ganymede that an atmosphere is not required for the fluidization of ejecta materials during the impact event usually assumed to be the cause of halos (Boyce et al., 2010). For our analysis, one of the Galileo SSI images acquired at high resolution of 220 m/pxl is available. Unfortunately, no NIMS data exist for this unique feature. The excavation depth of Khensu has been estimated to be less than 1.36 km (Tab. 4.1).

The main geological units related to Khensu are the peak, dark crater floor, bright crater rim, dark continuous ejecta including some even darker spots, and bright continuous ejecta (Fig. 4.9 a and b). Geomorphological analysis indicates the presence of a forbidden zone to the north of the crater, and we observed an off-centered positioning of the peak toward the northwestern side. Thus, an oblique impact from a northerly direction is inferred. The presence of the discontinuous ejecta is attributed to the influence of the topography, where

ridges play a significant role in their formation, while other ejecta remain concealed within the grooves.

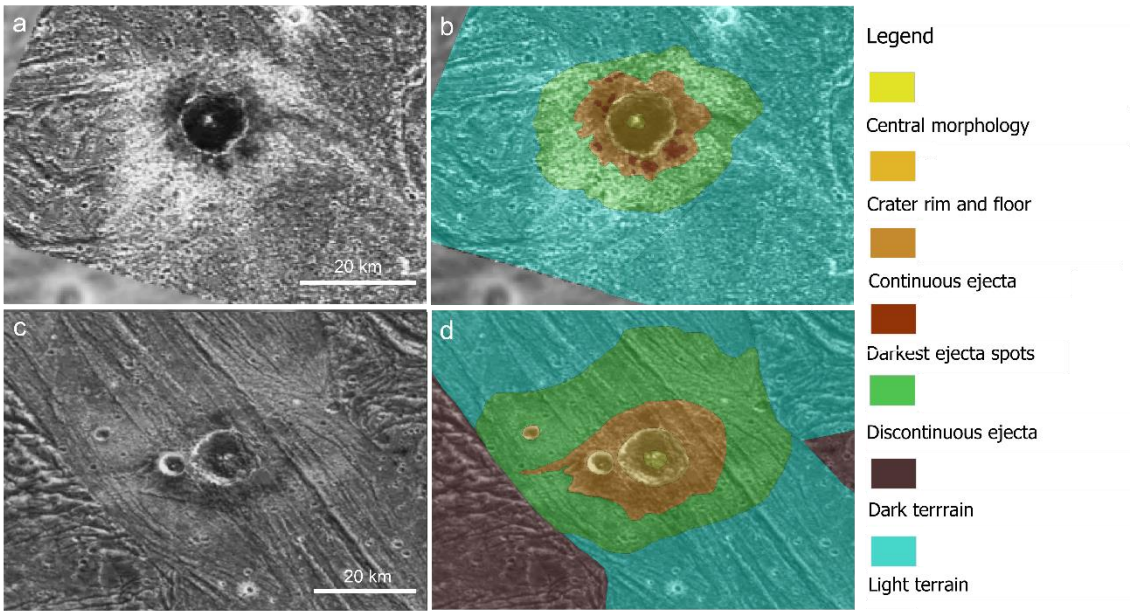

Figure 4.9: Dark halo craters (DHCs) Khensu and Nergal and bright ray crater (BRC): a) Galileo image and b) geologic map of Khensu, c) Galileo image and d) geologic map of Nergal.

4.4.3.3.2 Nergal (~38.8°N/~160.1°E)

Nergal, a 9 km diameter double halo crater like Khensu, is positioned in the northern portion of Ganymede's trailing hemisphere at ~38.8°N/~160.1°E within the light grooved terrain of Byblus Sulcus (Fig. 4.2). A high-resolution Galileo SSI imagery with 86 m/pxl is available. Similar to Khensu, Nergal was not observed by NIMS.

The four primary geological units identified in Nergal are the peak, rim and floor, a halo of dark material encircled by a halo of lighter material (Fig. 4.9 c, d). The peak exhibits a diameter of ~ 2.5 km. Located just outside the crater's rim, within the dark ejecta region, is an adjacent crater measuring about 3 km in diameter. Both craters presumably representing a double impact (Baby et al., 2023). The dark ejecta layer is thinner compared to the bright ejecta.

From our calculations, the excavation depth of Nergal is estimated to be around 0.7 km (Tab. 4.1) suggesting that both dark and bright materials originate from the near subsurface with the dark material comprising the dark halo situating just beneath the light terrain surface. Consequently, the dark terrain is inferred to be significantly thinner, spanning only a few meters in thickness. The bright ejecta is observed to be concentrated solely on the

impacted terrain, with no evidence of its presence on the neighboring dark terrain, furrows, or grooved terrain to the east. Additionally, a prominent ridge, likely broader and more elevated with an estimated thickness of ~ 1 km is visible through both the dark and bright ejecta areas.

4.4.4.4 Bright ray craters (BRCs) located at the border between dark and light terrain

4.4.4.4.1 Enkidu (~26.4°S/34.5°E)

Enkidu is a 122 km diameter large BRC and situated in the sub-Jovian hemisphere at ~26.4°S/34.5°E (Fig. 4.2). It shares the border between the dark terrain of Nicholson Regio and the light terrain of Harpagia Sulcus. Our analysis was conducted using the available image resolution of ~ 2 km/pixel. Unfortunately, no NIMS data are available to study this unique crater.

The main units identified are as follows: a central bright dome (diameter of ~ 31 km) of pancake shape almost filling a deeper nested crater, an outer flat floored crater that is terminated by the crater rim that forms a steep escarpment (Fig. 4.10). The bright ejecta form rays expanding ~9 crater radii in the light terrain. The rays that superpose the dark terrain are darker and less visible. The entire crater floor is composed of bright material, although the brightness gradually diminishes toward dark terrain side.

We also conducted mapping of three smaller craters superimposed on Enkidu's ejecta deposits. The nearest two neighboring craters feature a dark crater floor and dark ejecta, and have diameters up to ~ 11 km and 7 km implying excavation depths of ~ 1 km and ~0.62 km (Tab. 4.1). One is situated within Enkidu's discontinuous ejecta close to the border between dark and light terrain, with the majority of it located in the dark terrain. Its crater floor appears dark (Fig. 4.10 a, b). Presumably, the impact did not reach into the icy subsurface of Nicholson Regio. The second crater, located within Enkidu crater and close to its western rim, also features a dark floor and dark continuous ejecta (Fig. 4.10 a, b). Given the estimated excavation depth of 7.8 km (Tab. 4.1) it is expected that Enkidu completely impacted into the icy subsurface of the dark terrain of Nicholson Regio excavating bright ejecta material. Possibly, dark materials from Nicholson Regio were later transported in this portion of the crater during crater modification with the small crater superimposed on it. A third neighboring crater, with a diameter of ~ 7 km, is entirely situated in the light terrain and does not show any sign of darker ejecta (Fig. 4.10 a, b). Its

estimated excavation depth is ~ 0.6 km, where during this impact event likely only bright material became excavated from the light terrain subsurface.

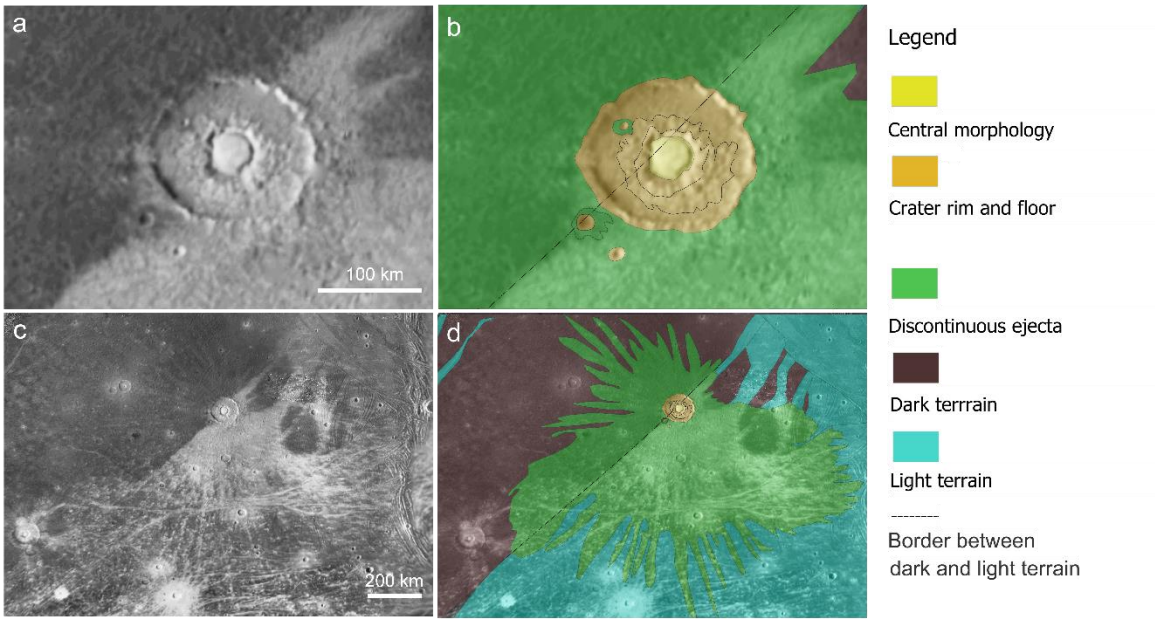

Figure 4.10: Bright ray crater (BRC) Enkidu: a) Voyager image and b) detailed geologic map of Enkidu crater, c) Voyager image and d) geologic map of Enkidu and its extended rays.

4.4.4.4.2. Melkart (~ 9.7°S/173.9°E)

The 103 km diameter large BRC, Melkart, is located at ~ 9.7°S/173.9°E. Like Enkidu, it is positioned at the border between the older dark terrain, Marius Regio, and the younger light grooved terrain situated between Tiamat Sulcus and Sippar Sulcus (Fig. 4.2). Melkart is one of the rare areas on Ganymede that have been observed during the Galileo mission by the SSI camera system as well as NIMS at high resolution (Stephan et al., 2008). Our analysis was conducted on the available image resolution of less than 200 m/pxl. The associated NIMS observation exhibits a resolution of 3.3 km/pxl.

Melkart's extended ejecta rays are emplaced on dark and light terrain (Fig. 4.11 a, b). The off-centered location of the pit-dome suggests an impact direction from SSW to NNE (Lucchetti et al., 2023). The eastern border between the dark and light terrain is clearly visible crossing the crater to the right of the central dome. On the contrary, the western border between these two terrain types does not show up within the crater and is probably hidden by the extensive ejecta blanket of Melkart in this part.

NIMS data indicate a slight change in abundance as well as grain size between the portions of the crater located within the dark and light terrain (Fig. 4.11 c, d). The border, however, does not fit exactly the border between these two terrains. The darker or less icy material is only concentrated along the inner crater rim. The excavation depth of Melkart could be estimated to be of ~6.7 km (Tab. 4.1). Thus, it is expected that Melkart impacted into the subsurface of dark and light terrain. Stephan et al. (2008) indicated that Melkart is not a very young crater (~3.6 to 3.9 Ga based on LDM). Therefore, the dark material within the crater could have originated from the dark terrain of Marius Regio, either during the crater modification phase or through subsequent weathering processes.

The western border between the light and dark terrain is hidden below the extensive ejecta blanket of Melkart. But, since no indication of this border can be seen inside the crater, it is assumed that the border is located outside the crater. However, similar processes resulting in the redeposition of dark material within the crater could also account for small amounts of dark material in the western portion of the crater.

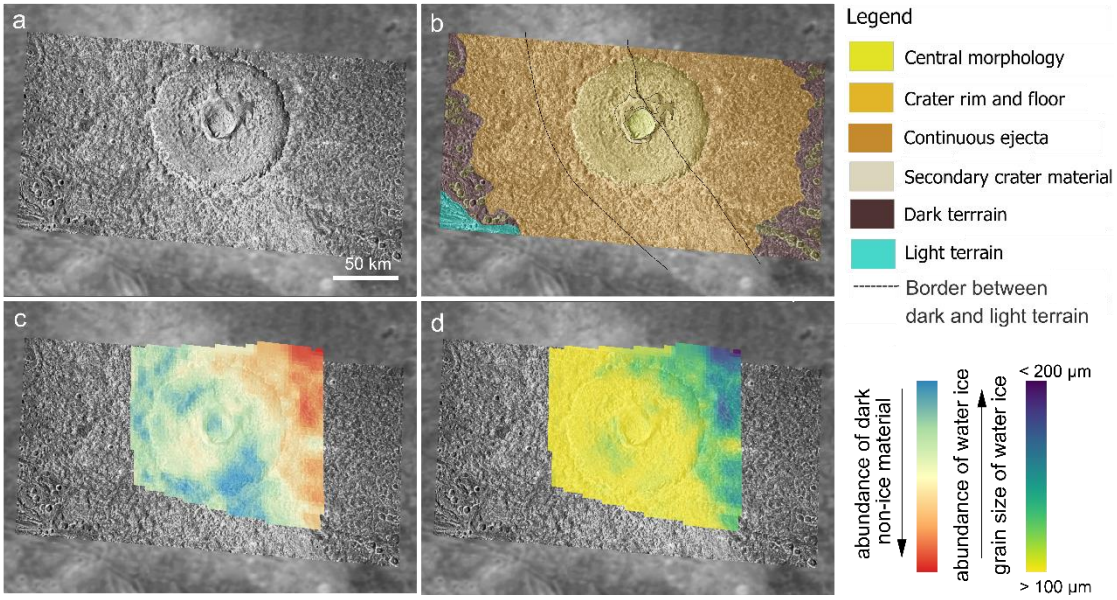

Figure 4.11: Bright ray crater (BRC) Melkart: a) Voyager + Galileo mosaic, b) geologic map, c) varying abundance of water ice/non-ice material and d) grain size of water ice as derived after Stephan et al. (2020) from NIMS data.

4.5 Discussion

Based on the current knowledge of the cratering process and excavation flow field of a hypervelocity impact as shown in Figure 4.1 (e.g., Maxwell, 1977; Melosh, 1989; Pierazzo

and Melosh, 2000, Kenkmann et al. 2014) information of a possible vertical stratigraphy of the subsurface can be gained. In the following we discuss the implications of the observed ejecta pattern (Fig. 4.12) with respect to the target stratification. Basic principles for interpretation are (i) that distal ejecta is emanating from a central, deeper source and proximal ejecta is sourced from a shallower position near the edge of the transient crater and (ii) and that an inverted (upside down) stratigraphy exists in the ejecta blanket with respect to the target stratification.

4.5.1 Formation scenarios for ray and halo crater types on Ganymede

Figure 4.12 a illustrates the stages involved in the formation of DRCs on dark terrain such as represented by Antum and Mir that both have bright crater interiors (Sections 4.4.4.1.1 and 4.4.4.1.2). To explain dark non-ice dominated ejecta, a top stratigraphic unit of a dark ice is required to exist before the projectile impacts the surface. During the excavation stage, a transient cavity forms, affecting both the dark terrain and the bright ice layer underneath. As the entire ejecta blanket is dark the original layer should have a thickness corresponding to the depth of the excavation zone. The crater interior is largely bright because of a bright ice layer underneath the dark layer. The subsequent modification stage, caused the bright icy materials of the lower part of the transient cavity to move upward to form a central uplift. The thickness of the dark layer should be similar to the maximum excavation depth. The measurements suggest that Antum excavated material from a maximum depth of ~ 1.2 km, while Mir reached a depth of ~ 0.7 km. Therefore, the thickness of the dark layer in both areas ranges between 0.7 to 1.2 km.

Figure 4.12 b illustrates the formation of a DRC on light terrain, specifically as expected for Kittu (Section 4.4.4.1.3). Kittu formed in the light terrain and consequently forms an inner bright halo. The bright layer, however, is not thick so that the more distal ejecta is governed by dark ice that is excavated from a source region of dark material that is closer to the point of impact and deeper seated. The interior of the crater is bright because the dark layer is underlain by bright ice that forms large parts of the displaced zone. This material is uplifted upon crater collapse and central uplift formation developing the pronounced bright icy central peak. Both, the dark and the bright ejecta materials originate from a maximum depth of ~ 1.2 km below the surface for Kittu with the bright ice layer superposing the dark ice layer. Therefore, it can be inferred that the combined thickness of

the two stratigraphic layers here, the light grooved and dark terrain materials, should be less than 1.2 km.

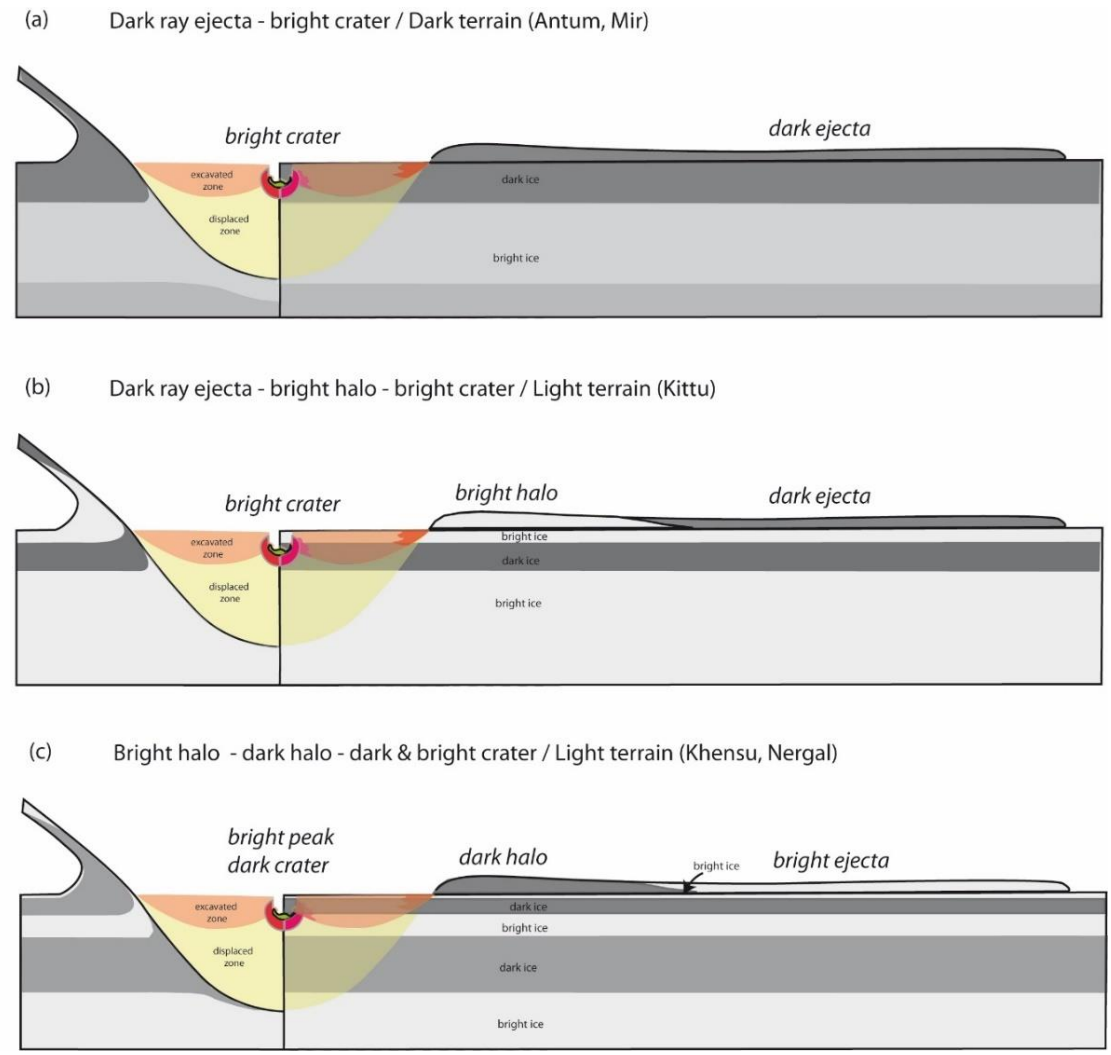

Figure 4.12: Schematic illustration of the subsurface layers required to explain various ejecta pattern. In the left part is the transient cavity illustrated and how the different layers are involved in the ejecta curtain. The larger right side shows the ejecta blanket and the position of different ice layers of the target prior to impact. The shown scenarios are applicable to craters a) in the dark terrain that contain a dark rayed ejecta blanket such as Antum and Mir, b) to dark ray craters formed in the light terrain with a bright crater, an inner bright ejecta/halo and extended dark rays such as observed for Kittu. c) to craters formed in the light terrain but with a dark crater, a dark inner and bright icy outer halo such as seen for Khensu and Nergal.

Figure 4.12c illustrates the stages of forming a dark halo crater in Ganymede's light terrain such as observed for the two small craters Nergal and Khensu (Section 4.4.3.3). These craters exhibit distinct features, including bright outer ejecta, dark ejecta surrounding the crater rim, a dark crater floor, and a bright peak. This indicates that the subsurface in this

area is extremely heterogeneous, with alternating layers of bright and dark ice. During the excavation stage, a transient cavity forms, affecting all of these layers. Initially, before the projectile impacts the surface, the top stratigraphic unit consists of a light grooved terrain. However, the bright ice layer should be so thin that the formation of a continuous ejecta blanket is suppressed. Instead, the dark inner halo is formed by the dark layer underneath. The dark layer may have a thickness of roughly half the maximum excavation depth of the specific crater, because the dark halo is surrounded by a halo of bright ejecta. This bright outer ejecta is formed due to a third, bright target layer considering that the outer ejecta is formed from a zone deeper sourced and closer to the point of impact. The two lowest layers 4 and 5 of the target are necessary to explain the dark crater interior and the bright tip of the central uplift. One, transition from bright to dark layers is responsible for the dark material inside the crater. In the final modification stage, the bright icy materials from the lowest portions of the transient cavity move upward to form a central uplift. The alternating layers of bright ice and dark ice, have a combined depth of 1.36 km for Khensu and 0.77 km for Nergal.

Large impacts such as Melkart and Enkidu excavate deep into the icy crust and do not show a clear variation in ejecta brightness thus suggesting a simple crustal structure dominated by bright ice (Section 4.4.4.4). During subsequent processes such as crater modification and later erosional processes due to sublimation and impact gardening some redistribution of dark material from the surrounding dark regions could be expected. Nevertheless, small craters such as the small dark craters superimposed within and outside of Enkidu's crater rim both featuring dark floors and ejecta, show very well the influence of the dark terrain material and resemble impacts such as Antum and Mir but with the differences that these craters do not excavate deep enough to reach the ice underneath. Therefore, thickness of the dark terrain of Nicholson Regio should not exceed 1 km as inferred from the excavation depth analysis of these craters.

If the target layers are not complete then the ejecta blanket should be somehow an image of it and is also not complete in one sector or the other. So, it is assumed that the impact resulting in Tammuz, exhibiting both bright and dark ejecta, may indeed have impacted along the boundary between a substantial section of the light terrain (an unresolved portion of Tiamat Sulcus) and a smaller area of the dark terrain linked to Marius Regio, which is highly disrupted in this region (Section 4.4.4.2). The estimated excavation depth is ~ 3.6 km, allowing it to penetrate more deeply into the bright icy layer compared to Antum and Mir. However, higher-resolution imagery is required to definitively confirm the exact

location and characterization of the crater and its ejecta pattern together with its geologic context.

The great variability of different halo and ray ejecta pattern reflects the heterogeneous structure of the ice crust of Ganymede. All patterns can be associated to a layered structure and the thickness of the variable layers can be roughly deduced. There is no need to explain dark crater interiors or dark halos by contamination with projectile material such as discussed in Schenk and McKinnon (1985, 1991) and Hibbitts et al. (2023). All investigated craters are larger than 9 km. This means that projectiles (carbonaceous chondrites or comets) will almost entirely melt and to a large degree vaporize upon release from shock loading (e.g. Pierazzo and Melosh, 2000). The tiny volume of the projectile in comparison with the large area of ejecta blanket and the crater interior would make it simply impossible to coat this area with re-condensated projectile material.

4.5.2 Thickness of dark terrain

Based on the furrows observed in the dark terrain of Galileo Regio, an estimated elastic thickness of ~ 0.5 km is suggested for this region (Nimmo and Pappalardo, 2004). Studies by Murchie et al. (1990) indicate a global average thickness for dark terrain ranging from 3 to 8 km, while McKinnon and Parmentier (1986) have estimated a thickness of 5 km for dark terrain. Models presented by Golombek and Banerdt (1986) relate the width and spacing of furrows suggesting a lithosphere thickness of 5-10 km at the time of furrow formation. However, when examining the relationship between crater rim height and crater diameter in dark terrains such as Nicholson Regio, Marius Regio, and Galileo Regio, it has been found that the thickness of dark terrain in these regions is ~ 1 km or less (Murchie et al., 1988). Even more, Prockter et al. (1998, 2000) proposed that formation of dark terrain material is thought to result from the concentration of admixed dark meteoritic material on the originally icy surface through processes such as sublimation, impact cratering, impact volatilization, and mass wasting.

Our analysis supports a thin uppermost layer of dark material on top of an ice-rich substrate, because the depth of excavation for the observed small craters with dark ejecta such as Antum and Mir suggests a dark terrain thickness not exceeding 1.2 km. This holds true, particularly within Marius Regio. But also, in other regions of dark terrain, such as Nicholson Regio, the dark terrain thickness is estimated to be ~1 km thick based on the excavation depth measurements of Enkidu's neighboring craters. Our analysis supports the

findings of Prockter et al. (1998). In regions of light terrain, such as where Kittu is present, the dark terrain thickness remains less than or equal to 1 km. Furthermore, in areas where Khensu is present, the excavated dark material originates from a depth of approximately 1.36 km, suggesting that this ejected material comes from three distinct stratigraphic layers: the upper light terrain, the intermediate dark terrain, and the lower bright ice layer. Consequently, the combined thickness of these three layers amounts to ~1.36 km, indicating that each of these layers is only a few meters thick. Similarly, in areas where Nergal is present, the excavated dark material originates from a depth of ~ 0.77 km, with the same three stratigraphic layers. Their combined thickness amounts to about 0.77 km, indicating each layer's thinness.

4.5.3 Implications for the light terrain formation

Large craters that impacted deep into the subsurface of both dark and light terrain do not show any significant differences between the subsurface properties indicating an ice-rich substrate for both terrains. Nevertheless, in some regions within the light terrain, such as the areas around DRC like Kittu, and DHCs like Nergal and Khensu, the presence of dark material close to the surface implies regional heterogeneities. The inferred vertical stratification has implications, whether the light terrain is formed by tectonic rifting or by spreading as discussed in Pizzi et al. (2017) and the studies presented in Pappalardo et al. (2004). Possibly, downward movement of the dark terrain material due to downfaulting could explain the existence of dark material in the subsurface. This would imply that rifting plays a significant role in the formation of light terrains on Ganymede in these locations. The extent of these dark layer should at least correspond to the extent of the developed crater diameter and the sandwiched portion of dark material in the subsurface should measure only a few meters in thickness.

It has to be noted that the studied craters lie relatively close to neighboring dark terrains of Galileo and Marius Regio as in case of Nergal and Khensu and Nicholson Regio in case of Kittu, and that Kittu is surrounded by numerous pieces of dark terrain. The uppermost icy layer in these regions is expected to be only a few meters thick and thus thinner than the underlying dark terrain material. Therefore, it cannot be fully excluded that some initial overflooding of dark terrain by icy material in the early phases of grooved terrain formation took place, which also could explain this observation.

4.6 Conclusions

We investigated halo and ray impact craters on Ganymede in order to use the composition/color and distribution of their ejecta blankets to decipher the stratigraphy of the icy subsurface in various light and dark terrains of Ganymede. The main conclusions of this study are:

- The ejecta of ice craters on Ganymede and the crater interiors are very sensitive tools to probe the vertical stratification of the ice crust.
- The investigated craters show that the ice crust of Ganymede is laterally heterogeneous.
- DRCs and DHCs are distinguishable by their average radial extent and standard deviations, with DRCs having the largest and DHCs the smallest values, while BRCs and BDRC fall in between.
- DRCs in the dark terrain allow to estimate the thickness of the dark terrain. The estimated thickness of dark terrain at Marius Regio likely does not exceed a thickness of about 1.2 km. The estimated thickness of dark terrain at Nicholson Regio likely does not exceed a thickness of about ~1 km.
- DRC in the light terrain such as where Kittu is present, the dark terrain material originated from a depth of ~1.2 km. The uppermost light terrain and near subsurface dark terrain here should be only few meters thick.
- A very thin uppermost ice layer on top of a dark layer in the light terrain could imply the possibility of flooding or spreading of older dark terrain by an icy substrate. This means some initial spreading may have played a role in Ganymede's light terrain formation.
- The DHCs, Khensu and Nergal suggest that locally the ice crust is composed of multiple dark and light ice layers. This has important implications for the geological history of Ganymede. In regions where Khensu is present, the excavated dark material originates from depths less than ~1.36 km. In areas with Nergal, the excavated dark material comes from depths less than ~0.77 km. As a result, the topmost light terrain and the dark terrain underneath is only a few meters thick.
- The DHC, Humbaba suggest that dark terrain material could be present at a maximum depth of ~ 3 km.
- Craters at geological boundaries indicate that these boundaries are not surficial features but extend into the crust. The BRCs such as Melkart and Enkidu at these

borders, with large excavation depths, indicate that they penetrate deep enough to reach underlying bright ice, implying the overlying dark terrain is relatively thin.

4.7 Outlook

Many more craters like the studied ones are suspected to exist on Ganymede's surface, most of them, however, are too small to study in this work. A better coverage of Ganymede by high-resolution images as well as spectral data could enable to study existing heterogeneities in the subsurface across Ganymede and should reveal more details of the processes responsible for the dark and light terrain formation. The JUICE mission with its unique payload such as the JANUS camera and MAJIS spectrometer experiment will enable to investigate these craters and more with an unprecedented resolution (Grasset et al., 2013; Stephan et al., 2021). The planned complete coverage of Ganymede's surface with a JANUS image resolution of 70 m during the GCO 5000 mission phase should make it possible to identify and define the distribution of these features and their association to major geologic terrain types. Particularly, the combination with color information given by the different filters of the JANUS camera in the visible and near-infrared light will help to avoid misinterpretations of different terrain types due to illumination conditions. Selected regions could be observed with a resolution of 7 m, when JUICE is orbiting the moon at relatively low altitude (GCO500 mission phase) and thus be analyzed in highest detail. Even more, joint observations of JANUS together with MAJIS to study the composition of the dark material and the surface ice properties could reveal differences in the chemical or physical properties of dark ejecta deposits originating from either excavated dark surface material from strongly weathered dark terrain or dark terrain resurfaced during the light terrain formation that became excavated from the subsurface of the light terrain. As mentioned above, since most of these craters are quite small an exact observation pointing will be required for JANUS observations alone and joint observations with MAJIS. Therefore, we would strongly support to push the planning of observing craters of the discussed types as region of interests for future high-resolution observations.

4.8 Acknowledgment

N. R. B. acknowledges the financial support of the DLR-DAAD PhD fellowship from the German Aerospace Center and the German Academic Exchange Service.

4.9 References

Baby, N. R., Wagner, R. J., Stephan, K., & Kenkmann, T., 2023. Stratigraphy, Crater Size–Frequency Distribution, and Chronology of Selected Areas of Ganymede's Light and Dark Terrains. The Planetary Science Journal, 4(9), 162. doi:10.3847/PSJ/acebed.

Bart, G. D., Daubar, I. J., Ivanov, B. A., Dundas, C. M., & McEwen, A. S., 2019. Dark halos produced by current impact cratering on Mars. Icarus, *328*, 45-57.

Belton, M. J., Klaasen, K. P., Clary, M. C., Anderson, J. L., Anger, C. D., Carr, M. H., ... & Pollack, J. B., 1992. The Galileo solid-state imaging experiment. Space Science Reviews, 60, 413-455.

Boyce, J., Barlow, N., Mouginis-Mark, P., & Stewart, S., 2010. Rampart craters on Ganymede: Their implications for fluidized ejecta emplacement. Meteoritics & Planetary Science, 45. https://doi.org/10.1111/j.1945-5100.2010.01044.x.

Collins, G. C., Patterson, G. W., Head, J. W., Pappalardo, R. T., Prockter, L. M., Lucchitta, B. K., & Kay, J. P., 2014. Global geologic map of Ganymede, US Geological Survey, 3237.

Collins, G. S., Melosh, H. J., & Marcus, R. A., 2005. Earth impact effects program: A web-based computer program for calculating the regional environmental consequences of a meteoroid impact on Earth. Meteoritics and Planetary science, 40(6), 817-840.

Daubar, I. J., Dundas, C. M., McEwen, A. S., Gao, A., Wexler, D., Piqueux, S., ... & Werynski, A., 2022. New craters on Mars: An updated catalog. Journal of Geophysical Research: Planets, 127(7), e2021JE007145.

Golombek, M., & Banerdt, W., 1986. Early thermal profiles and lithospheric strength of Ganymede from extensional tectonic features. Icarus, 68, 252-265. https://doi.org/10.1016/0019-1035(86)90022-9.

Grasset, O., Dougherty, M. K., Coustenis, A., Bunce, E. J., Erd, C., Titov, D., Blanc, M., Coates, A., Drossart, P., Fletcher, L. N., Hussmann, H., Jaumann, R., Krupp, N., Lebreton, J. P., Prieto-Ballesteros, O., Tortora, P., Tosi, F., and Van Hoolst, T., 2013. JUpiter ICy moons Explorer (JUICE): An ESA mission to orbit Ganymede and to characterise the Jupiter system: PSS, v. 78, p. 1-21.

Greeley, R., Klemaszewski, J.E., Wagner, R., & Galileo Imaging Team, 2000. Galileo views of the geology of Callisto. Planetary and Space Science, 48(9), 829-853.

Hansen, C. J., Bolton, S., Sulaiman, A. H., Duling, S., Bagenal, F., Brennan, M., ... & Withers, P., 2022. Juno's close encounter with Ganymede—an overview. Geophysical Research Letters, 49(23), e2022GL099285.

Hibbitts, C. A., 2023, Dark ray craters on Ganymede: Impactor or endogenous origin: Icarus, 394, 115400.

Holsapple, K. A., 1980. The equivalent depth of burst for impact cratering. Lunar Planet. Sci. Conf., XI, 1980, Proceedings, 3, 2379-2401.

Kaydash, V., Shkuratov, Y., & Videen, G., 2014. Dark halos and rays of young lunar craters: A new insight into interpretation. Icarus, 231, 22-33.

Kenkmann, T., Poelchau, M. H., and Wulf, G., 2014, Structural geology of impact craters: Journal of Structural Geology, v. 62, p. 156-182.

Kersten, E., Zubarev, A. E., Nadezhdina, I. E., Roatsch, T., Matz, K.-D., and Szczech, C. C., 2022. Updated Ganymede Mosaic from Juno Perijove 34 Images, Europlanet Science Congress, Granada, Spain, 18–23 Sep 2022, EPSC2022-450, https://doi.org/10.5194/epsc2022-450, 2022.

Kersten, E., Zubarev, A. E., Roatsch, T., & Matz, K. D., 2021. Controlled global Ganymede mosaic from voyager and Galileo images. Planetary and Space Science, 206, 105310.

Krohn, K., Jaumann, R., Otto, K., Hoogenboom, T., Wagner, R., Buczkowski, D. L., ... & Raymond, C. A., 2014. Mass movement on Vesta at steep scarps and crater rims. Icarus, 244, 120-132.

Lucchetti, A., Dalle Ore, C., Pajola, M., Pozzobon, R., Rossi, C., Galluzzi, V., ... & Palumbo, P., 2023. Geological, compositional and crystallinity analysis of the Melkart impact crater, Ganymede. Icarus, 401, 115613.

Maxwell, D. E., 1977. Simple Z model for cratering, ejection, and the overturned flap. In: Roddy, D. J., Pepin, R. O., and Merrill, R. B. (Eds.) Impact and explosion cratering, Pergamon Press, New York, 1003-1008.

McKinnon, W., and E.M. Parmentier, Ganymede and Callisto, 1986. In: Bums J. and Matthews, M. (Eds.), Satellites, University of Arizona Press, Tucson, 718-763.

Melosh, H. J., 1989. Impact cratering: A geologic process. Clarendon Press, Oxford, ISBN 0 19 504284 0, 245 pp.

Moore, J. M., Asphaug, E., Belton, M. J., Bierhaus, B., Breneman, H. H., Brooks, S. M., ... & Williams, K. K., 2001. Impact features on Europa: results of the Galileo Europa Mission (GEM). Icarus, 151(1), 93-111.

Murchie, S., Head, J., & Plescia, J., 1988. Crater densities and crater ages of different terrain types on Ganymede. Icarus, 81, 271-297. https://doi.org/10.1016/0019-1035(89)90054-7.

Murchie, S., Head, J., & Plescia, J., 1990. Tectonic and volcanic evolution of dark terrain and its implications for the internal structure and evolution of Ganymede. Journal of Geophysical Research, 95, 10743-10768. https://doi.org/10.1029/JB095IB07P10743.

Baby, N.R., Kenkmann, T., Stephan, K., Wagner, R., 2024. Polygonal impact craters on Ganymede, Meteoritics and Planetary Science, accepted.

Nimmo, F., and Pappalardo, R., 2004. Furrow flexure and ancient heat flux on Ganymede. Geophys. Res. Letters, 31. https://doi.org/10.1029/2004GL020763.

Pappalardo, R. T., Collins, G. C., Head, J. W., III, Helfenstein, P., McCord, T. B., Moore, J. M., Prockter, L. M., Schenk, P. M., Spencer, J. R., Dowling, T. E., and McKinnon, W. B., 2004, Geology of Ganymede, in Bagenal, F., ed., Jupiter. The Planet, Satellites and Magnetosphere, p. 363-396.

Passey, Q. R., and Shoemaker, E. M., 1982. Craters and basins on Ganymedeand Callisto: Morphological indicators of crustal evolution, In: Morrison, D. (Eds.) Satellites of Jupiter, Univ. of Ariz. Press, Tucson, pp. 379 - 434.

Perry, M. E., Barnouin, O. S., Daly, R. T., Bierhaus, E. B., Ballouz, R. L., Walsh, K. J., ... & Lauretta, D. S., 2022. Low surface strength of the asteroid Bennu inferred from impact ejecta deposit. Nature Geoscience, 15(6), 447-452.

Pierazzo, E., & Melosh, H. J., 2000. Understanding oblique impacts from experiments, observations, and modeling. Annual Review of Earth and Planetary Sciences, 28(1), 141-167.

Pizzi, A., Domenica, A. D., Komatsu, G., Cofano, A., Mitri, G., and Bruzzone, L., 2017, Spreading vs. Rifting as modes of extensional tectonics on the globally expanded Ganymede: Icarus, v. 288, p. 148-159.

Prockter, L. M., Head, J. W., Pappalardo, R. T., Senske, D. A., Neukum, G., Wagner, R., ... & Belton, M. J., 1998. Dark terrain on Ganymede: Geological mapping and interpretation of Galileo Regio at high resolution. Icarus, 135(1), 317-344.

Prockter, L. M., Figueredo, P. H., Pappalardo, R. T., Head III, J. W., & Collins, G. C., 2000. Geology and mapping of dark terrain on Ganymede and implications for grooved terrain formation. Journal of Geophysical Research: Planets, 105(E9), 22519-22540.

Schenk, P. M., & McKinnon, W. B., 1991. Dark-ray and dark-floor craters on Ganymede, and the provenance of large impactors in the Jovian system. Icarus, 89(2), 318-346.

Schenk, P. M., and McKinnon, W. B., 1985. Dark halo craters and the thickness of grooved terrain on Ganymede: J. of Geophys. Res., 90, C775-C783.

Schenk, P. M., Chapman, C. R., Zahnle, K., and Moore, J. M., 2004. Ages and interiors: the cratering record of the Galilean satellites, in Bagenal, F., Dowling, T. E., and McKinnon, W. B. (Ed.), Jupiter: The planet, satellites and magnetosphere: Cambridge, UK, Cambridge University Press, p. 427 - 456.

Schenk, P., Hamilton, D. P., Johnson, R. E., McKinnon, W. B., Paranicas, C., Schmidt, J., & Showalter, M. R., 2011. Plasma, plumes and rings: Saturn system dynamics as recorded in global color patterns on its midsize icy satellites. Icarus, 211(1), 740-757.

Schmidt, R. M., & Housen, K. R., 1987. Some recent advances in the scaling of impact and explosion cratering. International Journal of Impact Engineering, 5(1-4), 543-560.

Stephan, K., Hibbitts, C. A., and Jaumann, R., 2020. H2O-ice particle size variations across Ganymede's and Callisto's surface: Icarus, v. 337, p. 113440.

Stephan, K., Hibbitts, C.A., Ligier, N., Molyneux, P.M., Poulet, F., Prockter, L.M., Hendrix, A.R.m Collins, G.C., Ahrens, C., Jaumann, R., 2024. Ganymede’s Surface Composition, In: Volwerk, M., McGrath, M., Jia, X., Spohn, T. (Eds.) Ganymede. Cambridge University Press & Assessment, 147 - 164, 978-1-108-83295-3.

Stephan, K., Jaumann, R., Wagner, R., Clark, R. N., Cruikshank, D. P., Giese, B., ... & Matson, D. L., 2012. The Saturnian satellite Rhea as seen by Cassini VIMS. Planetary and Space Science, 61(1), 142-160.

Stephan, K., R. Wagner, C. A. Hibbitts, G. B. Hansen, and R. Jaumann, 2008. Ganymede's Impact Crater Melkart: An Example for a Combination of High-Resolution Spectral and Geological Analyses in the Outer Solar System, The Science of Solar System Ices (ScSSI): A Cross-Disciplinary Workshop, abstr. 9060.

Stephan, K., Roatsch, T., Tosi, F., Matz, K.-D., Kersten, E., Wagner, R., Molyneux, P., Palumbo, P., Poulet, F., Hussmann, H., Barabash, S., Bruzzone, L., Dougherty, M., Gladstone, R., Gurvits, L. I., Hartogh, P., Iess, L., Wahlund, J.-E., Wurz, P., Witasse, O., Grasset, O., Altobelli, N., Carter, J., Cavalié, T., D'Aversa, E., Della Corte, V., Filacchione, G., Galli, A., Galluzzi, V., Gwinner, K., Hauber, E., Jaumann, R., Krohn, K., Langevin, Y., Lucchetti, A., Migliorini, A., Piccioni, G., Solomonidou, A., Stark, A., Tobie, G., Tubiana, C., Vallat, C., van Hoolst, T., and Team, J. S., 2021. Regions of interest on Ganymede's and Callisto's surfaces as potential targets for ESA's JUICE mission, Planetary and Space Science, 208, 105324.

Thompson, T. W., Zisk, S. H., Shorthill, R. W., Schultz, P. H., & Cutts, J. A., 1981. Lunar craters with radar bright ejecta. Icarus, 46(2), 201-225.

Williams, D. A., Denevi, B. W., Mittlefehldt, D. W., Mest, S. C., Schenk, P. M., Yingst, R. A., ... & Dawn Science Team, 2014. The geology of the Marcia quadrangle of asteroid Vesta: Assessing the effects of large, young craters. Icarus, 244, 74-88.

Williams, D. A., Kneissl, T., Neesemann, A., Mest, S. C., Palomba, E., Platz, T., ... & Russell, C. T., 2018. The geology of the Kerwan quadrangle of dwarf planet Ceres: Investigating Ceres’ oldest, largest impact basin. Icarus, 316, 99-113.

Yingst, R. A., Mest, S. C., Berman, D. C., Garry, W. B., Williams, D. A., Buczkowski, D., ... & Schenk, P. M., 2014. Geologic mapping of Vesta. Planetary and Space Science, 103, 2-23.

5 General Discussion and Outlook

In this chapter the results of Chapter 2, 3 and 4 will be combined and discussed for answering the research question presented in Chapter 1 and presenting considerations for potential further studies.

i. The derived CSFDs presented in Chapter 2 generally support that dark cratered terrains are the oldest, while light terrains are younger, which is consistent with previous studies (Patterson 2010; Collins et al., 2013). Hence, CSFDs of light and dark terrains are very close, and suggest that the light terrain started to form shortly after dark terrain formation ended. Consequently, also the differences in CSFDs of the different light terrain units consisting of smooth and grooved light terrain are also relatively small and could have been formed subsequently to each other or at the same time period.

ii. In regions that appear to be more or less unaffected by secondary impacts the smooth portions appear to be formed before the grooved terrain, which could imply a change in tectonic style with the formation of smooth terrain in the beginning of the light terrain formation followed by the light grooved terrain formation. However, in more extensively resurfaced regions such as Mummu Sulcus this relationship is not clear and sometimes contradicted by cross-cutting relationships of the individual light terrain units. Furthermore, craters in the grooved terrain can be hidden in the grooves and therefore possibly not all relevant craters are included in the CSFDs of the light grooved terrain.

iii. The beginning of Ganymede's light terrain formation early in Ganymede's evolution is also independently supported by both of the used crater chronology models. Both models favor that the light terrain started to form within a time gap of only ~0.2 Ga after the adjacent dark terrain units were established. But they propose contrasting timeframes. According to the LDM, light terrains range in absolute age from ~3.6 Ga to 4 Ga, and dark terrains range from ~3.7 Ga to 4.2 Ga. Using the JCM, light terrain units exhibit absolute ages between ~0.7 Ga and > 4 Ga, while dark terrains range from ~3.5 to > 4 Ga. Dark lineated terrains and reticulate terrains possess intermediate ages between dark cratered terrains and light terrains. Prolonged tectonic resurfacing activities, primarily involving normal faulting, strike-slip faulting, and /or spreading tectonism, extensively modified the surface,

transitioning from dark cratered terrain to dark lineated terrain and eventually into new light terrain units. Within the light terrain, similar tectonic activities contributed to the formation of even more complex terrain units.

iv. Absolute surface ages of Ganymede's terrain units are necessary to relate the light terrain formation to global processes of Ganymede's evolution and could provide valuable constraints for the theoretical modelling of the thermal history of Ganymede. Even with results obtained by the Galileo mission, there are still unknowns or uncertainties about Ganymede's interior structure and thermal history (e.g., Schubert et al., 2004, 2010). It is not clear for how long the dynamo in Ganymede's core has been active or when it started, or if the water ocean really exists. Also, depth and thickness of the potential ocean is not fully known.

In previous studies explaining the formation of light terrains on Ganymede, various processes have been considered, including internal differentiation and subsequent global volume expansion, tidal heating due to Laplace resonance and orbital recession, nonsynchronous rotation in the past, and the possibility of large impacts. LDM favors light terrain formation through internal differentiation due to its shorter timeframe in Ganymede's geological evolution, while the JCM-derived ages require additional forces such as due to Laplace resonance, orbital recession, and/or nonsynchronous rotation as potential causes. It is uncertain whether large impacts alone can generate the necessary thermal anomalies for tectonic activity, as Ganymede's outer neighbor Callisto lacks tectonically resurfaced terrains. However, given the generally high CSFDs for dark as well as light terrains a relatively short time frame of the light terrain formation might be favorable.

v. Absolute model ages derived with the two existing impact cratering chronologies still remain to be uncertain (Neukum et al., 1998; Zahnle et al., 2003). The LDM chronology is based on the similarity of CFDS between Ganymede and inner solar system bodies, inferring asteroids from the Main Belt (MBAs) to represent the dominant type of impactors in the Jovian system (Neukum et al., 1998). This view has been put into doubt since MBAs currently provide no significant contribution to impacting the Jovian satellites (Zahnle et al., 2003; Schenk et al., 2004). Furthermore, Bottke et al. (2022, 2023) recently discussed that the similarity in CSFDs from inner and outer solar system bodies are a consequence of collisional evolution in various potential projectile families, which makes CSFDs

predominantly created from cometary bodies more or less indistinguishable from those of asteroidal impactors. The JCM chronology is based on current impact and cratering rates extrapolated back to the early solar system (Zahnle et al., 2003), but it has not yet been discussed and inferred if conditions in the early solar system, especially the period of migration of the four large planets could have caused much higher impact and cratering rates similar to the LDM chronology prior to ~3.5 Ga. Recently, impact and cratering rates given by Zahnle et al. (2003) have been updated, based on new findings and assumptions (Nesvorný et al., 2023). These results could no more be included in the studies presented in Chapter 2 and will be used as a topic in future studies.

In order to better constrain the surface age of Ganymede's light terrain units and thus the time frame of their formation various further topics for intense studies are necessary. These topics can be classified into the following four categories: (1) Extending the image data base by global high-resolution imaging; (2) improving the existing impact chronology models; (3) improving theoretical modelling focused on the thermal history of Ganymede to derive the most likely scenario of light terrain formation with time; (4) a landing mission with the capability to derive absolute ages of surface materials in order to calibrate an age with a crater frequency.

Particularly, since absolute surface ages are only based on impact and cratering rates of the members of a potential impactor family, radiometric ages of surface materials would be an important tool to calibrate crater frequencies with absolute ages. This can only be achieved with a landing mission, either with *in-situ* measurements of surface materials, or with a sample return to Earth. A lander, however, is currently highly unlikely but could be a potential mission scenario beyond the year 2050. Returning a lander from the surface of one of the Galilean satellites is problematical (as well as highly expensive) because of the high amount of energy and fuel needed for relaunch back on a course to Earth. To determine surface ages, *in-situ* measurements taken from soil and/or rock samples aboard a lander laboratory are necessary, involving destructive analysis of these samples (e.g., Van Gasselt et al., 2018). If samples such as, e.g., solidified cryovolcanic fluids (or impact melt) are even datable using radiometric measurements is not clear and depends of the composition of this material (Kargel, 1989). Furthermore, almost all landing

missions on the Galilean satellites suggested so far are targeted to Europa because of its astrobiological importance (McEwen et al., 2002). This icy satellite has a very young surface with a low impact crater frequency which makes it difficult to be used for calibrating a radiometric age with a crater frequency. A lander on either Ganymede or Callisto is unlikely to be planned in the next ~20-50 years. Unlike for the chronologies of inner solar system bodies, the ages of the Galilean satellite surfaces therefore will remain uncertain for a long time and can only be inferred from impact cratering chronology models, supported by models on the thermal evolution.

vi. The straight rims of polygonal craters discussed in Chapter 3 probably have been developed during the crater modification stage, primarily through slumping or faulting along preexisting fracture and fault planes of weakness. Although the dark cratered terrain is typically considered to be simply cratered, it surprisingly hosts polygonal craters in nearly equal numbers compared to the light terrain. This arises because the dark terrain is the oldest and naturally accumulates craters over time, influenced by fractures and likely invisible fracture planes beneath the surface. The existence of crater rim segments with straight alignment is attributed to the proximity of tectonic linear structures, including those concealed beneath the surface. This observation offers additional evidence supporting that these tectonic linear structures are deep-seated faults, which are not only existent in Ganymede's light terrain but occur across Ganymede's entire surface. The results also imply that the rheological properties of the subsurface in the dark and light terrain does not show any significant differences.

vii. Despite the differences in size, temperature, composition, and degree of differentiation between Ganymede and other celestial bodies, the presence of polygonal impact craters on Ganymede provides indirect evidence of the intense tectonic activity that Ganymede has undergone in comparison to two other moons, namely the warmer Ceres and the colder Dione. The abundance and appearance of polygonal craters independently of the geologic terrain supports that Ganymede's tectonic activity is not only concentrated on the light terrain, but possibly represents a combination of early impact generated surface deformation followed by tectonic resurfacing (Prockter et al., 2000, Rossi et al., 2023).

viii. The analysis of craters and their ejecta deposits have proven to be efficient to probe the vertical stratification of Ganymede's crust. Craters emplaced in Ganymede's dark terrain exhibiting different ejecta material, such as rays sometimes associated with visually dark non-ice material dominating the ejecta deposits rather than water ice, strongly support that the dark terrain is characterized by a thin layer (thickness < 1km) of accumulated dark material on top of a layer dominated by water ice. Excavation depth measurements of dark ray craters, such as Antum and Mir, reveal that the dark terrain's thickness does not exceed 1 km. The results support the assumption of Prockter et al. (1998, 2000) that the dark terrain is composed of a thin veneer of low albedo material, concentrated on the surface as a sublimation lag probably due to thermally driven segregation of ice and non-ice surface components (Spencer 1987 a, b) and downslope movement of the dark non-ice component (Oberst et al. 1999).

In contrast, a dark ray crater located in a light terrain region indicates the presence of a thin near-surface layer composed of dark material at ~ 1 km depth. The layer exhibits a thickness of only a few meters. Dark halo craters located in the light terrain can only be explained by dark material existing in the near subsurface. Even more, the distinctive two concentric dark and bright ejecta pattern implies the likely presence of heterogeneous stratigraphic layers beneath the surface, alternating between dark ice and bright ice. Excavation depth data further supports that the dark terrain material is sandwiched between bright ice layers, with a thickness of just a few meters.

Nevertheless, small craters fully located in the light terrain indicate that they could have impacted on small pieces of dark terrain located within the light terrain that were not fully resurfaced yet or that dark material still exists in the subsurface of the light terrain after the deformation of the area. Even more, impact events that are large enough to penetrate through the thin dark layer show no indication of major differences in the subsurface properties of dark and light terrain.

ix. Craters that excavated dark material from the subsurface could only be identified to be located in the grooved light terrain that were supposed to be affected by tectonic resurfacing processes such as rifting. This is consistent with the previous models of tectonic processes described by Pappalardo et al. (2004) and Pizzi et al. (2017). Many more of these special craters are expected to exist on Ganymede's surface.

But these craters are mostly too small to study using the current data base. Additional color data and/or spectral data of all these craters would enable to study compositional differences between material excavated from uppermost surface layer or subsurface. A more detailed answer to the subsurface heterogeneities of the light terrain could be given by future subsurface sounding. In order to find clear evidence for spreading such as implied by Pizzi et al. (2017) the distribution of these special kind of craters have to be mapped across Ganymede's entire surface and especially looked for in the smooth terrain. If the smooth light terrain is free of these craters, it could be indeed a sign for a process such as spreading, which brings cleaner ice to the surface. If indeed such craters also exist in smooth light terrain, they would provide evidence that tectonic resurfacing such as rifting is also responsible for the smooth light terrain formation.

6 Conclusions

In this thesis a study of Ganymede's light terrain is presented that complements previous work, focusing on structural analysis that used Ganymede's ubiquitous impact craters to indirectly further our understanding of the processes in Ganymede's light terrain and time frame of its formation. In Chapter 2, we presented the geologic mapping and crater size-frequency distribution (CSFD) measurements and the derivation of both relative and absolute surface ages applied to local-scale terrain units on Ganymede. This detailed approach enhances our understanding of the stratigraphy and serves as a crucial tool for resolving the causes of tectonic activities on Ganymede over various time periods. The studies on polygonal impact craters presented in Chapter 3 provide the first-ever report of these crater types spread across Ganymede's surface and provide an indirect additional view onto Ganymede's tectonic processes. As presented in Chapter 4, the potential of specific crater types, such as dark halo, dark ray, and combined dark and bright ejecta craters, to unveil subsurface stratigraphic details, were utilized to comprehend the vertical stratigraphy of the subsurface in the dark and light terrain and to gain evidence and more details about the processes such as potential rifting and spreading.

The results underline the potential of Ganymede's unique impact craters to indicate not only the age of the different terrain units but also to reveal heterogeneities in the subsurface

characteristics of both dark and light terrain and provides implications for the processes that could be responsible.

However, to fully reveal the nature of Ganymede's tectonic activity is limited by the current available data set with its varying and often insufficient resolutions as well as inconsistent illumination conditions. Future observations are necessary, as proposed by ESA's JUICE mission, which successfully launched on the 14th April 2023 and will reach the Jovian system after a 10-year journey. The results and implications of this study provides a very valuable input for preparing the observations of Ganymede in particular for the JANUS experiment. Unlike during the Galileo and the recent Juno mission, JUICE will be the first mission orbiting an icy satellite, in this case Ganymede, for a longer period of time. JANUS will provide a global coverage of Ganymede at a medium resolution of 70 m/pxl, which is at least 50 times better than most Galileo images and the observation of selected region with highest resolution of ~ 7m/pxl (Jaumann et al., 2024, Stephan et al., 2021). JANUS images will offer the detailed geologic mapping and characterization of details in the dark terrain and structural units of the light terrain. Digital elevation models of Ganymede's surface derived from JANUS stereo images in combination with topographic profiles given by the GALA instrument will offer a detailed characterization and quantification of tectonic processes but also crater morphologies and any cryovolcanic features.

Further, JANUS will therefore significantly improve the current estimates of the crater size-frequency distributions in Ganymede's terrain units. Together with possibly improved crater chronology models will finally enable to constrain the time, duration and nature of the formation scenarios responsible for Ganymede's past geologic activity. Furthermore, the images will not only help to identify and map Ganymede's unique craters and to study the variations in the subsurface properties of the dark and light terrains in highest detail, the planned complete coverage of color images with resolutions down to 200 m/pxl and selected areas with up to 50 m/pxl using spectral filters from about 0.35 to 1 µm will enable to study compositional differences of the dark non-ice materials. This study will be complemented by detailed spectral mapping using MAJIS instrument offering the correlation of geologic features with mineralogical information. Finally, RIME will sound Ganymede's subsurface to assess the dynamics and heterogeneities in the subsurface ice by detecting compositional or phase boundaries. Together with JANUS data (images and topographic information) with data acquired by MAJIS and RIME will enable the

derivation of stratigraphic and structural characteristics of Ganymede's crust and its possible deformational processes.

7 References

Allison, M. L., Clifford, S. M., 1987. Ice-covered water volcanism on Ganymede, J. Geophys. Res. 92, 7865–7876.

Baby, N. R., Wagner, R. J., Stephan, K., Kenkmann, T., 2023. Stratigraphy, Crater Size–Frequency Distribution, and Chronology of Selected Areas of Ganymede's Light and Dark Terrains. Planet. Sci. J. 4:162, https://doi.org/10.3847/PSJ/acebed.

Bagenal, F., Dowling, T. E., McKinnon, W. B., 2004. Editorial introduction. In: Bagenal, F., Dowling, T. E., McKinnon, W. B. (Eds.), Jupiter – the planet, satellites, and magnetosphere. Cambridge Univ. Press, Cambridge, U.K., pp. 1–18.

Belton, M. J. S., Klaasen, K. P., Clary, M. C., Anderson, J. L., Anger, C. D., Carr, M. H., Chapman, C. R., Davies, M. E., Greeley, R., Anderson, D., Bolef, L. K., Towsend, T. E., Greenberg, R., Head, J. W. III, Neukum, G., Pilcher, C. B., Veverka, J., Gierasch, P. J., Fanale, F. P., Ingersoll, A. P., Masursky, H., Morrison, D., Pollack, J. B., 1992. The Galileo Solid-State imaging experiment. Space Sci. Rev. 60, 413–455.

Bland, M. T., Showman, A. P., Tobie, G., 2009. The orbital–thermal evolution and global expansion of Ganymede. Icarus 200 (1), 207 - 221, doi:10.1016/j.icarus.2008.11.016.

Bland, M.T, McKinnon, W.B., 2015. Forming Ganymede's grooves at smaller strain: toward a self-consistent local and global strain history for Ganymede. Icarus 245, 247–262. doi:10.1016/j.icarus.2014.09.008.

Bland, M.T., Showman, A.P., 2007. The formation of Ganymede's grooved terrain: numerical modelling of extensional necking instabilities. Icarus 189, 439–456. doi:10.1016/j.icarus.2007.01.012.

Bottke, W. F., Marschall, R., Vokrouhlický, D., Nesvorný, D., Morbidelli, A., Deienno, R., Kirchoff, M., Marchi, S., Levison, H., 2022. Collisional Evolution of the Primordial Kuiper Belt, Scattered Disk, and Trojan Populations. Lunar Planet. Sci. Conf. XLIII, abstr. 2638.

Bottke, W. F., Vokrouhlický, D., Marshall, R., Nesvorný, D., Morbidelli, A., Deienno, R., Marchi, S., Dones, L., Levison, H. F., 2023. The collisional evolution of the primordial Kuiper Belt, its destabilized population, and the Trojan asteroids. Planet. Sci. J. 4:168, https://doi.org/10.3847/PSJ/ace7cd.

Cameron, M.E., Smith-Konter, B.R., Burkhard, L., Pappalardo, R.T., Collins, G.C., 2016. Strike-slip faulting on Ganymede: morphological mapping and failure mechanics. Lunar Planet. Sci. Conf. XLVII, abstr. 2630.

Cameron, M. E., Smith-Konter, B. R., Burkhard, L., Collins, G. C., Seifert, F., Pappalardo, R. T., 2018. Morphological mapping of Ganymede: Investigating the role of strike-slip tectonics in the evolution of terrain types. Icarus 315, 92-114, doi:10.1016/j.icarus.2018.06.024.

Carr, M. H., Belton, M. J. S., Bender, K., Breneman, H., Greeley, R., Head, J. W., Klaasen, K. P., McEwen, A. S., Moore, J. M., Murchie, S., Pappalardo, R. T., Plutchak, J., Sullivan, R., Thornhill, G., Veverka, J., 1995. The Galileo Imaging Team plan for observing the satellites of Jupiter. J. Geophys. Res. 100, No. E9, 18,935–19,955.

Cassen, P., Peale, S. J., Reynolds, R. T., 1980. On the comparative evolution of Ganymede and Callisto, Icarus 41, 232-239, doi:10.1016/0019-1035(80)90006-8.

Collins, G. C., Patterson, G. W., Head, J. W., Pappalardo, R. T., Prockter, L. M., Lucchitta, B. K., Kay, J. P., 2013. Global geologic map of Ganymede, U.S.G.S., 3227, doi:10.3133/sim3237.

Collins, G. C., Head III, J. W., Pappalardo, R. T., 1998a. The role of extensional instability in creating Ganymede grooved terrain: Insights from Galileo High-Resolution Stereo Imaging. Geophys. Res. Lett. 25(3), 233-236.

Collins, G. C., Head, J. W., Pappalardo, R. T., 1998b. Formation of Ganymede grooved terrain by sequential extensional episodes: Implications of Galileo observations for regional stratigraphy. Icarus, 135(1), 345-359.

Collins, G. C., Head, J. W., Pappalardo, R. T. and the Galileo SSI Team, 1998c. Analysis of regional stratigraphic relationships in Ganymede grooved terrain: Galileo results. Lunar Planet. Sci. Conf. XXIX, abstr. 1319.

Collins, G. C., Head, J. W., Pappalardo, R. T., and the Galileo SSI Team, 2000. A global database of grooves and dark terrain on Ganymede, enabling quantitative assessment of terrain features. Lunar Planet. Sci. Conf. XXXI, abstr.. 1034.

Collins, G. C., McKinnon, W. B., Moore, J. M., Nimmo,F., Pappalardo, R. T., Prockter, L. M., Schenk, P. M., 2009. Tectonics of the Outer Planet Satellites. In: Watters, T. R., Schultz, R. A (Eds.), Planetary Tectonics. Cambridge Univ. Press, Cambridge, U.K., p. 264-350, doi:10.1017/cbo9780511691645.008.

Cruikshank, D. P., Brown, R. H., Calvin, W. M., Roush, T. L., Bartholomew, M. J., 1998. Ices on the Satellites of Jupiter, Saturn, and Uranus, In: Schmidt, B., De Bergh, C., Festou, M. (Eds.), Solar System Ices. Interntl. Symposium „Solar System Ices“, Toulouse, France, 27-30 March, 1995. Kluwer Acad. Publ., Dordrecht, NL, doi:10.1007/978-94-011-5252-5_24.

Dalton, J. B., Cruikshank, D. P., Stephan, K., McCord, T. B., Coustenis, A., Carlson, R. W., Coradini, A., 2010. Chemical composition of icy satellite surfaces. Space Sci. Rev. 153, 113–154.

Dombard, A. J., McKinnon, W. B., 2001. Formation of Grooved Terrain on Ganymede: Extensional Instability Mediated by Cold, Superplastic Creep. Icarus 154, 321-336, doi:10.1006/icar.2001.6728.

Fabi, M., Kenkmann, T., Wulf, G., Baby, N., Stephan, K., Wagner, R., 2022. Kinematic restoration of Ganymede's dark terrain. Europlanet Science Congress 2022, Granada, Spain, 18-23-Sep. 2022, abstr. EPSC2022-134.

Gehrels, T., 1976. Pictures of Ganymede. In: Gehrels, T. (Ed.), Jupiter. Univ. of Arizona Press, Tucson/Az., pp. 406–422.

Giese, B., Oberst, J., Roatsch, T., Neukum, G., Head, J. W., Pappalardo, R. T., 1998. The local topography of Uruk Sulcus and Galileo Regio obtained from stereo images. Icarus 135 (1), 303-316.

Giese, B., Wagner, R., Neukum, G., Pappalardo, R., Head, J. W., and the Galileo SSI Team, 2001a. The topography of Ganymede’s Arbela Sulcus. Lunar Planet. Sci. Conf. XXXII, abstr. 1743.

Giese, B., Wagner, R., Neukum, G., Pappalardo, R., Head, J. W., and the Galileo SSI Team, 2001b. The topography of bright/dark terrain on Ganymede. Lunar Planet. Sci. Conf. XXXII, abstr. 1751.

Golombek, M. P., 1982. Limits on the Expansion of Ganymede and the thickness of the lithosphere. Lunar Planet. Sci. Conf. XIII, abstr., 269 – 270.

Hauber, E., Wagner, R., 2009. Planetary geology. In: Trümper, J. E. (Ed.), Landolt-Börnstein New Series VI/4B, Springer Publ., Berlin, Germany, pp. 271–352.

Head, J., Pappalardo, R., Collins, G., Belton, M. J. S., Giese, B., Wagner, R., Breneman, H., Spaun, N., Nixon, B., Neukum, G., Moore, J., 2002. Evidence for Europa-like tectonic resurfacing styles on Ganymede Geophys. Res. Lett. 29 (24), 4-1-4-4, doi:10.1029/2002gl015961.

Hibbitts, C. A., 2023. Dark ray craters on Ganymede: Impactor or endogenous origin: Icarus 394, p. 115400.

Hiesinger, H., Head, J. W., and the Galileo Imaging Team, 1998. Geologic Map of the Nippur Sulcus Region of Ganymede. Lunar Planet. Sci. Conf. XXIX, abstr. 1283.

Howell, S. M., Pappalardo, R. T., 2018. Band Formation and Ocean-Surface Interaction on Europa and Ganymede. Geophys. Res. Lett. 45, 4701, doi:10.1029/2018gl077594.

Hussmann, H., Sohl, F., Oberst, J., 2009. Basic data of planetary bodies. In: Trümper, J. E. (Ed.) Landolt-Börnstein New Series VI/4B, Springer Publ., Berlin, Germany, pp. 163–181.

Jaumann, R., Stephan, K., Wagner, R., Hussmann, H., Palumbo, P., Lucchetti, A., Postberg, F., Roatsch, T., Stark, A., 2024. Ganymede's stratigraphy and geologic evolution. In: Volwerk, M., McGrath, M., Xianzhe, J., Spohn, T. (Eds.), Ganymede. Cambridge University Press, in press.

Johnson, T. V., 1998. Introduction to icy satellite geology. In: Schmidt, B., De Bergh, C., Festou, M. (Eds.), Solar System Ices. Interntl. Symposium „Solar System Ices", Toulouse, France, 27-30 March, 1995. Kluwer Acad. Publ., Dordrecht, NL, pp. 511–523.

Kargel, J. S., 1989. Can we radiometrically date cryovolcanic flows on icy satellites ? Lunar Planet. Sci. Conf. XX, abstr., 498–499.

Kargel, J. S., 1998. Physical chemistry of ices in the outer solar system. In: Schmidt, B., De Bergh, C., Festou, M. (Eds.), Solar System Ices. Interntl. Symposium „Solar System Ices", Toulouse, France, 27-30 March, 1995. Kluwer Acad. Publ., Dordrecht, NL, pp. 3–32.

Kersten, E., Zubarev, A. E., Roatsch, T., Matz, K. D., 2021. Controlled global Ganymede mosaic from voyager and Galileo images. Planet. Space Sci. 206, 105310.

Klaasen, K. P., Clary, M. C., Janesick, J. R., 1984. Charge-coupled device television camera for NASA's Galileo mission to Jupiter. Opt. Eng. 23 (3), 334–342.

Lewis, J. S., 1997. Physics and chemistry of the solar system. Acad. Press, San Diego, Ca., 591p.

Lucchitta, B. K., 1980. Grooved terrain on Ganymede. Icarus, 44 (2), 481-501.

Lunine, J. I., Stevenson, D. J., 1982. Formation of the Galilean satellites in a gaseous nebula. Icarus 52, 14-39, doi:10.1016/0019-1035(82)90166-x.

McEwen, A. S., Pappalardo, R. T., Griffith, C., Johnson, T. V., Khurana, K., Moore, W., Large Satellites Panel, 2002. Large satellites: active worlds and extreme environments. In: Belton, M. J. S. (Chair), New Frontiers in the Solar System – an integrated exploration strategy, National Research Council, Nat. Acad. Press, pp. 119–149.

McKinnon, W. B., Parmentier, E. M., 1986. Ganymede and Callisto, In: Burns, J. A., Matthews, M. S. (Eds.), Satellites. Univ. of Arizona Press, Tucson, Az., pp. 718-763.

Moore, J. M., Asphaug, E., Morrison, D., Spencer, J. R., Chapman, C. R., Bierhaus, B., Sullivan, R. J., Chuang, F. C., Klemaszewski, J. E., Greeley, R., Bender, K. C., Geissler, P. E., Helfenstein, P., Pilcher, C. B., 1999. Mass movement and landform degradation on the icy Galilean satellites: Results of the Galileo nominal mission. Icarus, 140(2), 294-312.

Moore, J. M., Chapman, C. R., Bierhaus, E. B., Greeley, R., Chuang, F. C., Klemaszewski, J., Clark, R. N., Dalton, J. B., Hibbitts, C. A., Schenk, P. M., Spencer, J. R., Wagner, R., 2004. Callisto. In: Bagenal, F., Dowling, T. E., McKinnon, W. B. (Eds.), Jupiter – the planet, satellites, and magnetosphere. Cambridge Univ. Press, Cambridge, U.K., pp. 397–426.

Mueller, S., McKinnon, W. B., 1988. Three-layered models of Ganymede and Callisto: Compositions, structures, and aspects of evolution, Icarus 76 (3), 437-464, doi:10.1016/0019-1035(88)90014-0.

Murchie, S. L., Head, J. W. III, 1986. Global reorientation and its effect on tectonic patterns on Ganymede. Geophys. Res. Lett. 13 (4), 345-348.

Nesvorný, D., Dones, L., De Prá, M., Womack, M., Zahnle, K. J., 2023. Impact rates in the outer Solar System. Planet. Sci. J. 4:139, https://doi.org/10.3847/ace8ff.

Neukum, G., Wagner, R., Wolf, U., Ivanov, B. A., Head, J. W., Pappalardo, R. T., Klemaszewski, J. E., Greeley, R., Belton, M. J. S., and the Galileo SSI Team, 1998. Cratering Chronology in the Jovian System and Derivation of Absolute Ages. Lunar Planet. Sci. Conf. XXIX, abstr. 1742.

Oberst, J., Schreiner, B., Giese, B., Neukum, G., Head, J. W., Pappalardo, R. T., Helfenstein, P., 1999. The Distribution of Bright and Dark Material on Ganymede in Relationship to Surface Elevation and Slopes. Icarus 140, 283, doi:10.1006/icar.1999.6143.

Pappalardo, R. T., Collins, G. C., 2005. Strained craters on Ganymede, J. Struct. Geol. 27 (5), 827-838, doi:10.1016/j.jsg.2004.11.010.

Pappalardo, R. T., Collins, G. C., Head, J. W. III, Helfenstein, P., McCord, T. B., Moore, J. M., Prockter, L. M., Schenk, P. M., Spencer, J. R., 2004. Geology of ganymede. In: Bagenal, F., Dowling, T. E., McKinnon, W. B. (Eds.), Jupiter – the planet, satellites, and magnetosphere. Cambridge Univ. Press, Cambridge, U.K., pp. 363–396.

Pappalardo, R. T., Head, J. W., Collins, G. C., Kirik, R. L., Neukum, G., Oberst, J., Giese, B., Greeley, R., Chapman, C. R., Helfenstein, P., Moore, J. M., McEwen, A., Tufts, B. R., Senske, D. A., Breneman, H. H., Klaasen, K., 1998. Grooved terrain on Ganymede: First results from Galileo high-resolution imaging. Icarus 135, 276–302, doi:10.1006/icar.1998.5966.

Parmentier, E. M., Squyres, S. W., Head, J. W., Allison, M. L., 1982. The tectonics of Ganymede. Nature 295, 290-293, doi:10.1038/295290a0.

Passey, Q. R., Shoemaker, E. M., 1982, Craters and basins on Ganymede and Callisto - Morphological indicators of crustal evolution. In: Morrison, D. (Ed.), Satellites of Jupiter. Univ. of Arizona Press, Tucson, Az., pp. 379-434.

Patterson, G. W., Collins, G. C., Head, J. W., Pappalardo, R. T., Prockter, L. M., Lucchitta, B. K., Kay, J. P., 2010. Global geological mapping of Ganymede. Icarus 207 (2), 845-867, doi:10.1016/j.icarus.2009.11.035.

Pizzi, A., Domenica, A. D., Komatsu, G., Cofano, A., Mitri, G., Bruzzone, L. 2017. Spreading vs. Rifting as modes of extensional tectonics on the globally expanded Ganymede. Icarus 288, 148-159, doi:10.1016/j.icarus.2017.01.034.

Prockter, L. M., Head, J. W., Pappalardo, R. T., Senske, D. A., Neukum, G., Wagner, R., Wolf, U., Oberst, J., Giese, B., Moore, J. M., Chapman, C. R., Helfenstein, P., Greeley, R., Breneman, H. H., Belton, M. J. S., 1998. Dark Terrain on Ganymede: Geological Mapping and Interpretation of Galileo Regio at High Resolution. Icarus 135 (1), 317-344.

Prockter, L. M., Head, J. W., Pappalardo, R. T., Sullivan, R. J., Clifton, A. E., Giese, B., Wagner, R., Neukum, G., 2002. Morphology of Europan bands at high resolution: A mid-ocean ridge-type rift mechanism. J. Geophys. Res. 107, 5028, doi:10.1029/2000je001458.

Prockter, L. M., Figueredo, P. H., Pappalardo, R. T., Head, J. W. III, Collins, G. C., 2000. Geology and mapping of dark terrain on Ganymede and implications for grooved terrain formation. J. Geophys. Res. 105 (E12), 29,315-29,325, doi:10.1029/2000je000001.

Prockter, L. M., Lopes, R. M. C., Giese, B., Jaumann, R., Lorenz, R. D., Pappalardo, R. T., Patterson, G. W., Thomas, P. C., Turtle, E. P., Wagner, R. J., 2010. Characteristics of Icy Surfaces. Space Sci. Rev. 153, 63-111.

Rossi, C., Lucchetti, A., Massironi, M., Penasa, L., Pozzobon, R., Munaretto, G., Pajola, M., 2023. Multi-phase activity on Ganymede's dark terrain: Tectonic evolution of Galileo Regio. Icarus 390, 115305, doi:10.1016/j.icarus.2022.115305.

Rossi, C., Cianfarra, P., Salvini, F., 2020. Structural geology of Ganymede regional groove systems (60° N–60° S). Journal of Maps, 16 (2), 6-16.

Rossi, C., P. Cianfarra, F. Salvini, G. Mitri, and M. Massé (2018), Evidence of transpressional tectonics on the Uruk Sulcus region, Ganymede, Tectonophysics, 749, 72-87, doi:10.1016/j.tecto.2018.10.026.

Schenk, P. M., Chapman, C. R., Zahnle, K., Moore, J. M., 2004. Ages and interiors: the cratering record of the Galilean satellites. In: Bagenal, F., Dowling, T. E., McKinnon, W. B. (Eds.), Jupiter – the planet, satellites, and magnetosphere. Cambridge Univ. Press, Cambridge, U.K., pp. 427–456.

Schubert, G., Anderson, G. D., Spohn, T., McKinnon, W. B., 2004. Interior composition, structure and dynamics of the Galilean satellites. In: Bagenal, F., Dowling, T. E., McKinnon, W. B. (Eds.), Jupiter – the planet, satellites, and magnetosphere. Cambridge Univ. Press, Cambridge, U.K., pp. 281–306.

Schubert, G., Hussmann, H., Lainey, V., Matson, D. L., McKinnon, W. B., Sohl, F., Sotin, C., Tobie, G., Turrini, D., Van Hoolst, T., 2010. Evolution of icy satellites. Space Sci. Rev. 153, 447–484.

Shoemaker, E. M., Lucchitta, B. K., Wilhelms, D. E., Plescia, J. B., Squyres, S. W., 1982. The geology of Ganymede. In: Morrison, D. (Ed.), Satellites of Jupiter. Univ. of Arizona Press, Tucson, Az., pp. 435–520.

Showman, A. P., Malhotra, R. 1997. Tidal Evolution into the Laplace Resonance and the Resurfacing of Ganymede. Icarus 127, 93-111, doi:10.1006/icar.1996.5669.

Showman, A. P., Stevenson, D. J., Malhotra, R., 1997. Coupled orbital and thermal evolution of Ganymede. Icarus 129, 367–383.

Smith, B. A., Briggs, G. A., Danielson, G. E., Cook, A. F., Davies, M. E., Hunt, G. E., Masursky, H., Soderblom, L. A., Owen, T. C., Sagan, C., 1977. Voyager imaging experiment. Space Sci. Rev. 21, 103–127.

Smith, B. A., Soderblom, L. A., Johnson, T. V., Ingersoll, A. P., Collins, S. A., Shoemaker, E. M., Hunt, G. E., Masursky, H., Carr, M. H., Davies, M. E., Cook, A. F., Boyce, J. M., Owen, T., Danielson, G. E., Sagan, C., Beebe, R. F., Veverka, J., McCauley, J. F., Strom, R. G., Morrison, D., Briggs, G.A., Suomi, V.E., 1979a. The Jupiter system through the eyes of Voyager 1. Science 204, 951–957.

Smith, B. A., Soderblom, L. A., Beebe, R., Joyce, J., Briggs, G., Carr, M., Collins, S. A., Cook II, A. F., Danielson, G. E., Davies, M. E., Hunt, G. E., Ingersoll, A., Johnson, T. V., Masursky, H., Morrison, D., Owen, T., Sagan, C., Shoemaker, E. M., Veverka, J., 1979b. The Galilean satellites and Jupiter – Voyager 2 imaging results. Science 206, 927–950.

Sohl, F., Choukroun, M., Kargel, J., Kimura, J., Pappalardo, R., Vance, S., Zolotov, M., 2010. Subsurface water oceans on icy satellites: chemical composition and exchange processes. Space Sci. Rev. 153, 485 – 510.

Spencer, J. R., 1987a. Icy Galilean satellite reflectance spectra: Less ice on Ganymede and Callisto ? Icarus 70 (1), 99-110, doi:10.1016/0019-1035(87)90077-7.

Spencer, J. R., 1987b. Thermal segregation of water ice on the Galilean satellites. Icarus, 69 (2), 297-313, doi:10.1016/0019-1035(87)90107-2.

Squyres, S. W., 1980. Volume changes in Ganymede and Callisto and the origin of grooved terrain., Geophys. Res. Lett. 7, 593–596.

Stephan, K., Hibbitts, C.A., Ligier, N., Molyneux, P.M., Poulet, F., Prockter, L.M., Hendrix, A.R.m Collins, G.C., Ahrens, C., Jaumann, R. (2024) : Ganymede's Surface Composition. In: Volwerk, M., McGrath, M., Jia, X., Spohn, T. (Eds.), Ganymede. Cambridge Univ. Press, CAmbridge, U. K., pp. 147 – 164, 978-1-108-83295-3.

Stephan, K., Roatsch, T., Tosi, F., Matz, K.-D., Kersten, E., Wagner, R., Molyneux, P., Palumbo, P., Poulet, F., Hussmann, H., Barabash, S., Bruzzone, L., Dougherty, M., Gladstone, R., Gurvits, L. I., Hartogh, P., Iess, L., Wahlund, J.-E., Wurz, P., Witasse, O., Van Hoolst, T., 2021. Regions of interest on Ganymede's and Callisto's surfaces as potential targets for ESA's JUICE mission. Planet. Space Sci. 208, https://doi.org/10.1016/j.pss.2021.105324.

Stone, E. C., Lane, A. L., 1979a. Voyager 1 Encounter with the Jovian System. Science 204, 945-948, doi:10.1126/science.204.4396.945.

Stone, E. C., Lane, A. L., 1979b. Voyager 2 Encounter with the Jovian System. Science 206, 925-927, doi:10.1126/science.206.4421.925.

Sullivan, R., Greeley, R., Homan, K., Klemaszewski, J., Belton, M. J. S., Carr, M. H., Chapman, C. R., Tufts, R., Head, J. W., Pappalardo, R., Moore, J., Thomas, P., 1998. Episodic plate separation and fracture infill on the surface of Europa. Nature 391 (6665), 371-373.

Van Gasselt, S., Rossi, A. P., Loizeau, D., d'Amore, M., 2018. Exploration tools. In: Rossi, A. P., van Gasselt, S. (Eds.), Planetary Geology. Springer Praxis Books, Springer Internat. Pub. AG, pp. 33–53.

Zahnle, K., Dones, L., Levison, H. F., 1998. Cratering rates on the Galilean satellites. Icarus, 136 (2), 202-222.

Zahnle, K., Schenk, P., Levison, H., Dones, L., 2003. Cratering rates in the outer solar system. Icarus 163, 263–289.

8 Appendix A / List of thesis related-publications

Peer-reviewed Publications
Submitted

N.R. Baby, T. Kenkmann, K. Stephan, R. Wagner, E. Hauber (2024) Ray and Halo craters on Ganymede – indicator for subsurface properties of light terrain formation, submitted.

Published

N.R. Baby, T. Kenkmann, K. Stephan, R. Wagner (2024) Polygonal impact craters on Ganymede, Meteoritics and Planetary Science, accepted.

Baby, N. R., R. J. Wagner, K. Stephan, and T. Kenkmann (2023d), Stratigraphy, Crater Size-Frequency Distribution, and Chronology of Selected Areas of Ganymede's Light and Dark Terrains, *The Planetary Science Journal*, *4*, 162, doi:10.3847/PSJ/acebed.

Conference Papers

Baby, N., T. Kenkmann, K. Stephan, and R. Wagner (2023a), Polygonal Impact Craters on Ganymede, edited, p. 315.302.

Baby, N. R., T. Kenkmann, K. Stephan, and R. J. Wagner (2023b), Polygonal impact craters on Ganymede, edited, pp. EGU-354, doi:10.5194/egusphere-egu23-354.

Baby, N. R., T. Kenkmann, K. Stephan, and R. J. Wagner (2023c), Polygonal Impact Craters on Ganymede, paper presented at LPI Contributions, March 01, 2023.

Baby, N. R., K. Stephan, R. Wagner, T. Kenkmann, G. Collins, E. Hauber, and R. Jaumann (2022a), Stratigraphic relationships of different terrain units on Ganymede and possible implications towards their evolution, edited, pp. EPSC2022-1016, doi:10.5194/epsc2022-1016.

Baby, N. R., K. Stephan, R. Wagner, T. Kenkmann, N. Schmedemann, and E. Hauber (2022b), Stratigraphy of Ganymede's light terrain: a case study at Mummu and Sippar Sulci, edited, pp. EGU22-5168, doi:10.5194/egusphere-egu22-5168.

Baby, N. R., K. Stephan, R. Wagner, K. Krohn, and N. Schmedemann (2021), Stratigraphic studies of Ganymede's tectonic activity in the bright terrain: results from the Byblus Sulcus and Harpagia Sulcus regions, edited, pp. EPSC2021-2352, doi:10.5194/epsc2021-352.

Baby, N. R., K. Stephan, R. J. Wagner, T. Kenkmann, N. Schmedemann, and E. Hauber (2022c), Stratigraphy of Ganymede's Light Terrain: A Case Study at Mummu and Sippar Sulci, paper presented at 53rd Lunar and Planetary Science Conference, March 01, 2022.

9 Appendix B / Statement of data availability

I hereby verify that the datasets in Chapters 2, 3, and 4 of this thesis are accessible through the following link: figshare - My data